Tailoring calcium phosphate powder properties for additive manufacturing

Pedro Navarrete-Segado

THÈSE

En vue de l'obtention du

DOCTORAT DE L'UNIVERSITÉ DE TOULOUSE

Délivré par :

Institut National Polytechnique de Toulouse (Toulouse INP)

Discipline ou spécialité :

Génie des Procédés et de l'Environnement

Présentée et soutenue par :

M. PEDRO NAVARRETE SEGADO

le vendredi 1 octobre 2021

Titre :

Tailoring calcium phosphate powder properties for additive manufacturing

---

Ecole doctorale :

Mécanique, Energétique, Génie civil, Procédés (MEGeP)

Unité de recherche :

Laboratoire de Génie Chimique (LGC)

Directeur(s) de Thèse :

MME CHRISTINE FRANCES

M. DAVID GROSSIN

Rapporteurs :

M. ERIC CHAMPION, UNIVERSITE DE LIMOGES

M. KHASHAYAR SALEH, UNIVERSITE DE TECHNOLOGIE DE COMPIEGNE

Membre(s) du jury :

MME ANNE LERICHE, UNIVERSITE DE VALENCIENNES, Président

M. DAVID GROSSIN, TOULOUSE INP, Membre

M. LIAM GROVER, UNIVERSITY OF BIRMINGHAM, Membre

MME CHRISTINE FRANCES, TOULOUSE INP, Membre

MME MALLORIE TOURBIN, TOULOUSE INP, Membre

M. RODRIGO MORENO, Instituto de Cerámica y Vidrio, Membre

For my parents

I hope you'll make mistakes. If you're making mistakes, it means you're out there doing something.

Neil Gaiman

Acknowledgement

From a young age, I always have been fascinated by scientists as Antoine Lavoisier and Marie Curie and dreamt as a researcher to contribute to science one day myself. After my professional stay in Japan, I wondered myself “Ph.D. degree or not?”; I enjoyed my stay abroad and it was my first experience as a researcher then the subject of the Ph.D. position brought together ideas, I always found fascinating. Today, the answer to my question is fairly clear. To do a Ph.D. is not an easy matter and definitely, you do not get a Ph.D. degree done overnight, however, I can look back and feel the gratification of seeing what I have learned, both professionally and about myself. Even if these few words are not enough to thank all the people, I would like to take the opportunity to personally express my deepest gratitude to those who kindly contributed to the success of my Ph.D. offering their help, their advice, and/or their support. If I have today a successful PhD diploma is due to the support and contribution of many people for whom I am completely grateful!

Because their expertise, brilliant ideas, constructive criticism, patience (especially with my French), and full support have made this thesis possible I would like to start thanking my mentors and supervisors. Dr. Christine Frances, thank you for allowing me to be one of her students in the National Polytechnic Institute of Toulouse (Toulouse INP), and as part of the Chemical Engineering Laboratory (LGC), and for the many scientific exchanges and discussions that we have shared during these three years. It has been an honour to work together with such a great professional. Dr. Mallorie Tourbin, always so attentive and kind, I will be eternally grateful for all your support, advice, and encouraging discussion. You both have my gratitude for introducing me to the powder technology and particle engineering world. Thank you very much to Dr David Grossin from the Interuniversity Center of Materials Research and Engineering (CIRIMAT) from which I was part too. You were always one step ahead of everyone. That you always managed to make time for offering help was very appreciated and indispensable for the thesis. A brilliant mind in the field of additive manufacturing and ceramics.

This work would not be feasible without the financial support from the EU research framework programme H2020/ Marie Skłodowska-Curie Actions and the DOC-3D PRINTING project. Thank you for letting my dream come true. Thanks to all the project consortium members, for the time and inspiring ideas we shared on the many different workshops, schools, and congresses. Specially thank you to Guillaume Gentils for his help managing the project and making sure everything works well even the smallest details. Thank you to all the early-stage researchers from the project, more individually to the ones with which I had the opportunity to create not only a professional relationship if not a solid friendship, sharing trips, beers, and life concerns. Eren Ozmen, Nicolas Somers, Ambra Paterlini, Qirong Chen, Giovanni Urruth, Chloé Goutagny, and Asif Ur Rehman between others thank you for your love, affection and support throughout this journey, I am gonna miss you all….

A special thanks to all the technical staff of CIRIMAT and LGC laboratories. Thank you to Marie-Line de Solan Bethmale, Gwénaëlle Guittier, Christine Rey-Rouch, and Marie-Line Pern from the *Service Analyse et Procédés* (SAP) team for your kindness, guidance, and the high quality of your analyses and training, helping me out with instrumentation and the numerous characterisation techniques which make part of this work. From the side of CIRIMAT researchers and technical staff, I have to mention Christophe Drouet (for your kindness and predisposition to help), Cédric Charvillat (a true expert of XRD and TGA analyses which helped me a lot!), Olivier Marsan (expert in FTIR and RAMAN analyses, many thanks!), Carole Thouron (for the help with the mechanical tests and her patient), Yann Thebault and Djar Oquab (for your help with the SEM analyses), Jeremy Soulie, Ghislaine Bertrand, Christian Rey, Diane Samelor, Daniel Sadowski, Dominique Poquillon, Richard Drevet (for your professionality, I wish you the best my friend), Benjamin Duployer and Christophe Tenailleau (for the nice quality of the micro-computed tomography analyses) for their help and for supporting me during the last three years. Caroline, Daniele, Dominique and Katia are thanked for their help with all the paperwork.

During this thesis, I carried out a series of secondments during different periods in the company Marion Technologies (Verniolle) and the Laboratory of Ceramic Materials and Processing (Maubeuge) as part of the Polytechnic University of Hauts-de-France where I acquired the know-how and expanded my knowledge on the processing and additive manufacturing of ceramic materials. Thank you to all the researchers, workers, and students for your kindness and for having integrated me into your work environment even if the duration of the stay was short. These stays were key points for the good development of the thesis.

I should not forget to thank the many colleagues from the different laboratories LCC, LGC, and CIRIMAT with whom I had the chance to share the scientific ideas, workplace, lunch breaks, coffees, and in the end the daily life. I will always remember the nice atmosphere and laughs. They are too many and from very diverse nationalities (France, Italy, Chile, China, Mexico, Brazil, Colombia, Portugal, India, Lebanon, Greece…) to list them all but I guess they know whom I mean and I want to let them know that they always will have a friend in me, wherever we are and that I hope our paths will cross again in the future. To the Alambic group of PhD-students for organizing the great activities I enjoyed and that boosted me with new energy, I'm happy of having been part of the group with many great people.

A huge "thank you" to those that have been my "partners in crime" during this journey, not only as university colleagues but also as flatmates, Dr Alejandro Montón Zarazaga and future Dr. Manuel Flores Perez. Many thanks for having shared all these moments, without you these three years would have been harder and more sorrowful. Guys, you always will be in my heart and you can count on a home in Andalucía or wherever I am. Wishing you the best of luck in your future careers.

A special mention to those that have been my mentors even before I started to think about doing a PhD but they are largely to blame for the fact that today I can define myself as a doctor. Dr. Manuel Melguizo Guijarro and Dr. Antonio Peñas Sanjuán, thank you for awakening my research interest and for

helping me unconditionally during my first steps in the world of research. It looks like yesterday when you first accepted me into your labs. You will always be my model researcher in whom I aspire to become one day. Thank you for being the firsts on allowing me to even start my career in science.

Thank you to Dr. Pablo Orús Calvet and the almost doctor Amelia Dominguez Celorrio for the time shared during our master's degree. It was the start of a long friendship that during the last years carried us very far; from the great Cathedral-Basilica of Our Lady of the Pillar, passing through the Nikko Toshogu Shrine until the top of the Rockefeller Center. If my previous mentors seeded my research interest, you guys were responsible for growing it and keeping it alive. I will be eternally in debt to you for teaching me the good way in research.

Thank you to all the EU-Japan Vulcanus trainees especially for the promotion 2017-18. It was a pleasure to share my first experience abroad with you. Thanks to the Kokubunji team, I will always remember the good time we spent together. Also, Fehmi Yasin, thank you for your kindness, I hope you still cook and play football as good as then. Moreover, from the bottom of my heart thank you to David Álvarez and Carlos Conejo for still keeping in contact after these years, you are the guys more professional and humbler I have ever known. I hope our friendship will stay for many years more wherever we are!

Thank you to my dear mentor Dr. Tomihiro Hashizume during my professional stay at Hitachi, Ltd., Japan, for showing me the work in research from the industrial side. I will always keep in memory the charming moments we shared at work, playing football, and sharing beers with the rest of the workers. I will have always in my memory the lovely people in Hatoyama and Kokubunji laboratories, I wish the best of luck in life.

To the different students, I had the opportunity to mentor during these three years, I wish you the best for your career in industry and research. Especially Marie-Anne Batel who recently started a Ph.D. degree. I hope this degree will bring you the experience and knowledge allowing you to become a great researcher.

Thank you to my childhood friends group “Destroyers” for being always there since I have memory. Ignacio, Manolo, Antonio, Josepe, Dani, and the rest of the people from my hometown that continuously supported me and indeed, being with them I feel at home.

Thank you to Pedro, Ana, Fran, also from my hometown and who had been so good friends for many years. Thank you too for being present and for your valuable support during my thesis defence.

Thank you to the three Marias (short, tall, and chusa), my neighbours (Nora and Flo), the Italian team (Lorenzo, Edoardo, Andrea, Sara, Canio), and Camila, you made my stay in Toulouse much, much better and I really enjoyed the time we spent together. Good luck in life and in your future projects.

To my friend and coach Alberto “Namek”, for keeping my mind and body fit through these three years with the very nice discussions and his excellent recommendation of series, movies, and comics as well as the challenging gym training routines.

To the many content creators of the playlists and movie soundtracks for accompanying me during the office work until very late and during the weekends when I also had to work hard.

To my dear family, for the unconditional love and support, Mama, Papa, my brother. Thanks for all the advice, without your support all these things are impossible. I owe you everything. Also thank you to Tyrion (my cute ginger European shorthair cat) for letting me cuddle it just as an anti-stress ball.

Last but not least, to my dear and beautiful girlfriend Luz del Mar Rus López for your endless and infinite love and support, also your cleverness, ingenuity, and great graphic design ideas and suggestions made this achievement easier. Even in the hardest moments, you demonstrated enough patient to put up with my bad temper and to encourage me. I love you so much.

Finally, I hope this thesis is useful for anyone who read this and especially for the students.

Thanks to all and please keep in touch,

Pedro

Abstract

English: Calcium phosphates ceramics (stoichiometric hydroxyapatite (HA), β-TCP, substituted calcium phosphates, and biphasic compounds) are privileged biomaterials as orthopaedic implants or dental restorations in medical or aesthetics applications. In combination with additive manufacturing technologies, bioceramic parts can be designed with complex shapes with better biocompatibility and bioactivity than metals improving the osseointegration/osseoincorporation of the implant. Powder bed fusion (PBF) and VAT photopolymerization are promising additive manufacturing (AM) groups of techniques allowing the production of functional complex net-shaped or fully dense parts. However, specific tailored ceramic powders for these 3D printing techniques need to be produced. In this context, the challenge here is the evaluation of the characteristics of a suitable feedstock depending of the additive manufacturing technique. HA was chosen as starting material for the production of scaffolds for bone tissue regeneration. In the course of tailoring the AM feedstock properties, depending on the additive manufacturing technique different processes can be necessary. In the case of the PBF techniques, the processability of the powder feedstock is better achieved when using laser-reactive and flowable dry microspheres. In this regard, this thesis deals with the tailoring of the HA particles morphology through a combination of processes such as, synthesis, wet milling, spray drying, and mixing of the powder with absorption additives. For a second AM group of technologies, like VAT photopolymerization, different characteristics are required for the material feedstock. In this case, the production of slurries composed of stable and low viscosity HA powder-filled photosensitive resins was essential. Their preparation was achieved by a milling step of the powder and a proper homogenization of the different components (photoinitiator, monomers, and diluent). Thus, as part of this PhD work the understanding of the relationships between the powder properties and the processing parameters was of special importance. For this reason, a wide variety of powder and suspension characterization methods was employed to assess the effect of the formulation and the operating parameters on the final product properties. It included the analysis of the chemical composition and structure of the compounds, as well as the physical properties of the particles dispersed in a liquid or in a dry state (morphology, flowability, stability, and rheology of suspensions). Finally, the suitability of the feedstock produced was examined through direct testing on the AM technologies and the quality of the printed parts was evaluated in terms of relative density, porosity, and mechanical properties.

Français : Les céramiques de phosphates de calcium (hydroxyapatite stœchiométrique (HA), β-TCP, phosphates de calcium substitués et composés biphasiques) sont des biomatériaux privilégiés comme implants orthopédiques ou pour réaliser des restaurations dentaires dans des applications médicales ou esthétiques. En association avec les technologies de fabrication additive (FA), les pièces biocéramiques peuvent être conçues avec des formes complexes tout en ayant une meilleure biocompatibilité et bioactivité que les métaux améliorant l'ostéointégration/ostéoincorporation de l'implant. La fusion sur lit de poudre (FLP) et la photopolymérisation (VAT) sont des familles de techniques de fabrication additive prometteuses permettant la production de pièces complexes fonctionnelles sous forme de réseaux poreux ou entièrement denses. Cependant, un défi est de produire une poudre céramique ayant des propriétés spécifiques pour ces techniques d'impression 3D. Dans ce contexte, l'enjeu dans cette thèse est l'évaluation des caractéristiques de la matière première adaptée à chaque technique de fabrication additive. HA a été choisie comme matériau de départ pour la production de pièces pour la régénération du tissu osseux. En fonction de la technique de fabrication additive utilisée, différents procédés peuvent être nécessaires pour l'optimisation des propriétés de la matière première à imprimer. Dans le cas des techniques FLP, de meilleurs résultats sont obtenus lors de l'utilisation d'une poudre constituée de microsphères réactives au laser et présentant de bonnes propriétés d'écoulement. Dans cette thèse l'optimisation de la morphologie des particules de HA a été étudiée grâce à une combinaison de procédés tels que la synthèse, le broyage en voie humide, le séchage par atomisation et le mélange de la poudre avec des additifs d'absorption. Pour les technologies de FA telles que la photopolymérisation VAT, des caractéristiques différentes sont requises pour la matière première. Dans ce cas, il est essentiel de produire des suspensions composées de résines photosensibles chargées de poudre d'HA, stables et de faible viscosité. Leur préparation a été réalisée par une étape de broyage de la poudre suivi d'une bonne homogénéisation des différents composants (photoinitiateur, monomère, et diluant). Dans le cadre de cette thèse, la compréhension des relations entre les propriétés de la poudre et les paramètres des procédés sont d'une grande importance. Une large gamme de techniques de caractérisation des poudres et des suspensions a été utilisée pour évaluer l'effet de la formulation et des paramètres opératoires sur les propriétés du produit final à chaque étape. Ces techniques ont permis l'analyse de la composition chimique et de la structure des composés, ainsi que la détermination des propriétés physiques des particules dispersées dans un liquide ou à l'état sec (morphologie, coulabilité, stabilité, et rhéologie des suspensions). Enfin, l'adéquation de la poudre produite a été évaluée directement par des expériences réalisées avec les technologies de FA, et la qualité des pièces imprimées a été analysée en termes de densité relative, de porosité et de propriétés mécaniques.

Table of contents

General Introduction

The rising incidence of bone disorders and the increasing ageing population has generated a growing interest for new efficient therapies. Bone tissue engineering is considered a means for the development of alternatives that could replace conventional bone grafts with the aim of repairing or reconstructing bone defects through the combination of biomaterials, signalling factors, and cells. Calcium phosphate bioceramics are well-known materials in this field because of their excellent bioactive properties, serving as resorbable scaffolds for the bone cells' anchorage, promotion, growth, and differentiation. Thus, helping the bone regeneration process. Most frequently used calcium phosphates are hydroxyapatite (HA) and tricalcium phosphate (TCP), depending on the type of calcium phosphate employed, bioactivity properties can change due to differences in stability, solubility, mechanical strength, and ion release. For this reason, they are usually employed as mixtures to fully benefit from their advantages and minimize their disadvantages.

One of the biggest current challenges in the field is the translation of skeletal tissue engineering to clinical practice. The use of additive manufacturing techniques for bone biofabrication could be the key for its progress. This due to their valuable inherent capability for reproducibility, accuracy and customisation of printed parts. However, the printing of complex and rigid skeletal tissue has not yet reached an optimal maturity state for a real application. In fact, many problems can arise during the printing process and post-processing that can worsen the properties of the scaffolds. Specifically, the main challenges in additive manufacturing of bioceramic scaffolds include the low resolution and speed, optimization of pore parameters, the use of bioincompatible techniques, and the low mechanical strength or brittleness obtained. Ceramic feedstock properties are one of the most influencing parameters that can influence the scaffolds quality during their production. Non-compliance of the requirements of the printer by the feedstock, difficult the obtention of parts meeting the properties needed for its application. For this reason, an extensive knowledge is required about their production and the tailoring of their characteristics.

In this context and as part of the EU research framework programme H2020/ Marie Skłodowska-Curie Actions the DOC-3D PRINTING network (cordis.europa.eu/project/id/764935) was conceived (Marie Curie grant agreement number 764935). It is a transnational multidisciplinary EU network focused on ceramics additive manufacturing applied on medical and aerospace fields. The team includes six academic, one non-profit association and seven non-academic (large companies and SME) partners with varied expertise. The 14 early-stage researchers (PhD) composing the network are intended to study and develop the whole value chain of ceramics 3D printing from elaborating feedstock to testing in products for commercialisation. More specifically, the present three-years long doctoral study focuses on the "**tailoring of calcium phosphate powder properties for additive manufacturing technologies**" with the "Centre Inter-universitaire de Recherche et d'Ingénierie des Matériaux" (CIRIMAT) and the "Laboratoire de Génie Chimique" (LGC), which are part of the national polytechnic institute of Toulouse (Toulouse INP), acting as host institutions. As result, this manuscript composed of six chapters was made gathering the state-of-the-art knowledge on the topic and the different scientific results obtained during the course of the study.

Chapter I serves as a bibliographic introduction to the most relevant concepts presented in the work. First, calcium phosphate materials are, as main protagonists, introduced and their properties are detailed. Then, the different additive manufacturing technologies are located giving a special relevance to the two techniques treated in this work, the powder bed selective laser process (PBSLP) and the masked stereolithography (MSLA). It concludes with a brief explanation of the two techniques with highest significance for our work on the calcium powders tailoring: the stirred bead mill (SBM) and the spray drying (SD) processes.

Chapter II brings a first contact with the materials and methods used along our work. Brief theoretical explanation of the techniques used for the characterization of the prepared feedstock and printed products. It also includes the procedures followed for the synthesis of HA and chlorapatite (ClA) calcium phosphate powders as well as the study of their composition.

In the course of optimizing the feedstock qualities, depending on the additive manufacturing technique, some other processes can be indispensable. In the case of PBSLP technique, the processability of the powder feedstock is better achieved when using flowable dry spherical agglomerates of several tens of microns as diameter. In this regard, chapters III and IV deal with the tailoring of the HA particles morphology through a combination of milling and spray drying processes, respectively. Both procedures are exhaustively studied for better understanding and optimization of process conditions.

The importance of the characteristics of the HA and ClA powders is disclosed in chapter V through the analysis of their performance in a PBSLP process. A study of the processing window depending on the properties of the powder employed as well as the printing parameters is offered, including the analysis and the evaluation of the quality of the obtained printed parts.

As mentioned previously, a second AM technology, the MSLA process, was also envisaged for the tailoring of the powders. Chapter VI presents the evaluation of different prepared HA-filled photocurable slurries for their use as feedstock in an MSLA process. Finally, the properties of the printed HA scaffolds as bone graft substitutes are assessed.

Short Thesis outline

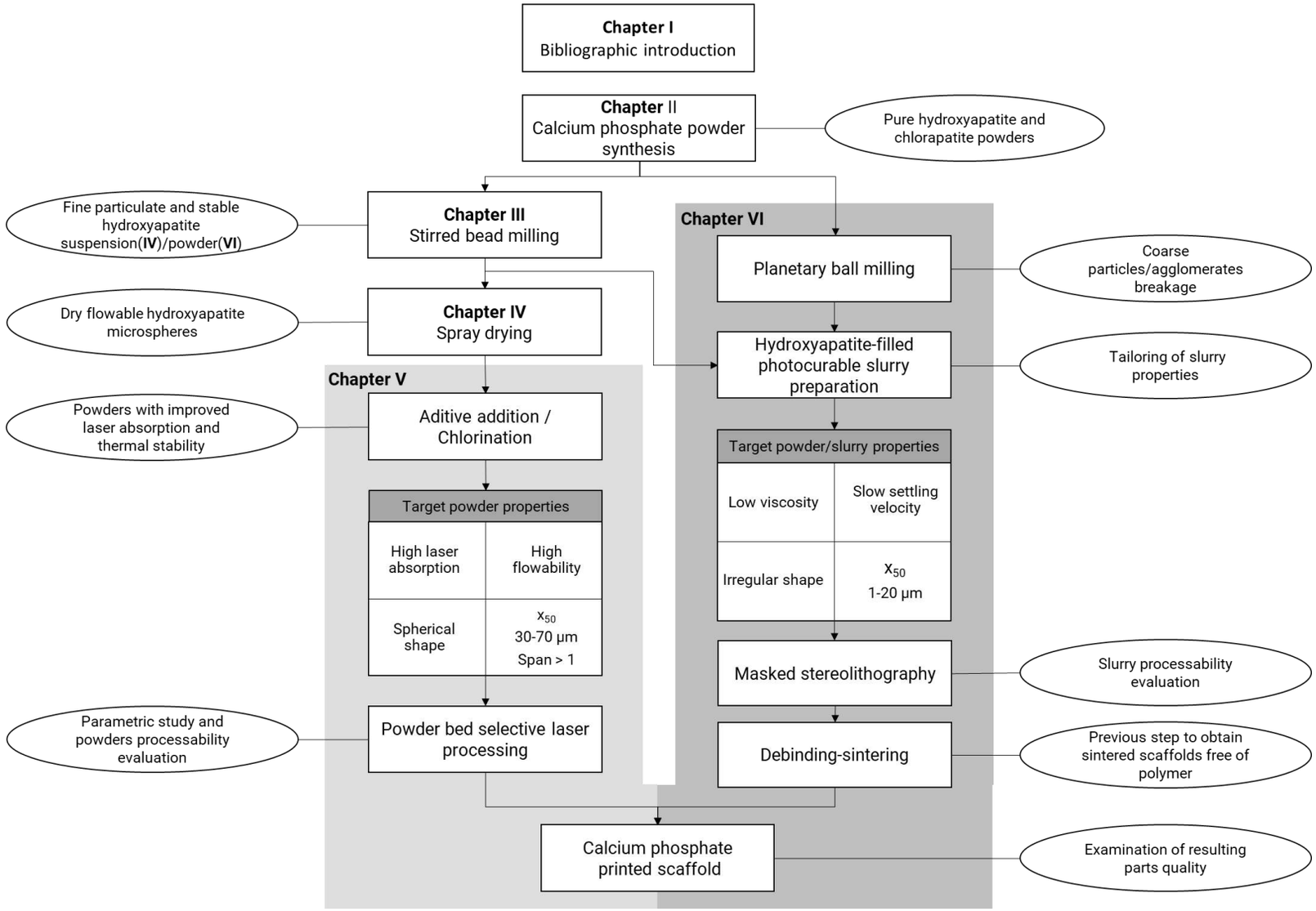

List of abbreviations

v_{Stokes}, v_{∞}	Stokes's velocity
v_{as}	Asymmetric stretching
v_s	Symmetric stretching
µ-CT	X-ray microtomography
3D	Three-dimensional
A	Absorptance
AAS	Atomic absorption spectroscopy
ACP	Amorphous calcium phosphate
AM	Additive manufacturing
AMCSD	American mineralogist crystal structure database
APS	Atmospheric plasma spray
ASTM	American society for testing and materials
ATCP	Amorphous tricalcium phosphate
BAP	Bioapatite
BCP	Biphasic calcium phosphate
BET	Brunauer-Emmett-Teller
BJH	Barrett-Joyner-Halenda
BS	Backscattering
CAD	Computer-aided design
CaO	Calcium oxide
CaP	Calcium phosphate
CDHA	Calcium-deficient hydroxyapatite
CEN/TC	European committee for standardization/technical committee
CHN	Carbon hydrogen nitrogen analyzer
CIF	Crystallographic information framework
CIRIMAT	Centre inter-universitaire de recherche et d'ingénierie des matériaux
ClA	Chlorapatite
ClHA	Chlorine-substituted HA
COD	Crystallography open database
CT	X-ray computed tomography
DC	Darvan C
DCPA	Dicalcium phosphate anhydrous
DCPD	Dicalcium phosphate dihydrate
DED	Directed energy deposition
DEF	Diethyl fumarate
DLP	Digital light processing
DMD	Digital micromirror device
DSC	Differential scanning calorimetry
ECM	Extracellular matrix
EDS	Energy dispersive X-ray spectroscopy
EDTA	Ethylenediaminetetraacetic acid
EP	Epoxy resin.
ESEM	Environmental scanning electron microscope
FA	Fluorapatite
FDM	Fused deposition modelling
FEG	Field emission gun
ffc	Flowability coefficient, flow function coefficient
FHA	Fluorine-substituted HA
FTIR	Fourier transform infrared spectroscopy
G	Graphite
GM	Grinding media
HA	Hydroxyapatite
HA_Cyl	Calcium phosphate cylinders
HA_Cyl_PT	Calcium phosphate cylinders after post-treatment.
HAm	Hydroxyapatite microspheres
HDPE	High-density polyethylene
HR	Hausner ratio
HR	High reactive
ICDD	International centre for diffraction data
ICP	Inductively coupled plasma
ICP/AES	Inductively coupled plasma atomic emission spectroscopy
ICSD	Inorganic crystal structure database

IPA	Isopropyl alcohol
ISO	International Organization for Standardization
IUPAC	International union of pure and applied chemistry
JCPDS	Joint committee on powder diffraction standards
LAB	Laser-assisted bioprinting
LBM	Laser beam melting
LCD	Liquid-crystal display
LDV	Laser doppler velocimetry
LED	Light-emitting diode
LED	Linear energy density
LFD	Large field detector
LGC	Laboratoire de génie chimique
MBAm	N,N'-Methylenebisacrylamide
M_{CaO}	Molar weight of calcium oxide
MCPA	Monocalcium phosphate anhydrous
MCPM	Monocalcium phosphate monohydrate
M_{HA}	Molar weight of hydroxyapatite
MSLA	Masked stereolithography
$M_{\beta\text{-}TCP}$	Molar weight of β-tricalcium phosphate
Nd:YAG	Neodymium-doped yttrium aluminium garnet
NF	Norme Française (French standard)
NMR	Nuclear magnetic resonance
OA, OAP, OXA	Oxyapatite
OCP	Octacalcium phosphate
OHA	Oxyhydroxyapatite
PBF	Powder Bed Fusion
PBM	Planetary ball mill
PBM	Population balance modelling
PBSLP	Powder bed selective laser processing
PCL	Polycaprolactone
PDLLA	Poly-d,l-lactic acid
PEG200	Polyethylene glycol 200
PGT	Princeton Gamma Tech
PHBV	Poly(3-hydroxybutyrate-co-3-hydroxyvalerate)
PLA, PDLA, PLLA	Poly(lactic acid)
PM	Powder mixture
PP	Polypropylene
PPF	Polypropylene fumarate
PSD	Particle size distribution
PVA	Polyvinyl alcohol
R	Reflectivity
Ra	Raw area
Ra	Roughness average
S.A.	Société anonyme (anonymous society, company)
SAED	Selected area electron diffraction
SAP	Analysis and processes service
SBM	Stirred bead mill
SD	Spray drying
SED	Surface energy density
SEM	Scanning electron microscopy
SHA	Substituted hydroxyapatite
SLA	Stereolithography
SLM	Selective laser melting
SLS	Selective laser sintering
SMEs	Small and medium-sized enterprises
T	Transmission
TA6V	Titanium alloy with aluminium and vanadium
TCP	Tricalcium phosphate
TEM	Transmission electron microscopy
TGA	Thermogravimetric analysis
TRIS	Tris(hidroximetil)aminometano
TSI	Turbiscan stability index
TTCP	Tetracalcium phosphate
UV	Ultraviolet
UV-Vis	Ultraviolet-visible
VP	Variable pressure

WDS	Wavelength dispersive spectrometry
XRD	X-ray diffraction
YSZ	Yttria-stabilized zirconia
α-TCP	α-Tricalcium phosphate
β-TCP	β-Tricalcium phosphate

Symbols

ε	Porosity of the grinding media filling at rest [-]
h_{space}	Hatching distance [cm]
P_{laser}	Laser power [W]
R_b	Bragg error [%]
R_{exp}	Residual exponential distribution [%]
R_{wp}	Weighted residual profile [%]
U_E	Electrophoretic mobility [$cm^2.V^{-1}.s^{-1}$]
t_{layer}	Layer thickness [cm]
v_{scan}	Scanning speed [$cm.s^{-1}$]
$\dot{\gamma}$	Shear rate [s^{-1}]
$[\eta]$	Intrinsic viscosity [s^{-1}]
A_{UCT}	Cross-sectional area [mm^2]
B	Build rate coefficient [$mm^3.s^{-1}$]
C_{DC}	Darvan C concentration [$mg.m^{-2}$]
d	Diameter [µm]
$E(t)$	Residence time density function [-]
E_d	Volumetric energy density [$J.cm^{-3}$]
E_m	Specific energy [$kJ.kg^{-1}$]
f_c	Unconfined yield strength [-]
ff_c	Flowability coefficient, flow function coefficient [-]
g	Optical parameter given by Mie theory
HR	Hausner ratio [-]
h_{space}	Hatch distance [mm]
K	Consistency index [$Pa.s^n$]
k	Thermal conductivity [$M.m^{-1}.K^{-1}$]
m_p	Product mass [kg]
n	Number of revolutions [s^{-1}]
n	Flow behaviour index [-]
n	Empirically determined exponent dependent on the particle Reynolds number [-]
N_c	*N*umber of bead contacts [-]
N_c	Normal load [MPa]
N_f	Normal force at specimen failure [MPa]
N_{GM}	*N*umber of grinding beads in the mill [-]
N_p	Number of feed particles inside the mill [-]
P	Power input (power draw) [W]
P	Spray air pressure [bar]
P_0	No-load power [W]
P_{laser}	Laser power [$J.s^{-1}$]
P_s	Probability that a particle is caught and sufficiently stressed [-]
Qs	Feed rate [$kg.h^{-1}$]
Qs	Optical parameter given by Mie theory
R	Reynolds number [-]
R^2	Coefficient of determination [-]
SE_{GM}	Stress energy of the grinding media [J]
SI	Stress intensity [$J.kg^{-1}$]
Sig	Sigma [%]
SN	Stress number [-]
t	Comminution time [s]
t	Process duration [s]
T_{int}	Inlet temperature [ºC]
t_{layer}	Powder layer thickness [mm]
V_{GC}	Grinding chamber volume [m^3]
V_{GM}	Overall solid volume of the grinding media [m^3]
V_p	Average volume of one product particle [m^3]
$V_{p,tot}$	Total volume of the product particles [m^3]
V_r	Stirrer speed [$m.s^{-1}$]
v_{scan}	Scanning speed [$mm.s^{-1}$]
w	Terminal settling velocity of a solitary particle in a fluid [$m.s^{-1}$]
w_{HA}	Hydroxyapatite solid mass fraction [-]

w_m	Settling velocity of sediment particles dispersed at the volumetric concentration c [m.s^{-1}]
w_p:w_{GM}	Powder/grinding media weight ratio [-]
x_{10}	the 10th percentile [µm] (diameter of a sphere at which 10% of the particles in the sample are smaller)
x_{50}	Median particle size [µm] : the 50th percentile (diameter of a sphere at which 50% of the particles in the sample are smaller)
x_{90}	The 90th percentile [µm] (diameter of a sphere at which 90% of the particles in the sample are smaller)
x_f	Final particle size [µm] (after milling process)
x_{GM}	Grinding media size [µm]
x_i	Initial median particle size [µm] (before milling process)
α	Acceleration [m.s^{-2}]
β	Effective packing factor of ceramic powder
ε	Dielectric constant of the medium [-]
η	Viscosity [Pa.s]
η_{medium}	Viscosity of the medium [Pa.s]
η_r	Relative viscosity
κ	Debye length [m^{-1}]
κα	Thickness of electrical double layer to particle diameter ratio [-]
λ	Wavelength
λ^*	Photon transport mean free path
ρ_{GM}	Grinding media density [kg.m^{-3}]
ρ_{GM}	Grinding media density [kg.m^{-3}]
τ	Shear stress [Pa]
φ	Volume fraction [-]
φ_{GM}	Beads filling degree [-]
χBS	Average of χi
χi	Average backscattering for each minute of measurement
E	Electric field [V.m^{-1}]
φ_m	Maximum volume fraction of solids in the suspension [-]

Chapter I. Bibliographic introduction

This chapter gives a general description of the most relevant materials and methods we made use of during the course of this thesis work. First, calcium phosphates are detailed referring to the most important works on the topic, thus gathering information about their composition, classification, properties, and applications.

It is followed by a listing of the existing additive manufacturing technologies and their different approaches to bone scaffold fabrication using calcium phosphates as feedstock material. Special emphasis is given to the two techniques used in this work, powder bed selective laser process (PBSLP) and masked stereolithography (MSLA). A description of these processes and the main parameters involved are given. Precisely, a review published in Open Ceramics and titled "A review of additive manufacturing of ceramics by powder bed selective laser processing (sintering/melting): Calcium phosphate, silicon carbide, zirconia, alumina, and their composites" was previously reported with the contribution of the present author (Grossin, Monton, Navarrete-Segado et al., 2021). Extracts of the sections contributed by the author to this review will be provided for the sections related to the PBSLP technique: 2.1.1 Powder feedstock criteria, 2.1.2 Process parameters and strategy, and 2.1.3 PBSLP of calcium phosphate ceramics.

The discussion of the material feedstock requirements of each of the two techniques (PBSLP and MSLA) leads us to the last part of the chapter. It consists of the definition of the two main processes we employed for the tailoring of calcium phosphate powders properties: stirred bead milling and spray drying. Thus, this chapter ends with a short explanation of the technique fundament and the influence of the operating parameters on the final product properties.

1. Introduction to calcium phosphates

Calcium phosphate (CaP), with empiric formula $Ca_3(PO_4)_2$, is a family of minerals containing calcium cations (Ca^{2+}) together with orthophosphate (PO_4^{3-}), metaphosphate (PO_3^-), pyrophosphate ($P_2O_7^{4-}$) anions, or hydrogen phosphate (HPO_4^{2-}). CaP is the main form of calcium found in bovine milk and it is known that bone tissue is 60% composed of carbonated hydroxyapatite (HA); it receives the name of bone mineral (also called inorganic bone phase, bone salt, or bone apatite) (Eliaz and Metoki, 2017). CaPs with a Ca/P atomic ratio between 1.5 and 1.67 are called apatites (e.g., HA or fluorapatite). Following, a brief overview of CaP bioceramics structure, properties, and biomedical applications is offered. A more extended description of these ceramics based on calcium phosphate and their application in the field of bone regeneration was stated by Eliaz and Metoki (Eliaz and Metoki, 2017).

The structure of bones, teeth, and other calcified tissues has been studied from the last quarter of the 17th century (Wdfert, 1697). According to the available literature, in 1881 Roscoe and Schorlemmer published the following statement: "Gahn, in 1769, discovered the existence of calcium phosphate in bones, but it was not until this fact was published by Scheele in 1771 that phosphorus was obtained from bone ash, which has from that time invariably served for its preparation" (Dorozhkin, 2012). The organic-inorganic composite nature of bone has been known since at least 1788. In the last decade of the 18th century, the existence of acidic CaPs was discovered by the French chemists Antoine François Comte de Fourcroy and

Nicolas Louis Vauquelin. A summary of the different CaP phases and their corresponding formulas are summarized in Table 1 (Canillas et al., 2017). CDHA, HA, FA, ClA, and OA belong to the apatite group while MCPM, MCPA, DCPD, and DCPA belong to the acidic phases group. It is important to reference the early books on the field. The earliest collected book of 1983 was edited by de Groot (de Groot, 1984), followed by a book of 1984 edited by Misra (Misra, 1984), while three most important monographs on apatites and other calcium orthophosphates were published in 1991 by LeGeros (LeGeros, 1991) and Aoki (Aoki, 1991), as well as in 1994 by Elliott (Elliott, 1994). An example of a more recent contribution on the synthesis, characterization, and applications of calcium phosphates was offered by Rey et al. (Rey et al., 2017).

Table 1. Summary of CaP phases, their corresponding Ca/P molar ratios, abbreviations, and formulas.

Name	Chemical formula	Ca/P	Typical abbreviations
Monocalcium phosphate monohydrate	$Ca(H_2PO_4)_2 \cdot H_2O$	0.5	MCPM
Monocalcium phosphate anhydrous	$Ca(H_2PO_4)_2$	0.5	MCPA or MCP
Dicalcium phosphate dehydrate (mineral brushite)	$CaHPO_4 \cdot 2H_2O$	1.0	DCPD
Dicalcium phosphate anhydrous (mineral monetite)	$CaHPO_4$	1.0	DCPA or DCP
Octacalcium phosphate	$Ca_8(HPO_4)_2(PO_4)_4 \cdot 5H_2O$	1.33	OCP, OCPt
Alpha-Tricalcium phosphate	α-$Ca_3(PO4)_2$	1.5	α-TCP
Beta-Tricalcium phosphate	β-$Ca_3(PO4)_2$	1.5	β-TCP
Amorphous calcium phosphates	$Ca_xH_y(PO_4)z \cdot nH_2O$, n=3−4.5;15%–20%$H_2O$	1.2-2.2	ACP
Calcium-deficient hydroxyapatite	$Ca_{10-x}(HPO_4)_x(PO_4)_{6-x}(OH)_{2-x}$ (0<x<1)	1.5-1.67	CDHA, CDHAP, pHA, pHAP or Ca-def HAP
Hydroxyapatite	$Ca_{10}(PO_4)_6(OH)_2$	1.67	HA, HAP or OHAP
Fluorapatite	$Ca_{10}(PO_4)_6F_2$	1.67	FA or FAp
Chlorapatite	$Ca_{10}(PO_4)_6Cl_2$	1.67	ClA or ClAp
Oxyapatite	$Ca_{10}(PO_4)_6O$	1.67	OA, OAP or OXA
Tetracalcium phosphate (mineral hilgenstockite)	$Ca_4(PO_4)_2O$	2.0	TetCP or TTCP

1.1 Important properties for bone grafting

Calcium phosphates are widely used in medical applications in many different ways such as coating, paste, scaffold, and cement. In the case of bone graft, the main role is to provide a framework for the regeneration of new bone tissue, soft tissue, vascular-, and other metabolic components (Habraken et al.,

2016). For correct performance, these materials have to gather several critical properties. Some of these properties are listed in Table 2.

Bioactivity can be defined in different ways depending on the field in which it is used. In the field of polymeric materials applied to biology, the International Union of Pure and Applied Chemistry (IUPAC) defines it as "the capacity of a substance to elicit a response from a living system" (Vert et al., 2012). In the domain of inorganic biomaterials, bioactivity is defined as the ability to induce a biological response in the biomaterial/host tissue interface allowing the formation of bonds between tissue and material (ISO 23317, (Hench, 1991)). In the case of calcium phosphates, they can partially dissolve themselves releasing ionic products *in vivo*, like calcium and phosphate ions, and precipitating a biological apatite on the surface of the ceramics. However, some CaPs can be highly **biostable** maintaining their physical and chemical integrity after implantation into living tissue (e.g., highly crystallized HA) (Fulmer et al., 2002). Most CaPs ceramics are also **biocompatible**, meaning that they do not unchain any kind of response from the immune system of the organism or tissue. This high degree of biocompatibility of CaP materials is directly related to its similarity to the composition of the bone mineral due to the high presence of them in the body in both solid and dissolved form (Posner and Betts, 1975).

In Figure 1 are represented **osteoinduction**, **osteogenesis**, and **osteoconduction**, the three essential elements of bone regeneration along with the final bonding between host bone and grafting material which is called **osteointegration** (Hench, 1991). Suggested definitions by Albrektsson and Johansson (Albrektsson and Johansson, 2001) of these terms are offered below:

- Osteoinduction represents the ability of a biomaterial to induce the recruitment and differentiation of local cells allowing the formation of a mineralizable bone matrix at a non-bone site. Thus, an osteoinductive biomaterial stimulates the progenitor cells present in the surrounding tissues of the implantation area and causes their differentiation into bone cells. This capacity is strongly linked to the presence of growth factors such as bone morphogenetic proteins and cytokines which are either associated with the material or present in the surrounding biological fluids.
- Osteogenesis is made possible by the presence of bone-forming cells, such as osteoblasts, capable of inducing bone neoformation. An osteogenic biomaterial would contain bone-forming cells or allow their recruitment to induce rapid bone neoformation inside or on the surface of the biomaterial.
- Osteoconduction is defined as the ability of a material in contact with healthy bone tissue to act as a support to guide the new bone formation and allow the formation of an intimate and solid interface. It closely depends on the porosity of the material (size and shape), the specific surface area and the surface state of the biomaterial which will influence the migration and the cellular and vascular colonization of the substitute from healthy tissues.

The use of CaPs in the bone replacement field requires good mechanical properties. This is due to the high average load that the parts undergo during their lifetime. For example, the hip joints have to endure peak loads as high as 10 times body weight during jumping. Depending on the activity the repetitively and fluctuation of the stresses are different. CaPs are brittle (primary ionic bonds) with relatively low tensile stress (6 to 10 MPa) and low impact resistance because of their porosity acting as preferred initiation sites for crack propagation. However, their compressive strength is higher than that of normal bone. For that reason, CaPs are more used in non-load bearing implants like middle ear surgery, as a coating on dental and orthopaedic metallic implants (**interfacial stability**), or as the filler of bone defects in the skeleton and oral cavity.

Table 2. Major properties of calcium phosphates for medical applications following the order of mention in the text. Adapted from (Eliaz and Metoki, 2017)

Property	Definition/Function
Bioactivity	The inherent ability of a material to participate in specific biological reactions or have an effect on living tissues
Biostability	The ability of a material to maintain its properties in vivo
Biocompatibility	The ability of a material to perform with an appropriate host response in a specific application
Osteoinduction	The ability of a biomaterial to induce the recruitment and differentiation of local cells allowing the formation of a mineralizable bone matrix at a non-bone site.
Osteogenesis	The process of laying down new bone material by bone-forming cells, such as osteoblasts
Osteoconduction	The ability of a material in contact with healthy bone tissue to act as a support to guide the new bone formation and allow the formation of an intimate and solid interface
Osseointegration	The ability of the material to bind to host tissue without a layer of fibrous tissue
Interfacial stability and good adhesion	Prevent mechanical failures under load-bearing conditions
Bioactive fixation	Reactive surfaces form chemical bonding with bone, thus minimizing the fibrous capsule formation
Resorption	Gradual degradation over time to replace the biomaterial with the natural host tissue
Crystallinity	A higher level of crystallinity prevents fast resorption (dissolution) of the bioceramic in body fluids
Wettability	The property that indicates a material's ability to attract/repel water molecules

A stable interface between the cementless implants and bone is required for a correct bioceramic tissue fixation. There are four types of attachments: (1) **Bioactive fixation**, where some bioceramics like HA show reactive surfaces able to form chemical bonds, minimizing the fibrous capsule formation. (2) Dense, porous (or nonporous) resorbable bioceramics like TCP are progressively replaced by bone tissue. (3) Biological fixation, where the porous surface of the material induces a mechanical attachment. (4) Morphological fixation, in this case, is a dense, nonporous, nearly inert ceramic that by cementing the device into the tissue or by press-fitting into a defect it is attached by bone growth into surface irregularities.

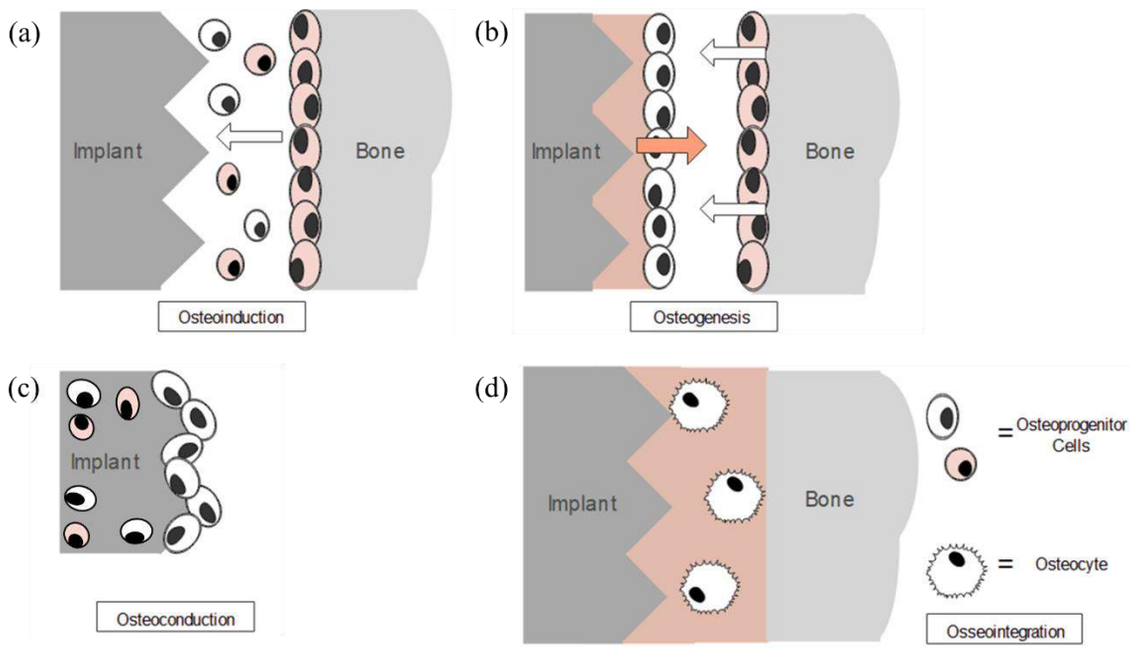

Figure 1. Osteoinduction (a) is the ability of a material to recruit and induce progenitor cells to differentiate towards the osteoblastic lineage. Osteogenesis (b) is initiated by the osteogenic cells migrating from the host bone border (direct osteogenesis, white arrows) and by the osteogenic cells colonizing the implant surface (contact osteogenesis, orange arrow). Osteoconduction (c) involves support of osteogenic cells adhesion/proliferation and integration of cells in the implant. An adequate formation and bone viability (presence of osteocytes) surrounding the implant allows for successful osseointegration (d) at the bone-implant interface. Adapted from (Alejandro et al., 2011).

Resorption is the term used to describe the absorption of a bioceramic in the body, either by dissolution or by cells (such as macrophages and osteoclasts). This property depends on the phase content of the CaP, **crystallinity**, particle size and porosity. Some phases like TCP may resorb fast and replace the coating or cement with bone. More specifically, concerning HA, its resorption rate in a physiological environment depends on its crystallinity. Low crystallinity HA resorbs slowly, while high crystallinity renders HA almost non-resorbable (and exhibit low solubility) (Ben-Nissan, 2014). Grain size, porosity, specific surface, and ionic substitution are other factors that influence the resorption of HA. A small grain size with a high specific surface gives a larger exposed area to osteoclastic resorption, bone-resorbing cells, favouring the resorption. Moreover, a higher degree of porosity means a higher surface area in contact between the implant and the body fluids, inducing a faster dissolution rate. Some studies have demonstrated how the increase of the specific surface area and pore volume of biomaterials produce an acceleration of the

kinetic process of biological apatite deposition and therefore enhance bone formation. The lattice defects in the CaPs structure can influence the solubility of the scaffolds, it explains the large differences in solubility between scaffolds prepared with the same CaP. The rate of bone substitution also depends on age, sex and general metabolic health of the recipient, even on the anatomic site. The desired resorbability rate is the rate comparable to the formation of bone tissue (between a few months and a few years), in the case of CaP, it may take 3 to 36 months to be replaced by bone (Dorozhkin and Epple, 2002).

The **wettability** (or hydrophilicity), and hence the surface energy of CaPs, is a key factor in osteogenesis regulation. Generally, a positively charged surface becomes hydrophilic, and some plasma proteins essential for cell interaction adsorb to the surface. Hydrophilic (high surface energy) implants experience enhanced fibroblast cell response. Aronov et al.(Aronov et al., 2006) through a post-treatment were able to tune the wettability of HA ($10°<\theta<100°$, where θ is the contact angle) by exposure to low-energy electron irradiation. It also affects other cellular activities like maturation, differentiation, and osseointegration. Higher surface energy exhibited faster cell activation and differentiation than those with lower surface energy.

Another important factor is the chemical resistance of the implants. The human body is a very aggressive environment for metals since it contains water, salt, dissolved oxygen, bacteria, proteins, and various ions such as chloride and hydroxide. HA coatings have been demonstrated to have excellent corrosion resistance; that is why they are widely used to coat base metals to ensure biocompatibility of the ceramic on the metal surface (Sudha et al., 2018). Furthermore, another benefit of HA is its dielectric properties because electromagnetic fields have been shown to accelerate healing in bone fractures (Kao et al., 2019).

1.2 Individual Calcium Phosphate phases and their properties

In this section, the properties of the most used calcium phosphates phases for the clinical purpose will be described.

The solid-state phase diagram of the CaP system is relatively unexplored maybe due to the importance that metastable phases, water, and kinetics have in this system (Eliaz and Metoki, 2017). Water and temperature have a large effect in defining thermodynamically stable salts. One of the different versions of this phase diagram without water vapour is showed in Figure 2 (Groot, 1988). It puts in evidence the HA calcium phosphate phase which is in the scope of the present work.

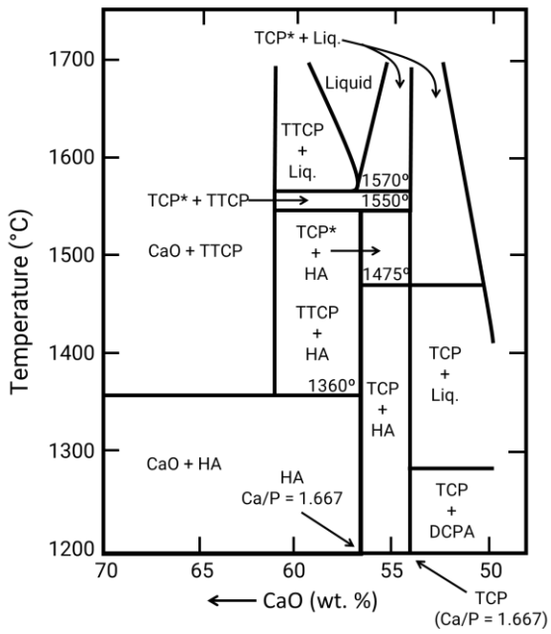

Figure 2. Phase diagram of CaO/P_2O_5 mixtures without water vapour. Adapted from (Groot, 1988). TCP refers to the super α polymorph (also called alpha prime, α') of tricalcium phosphate obtained at temperatures above approximately 1500ºC (Hench and Best, 2013).*

Table 3 summarizes the values of solubility, density, and pH stability ranges of the CaP materials having more interest in biomedical applications. A clear relation between a lower Ca/P atomic ratio with higher solubility and acidity of the CaP phase can be observed. The comparative solubility in acidic buffer decreases in the following order: ACP >> α-TCP >> β-TCP > CDHA >> HA. The information of their crystallographic structure is summarized in Table 4.

Table 3. Solubility, density and pH stability ranges of CaP phases of interest for biomedical applications. Adapted from (Eliaz and Metoki, 2017)

Ca/P Molar Ratio	Name	pH Stability Range	Density ($g.cm^{-3}$)	Solubility at 25°C, -log(Ks)	Solubility at 25°C, g/L
0.5	MCPM	0.0–2.0	2.22	1.14	~18
1.0	DCPA	2.0-5.5 (>80 °C)	2.929	6.90	~0.048
1.0	DCPD	2.0-6.0	2.319	6.59	~0.088
1.33	OCP	5.5-7.0	2.673	96.6	~0.0081
1.5	α-TCP	Precipitated from aqueous solutions only at T>1125 °C	2.814	25.5	~0.0025
1.5	β-TCP	Precipitated from aqueous solutions only at T>800 °C	3.067	28.9	~0.0005
1.2-2.2	ACP	~5-12*	-	**	-
1.50-1.67	CDHA	6.5-9.5	-	85.1	~0.0094
1.67	HA	9.5-12.0	3.155	116.8	~0.0003
2.0	TTCP	Precipitated from aqueous solutions only at T>1300 °C	3.056	38-44	~0.0007

** Always metastable. The composition of the precipitate depends on the composition and pH of the electrolyte solution. ** Cannot be measured precisely. However, the following values were found: 25.7 ± 0.1 (pH = 7.40), 29.9 ± 0.1 (pH = 6.00), 32.7 ± 0.1 (pH = 5.28).*

Table 4. Crystallographic data on selected CaP phases. Adapted from (Eliaz and Metoki, 2017)

Name	Space Group	Unit Cell Parameters	JCPDS *,** File	Main diffraction lines
MCPM	Triclinic $P\bar{1}$	a = 6.250, b = 11.892, c = 5.629 Å α = 96.67°, β = 114.20°, γ = 92.95°	00-009-0347	
DCPA	Triclinic $P\bar{1}$	a = 6.910, b = 6.627, c = 6.998 Å α = 96.34°, β = 103.82°, γ = 88.33°	00-003-0398, 00-004-0513, 00-009-0080, 01-075-1520, 04-009-3755, 04-009-6216, 04-011-3070	
DCPD	Monoclinic *Ia*	a = 5.812, b = 15.180, c = 6.239 Å β = 116.42°	00-009-0077, 00-011-0293, 04-008-2081, 04-013-3344	
OCP	Triclinic $P\bar{1}$	a = 9.529, b = 18.994, c = 6.855 Å α = 92.33°, β = 90.13°, γ = 79.93°	00-026-1056, 00-044-0778, 04-013-3883, 04-016-3473	
α-TCP	Orthorhombic (Monoclinic $P2_1/a$)	a = 15.220, b = 20.710, c = 9.109 Å α = β = γ = 90°	**00-009-0348,** 04-018-9895, 00-029-0359	441, 170
β-TCP	Rhombohedral $R3c$	a = b = 10.439, c = 37.375 Å α = β = 90.00°, γ = 120.00°	**00-009-0169**, 00-070-2065, 04-002-4776, 04-008-8714	0.2.10
CDHA	Hexagonal $P6_3/m$	a = b = 9.4157–9.4490, c = 6.8777–6.8865 Å α = β = 90°, γ = 120°	00-046-0905	
HA	Monoclinic $P2_1/b$ or Hexagonal $P6_3$/m***	a = 9.84214, b = 2a, c = 6.8814 Å, γ = 120.00° (monoclinic). a = b = 9.418, c = 6.884 Å a = b = 90.00°, γ = 120.00° (hexagonal)	**00-009-0432**, **00-072-1243**, 00-024-0033, 01-074-0565, 01-074-0566, 01-084-1998, 01-089-4405, 04-007-2837, 04-007-5086, 04-016-1185	210, 211
TTCP	Monoclinic $P2_1$	a = 7.018, b = 11.980, c = 9.469 Å, α = γ = 90.00°, β = 90.88°	**00-025-1137**, 070-1379, 00-011-0232, 00-025-1137	040

**JCPDS: Joint Committee on Powder Diffraction Standards; **In bold: Standard ISO 13779-3:2008 recommended files for use in experimental studies; ***At temperatures of < 212 °C stoichiometric HA is monoclinic. However, in biology, a transformation from monoclinic to hexagonal can be induced due to small quantities of impurities.*

The following described CaP phases are relevant in the context of this work either they are used as the main material for the 3D-printing technology operated in the present thesis or they appear as by-products during the shaping process:

-Hydroxyapatite (HA):

Stoichiometric HA, also called hydroxylapatite (HA), has the chemical formula $Ca_5(PO_4)_3(OH)$ but it is usually written $Ca_{10}(PO_4)_6(OH)_2$ to denote that the hexagonal unit cell is comprised of two repeating patterns. It is named pentacalcium hydroxide tris(phosphate) in the IUPAC nomenclature. After fluorapatite (FA), HA is the second most stable and least soluble of CaPs (see Table 3). Although not highly soluble, HA is used as a model for the inorganic component of bones and teeth, thanks to the ability of its surface to provide nucleating sites for precipitation of apatite crystals in culture medium (typically, saturated with calcium and phosphate ions) and in body fluids. HA is recognized as a bioactive substance, since it forms a strong chemical bond with host bone tissue, for hence it is considered as a good bone graft material. It is also osteoconductive, non-toxic, non-immunogenic, and its crystallographic structure is similar to that of bone mineral with an adequate amount of carbonate substitution.

Stoichiometric HA has been described as monoclinic, space group $P2_1/b$ (see Table 4). However, the most common form in biology and medicine is hexagonal and comes after a monoclinic-to-hexagonal phase transition at temperatures above ~250°C. This crystal structure has been described in the space group *P*63/*m* (No. 176) with lattice parameters $a = b = 9.432$ Å a nd $c = 6.881$ Å, Z = 1. The hexagonal phase of HA is more stable at ambient temperature due to the strains in the hexagonal lattice produced by pointing either upward or downward of the hydroxide ions in the structure. These strains are compensated by substitutions or ion vacancies. Thus, the hexagonal phase of HA is a common form in biology and medicine (Dorozhkin, 2009). This hexagonal structure is illustrated in Figure 3.

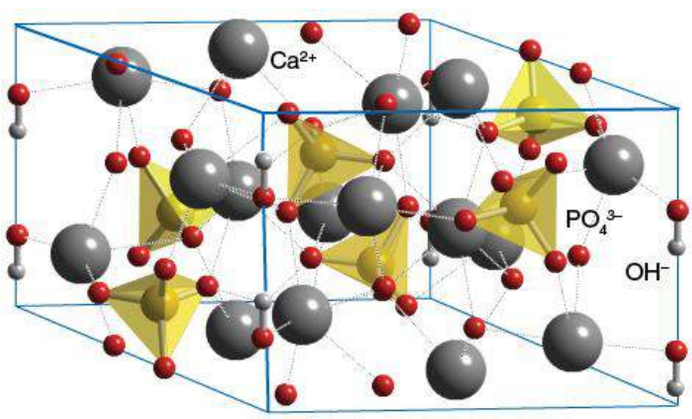

Figure 3. The unit cell of hexagonal HA (space group P63/m). Retrieved from (Eliaz and Metoki, 2017).

It is known, HA is osteoconductive, but not osteoinductive; these properties between others can be turned through ionic substitution although (Samavedi et al., 2013). The anionic substitution of carbonate for phosphate has been shown to increase HA solubility (and bioactivity), while the substitution of fluoride for hydroxide increases stability. Other studies have demonstrated that cationic substitutions such as magnesium in place of calcium can have favourable biological effects by providing trace ions. There are several JCPDS files for HA (Table 4). The difference between them is both the crystal orientation and in pairing with a crystallographic system.

Different studies showed that the atomic Ca/P ratio in biomineralized tissues can vary significantly due to ion substitutions and vacancies. HA is recognized as the final solid mineral of the bone. All other phases are considered minor or precursor phases, they are acid-stable and will convert to the thermodynamically stable HA at high pH (Palmer et al., 2008). The key properties of HA are summarized in Table 5.

Table 5. Physicochemical, mechanical and biological properties of HA. Adapted from (Eliaz and Metoki, 2017)

Property	Value	Comments
Binding energy	-280.6 eV	
Kohn-Sham gap	-5.4 eV	
Dielectric constant	7.40-10.47	-
Thermal conductivity	0.013 W / (cm.K)	-
Relative density	95%-99.5%	-
Decomposition temperature	>1000 °C	-
Melting point	1614 °C	-
Tensile strength	38-300 MPa ~3 MPa	For dense HA For porous HA
Compressive strength	120-900 MPa 2-100 MPa	For dense HA For porous HA
Bending strength	38-250 MPa 2-11 MPa	For dense HA For porous HA
Young's (elastic) modulus	35-120 GPa	For dense HA
Fracture toughness	0.7-1.2 MPa·$m^{1/2}$	Decreases almost linearly with porosity
Fracture energy	2.3-20 J/m^2	Behaves like a typical brittle ceramic
Vickers hardness	3-7 GPa	For dense HA
Poisson's ratio	0.27	For synthetic HA (bones ~0.3)
Biocompatibility	High	-
Bioactivity	High	-
Biodegradation	Low	-
Cellular compatibility	High	-
Osteoinduction	Nil	-
Osteoconduction	High	-

It has been found, the higher the Ca/P atomic ratio the higher the strength of HA is, reaching the maximum at Ca/P ~1.67 and decreasing suddenly when Ca/P > 1.67 (Suchanek and Yoshimura, 1998). Moreover, the strength decreases almost exponentially with increased porosity. Although, changing the pore geometry it is possible to modulate the strength of porous bioceramics. Porous HA is quite less fatigue resistant than dense HA. Exists an anisotropy in the stress-strain behaviour of perfect HA crystals (Ching et al., 2009).

However, well-crystalline HA can be prepared from aqueous solutions. We can find different clinical uses of HA due to the chemical and phase (and, sometimes, shape) similarities to the biological mineral in bone and teeth. Synthetic HA has been widely used as a coating on orthopaedic and dental implants range from augmenting atrophic alveolar ridges to repairing long bone defects, ununited bone fractures, middle ear prostheses, spinal fusions, and craniofacial repair. HA nanoparticles, as well as scaffolds, have been used also for controlled drug delivery. For further information, different reviews of these and other applications have been previously reported (Aoki, 1991; C. C. Berndt and Gross, 2002; Damien and Revell, n.d.; de Groot et al., 1998; Ferraz et al., 2004).

-Ca-deficient Hydroxyapatite (CDHA):

Ca-deficient hydroxyapatite (CDHA) with chemical formula $Ca_{10-x}(HPO_4)_x(PO_4)_{6-x}(OH)_{2-x}$ ($0<x<1$), belongs to the apatite family. Comparing its structure with the stoichiometric hydroxyapatite both have some ions of calcium and hydroxide missing and incorporating protons. However, in the CDHA these protons replaced some of PO_4^{3-} ions with HPO_4^{2-}. The formation of HPO_4^{2-} is due to the occupation by H_2O molecules at the vacant OH^- sites and hydrogen bonding to the nearest PO_4^{3-}. The loss of OH^- ions from its unit cell is reflected in the OH^- stretching and vibrational bands, less intense in CDHA compared with that of stoichiometric HA. CDHA has a higher chemical activity than pure HA and it is possible to synthesize it by a homogeneous precipitation method using solutions with a Ca/P ratio of 1.00-1.67. It seems to be more efficient in inducing the precipitation of bone-like apatite than stoichiometric HA; naturally, it is known that CDHA plays an important role in bone remodelling and bone formation. It shows high solubility in water or body fluids while high crystalline pure HA exhibit low solubility. Comparing with β-TCP, it shows more favourable properties with a higher reproducibility of the seeding efficacy and it has been considered as new bone substitution material due to its high specific surface area (Dorozhkin, 2009; Elkhooly, 2008).

- Tricalcium phosphate (TCP) polymorphs

TCP has greater solubility than HA and is rapidly resorbed in vivo with new bone growth replacing the implanted TCP. It is thermodynamically stable only at elevated temperatures (1000–1500°C). The term TCP is used to designate phases with the chemical composition $Ca_3(PO_4)_2$ with a Ca/P ratio close to 1.5. There are four TCP polymorphs: α; β; γ; and super α. The γ polymorph is a high-pressure phase while the super α (or α') polymorph is observed at temperatures above approximately 1500°C. Then, the most frequently observed polymorphs in bioceramics are α- and β-TCP (Hench and Best, 2013):

- β-Tricalcium Phosphate (β-TCP):

β-TCP cannot be precipitated from aqueous solutions. Mg-stabilized β-TCP (Whitlockite) has been identified during pathological calcification, such as dental calculus formation and in renal stones, as well as in arthritic cartilage. However, β-TCP has not been observed in enamel, dentin, or bone. In biomedical applications, β-TCP is used in CaP bone cement and other types of bone substitution bioceramics, as well as in dentistry. HA in combination with β-TCP both form BCP and is used as a bone-substitution bioceramic. A review of the toxicology of β-TCP and other CaPs as food ingredients is provided in the Ref. (Weiner et al., 2001). Due to the low interfacial energy of β-TCP to apatite, it can provoke the precipitation of an apatite layer upon incubation in aqueous ionic solutions. β-TCP is purely osteoconductive, while with the addition of bone marrow aspirate is possible to provide it too osteoinductive and osteogenic factors to the scaffold material (Elkhooly, 2008).

- α-Tricalcium Phosphate (α-TCP):

α-TCP may be considered a high-temperature phase of β-TCP since α-TCP can be prepared from β-TCP by heating at above 1125ºC and quenching to prevent the reverse transformation. α-TCP is more reactive in aqueous systems than β-TCP, it has a higher specific energy, and can be hydrolysed in aqueous

solutions to CDHAP. The main problem to use α-TCP in bone replacement is its quick resorption rate (faster than the formation of a new bone), limiting its use in biomedical applications.

-Tetracalcium Phosphate (TTCP):

Tetracalcium phosphate is the compound $Ca_4(PO_4)_2O$. It is the most basic of the calcium phosphates and has a Ca/P ratio of 2, making it the most phosphorus-poor calcium phosphate. TTCP cannot be precipitated from aqueous solutions. It can be prepared only by a solid-state reaction above 1300°C. This reaction has to be carried out under a dry atmosphere or vacuum to avoid the decomposition of TTCP to HA due to the presence of water vapour. TTCP is usually obtained as an unwanted byproduct as a result of the thermal decomposition of HA to a mixture of high-temperature phases of α-TCP, TTCP, and CaO.

-Biphasic calcium phosphate (BCP):

Biphasic calcium phosphates (BCPs) are a family of two-phase ceramics that combine the low solubility and osteoconductivity of HA with the osteoinductivity of a more soluble phase such as TCP. It has been used as a bone graft material during the last decade. It can be produced by mixing HA and TCP, or through the sintering of CDHA at a high temperature (>700ºC) to result in a mixture of two different phases. The HA/TCP ratio is determined by the calcium deficiency of the unsintered apatite (the higher the deficiency, the lower the ratio) and the sintering temperature. Depending on the method of preparation (precipitation, hydrolysis or mechanical mixture) and the conditions of the reaction (pH and temperature) different calcium deficiency is obtained. The bioreactivity of BCP bioceramics can be tuned by manipulating the composition (HA/β-TCP ratio) and/or its crystallinity. Currently, BCP bioceramics are recommended for use as an alternative or additive to the autogenous bone for orthopaedic and dental application. Different ratios of HA/TCP ceramics have been compared as scaffolds for optimum stem-cell induced bone formation. A ratio of 20/80 HA/TCP was found to have the greatest effect on bone formation, where pure HA and pure TCP had the least effect on bone formation (Daculsi and Legeros, 2008).

1.3 Substituted hydroxyapatite (SHA)

Numerous reviews have reported the production and properties of CaP materials, more importantly for HA. One of the most recent reviews summarizing the HA was written by Sadat-Shojai et al.(Sadat-Shojai et al., 2013). The advantages and disadvantages involved in each method are clarified in detail. It is also possible to obtain the CaPs mineral phase from a wide variety of natural sources. In this case, the material is defined as bioapatite (BAP), serving as a secondary option to synthetic apatite. When nanosized BAP is isolated and obtained from biogenic sources can be considered as the best material for bone tissue regeneration, exhibiting higher resorbability and bioactivity than synthetic HA. Because of this, many scientific studies and research projects have tried to chemically and structurally mimic the BAP through the ionic substitution of synthetic HA. These substitutions affect the lattice parameters and crystallinity of the substituted hydroxyapatite (SHA) influencing its solubility. Bone-forming agents, microbial agents, and drug delivery systems are some of the applications of these SHAs. Geological apatites are examples of ionic substitution in apatites. The geological conditions reached such as the variety of elements available and the high temperatures make apatite susceptible to substitutions. OH^-, F^-, and Cl^- anions (also called column anions), can be incorporated in the channel sites in almost any proportion constituting the stoichiometric core apatites. Then, the phosphate group can be substituted by anionic complexes, while calcium can be replaced by bivalent and trivalent metal cations (Figure 4). Half of the elements of the periodic system can be incorporated in apatite atomic structure, although the conditions needed for it make it unfeasible in a laboratory (Šupová, 2015).

The scope of this work involves high-temperature processing, thus requiring a certain familiarization with the thermal stability and transition upon heating of HA and SHAs. Substitution of calcium and phosphates in SHAs produce a phase instability at temperatures less than 900ºC. However, for the anion substitution at the hexagonal axis, F in FA and Cl in ClA are the last to leave upon heating, leading to high-temperature stability. To summarize these substitutions, they can be better represented in an onion diagram, with the stoichiometric apatite (HA, FA, and ClA) in the inner circle followed by anionic substitutions, replacing PO_4, ordered in a decreasing substitution capability. The rest onion layers involve monovalent, divalent and trivalent cation substitutions of calcium (Tõnsuaadu et al., 2012).

The anion position in the hexagonal axis plays an important role in the stability of apatite decreasing in the following order F > Cl > OH. Thus, fluoride is the most negative and is small enough to be located in between the calcium triangle giving high stability to the FA. It melts at 1644ºC and decomposes in a dry atmosphere. In stability, it is followed by ClA which undergoes a phase change from hexagonal to monoclinic upon heating at 200-300 ºC and is stable to 1200ºC when pores, large grains, and point cracks are observed. It has poor sinterability compared with HA. ClA as well as all apatites can lose the column anions when heating between 900 and 1200ºC in vacuum (Tõnsuaadu et al., 2012). The use of ClA as a substitute for HA in plasma spraying has been studied showing a lower decomposition of the previous one, thus confirming higher thermal stability (Demnati et al., 2015).

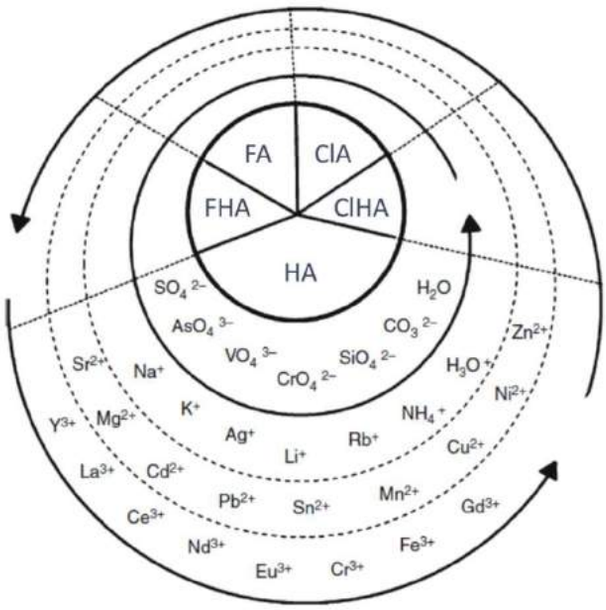

Figure 4. Onion diagram with core apatites in the centre and substitution elements in different layers. Anionic substitutions in the inner layer, followed by monovalent, divalent and trivalent cationic substitutions in the outer layers. Ordered in a decreasing ability of substitution. Retrieved from (Tõnsuaadu et al., 2012). FHA = Fluorine-substituted HA, ClHA = Chlorine-substituted HA.

Figure 5 summarizes the thermal stability and the transitions due to loss of water, carbonate and decomposition of apatites. Carbonate substitution of apatites produces thermal instability, while as explained above, between core apatites the FA is the most stable followed by ClA and HA.

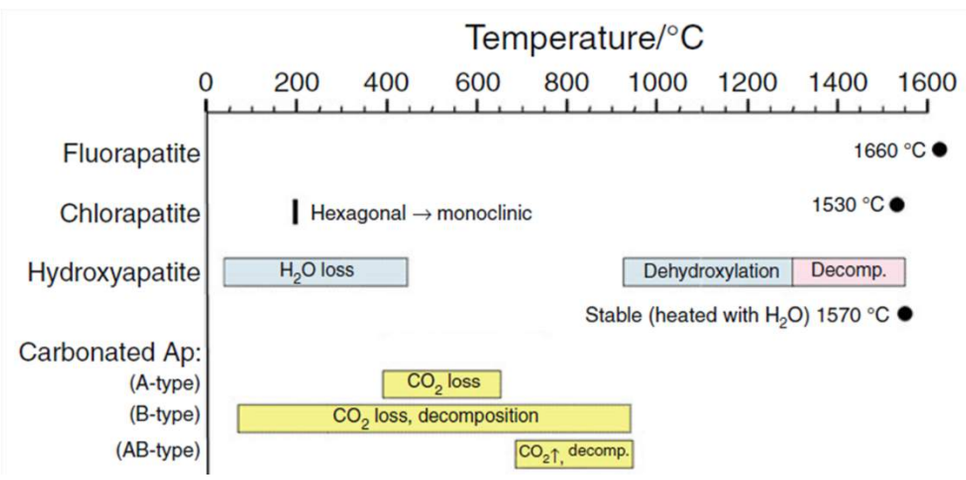

Figure 5. Thermal events for apatites (FA, ClA, HA, and carbonated apatites). (Black circles and black bar (ClA) indicate the melting point and phase change, respectively). Adapted from (Tõnsuaadu et al., 2012).

The knowledge of the thermal stability between different apatites was of special interest since the processing of these materials at high temperatures was within our scope. The comparison between the performance of some of them in additive manufacturing technologies was studied and will be detailed in future chapters.

2. Additive manufacturing for hydroxyapatite bone scaffolds production

2.1 Introduction to additive manufacturing technologies

Since the introduction of the additive manufacturing (AM) concept by Chuck Hull in 1986 via a process known as “stereolithography (SLA)”(Hull, 1986; Japanese Technology Evaluation Center (Loyola College in Maryland) et al., 1997), it has been used for many applications without the need for specific tooling. For most people, the term 3D printing conjures up only images of desktop polymer extrusion printers, but it embraces much more than that. In the last 30 years, the focus of 3D printing has grown from making prototypes using vats of resin and beds of powder, to include making production parts with metal and ceramics. These processes have collectively now become referred to as additive manufacturing (AM). ASTM and ISO (ISO/ASTM 52900) standardization activities have grouped additive processes into seven categories, however some new technologies are emerging, such as the AMBIT™ which is a combination of AM and machining in a single machine (Figure 6).

Additive manufacturing integrates such techniques as computer-aided design (CAD), computer-aided manufacturing, numerical control techniques, laser techniques, polymers, and 3D computed tomography techniques. The 3D geometry information is determined by CAD models of the parts, or by scanning objects in two dimensions and processing the acquired data into a 3D model. Then a 3D sample is fabricated from sheet material or powder (Wen et al., 2017).

The growth of such techniques in the area of biomedical devices has been slow due to the strict analysis criteria, reproducibility and part quality production in such a recent technology. However, the use of AM technologies in bone tissue engineering has been growing in recent years (Table 6).

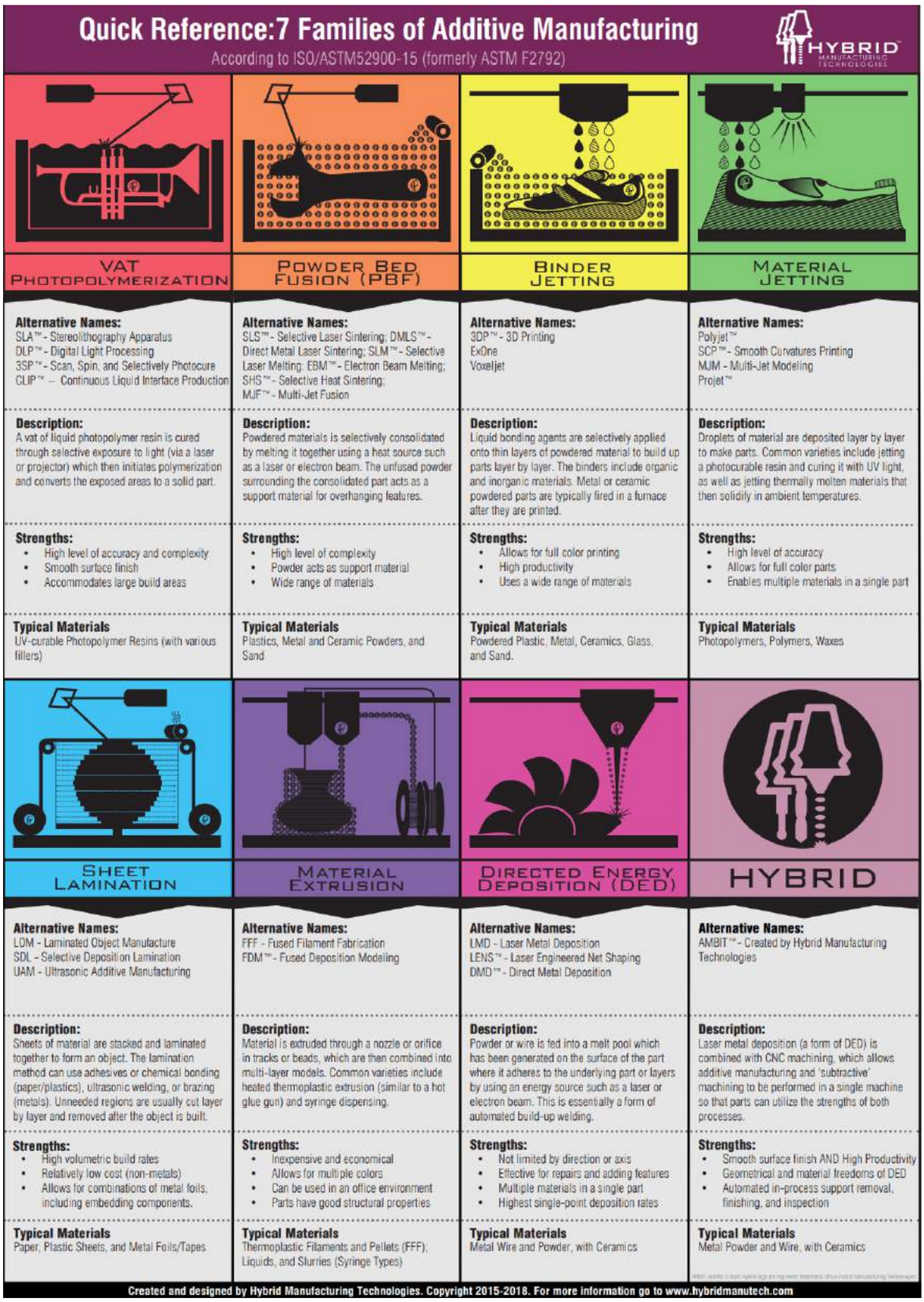

Figure 6. Quick reference guide of AM technologies. It provides a basic illustration of each process and an overview description of how it works. Retrieved with permission from Hybrid™ Manufacturing Technologies (hybridmanutech.com).

Table 6. AM techniques used for bone scaffold fabrication through calcium phosphate materials feedstock. Adapted from (Bose et al., 2013). MBAM = Methylenebisacrylamide, PLLA = Poly(lactic acid), PPF = Poly(propylene fumarate, DEF = Diethyl fumarate, PDLLA = Poly-d,l-lactic acid, PP = Polypropylene, PCL= Polycaprolactone.

Technique	Process details	Processed materials for bone tissue engineering	Advantages (+) and disadvantages (-)
3D plotting/direct ink writing	→ Strands of paste/viscous material (in solution form) extrusion based on the predesigned structure → Layer by layer deposition of strands at a constant rate, under specific pressure → Disruption of strands according to the tear of speed	→ HA[1]	+: → Mild condition of the process allows drug and biomolecules (proteins and living cells) plotting -: → Heating/post-processing needed for some materials restricts the biomolecule incorporation
Laser-assisted bioprinting (LAB)	→ Coating the desired material on a transparent quartz disk (ribbon) → Deposition control by laser pulse energy → Resolution control by the distance between ribbon/substrate, spot → size and stage movement	→HA[2] →HA/MG63 osteoblast-like cell[3] →Nano HA[4]	+: → Ambient condition → Applicable for organic, inorganic materials and cells → Quantitatively controlled → 3D stage movement → Homogeneous ribbons needed
Selective laser sintering (SLS)	→ Preparing the powder bed → Layer by layer addition of powder → Sintering each layer according to the CAD file, using a laser source	→Nano HA[5] →CaPs/PHBV[6] →Carbonated HA/PLLA[6]	+: → No need for support → No post-processing is needed -: → Feature resolution depends on laser beam diameter
Stereolithography (SLA)	→ Immersion of platform in a photopolymer liquid → Exposure to focused light according to the desired design → Polymer solidifying at the focal point, the non-exposed polymer remains liquid, → Layer by layer fabrication by platform moving downward	→PPF/DEF-HA[7] →PDLLA/HA[8] →Acrylamide/MBAM/β-TCP[9]	+: → Complex internal features can be obtained → Growth factors, proteins, and cell patterning is possible -: → Only applicable for photopolymers

Fused deposition modelling (FDM)	→ Strands of heated polymer/ceramics extrusion through the nozzle	→PP/β-TCP[10] →PCL/β-TCP[11,12]	+: → No need for platform/support -: → Material restriction due to the need for molten phase
Robotic-assisted deposition/ robocasting	→ Direct writing of liquid using a nozzle → Consolidation through a liquid-to-gel transition	→HA/PLA[13] →HA/PCL[13]	+: → Independent 3D nozzle movement → Precise control on thickness → No need for platform/support -: → Material restriction

[1](Detsch et al., 2008) [2](Doraiswamy et al., 2007) [3](Harris et al., 2008) [4](Catros et al., 2011) [5](Shuai et al., 2011) [6](Duan et al., 2010a) [7](Lee et al., 2009) [8](Ronca et al., 2013) [9](Bian et al., 2011)[10](Kalita et al., 2003)[11](Lam et al., 2007) [12](Lam et al., 2009)[13](Russias et al., 2007).

In the present work, we will focus our explanation on Powder Bed Fusion (PBF) and VAT photopolymerization categories, specifically on powder bed selective laser processing (PBSLP) and masked stereolithography (MSLA) techniques. These two technologies were envisaged for the preparation of the ceramic feedstock and their feasibility was tested. Important differences exist between these two techniques regarding the powder/slurry feedstock requirements. The process description, powder feedstock criteria, process parameters, and a summary of the most important works published on the application of these techniques for the processing of calcium phosphates are detailed in the following sections.

2.1 Powder bed selective laser sintering (PBSLP)

The term PBSLP has been recently defined as a substitute of the traditional but not properly standardized terms: selective laser sintering and selective laser melting. Both techniques are part of the Powder Bed Fusion (PBF) category, ISO/ASTM 52900 "Additive manufacturing—General principles—Terminology" but due to the inclusion of ceramics as material feedstock, the use of these terms to describe the process became uncertain. The reason is the fact that some materials such as ceramics experience a change in their composition before sinter/melt. Then, as the process induces densification from powders to produce a solid part by increasing the temperature both phenomena can be carried out, however, the exact mechanism taking place in ceramics is not evidenced yet. Therefore, to avoid a misusing of the terms already mentioned, this new term, powder bed selective laser processing, was proposed by Grossin et al. (Grossin, Monton, Navarrete-Segado et al., 2021) which will be employed for the rest of this work.

The technique is based on the creation of 3D solid pieces from computer-aided design/manufacturing (CAD/CAM) data by processing (sintering/melting) of powdered materials by laser irradiation through the consequence of multiple layers. The laser is considered the most important part of the PBSLP machine. Commercial printers are equipped with CO_2 (λ:10600 nm) and/or Nd:YAG (λ:1064 nm) lasers. Then, other relevant parts of their design are the two pistons forming the building platform and powder reservoir, and the layer deposition device. Each layer starts with the coordination of the movement of the pistons and the layer deposition device creating a homogeneous powder bed with controlled thickness before laser irradiation. The exceeded powder is collected and can be sieved to remove partially treated powder for recycling.

Laser type, spot size and energy density are three parameters that should be studied meticulously evaluated for each material. These and other parameters will be deeply discussed in future sections. In addition, the different strategies followed to surpass the challenges found for the application of PBSLP on ceramic materials, will be examined, more specifically on calcium phosphates.

2.1.1 Powder feedstock criteria

Extract corresponding to section "3.3. Powder feedstock criteria" in the review (Grossin, Monton, Navarrete-Segado et al., 2021) previously contributed by the author.

A successful powder bed in PBSLP technologies relies on a careful optimization of the powder properties (Figure 7). Ensuring that a ceramic powder has good handling for PBSLP processing is still not possible only by analytical analysis, it is usually needed a trial-and-error investigation on the equipment as well. Even if it is not possible to evaluate the handling of the powder with an exact accuracy there are different existing methods to evaluate their main features and deliver valuable information helping on the development of new or improved PBSLP powder feedstock (Schmid et al., 2013).

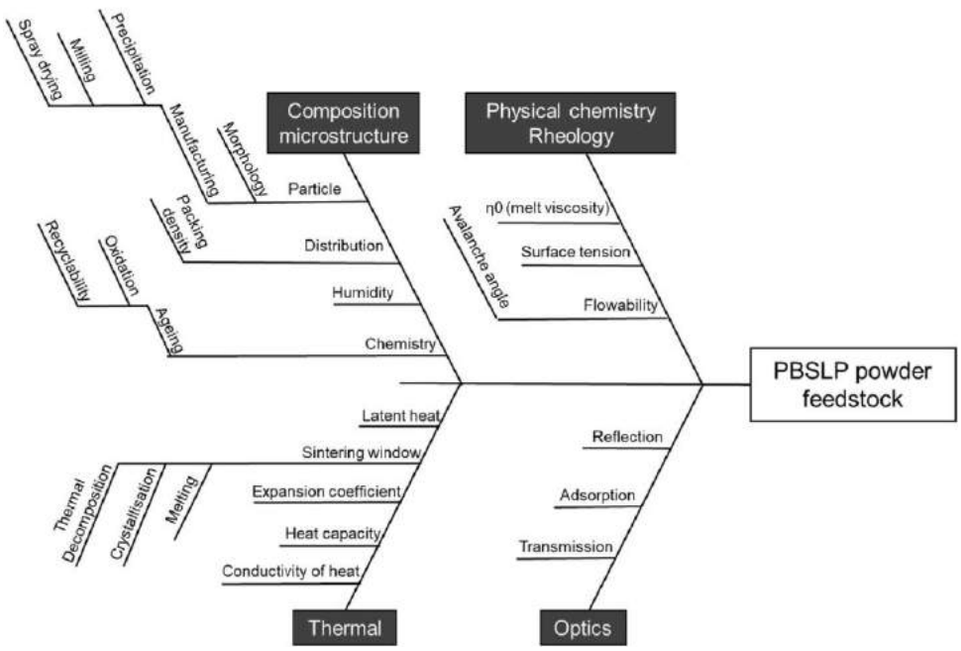

Figure 7. Ishikawa diagram with influencing parameters for PBSLP powders. Retrieved from (Grossin et al., 2021).

Powder flow behaviour is known to have a direct impact on the quality and homogeneity of a spread powder bed and for hence, on the density of the powder and parts. Spierings (Spierings et al., 2016) made an elaborate work collecting the comparisons that different authors made between existing powder flowability measurement techniques (static and dynamic) to determine the flow properties of powders (Table 7). Krantz (Krantz et al., 2009) established that no single technique is suitable for a full characterization of a powder; it is required the use different techniques to fully understand the flow properties of the powder and predict its behaviour under different process conditions. And hence, the powder flow characterization technique should match the powder application to select the most appropriate characterization technique. AM processes use a ruler or a rotating cylinder as layer creation devices, where the powders have a high free surface and can be aerated to some degree depending on the speed of the device. Minimum limits on the flowability requirements will depend on the machine-specific differences, e.g., layer creation device.

Table 7. Comparative of some existing powder flowability measurement techniques.

Powder flowability measurement technique	**Details**	**Drawbacks**
Ring shear cell tester (ASTM D6773)	- Industrial standard for measurement of powder flowability, compressive strength, compressibility, consolidation time, internal and wall friction, and bulk density.	- A compressive load is used during the assessment of powder, which does not suit well with the situation during AM process.
Hausner ratio HR (ASTM D7481-09)	- Common and widely used technique because of its simplicity. - Hasuner ratio (HR) is defined as the ratio between tapped and bulk density.	- HR measurement differs from an AM process where thin powder layers are created and no compression or tapping is applied. HR is not considered to be ideal for application in AM. - Powders often do not reach stable density after a certain number of tapping cycles, and a high dependency on the number of tapping has been elucidated.
Angle of repose/Hall flowmeter (ISO-4490/ASTM B213)	- Recommended by ASTM as the characterization method for metal powders for AM since the methodology is closer to the AM processing conditions than other techniques. - Time required to discharge the powder and the angle formed for the powder pile are used as a measure for flowability.	- Operators filling method can influence the results. - The diameter of the cone opening can be too small for some powders making it difficult to quantitatively compare different powders. - Not considered as best suited since the stress state of the powder in the developed powder cone is still different from the AM process.
Avalanche test	- Nearer to the PBSLP process than the other techniques. - Good correlation with the angle of repose method since similar stress states are induced to the powder. - Avalanche angle, surface fractal, volume expansion rate and many more parameters can be measured.	- Not standardized yet

Particle morphology (e.g., shape and surface) and size distribution of the powder have an important effect on the final properties of the sintered artefact since they are directly related to the flowability and packing density of a powder bed. As a rule of thumb in different scientific fields, we can assume that for powders of narrow particle size distribution, the most spherical and larger the particles, the better their flow behaviour (Fu et al., 2012; Liu et al., 2008; Lu et al., 2015; Stanford et al., 2003). The benefits of using multimodal powders as powder feedstock have been often exposed since the packing with a bimodal size distribution allows the smaller particles to fill the interstitial voids between the larger particles. A suitable size ratio between coarse and fine particles (over 1:10) and a weight fraction of large particles about 70% are the conditions showing maximum packing (Karapatis and Egger, 1999; Sofia et al., 2018, 2016).

The laser is considered the most important part of a PBSLP device. Commercial devices can be equipped with either CO_2 lasers or Nd:YAG lasers (also called fibre lasers), being the last one the most common for industrial applications. One of the most important properties that will influence the laser-material interaction is the capacity of the powder to absorb the laser and transform the energy into heat to be sintered/melted. This is one of the issues that researchers have to face for the development of new ceramic PBSLP powder feedstock. The wavelength of the laser should match with the maximum absorptivity of the powder to ensure the absorption of the energy. Some authors as Tolochko (Tolochko et al., 2000) and Ho (Ho et al., 2002) studied this matter with some important statements such as that the particle size distribution doesn't affect the laser absorptance of the material and that the use of composites can improve this property and hence, the interaction with the laser.

There have been some attempts of using reactive raw materials to fabricate 3D models of high-temperature structural materials like Al_2O_3 through an exothermic combustion reaction with low laser energy (Kamitani et al., 2000). The main problem comes from connecting the layers of the piece by having different reactivity. For this reason and because there are not many works on the use of this method in ceramic materials, this topic will not be covered in this review.

2.1.2 Process parameters and strategy

Extract corresponding to section "3.4. Process parameters and strategy" of the review (Grossin, Monton, Navarrete-Segado et al., 2021) previously contributed by the author.

Many parameters belonging to the laser machine influence the build-up process and, in the end, over the part's relative density. The user must manage it to have the best performance as possible by modifying those parameters (Figure 8).

The power and the scanning speed are very related parameters since they define the amount of energy transferred in an area. While the power indicates the amount of energy transferred per second, the speed will control the time spent in the same area. An equilibrium between both has to be reached to avoid the formation of pores, either by too much or insufficient energy. For the same scanning strategy, the scanning speed, together with the hatching distance and the layer thickness will control the build rate. The build rate coefficient is the volume of material produced per hour, normally expressed in $cm^3.h^{-1}$ and is used to compare processes productivity:

$$B = h_{space} * t_{layer} * v_{scan} \quad (1)$$

where B is the build rate coefficient ($mm^3.s^{-1}$), h_{space} the hatching distance (mm), t_{layer} the layer thickness (mm), and v_{scan} is the scanning speed ($mm.s^{-1}$).

A higher scanning speed will lead to higher productivity; therefore, it is important to try to increase it. Always taking into account that too high speed will produce poor sintering or melting of the part resulting

in the formation of pores. Alternatively, excessively slow speed can evaporate the material forming pores and imperfections as well.

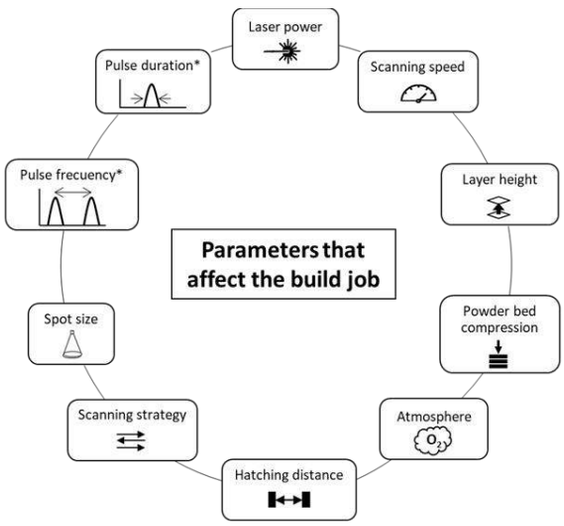

*Figure 8. Example of process parameters that can be programmed. *Belonging to pulsed lasers.*

The layer height or layer thickness is the distance between layers and it also has an impact on the build rate. A lower number of layers spread means that the recoater will be used fewer times having a big impact on the processing time. Additionally, the higher the layer thickness is, the lower the resolution of the part will be. In addition, if this distance is too large, it can lead to a poor attachment between layers and the breaking of the part. For all this, the layer height must be the highest as possible, but shorter enough to ensure the attachment between layers and avoid possible breaks.

The hatching distance refers to the distance between centres of adjacent laser beam tracks. This parameter affects the build rate as previously explained. It is necessary to find the correct distance between tracks to avoid zones with no or not enough interaction with the laser beam leading to unreacted powder, even if there is some powder stroke by two different laser tracks, causing an overlap. A distance to obtain a good quality part but at the same time optimizing the build rate of the process should be pursued.

During the PBSLP process, it is possible to shift the laser beam focus, or “defocus”, by displacing the building platform in the z-axis to increase the laser spot size (Metelkova et al., 2018). The diameter of the spot during the PBSLP process can influence the energy transmitted and the area affected by the powder bed. It can also originate different microstructure to the piece due mainly to a different cooling rate. Additionally, some PBSLP machines are equipped with a rotating cylinder as part of the recoating device been able to perform a controlled compression of the powder bed after its spreading. The compression would increase the packing density of the powder bed and hence have a direct influence on the final density and quality of the printed parts. The chemical species present in the chamber atmosphere during PBSLP can induce different effects on the material being irradiated since high temperatures are reached. While an inert atmosphere can avoid any chemical reaction (i.e. combustion, phase transition…) from taking place during

the process, atmospheric "air" could favour it. It is the work of the user to find the best conditions to print the material in question.

Even if there are many parameters involved, most of the current research on the process optimization have only in consideration the energy density (E_d) or energy input in a defined volume that can be calculated through:

$$E_d = \frac{P_{laser}}{v_{scan} . h_{space} . t_{layer}} \quad (2)$$

where E_d is the energy density or energy input in J.mm^{-3}, P_{laser} is the laser power (J.s^{-1}), v_{scan} the scanning speed (mm.s^{-1}), h_{space} the hatch distance (mm), and t_{layer} the powder layer thickness (mm). This parameter should be considered an approximation since a lot more aspects affect the real energy transferred to the powder bed such as the direction of gas flow, laser diameter, scan strategy, offset at the surface of the melt, and so on (Peng and Chen, 2018; Prashanth et al., 2017). Although recent studies have started to evaluate the effect of the scan strategy during the fabrication process (Suryawanshi et al., 2016; Thijs et al., 2013). The use of the diameter of the laser beam (d_{spot}) in equation (2) instead of h_{space} can be found in some studies. Even if the basic concept is the same, both parameters should be coordinated to control a certain overlap ratio (Peng and Chen, 2018).

Figure 9 illustrates the different parameters that compose the E_d for a better understanding. Thus, E_d is the energy that the laser beam transfers per unit volume of powder bed and serves as a broad guideline for parameter selection. However, it is a thermodynamic quantity, and E_d does not include the kinetics of the irradiated material physics missing a correct understanding of the mass and heat transfer between the laser track and the surrounding material such as spattering of irradiated material. A careful approach is recommended when comparing results from experiments done under different conditions even to the same material and when testing new parameters (Scipioni Bertoli et al., 2017).

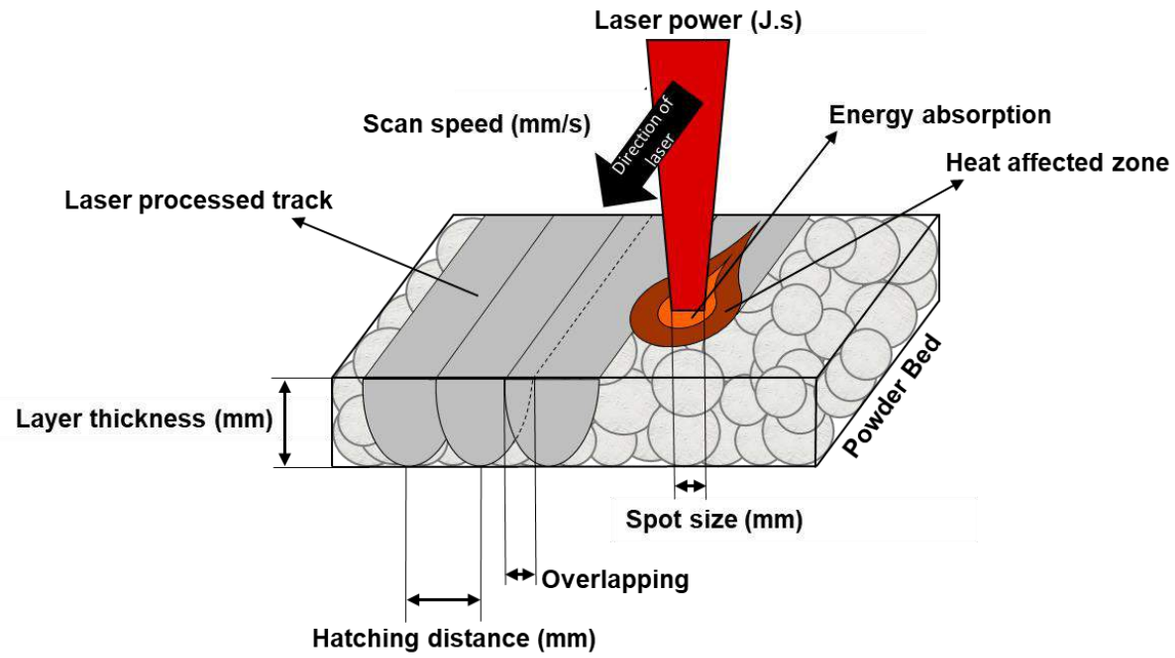

Figure 9. Scheme of variable parameters involved during the PBSLP process and from which the E_d can be calculated.

The scanning strategy is the pattern that the laser beam follows to irradiate the selected region of the powder bed. It controls the energy density distribution during the process and as explained above, it has an important effect on the final structural properties of the printed parts. Figure 10 illustrates some examples of scanning strategies used in PBSLP. It is important to find the scanning strategy in which an optimal energy density distribution occurs for each material thus avoiding adverse effects like decomposition, thermal cracks, and so on.

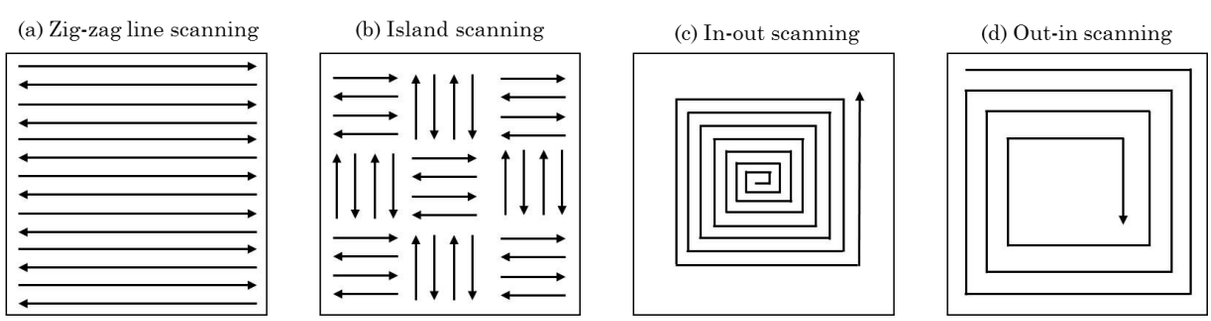

Figure 10. Examples of different scan strategies that the laser can follows during PBSLP.

2.1.3 PBSLP of calcium phosphates

Extract corresponding to section "4.1. Calcium phosphate" of the review (Grossin, Monton, Navarrete-Segado et al., 2021) previously contributed by the author.

Calcium phosphate (CaP) bioceramics are widely used in medical applications in many different ways such as coatings, paste, scaffolds, and cements. The use of a PBSLP process could allow the manufacturing of patient-matched tissue engineering scaffolds with controlled interconnected porous networks and shapes made of CaP. With the present document, we wanted to explain the more recent studies focused on the two phases forming biphasic calcium phosphate (BCP) since they are the CaP phases most used to produce scaffolds through the PBSLP process. Hydroxyapatite (HA) and β-Tricalcium phosphate (β-TCP) form BCP at different ratios to be used as bone-substitution bioceramics.

In the case of bone graft, the main role of a scaffold would be to provide a framework for the regeneration of new bone tissue, soft tissue, vascular-, and other metabolic components. CaP materials gather several critical properties needed for the correct performance of a bone graft material. For example, they can promote the formation of new biological tissue reducing the response from the immune system of the organism or tissue through its osteoconductivity (or osteoinductivity) and biocompatibility. Resorption is the term used to describe the absorption of a bioceramic in the body, either by dissolution or by cells (such as macrophages and osteoclasts). The desired resorbability rate is the rate comparable to the formation of bone tissue (between a few months and a few years), in the case of CaP, it may take 3 to 36 months to be replaced by bone. This property depends on the phase content of the CaP, crystallinity, lattice defects, particle size, and porosity. Some CaP phases like TCP may resorb fast and replace the coating or cement with bone. Other CaP phases like HA have a low resorption rate but they are osteoconductive materials acting as scaffolds promoting the formation of new bone (Eliaz and Metoki, 2017).

The use of CaP bioceramics in the bone replacement field requires also good mechanical properties. This is due to the high average load that the parts undergo during their lifetime. CaPs are brittle (primary ionic bonds) with relatively low tensile stress (6 to 10 MPa) and low impact resistance because of their porosity acting as preferred initiation sites for crack propagation. However, their compressive strength is higher than that of normal bone. For that reason, CaPs are more used in non-load bearing implants. One important advantage is the chemical resistance of ceramic implants compared to metal implants. The human body is a very harsh environment for metals since it contains water, salt, dissolved oxygen, bacteria, proteins, and various ions such as chloride and hydroxide. HA coatings have been demonstrated to have excellent chemical resistance; that is why they are widely used to coat base metals to ensure the biocompatibility of the ceramic on the metal surface. Furthermore, another benefit of HA is their dielectric properties (piezoelectricity) because electromagnetic fields have been shown to accelerate healing in bone fractures (Elkhooly, 2008; Kao et al., 2019).

Some solutions have been conceived to compensate for the low absorption of the laser by CaP powders during PBSLP. An increase of the energy density delivered during the process is usually performed by intensifying the power of the laser, reducing its speed, and/or by using other sources of energy. But it leads to a loss of productivity, poor final quality of the scaffolds, and cost-ineffectiveness. A method to deal with the low absorptivity of CaP materials of Nd:YAG laser and perform the bonding of CaP particles and the subsequent manufacturing of biomedical devices is disclosed by Colin et al. (Colin et al., 2014). It consists of the mixing of the ceramic substrate with an absorption additive before the PBSLP process. In this method, the ceramic powder constitutes the predominant portion by weight of particles together with a dispersed absorption additive. This additive has a higher specific absorptivity at the wavelength of the laser used than the ceramic components and it can be biocompatible, biodegradable, soluble, and/or heat degradable. It is used for transferring the radiant energy of the laser into thermal energy to melt/sinter the ceramic material in the mixture. This method is considered a direct PBSLP process.

The decomposition due to high temperature and the subsequent adverse effect on the mechanical properties is another important challenge that researchers have to face when printing CaP materials through the PBSLP process. It has been already studied in plasma spray coating processes that the sintering temperature usually triggers the phase transformation of HA or β-TCP scaffolds into other CaP phases. Phases such as tetracalcium phosphate (TTCP), α-TCP, and/or calcium oxide (CaO) can be produced before melting, which can influence the densification process. Porosity and grain size changes produced by the phase transition were found to play an important role in the mechanical performance of sintered HA. The decomposition of HA is a process of continuous reactions depending on the obtaining conditions. Ramesh et al. (Ramesh et al., 2013) performed a study of the sintering properties of HA powders prepared by different methods concluding that the HA powder prepared via the wet precipitation method shows better thermal stability, translated in less phase transformation and superior better mechanical properties. However, the usual mechanical behaviour limitations of CaP materials, in terms of brittleness, poor fatigue resistance, low tensile strength, and low fracture toughness value preclude HA from use in load-bearing situations.

To deal with the drawbacks previously mentioned, numerous works using CaP powders as part of composite materials to produce scaffold through the PBSLP technique have been reported (Eosoly et al., 2010; L. Hao et al., 2007; Minh et al., 2014; Xia et al., 2013).

In one direct method approach, the CaP powder is used as a filler in a mixture together with a polymer matrix and provides bioactive properties and higher strength to the scaffold (Cruz, 2010; Eosoly et al., 2010; Xia et al., 2013). Poly-ε-caprolactone, polyethylene (PE), high-density polyethylene (HDPE), and poly(l-lactic acid) (PLLA) are the most often used polymers in such composite materials. Due to the lower temperature needed to melt and bond the polymer particles, the ceramic phase transformation is avoided. Although the time of implantation can have some adverse effects on polymeric materials losing some of their properties. These polymers are not removed after the PBSLP process, being the main part of the final

scaffold used in the application. For this reason, these works are part of the direct PBSLP category. Even if the application is currently limited to the field of the filling of bone defects this method results in the production of promising improved bioactive scaffold with higher strengths and stiffness than the unfilled polymer (Figure 11a).

A different approach is an indirect method, consisting of the use of polymers as a binder together with calcium phosphate powders as the main matrix in the composite. The organic polymer is melted during the PBSLP process to obtain a green part, afterward, the green part is sintered removing completely the binder and producing the final porous ceramic part. Then the final part will be composed of pure ceramic. Recently, Zeng et al. (Zeng et al., 2020) achieved the production of microporous BCP scaffolds by low-temperature PBSLP keeping the physicochemical properties of BCP and improving the mechanical strength, porosity, and bioproperties. In this case, epoxy resin was used as a sacrificial organic polymer and was completely decomposed and removed by a posterior sintering process.

Shuai et al. (Shuai et al., 2013, 2011, 2010) attained the fabrication of pure CaP ceramic scaffolds of nano-HA and BCP in different proportions using a homemade PBSLP system equipped with a CO_2 laser. Although the presence of CaP secondary phases due to the phase transformation during the sintering process was confirmed by XRD analysis. Nano-HA powder used had a needle-like or irregular shape and β-TCP powders were mostly spherical with also a nanometric size. A ratio of TCP/HA (30/70) was found to exhibit the most outstanding resorption properties. Figure 11b shows the porous BCP scaffold with 3D orthogonal porous square channels with 13 mm in width, 7 mm in height, spaced by 2 mm, and a porosity of 61% measured with the Archimedes method.

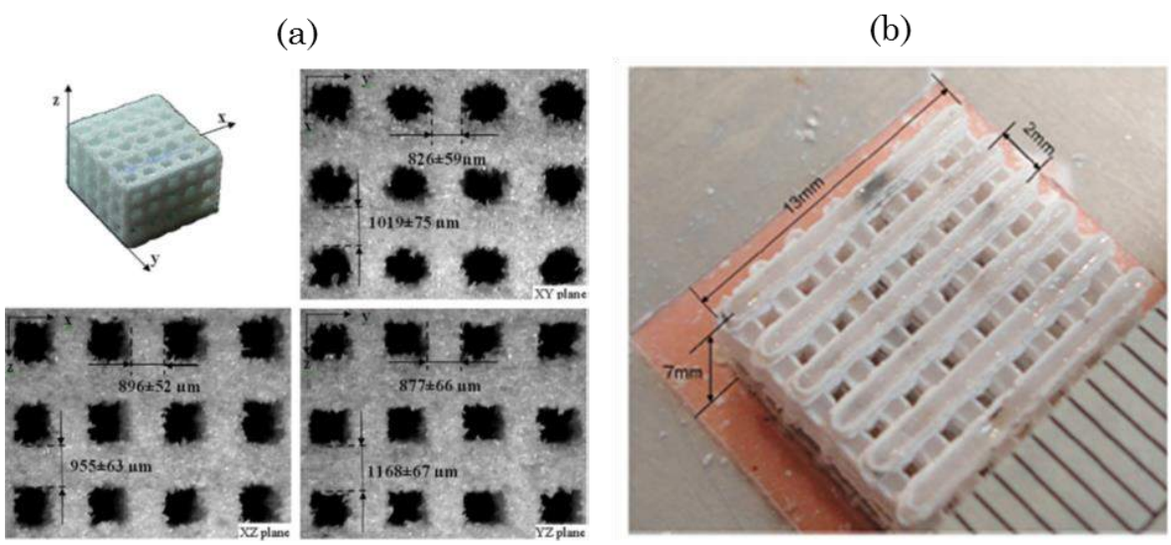

Figure 11. Sintered scaffolds made by PBSLP process using different calcium phosphate materials and composites. (a) nano-HA/poly-e-caprolactone (Eosoly et al., 2010) and (b) BCP (Shuai et al., 2013).

To summarize, the main advantages of using the PBSLP technique for the fabrication of CaP pieces lie in the flexibility to produce complex and well-controlled porous scaffolds with no need for supports or post-processing. There are some requirements that the powder feedstock has to fulfill to obtain good results, and as we observed, different approaches have been developed within the last years. Diverse powder feedstocks have been developed combining CaP materials between them and with a wide variety of additives and/or polymers/bioglasses to surpass the issues of CaP materials in PBSLP. There is still a need for research on the improvement of the mechanical properties and the resolution of the scaffolds to ensure their correct performance in bone tissue engineering applications. Their brittleness still limits their clinical application, especially for load-bearing implants. Although they showed promising results in terms of bioactive properties. Even if the tendency is to start modifying the initial powder feedstock, the improvement of PBSLP devices with a better design and a range of parameters adapted for better processing of ceramic materials will be crucial for their future in PBSLP processes. A summary of the most recent works on the application of PBSLP of CaP materials is offered in Table 8.

*Table 8. Summary of the process conditions and properties of the CaP sintered scaffolds by the PBSLP process. PM= Powder mixture *Values will be given when available in the publication. HDPE: high-density polyethylene, PHBV: poly(3-hydroxybutyrate-co-3-hydroxyvalerate), PLLA: poly(l-lactic acid), PCL: polycaprolactone, EP: Epoxy resin.*

Ref.	Powder feedstock	Laser & strategy	Post-processing	Properties of processed parts*
(L Hao et al., 2007)	HA (20%) / HDPE $0< x_{50}<105$ µm & 105 µm < x_{50}	CO_2 3.6-6.0 W Scan speed 3.6 m/s Line spacing 63 µm Layer thickness 150 µm Powder bed T: 128ºC	No post-processing	Porosity: 45-55 % Wettability: 60-140 deg.
(Xiao et al., 2008)	PM1: Apatite / Wollastonite (x_{50}: 45-90 µm) + 5% acrylic binder PM2: Apatite / Wollastonite (64% x_{50} 45-90 µm 21% PS 0-45 µm) + 15% acrylic binder	CO_2 250W Spot size 0.6/1.1 mm Layer thick. 125 µm Line spacing (spot size/2) (Indirect)	Heat treatment process + infiltration of CaP glass	Bend strength: PM1 35 MPa PM2 70MPa PM2 with CaP glass infiltrated 100 MPa Porosity: 40%
(Duan et al., 2010b)	PM1: PHBV (x_{50}: 53.18 µm) PM2: nanoCaP 15%/ PHBV (x_{50}: 46.34 µm) PM3: PLLA (x_{50}: 40.03 µm) PM4: nano-carbonated HA 10%/ PLLA (x_{50}: 39.78 µm)	CO_2 laser 13-15W Spot size 457 µm Scan speed 1257 mm/s Line spacing 100-150 µm Layer thick. 100-150 µm Part bed T: 35-45°C	No post-processing	Porosity: 62.6-68.5% Compressive strength (dry scaffolds): 0.47-0.62 MPa Strength modulus (dry scaffolds): 5-6.5 MPa
(Cruz, 2010)	HA 60% (x_{50}: 111 µm) / PLLA (x_{50}: 163 µm)	CO_2 laser 5-7.5 W Scan speed 200-300 mm/s Line spacing 100-150 µm Energy density 2.66-8.96 cal/cm2	No post-processing	Compressive strength: 2.4-4.6 MPa Bend strength: 1.6-4 MPa Density: 0.78-1.1 g/cm3
(Eosoly et al., 2010)	HA 30% (x_{50}: 38 µm) / PCL (x_{50}: 125 µm)	CO_2 laser fill 8.32-11.68 W (outline laser 3.32-6.68 W) Spot size: 410 µm Line spacing 100-200 µm Layer thickness 150 µm Part bed T: 38°C	No post-processing	Density: 0.33 g/cm3 Compressive strength: 1-2 MPa
(Shuai et al., 2013)	Nano-HA (x_{50}: 0.06-0.1 µm) 0%/10%/30%/50%/70%100%/ β-TCP (x_{50}: 0.1-0.3 µm)	CO_2 laser 12 W Spot size 800 µm Scan speed 100 mm/min Layer thick. 200 µm	No post-processing	For HA 70%/ β-TCP scaffold: Porosity: 61% Fracture toughness: 1.33 MPa.m$1^{/2}$ Compressive strength: 18.36 MPa Higher bone-forming ability and balanced biological stability and dissolution rate.

(Xia et al., 2013)	PM1: 0%-5%-10% needle-like nano-HA (150 nm long, 20 nm wide)/ PCL PM2: needle-like nano-HA 5%/10%/ PCL	CO_2 laser fill 4.5 W (outline laser 3 W) Spot size 150 µm Internal scan speed 1.25 m/sec Peripheral scan speed 0.55 m/sec Support scan speed 1.33 m/sec Layer thick. 150 µm	No post-processing	Porosity: 70.31-78.54% Compressive strength: 1.38-3.17 MPa More effective osteogenesis than pure PCL scaffolds
(Colin et al., 2014)	Examples 1 & 2 respectively: PM1: HA 95-99% (x_{50}: 5-25 µm) / Absorption additive (Carbon) PM2: TCP (x_{50}: 5-25 µm) / Absorption additive (SiC) (x_{50}: 1 nm – 100 µm)	PM1: Nd: YAG laser 40 W Scan speed 100 mm/s Line spacing 200 µm PM2: Nd: YAG laser 100 W at 10% 10% defocused Scan speed 20 mm/s	PM1: Thermal treatment to improve mechanical strength at 1100°C-2h PM2: Thermal treatment at 300-1200°C for 10 minutes to 5 hours.	N/A
(Ferrage, 2018)	Pure HA (x_{50}: 75 µm)	CO_2 laser 220W Spot size 200 µm Scan speed 100 mm/s Line spacing 800 µm Layer thick. 100 µm	No post-processing	Decomposition of HA into TTCP and CaO was observed. Density: 3,0691 (helium pycnometer)
(Zeng et al., 2020)	EP (x_{50}: 20 µm) 35%/40%/45%/50% in wt. / BCP (70/30 ratio of HA and TCP) (x_{50}: 80 µm)	CO2 laser 1.8W Spot size 200 µm Scan speed 200 mm/s Line spacing 150 µm Layer thick. 100 µm	Sintering of green part at 1100ºC for 4h for binder removal. (Indirect method)	Scaffold with EP and BCP 50/50 ratio showed superior mechanical properties: Compressive strength: 113.25 KPa Porosity: 80.8% Elastic modulus: 4.38 MPa This scaffold showed the most outstanding bioproperties in terms of osteogenic differentiation, ALP staining, ALP activity, and OCN immunocytochemistry.

2.2 Masked stereolithography (MSLA)

The word "stereolithography" can be defined as a combination of the Greek word "stereo", meaning solid, and "(photo)lithography", which means "writing" employing light. Then, in a Stereolithography Apparatus (SLA) 3D printer we are continuously drawing solids with light layer to layer. SLA processes are divided into three main categories, laser-based stereolithography (laser SLA), digital light processing (DLP), and masked SLA (MSLA), also called Liquid Crystal Display (LCD). Even if the three types of techniques use the same technology concept, they can produce different outputs (Zyzalo, 2008). Figure 12 illustrates the three types of SLA printing technologies.

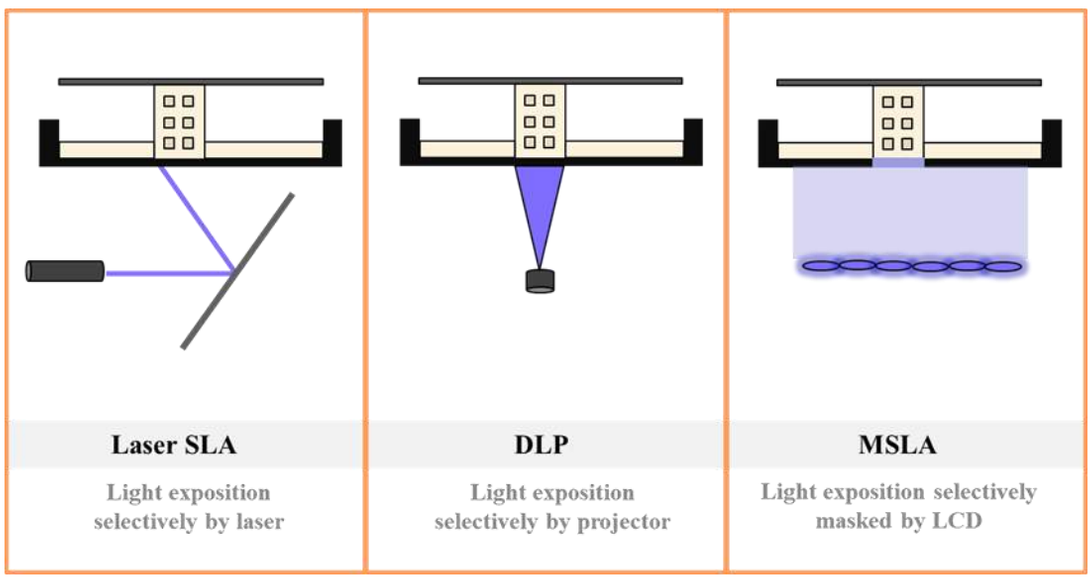

Figure 12. Illustration comparing the three different VAT photopolymerization printing technologies: Laser SLA, DLP, and MSLA.

Laser SLA was the original idea of stereolithography. In this technology, the UV laser draws each layer of the object led by two mirrors driven by a motor to rapidly aim the laser beam through the print area. The solid object design is layer by layer defined by a series of points and lines that the laser has to trace. DLP instead uses a digital projector to flash a single image for each layer across the entire platform at once.

MSLA is the last of these technologies arriving on the market and it has substantially grown in the last years. The LCD devices are the same used on mobile phones, TV, and computers. Their cost is much lower than DLP apparatuses because they do not require the use of a digital micromirror device (DMD) which is the base of the DLP technology, although LCD screens have a shorter service life and need to be replaced regularly. They are available in sizes from 3" to 80", for hence the light emitted is direct, homogeneous, and perpendicular all along the printing surface. This avoids the use of expensive and complex lens projection systems and the distortions on parts observed in DLP. This technology not only almost replaced the DLP technique, but it also started to replace the laser SLA in fields like odontology where the laser is a standard. However, one of the main disadvantages of MSLA is the excessive overheating produced by the LED system. It requires the use of cooling systems to avoid the heating of the resins during

long printing sessions (Quan et al., 2020; Zyzalo, 2008). A deeper explanation of its fundament can be found below.

2.2.1 Process description and parameters

The MSLA technique, as part of the VAT photopolymerization category uses a UV-light source to cross-link a photocurable resin feedstock (Figure 13). MSLA has significant advantages in printing resolution, efficiency, and working conditions when compared with other AM technologies, such as extrusion-based methods. Indeed, the use of light masked with an LCD, instead of one focused laser point like in laser SLA, provides this technology with high precision and printing speed. In addition, it is a non-direct contact technique providing a relatively mild condition to cells. The production of medical devices functionalized artificial tissues, and specific drug delivery systems are some of their medical applications (Iuliano et al., 2020).

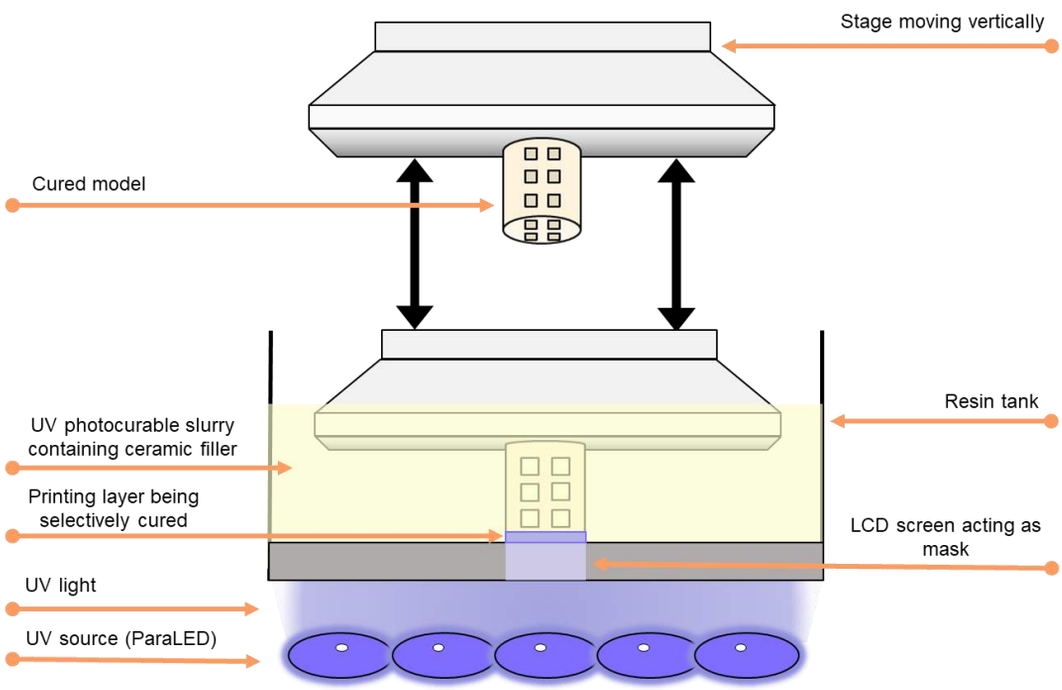

Figure 13. Schematic diagram of MSLA process.

MSLA 3D printing technique uses a LED array as a light source together with an LCD photomask to display the light image from the LED array. This array of 405 nm UV-LED replaces the laser source, contributing to diminishing their price. LCD photomask is digitally displayed and composed of square pixels. The resolution of the layer is then highly influenced by how the LCD photomask is manufactured since individual pixels are deactivated on the LCD to let the LED light pass through forming the resulting layer.

Although some biocompatible resins exist (e.g., photocurable hydrogels) (Preobrazhenskiy et al., 2021; Qin et al., 2014; Wu et al., 2019), the majority of the resins used in VAT photopolymerization processes are poisonous to cells. For hence, after the printing of parts containing the ceramic powder,

successive debinding and sintering processes are required. The debinding process is crucial to confirm that the totality of the resin has been pyrolyzed avoiding their toxic effects in the final part. Then the sintering of the green parts at higher temperatures is further required to achieve densification improving the mechanical properties of the part (Chen et al., 2019). This debinding-sintering step can be performed as once or divided into two different processes. Depending on the pyrolyzing and sintering behaviours of the resin and ceramic powder the process conditions need to be tailored (e.g. maximum temperature needed for the powder sintering) (Feng et al., 2020; Li et al., 2020). The sintering process can take several days to be performed in a muffle furnace. However, the use of microwave sintering to process the parts can shorter this duration while also generating micropores on the macropore surface improving the material-driven bone formation of a scaffold for bone tissue engineering (Pei et al., 2017; Wu et al., 2013).

Figure 14 shows the Ishikawa diagram of the parameters (causes) that influence the part quality characteristics (effects) during an MSLA process. Many parameters are shared with the other VAT photopolymerization techniques (Singe Gowda et al., 2014). It is important to mention the differences in light energy between the three, following the order, laser SLA > DLP > MSLA, being the laser the most powerful light source of the three. Thus, for the same resin, the parameters need to be adjusted in accordance when using different devices. In some cases, due to high exposure time needed for the reaction make impossible the use of a resin in apparatuses with a low energy source. On the other side, an overexposition of light on the resin will cross-link the surrounded resin producing the deformation of the part.

The layer thickness of the parts is the thickness in which the model is sliced, affecting the printing resolution as well as the printing speed. The orientation of the model can also affect the mechanical properties (Farzadi et al., 2014). The concentration and compatibility between the ceramic particles and the additives have an important influence on the reactivity, sedimentation, and rheology of the suspensions affecting the final part quality (Xing-Bang et al., 2019).

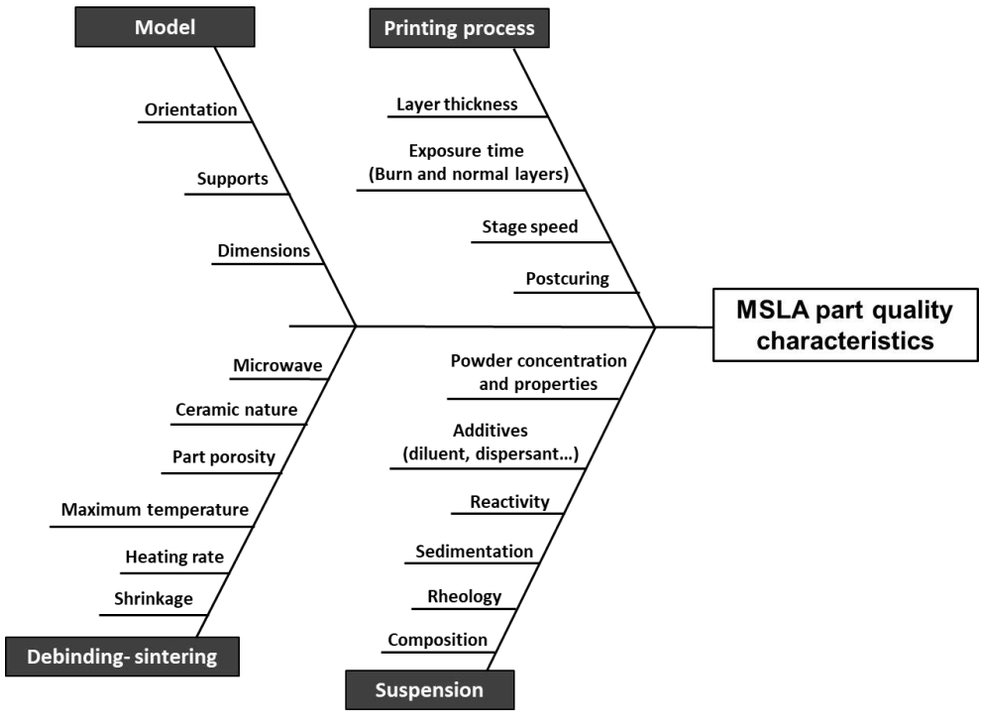

Figure 1. Ishikawa diagram with the process parameters affecting the MSLA parts quality characteristics.

2.2.2 Suspension feedstock criteria

In an MSLA process, as in the rest of VAT photopolymerization techniques, the liquid feedstock is mainly composed of photocurable resins. For a photopolymer to be suitable for SLA, it must provide certain characteristics such as a suitable rheological behaviour. The highest slurry viscosity that can be employed in SLA is approximately 5 Pa.s (Melchels et al., 2010). These resin feedstocks are usually composed of a photoinitiator, monomers or oligomers, diluents, light absorbers, and various fillers such as ceramic powders. It is common to use diluents to reduce the viscosity, always controlling that the rest of the properties (e.g., reactivity and rate of polymerisation) are not compromised.

At the moment of adding solid particles into a resin, it is important to understand how the resin is affected and which new properties for the suspension need to be controlled. The presence of particles can increase the suspension viscosity depending on its concentration. Then, usually, the use of dispersants helps to reduce this unfavourable effect by avoiding the formation of agglomerates through effective interparticle repulsion. The use of polydisperse particles instead of narrow PSDs allows the particles to pack more easily, having more free space for the individual particles thus flowing more easily. For particles with the same dispersion level, a too small average particle size will increase the suspension viscosity (Komissarenko et al., 2018). However, small particles tend to settle slower when comparing with particles of large sizes. The settling velocity can be one of the most important properties since too fast sedimentation can make the particles at the bottom blocking the light making impossible to continue with the printing process (Song et al., 2019). Researchers have to find the equilibrium between the viscosity and stability of the suspension

without surpassing the limits of resin processability for the technical specifications of the printer (Feng et al., 2020).

We already explained that the debinding step is a critical process. The resin components have different evaporation/decomposition temperatures and behaviours. A weight reduction and also in dimension usually happens, which depends on the concentration and composition of organic components, as well as, the temperature cycle. In addition, ceramic powder morphology properties, such as particle size and PSD can influence the debinding behaviour. A constant gas evolution rate is pursued to avoid too high internal gas pressures inside of the green body that could initiate cracks (Chen et al., 2019; Fernandes, 2019). The "surface-to-volume ratio" also affects the debinding characteristics. For hence, it is necessary to optimize the debinding cycles for specific geometries allowing the crack-free debinding of parts (Pfaffinger et al., 2015).

When comparing different ceramics, it has been found that for CaPs like TCP, large particles can be processed (x_{50} in the range of 1µm-20 µm). If dispersion and stabilization problems of the ceramic slurries are overcome, these bigger particles allow a much easier debinding process. The shorter cycle times lead to overnight processes in some cases. The higher is the ceramic load the lower will be the shrinkage. Thus, higher solid loadings are pursued. A lower shrinkage during the thermal treatment led to better control of the final dimensions of the parts. However, a high solid loading can difficult the debinding process complicating the diffusion of gases (Pfaffinger et al., 2015).

Regarding the influence of the ceramic feedstock during the sintering, it is known that HA powders produced by the wet precipitation method exhibit superior sinterability properties especially at low sintering temperatures between 1000ºC and 1200ºC. Indeed, it is less susceptible to decomposition into residual phases and shows superior hardness and fracture toughness (Ramesh et al., 2013). Powder morphology and the agglomeration state are other features that control the sinterability of the compacted material. Particle size determines the activation energy and the grain growth of the ceramic (Ellis and McNamara, 1989; Murray et al., 1995). Then, the presence of agglomerates in the powder, especially, of hard nature, tends to disrupt the densification process and can lead to the formation of defects in the microstructure, limiting the strength of the sintered part (Ramesh et al., 2004).

The main characterization methods to evaluate the properties of a suspension will be described in the next chapter.

3. Tailoring of HA powder properties for additive manufacturing technologies

3.1 Target powder/slurry properties

HA was chosen as starting calcium phosphate for the utilization of the different AM technologies. It has a feasible production process making it an accessible material for the evaluation of the multi-step process parameters needed to obtain the desired powder properties intended for AM. Before start tailoring the feedstock properties, it is important to identify the requirements of the material for the technology in

which it will be used. Previously, some indications were provided about the feedstock needs that the AM technologies envisaged in the present work require. We can summarize them in two groups dividing the properties that the powders should meet for each of the two techniques PBSLP (Table 9) and MSLA (Table 10).

For the PBSLP process (powder bed fusion category), **highly-flowable powder is desirable** to produce homogeneous powder beds during the process. As an example, in the powder flowability classification described by Barbosa-Canovas et al. (Barbosa-Cánovas, 2005), the ratio of tap and bulk density (Hausner ratio, HR) provides a statement on the flowability of powders. Thus, PBSLP powders should be typically under an HR limit of 1.25 (high powder flowability) to be considered a suitable powder with enough powder density (Schmid et al., 2013). It is known that powder flowability is significantly affected by particle size, shape, and size distribution. For powders with the same median particle size, higher size dispersion increases the flowability and for powders of equal dispersion, an increase of the particle size increases the flowability (Liu et al., 2008). The size polydispersity or size distribution span of powders can be calculated as:

$$Span = x_{90} - x_{10}/x_{50} \quad (3)$$

It can be used to classify the powders as monodisperse (span close to zero) or polydisperse (high span). In addition, spherical particles show higher flowability (Fu et al., 2012). In this case, the material interacting with the laser is the ceramic powder whose response will be highly influenced by the type of laser used. It is known that calcium phosphates poorly absorb the light emitted by a fiber laser source (λ = 1070 nm) which is the most common in PBSLP apparatuses (Tolochko et al., 2000). Taking this information into account, the addition of absorptance additives will be considered to produce blends with **increased fiber laser energy absorptance** needed for their processing. Moreover, the production of **spherical agglomerated particles** with at least a median particle size of $\mathbf{x_{50} > 20\ \mu m}$ and a **span higher than 1** was stated as a target. Meeting these properties, it was expected that the resulting powder would yield an **HR of less than 1.25**. These powder properties will be then pursued through a multi-step process: First, the synthesis of stoichiometric HA will provide the initial micron-sized particles with irregular shapes (Chapter II). Then, the as-synthetized powder can be wet ground in a stirred bead mill to produce suspensions with sub-micron particles as well with irregular shapes (Chapter III). Consequently, these suspensions will be spray-dried to produce the dry spherical HA agglomerates of a few tens of microns (Chapter IV). In addition, to improve the interaction laser-material the mixing with absorption additives will be carried out before evaluating its processability in a PBSLP apparatus (Chapter V). The chlorination of the spherical HA agglomerates to produce an SHA with better thermal stability as Chlorapatite (described in Chapter II) was also performed for feedstock comparison in PBSLP.

Table 9. PBSLP target powder properties

Particle shape	Particle size (x_{50})	Distribution span	Flowability (HR)	Laser absorption (%)
Spherical	30-70 µm	> 1	< 1.25	Should be > 60

For the MSLA process (VAT photopolymerization category), powder showing **effective redispersion** in a photocurable resin, **low settling velocity, a low increase of suspension viscosity, and good debinding-sintering behaviour** (avoiding the formation of cracks) is envisaged. Powder agglomeration would lead to uneven distribution of raw materials and faster sedimentation. Thus, particle size in suspension will be examined to evaluate and avoid agglomeration. This could require the use of dispersants. The Turbiscan^{LAB} stability index (TSI) which will be described in the next chapter can evaluate the stability of a suspension. The lower the index value the higher the stability of the suspension. A value of **TSI < 2** for the whole duration of the printing process was fixed as an objective. This value would be the limit before showing important stability destabilization corresponding to large sedimentation, wide particle size variation, and small phase separation. As explained previously a **viscosity at a low shear rate under 5 Pa.s** should be kept for the utilization of the suspension in the MSLA equipment. It is known that particle size plays an important role in the stability and viscosity in suspension, then different sizes will be evaluated to find the one yielding the most suitable suspension properties (Song et al., 2019; Xing-Bang et al., 2019). In addition, the particle size can influence the debinding-sintering behaviour preventing the formation of cracks in the sintered parts. Calcium phosphates show a correct sintering behaviour with a **particle size in the range of 1-20µm** (Pfaffinger et al., 2015). Thus, the target x_{50} was fixed within this range. A different procedure was followed for the tailoring of the HA powder intended for MSLA. HA powder obtained through synthesis and calcination was used as starting material. Then, a controlled milling process results on powders with different particle sizes that could be evaluated and compared as filler in a liquid photocurable resin. Their processability in an MSLA apparatus will be evaluated in Chapter VI.

Table 10. MSLA target powder/slurry properties

Particle shape	Particle size (x_{50})	Dispersion stability (TSI)	Viscosity at a low shear rate
Irregular	1-20 µm	< 2	< 5 Pa.s

The two main processes used for the tailoring of HA powder and the two with the highest complexity were the stirred bead mill and the spray-drying processes. For this reason, two complete chapters were dedicated to their optimization. It allowed us to better control and understand the parameters involved in the processes and their effects on the product. A short introduction of both processes is written below.

3.2 Stirred bead mill process

This section is dedicated to giving an overview of stirred bead mill process by describing its principles, presenting its applications, advantages, and parameters. The literature shows the large potential of stirred bead mills to produce sub-micron ground particles (Hennart et al., 2010). A horizontal stirred bead mill uses a grinding chamber filled with small beads whereby comminution takes place by collision and attrition between the beads. Three types of stirred media mills can be distinguished depending on the stirrer design and mill chamber geometry (Figure 15). The design of a mill is optimized to enhance the power density in the mill. The mill design strongly influences the motion of the grinding medium affecting the stress-energy and the surface area of the impeller in contact with the grinding media.

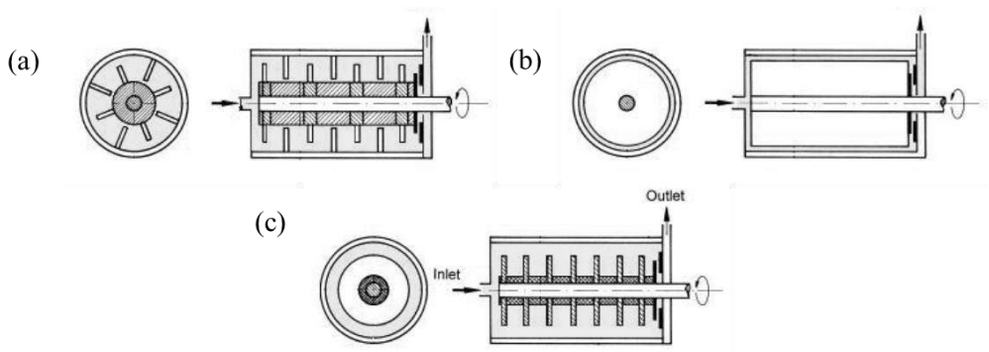

Figure 15. Types of mills and their stirrer. (a) pin-counter-pin stirrer. (b) annular gap mill (c) disc stirrer. Retrieved from Kwade (Kwade, 1999).

The stirring effect is most often caused by an agitator system (pin-counter-pin or disc stirrer) mounted on a shaft or by the rotation of the inner cylinder in an annular mill. The mill feed is pumped from the top of the grinding chamber. During continuous operation, the suspension has a horizontal flow and passes through the chamber until being discharged from the opposite side of the device. In a discontinuous process, the suspension passes several times inside the chamber mill (pendulum or recycling modes).

Kwade et al. (Kwade and Schwedes, 2007) describe milling experiments using two key parameters. These are the stress number SN (number of collisions that a product particle requires to break to reach a given size) and the stress-energy (energy of a collision between two grinding beads in the mill). At low and medium solid concentrations and suspension viscosities, it is most probable that at each contact of two beads and thus, at each stress event only one particle is stressed intensively. Under this condition in batch mode, the average number of stress events of each product particle, the stress number *SN*, is determined by the number of bead contacts, *Nc*, by the probability that a particle is caught and sufficiently stressed at a bead contact, P_s, and by the number of feed particles inside the mill, N_P:

$$SN = \frac{N_c P_s}{N_P} \tag{4}$$

The number of bead contacts can be assumed to be proportional to the number of revolutions *n*, to the grinding time *t*, and to the number of grinding media N_{GM} in the mill (in function of grinding chamber

volume, V_{GC}, the grinding media filling ratio φ_{GM}, the porosity of the grinding media filling at rest ε, and grinding media diameter x_{GM}).

$$N_c \propto n \cdot t \cdot N_{GM} \propto n \cdot t \cdot \frac{V_{GC}\varphi_{GM}(1-\varepsilon)}{\frac{\pi}{6}x_{GM}^3} \quad (5)$$

The probability of obtaining a particle stress higher enough at a bead contact depends on the operation type. For the grinding of tough agglomerates or crystalline materials, such as minerals or ceramics, the probability is proportional to the active volume between two beads. Then, the following proportionality of the stress number *SN* can be derived:

$$SN \propto \frac{\varphi_{GM}(1-\varepsilon)}{\{1-\varphi_{GM}(1-\varepsilon)\}c_v}\frac{n \cdot t}{x_{GM}^2} \quad (6)$$

Where c_v is the solids volume concentration, n the number of revolutions (s^{-1}), and t the comminution time (s). Then, for grinding of crystalline materials the stress number SN is inversely proportional to the square of the diameter of the grinding media. We supposed through these equations that the number of particles is equal to the ratio of the overall volume of the feed particles $V_{p,tot}$, to the average volume of the feed particles, V_p as follows:

$$N_p \propto \frac{V_{p,tot}}{V_p} = V_{GC} \cdot \frac{\{1-\varphi_{GM}(1-\varepsilon)\} \cdot c_v}{V_p} \quad (7)$$

Kwade (Kwade and Schwedes, 2007) specified that, for weak to medium-hard crystalline materials, as a measure of the stress intensity the so-called stress-energy SE_{GM} can be used, if the same feed material with constant particle size distribution is ground. He proposed to express the stress-energy of beads as follows:

$$SI \propto SE_{GM} \propto x_{GM}^3 \rho_{GM} V_r^2 \quad (8)$$

being V_r the circumferential speed of the stirrer.

The stress numbers and stress energies acting during stress events influence the result of the grinding process. Since the stress-energy can be considered as the specific energy, E_m, consumed at each stress event, the overall specific energy consumption of the mill will be proportional to the product of the stress-energy (stress intensity) *SI* and the stress number *SN*:

$$E_m \propto SN \cdot SI \quad (9)$$

In addition, the consumed specific energy after a grinding time, t, can be described as follows:

$$E_m(t) = \frac{E(t)}{m_P} = \int_0^t \frac{(P(\tau) - P_0)d\tau}{m_p} \quad (10)$$

Where m_p is the mass of the ground product and $P(\tau)$, the power draw of the motor at a time τ. P_0 is the no-load power.

A variety of materials, inorganic and organic materials were, for example, reduced to the sub-micron size range. The pharmaceutical industry focuses on the grinding of organic products. The use of additives such as polymers or cyclodextrins is common. The use of additives allows reaching better physical stability, finer grinding, and/or chemical stability. In these cases, the polymer acts as a surfactant to enhance the physical stability of ground particles (Li et al., 2016).

Other important aspects and issues have been examined regarding this type of milling process:

- Heavy metals contamination issues: The material hardness of the media is a relevant factor, the harder the medium the less contamination. Also, the type of material being mill influences the contamination detected depending on its hardness. The size of the media is also important, bigger media size tends to generate more media wear (Breitung-Faes and Kwade, 2008). The grinding bead wear has been demonstrated to be a function of the specific energy input, thus its level of wear is determined by the shape and hardness of beads and feed material (Becker and Schwedes, 1999).
- Modelling and characterization of mills: Several types of models can be useful for the prediction of the grinding process, upscaling, etc. Population balance modelling (PBM) has demonstrated to often be the best way to fit experimental data. This mathematical tool studies and describes the evolution of particle size in a particle size reduction process (Sommer et al., 2006; Varinot et al., 1999).
- The stability of ground particles: The stability of the product and its final particle size was found to be a function of the electrostatic properties of the particles and pH of the solution (Mende et al., 2003).
- Effect of process parameters on ground product quality: Many researchers have investigated the influence of process parameters on the final particle size and product quality. A summary of factors influencing the final ground product quality can be found in Figure 16.

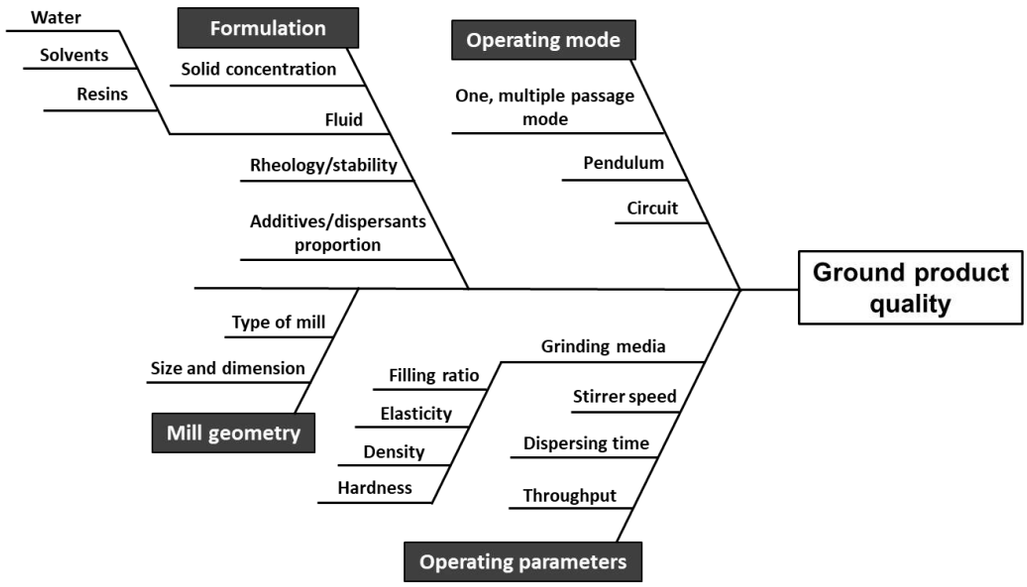

Figure 16. Ishikawa diagram with factors influencing the grinding result.

Table 11 summarizes the effect of the operating parameters [stirrer speed (Breitung-Faes and Kwade, 2014; Gao et al., 1996; Kwade, 2003), grinding media size (Herbst and Sepulveda, 1978; Tanaka, 1995), solid concentration (Inam et al., 2011; Strobel et al., 2018), and filling ratio (Guo et al., 2021; He et al., 2006)] on the final product taking into account the tendencies observed by different authors on the milling of diverse materials. It should be noted that the influence of the parameters such as stirrer speed, grinding media size, and solid concentration is difficult to quantify. The tendencies can vary in function of the material processed and also on the authors depending if they focus their interest on the kinetic breakage, product particle size, or the energetic efficacy of the process (Ouattara, 2010). An increase in the grinding media filling ratio improves the milling process; however, the value should not exceed 75-80% of the chamber volume since it could impede the free movement of the beads.

Table 11. Summary of the effect of the operating parameters on SBM process results. Influence can vary depending on the material treated.

Parameter / (At same E_m) Effect on	Stirrer speed ↑	Grinding media size ↑	Solid concentration ↑	Product flow rate ↑	Grinding media filling rate ↑
Kinetic breakage	↑	↑	↓	↓	↑
Product particle size	↓	↑	↓	↑	↓
Polydispersity	↓	—	—	—	—
Energetic efficacy	—	↑ (When optimal)	—	—	↑
Thermal effect	↑	—	—	—	—
	The influence depend on the material treated.				Should not be higher than 75-80%

Increasing parameter | Increasing variable | Decreasing variable

Stirred bead milling technology has proven to be for many industries a modern, sophisticated, flexible, and energy-efficient grinding solution for fine and ultra-fine grinding of materials. Obtaining the correct particle and PSD is crucial for many applications. Its use to process HA powders has not been amply investigated yet. A synthesis of the existing literature on the milling of HA using stirred bead mill will be presented in Chapter III.

Chapter III is dedicated to the study of the most important factors influencing the HA ground product characteristics. The aqueous suspension formulation (ceramic concentration, dispersant proportion…) and its influence on the suspension viscosity and stability, as well as, on the product quality after milling is evaluated. Then the different operational parameters such as stirrer speed, and grinding media size were under examination. Optimal parameters for energy saving on the production of HA powders depending on the needs were pursued. First, a suspension containing sub-micron-sized particles was obtained for its use in a posterior spray-drying process to produce spherical agglomerates. Then, another type of suspension composed of micron-sized particles was obtained to be used (after filtering and drying them) in VAT photopolymerization technologies.

3.3 Spray drying of hydroxyapatite

In the same way as the previous section, in this one we will expose a general overview of the spray-drying process, starting with the technology basics, a short review of its applications, and the main parameters affecting the properties of the spray-dried powder.

The spray drying process is a one-step drying operation process in which a liquid feed is atomized into fine droplets defined as “spray” and just after evaporated by a hot drying gas having as product a dry powder. Four basic stages define the process: atomization of the feed, droplet air contact, droplet drying, and separation of the dried particles from the gas.

Samuel Peroy invented the spray drying process describing its principle in a patent issued in 1872 (“Improvement in drying and concentrating liquid substances by atomizing,” 1872). This invention comes from the need to reduce the food's weight and other materials during transportation. Manufacturers have continued improving the technology to adapt it to the large scale and for its application in many fields such as food, chemicals, and pharmaceutical (Broadhead et al., 1992; He et al., 1999; Langrish and Fletcher, n.d.). The dairy industry including whole milk, fat-enriched milk, and skim milk is the largest employer of spray dryers in food processing (Chen and Mujumdar, 2008). In the case of pharmaceutical applications, the most treated has been the obtention of dry extracts of active raw materials from plants. A broad range of active ingredients and excipients in pharmacy are produced yearly by spray drying (Sollohub and Cal, 2010).

Some of the spray drying main advantages that make it an interesting technology for the industry are described:

- Control of product size and morphology (Nandiyanto and Okuyama, 2011). In some pharmaceutical applications, the control of the PSD of products is of special relevance, for example, in pulmonary therapy (Seville et al., 2007).
- Maximum efficiency, minimal environmental impact, and continuous operation. Shortening the number of operations to reach the same product quality meaning a reduction of production costs (Jain et al., 2012).
- Enhancing the solubility of poorly soluble drugs. Through this process, amorphous materials and metastable form are obtained. Thus, improving the solubility and bioavailability of the products (Chen et al., 2004; Jung et al., 1999; Yi et al., 2008). The co-spray drying of ibuprofen with ordered mesoporous silica acts as an example (Ruffel et al., 2020; Shen et al., 2010).
- The microencapsulation of active ingredients modifies the release profile while protecting it from degradation (Ré, 1998). It has been largely used for the microencapsulation of food materials, for example, the encapsulation of flavours in Arabic gum since the 1930s (Krishnan et al., 2005).

The atomizer is the device producing the atomization of the feed. Exist different types on the market: spinning disk, pressure nozzle, pneumatic atomizer, two-fluid nozzle, and sonic nozzle. By choosing the type of atomizer we can control the droplet size which will influence the final particle size. For small-scale production, the lower consumption of atomizing gas by the two-fluid nozzle is preferred. The type of contact between the spray and the hot gas (air or nitrogen) is determined by the direction of both spray and drying air (Crosby, 1989; Ziaee et al., 2019). Several types exist:

- Co-current dryer: Spray and hot airflow in the same direction inside the chamber. It is considered the best design for heat-sensitive substances (e.g., active pharmaceutical ingredients). The hottest drying air is in contact with the droplets just after being released from the nozzle, producing a quick drying compared with other designs.
- Counter-current dryer: The hot air flows in the opposite way of the spray. This type is recommended for materials keeping internal moisture since longer cycles of heat are required to draw the moisture.
- Mixed flow (fountain type): It is a combination of the two previous air flows. The solution is sprayed by the atomizer that is placed in the central part of the drying chamber. The particles move through the drying chamber experiencing both co-current and counter-current phases. This mode is suitable for heat-stable products where coarse powder requirements necessitate the use of nozzle atomizers, spraying upwards into an incoming airflow, or for heat sensitive products where the atomizer sprays droplets downwards towards an integrated fluid bed.

Dried particles are separated from the gas stream and collected by a conical container called cyclone. The gas containing the particles enters into the cyclone with an inlet velocity and moves in a spiral pattern. The strong swirling flow forms a vortex inside, then the large particles won’t be able to follow the curve of the vortex. They will progressively collide with the cyclone walls (by the effect of centrifugal force), lose speed, and finally fall at the bottom of the cyclone being collected. Small particles will remain in the gas

stream exiting the cyclone by the gas outlet located at the top. This kind of separation is considered an efficient method since it is a cheap and continuous process without consuming energy, fitting conditions of temperature, and process pressure.

Many parameters can be adjusted by the operator to modify the properties of spray-dried substances (Buckton et al., 2002; Littringer et al., 2012; Maa et al., 1997). Table 12 summarizes the parameters and their effect on the final properties of the spray-dried product.

Table 12. Spray drying parameters and their influence on the properties of the spray-dried product. Adapted from Buchi® "Mini Spray Dryer B-290 process parameters" and (Santos et al., 2018).

Parameter / Effect on	Inlet temperature	Aspirator	Humidity drying gas	Spray gas flow	Feed rate	Solid concentration	Organic solvent instead of water
Outlet temperature	↑↑	↑	↑	↓	↓	↑	↑↑
Particle size	—	—	—	↓↓	↑	↑↑	↓
Humidity in final product	↓	↓	↑	—	↑	↓	↓↓

↑↑ High influence ↑ Moderate influence ↑ Minor influence

Increasing parameter | Increasing variable | Decreasing variable

Before carrying out spray drying experiments, several questions related to the material should be answered: Kind of material, historical references about its spray drying, temperature sensitivity, phase-change information, hygroscopicity, hazardousness, aqueous or solvent-based, explosion risk, particle size requirements.

We can find numerous research studies about the spray drying of hydroxyapatite, being the biomedical the most recurrent application of the agglomerated products. Either the spray drying is used as a means for the production of HA chemically (Erdem, 2013) and from natural sources (Kusrini et al., 2012) or to tailor the powder properties for its use in medical applications (e.g., plasma spray) (Bastan et al., 2016; Murtaza et al., 2012). In addition, the influence of the experimental conditions on the final dried HA powder has been largely studied (Bastan et al., 2017; Yang and Wang, 2001).

Chapter IV is then devoted to the study of the parameters influence on HA spray dried product. The aqueous suspension formulation (binder dosage, solid concentration…) and the impact on suspension stability and viscosity are evaluated. Also, its influence on the final product quality was under examination. Operational parameters' effect on final HA microspheres was evaluated. Finally, the tailoring of HA powders was carried out to obtain powders with certain morphology enhancing the flowability properties needed for a PBSLP process.

The next chapter (chapter II) presents the materials and methods used along with the whole thesis work. It will serve as an introductory description of the techniques used for the characterization and evaluation of thesis products. It also includes the methods followed for the synthesis of HA and ClA which are the starting powders used during our work.

4. REFERENCES

Albrektsson, T., Johansson, C., 2001. Osteoinduction, osteoconduction and osseointegration. European Spine Journal 10, S96–S101. https://doi.org/10.1007/s005860100282

Alejandro, J., Carlos, J., Alexander, D., Casale, M., Arzate, H., 2011. Mechanobiology of Oral Implantable Devices, in: Pignatello, R. (Ed.), Biomaterials Science and Engineering. InTech. https://doi.org/10.5772/23611

Aoki, H., 1991. Science and medical applications of hydroxyapatite. JAAS, Tokyo.

Aronov, D., Rosen, R., Ron, E.Z., Rosenman, G., 2006. Tunable hydroxyapatite wettability: Effect on adhesion of biological molecules. Process Biochemistry 41, 2367–2372. https://doi.org/10.1016/j.procbio.2006.06.006

Barbosa-Cánovas, G.V. (Ed.), 2005. Food powders: physical properties, processing, and functionality, Food engineering series. Kluwer Academic/Plenum Publishers, New York.

Bastan, F., Karaarslan, Ö., Erdoğan, G., Ustel, F., 2016. Investigation of Bond Strength of Spray Dried Hydroxyapatite-Wollastonite Composite Powder After Plasma Spray. pp. 79–86. https://doi.org/10.1007/978-981-10-1082-8_8

Bastan, F.E., Erdogan, G., Moskalewicz, T., Ustel, F., 2017. Spray drying of hydroxyapatite powders: The effect of spray drying parameters and heat treatment on the particle size and morphology. Journal of Alloys and Compounds 724, 586–596. https://doi.org/10.1016/j.jallcom.2017.07.116

Becker, M., Schwedes, J., 1999. Comminution of ceramics in stirred media mills and wear of grinding beads1Extended version of the presentation at the 9th European Symposium on Comminution, September 8–10, 1998, Albi, France.1. Powder Technology 105, 374–381. https://doi.org/10.1016/S0032-5910(99)00161-8

Ben-Nissan, B. (Ed.), 2014. Chapter 2 Clinical Applications of Hydroxyapatite in Orthopedics, in: Advances in Calcium Phosphate Biomaterials, Springer Series in Biomaterials Science and Engineering. Springer Berlin Heidelberg : Imprint: Springer, Berlin, Heidelberg, pp. 19–49. https://doi.org/10.1007/978-3-642-53980-0

Bian, W., Li, D., Lian, Q., Zhang, W., Zhu, L., Li, X., Jin, Z., 2011. Design and fabrication of a novel porous implant with pre-set channels based on ceramic stereolithography for vascular implantation. Biofabrication 3, 034103. https://doi.org/10.1088/1758-5082/3/3/034103

Bose, S., Vahabzadeh, S., Bandyopadhyay, A., 2013. Bone tissue engineering using 3D printing. Materials Today 16, 496–504. https://doi.org/10.1016/j.mattod.2013.11.017

Breitung-Faes, S., Kwade, A., 2014. Use of an Enhanced Stress Model for the Optimization of Wet Stirred Media Milling Processes. Chem. Eng. Technol. 37, 819–826. https://doi.org/10.1002/ceat.201300686

Breitung-Faes, S., Kwade, A., 2008. Nano particle production in high-power-density mills. Chemical Engineering Research and Design, Particle Technology 86, 390–394. https://doi.org/10.1016/j.cherd.2007.11.006

Broadhead, J., Rouan, S.K.E., Rhodes, C.T., 1992. The spray drying of pharmaceuticals. Drug Development and Industrial Pharmacy 18, 1169–1206. https://doi.org/10.3109/03639049209046327

Buckton, G., Chidavaenzi, O.C., Koosha, F., 2002. The effect of spray-drying feed temperature and subsequent crystallization conditions on the physical form of lactose. AAPS PharmSciTech 3, 1–6. https://doi.org/10.1208/pt0304

C. C. Berndt, Gross, K.A., 2002. Biomedical application of apatites. In Phosphates: Geochemical, Geobiological and Materials Importance. Mineralogical Society of America: Washington, DC, USA, pp. 631–672.

Canillas, M., Pena, P., de Aza, A.H., Rodríguez, M.A., 2017. Calcium phosphates for biomedical applications. Boletín de la Sociedad Española de Cerámica y Vidrio 56, 91–112. https://doi.org/10.1016/j.bsecv.2017.05.001

Catros, S., Fricain, J.-C., Guillotin, B., Pippenger, B., Bareille, R., Remy, M., Lebraud, E., Desbat, B., Amédée, J., Guillemot, F., 2011. Laser-assisted bioprinting for creating on-demand patterns of human osteoprogenitor cells and nano-hydroxyapatite. Biofabrication 3, 025001. https://doi.org/10.1088/1758-5082/3/2/025001

Chen, Q., Zou, B., Lai, Q., Wang, Y., Xue, R., Xing, H., Fu, X., Huang, C., Yao, P., 2019. A study on biosafety of HAP ceramic prepared by SLA-3D printing technology directly. Journal of the

Mechanical Behavior of Biomedical Materials 98, 327–335. https://doi.org/10.1016/j.jmbbm.2019.06.031

Chen, R., Tagawa, M., Hoshi, N., Ogura, T., Okamoto, H., Danjo, K., 2004. Improved dissolution of an insoluble drug using a 4-fluid nozzle spray-drying technique. Chem Pharm Bull (Tokyo) 52, 1066–1070. https://doi.org/10.1248/cpb.52.1066

Chen, X.D., Mujumdar, A.S. (Eds.), 2008. Drying technologies in food processing. Blackwell Pub, Oxford.

Ching, W.Y., Rulis, P., Misra, A., 2009. Ab initio elastic properties and tensile strength of crystalline hydroxyapatite. Acta Biomater 5, 3067–3075. https://doi.org/10.1016/j.actbio.2009.04.030

Colin, C., Bartout, J.-D., Shaker, E., 2014. Osseomatrix patent - WO2014154901A1. WO2014154901A1.

Crosby, E.J., 1989. Spray Drying Handbook. Drying Technology 7, 419–425. https://doi.org/10.1080/07373938908916598

Cruz, F., 2010. Fabrication of HA/PLLA Composite Scaffolds for Bone Tissue Engineering Using Additive Manufacturing Technologies, in: Elnashar, M. (Ed.), Biopolymers. Sciyo. https://doi.org/10.5772/10264

Daculsi, G., Legeros, R., 2008. 17 - Tricalcium phosphate/hydroxyapatite biphasic ceramics, in: Kokubo, T. (Ed.), Bioceramics and Their Clinical Applications, Woodhead Publishing Series in Biomaterials. Woodhead Publishing, pp. 395–423. https://doi.org/10.1533/9781845694227.2.395

Damien, E., Revell, P.A., n.d. Coralline Hydroxyapatite Bone Graft Substitute: A Review of Experimental Studies and Biomedical Applications 9.

de Groot, K., 1984. Calcium Phosphate Bioceramics, in: Paul, J.P., Gaylor, J.D.S., Courtney, J.M., Gilchrist, T. (Eds.), Biomaterials in Artificial Organs: Proceedings of a Seminar on Biomaterials Held at the University of Strathclyde, Glasgow in September 1983, Strathclyde Bioengineering Seminars. Palgrave Macmillan UK, London, pp. 301–301. https://doi.org/10.1007/978-1-349-07283-5_41

de Groot, K., Wolke, J.G.C., Jansen, J.A., 1998. Calcium phosphate coatings for medical implants. Proc Inst Mech Eng H 212, 137–147. https://doi.org/10.1243/0954411981533917

Demnati, I., Grossin, D., Marsan, O., Bertrand, G., Collonges, G., Combes, C., Parco, M., Braceras, I., Alexis, J., Balcaen, Y., Rey, C., 2015. Comparison of Physical-chemical and Mechanical Properties of Chlorapatite and Hydroxyapatite Plasma Sprayed Coatings. TOBEJ 9, 42–55. https://doi.org/10.2174/1874120701509010042

Detsch, R., Uhl, F., Deisinger, U., Ziegler, G., 2008. 3D-Cultivation of bone marrow stromal cells on hydroxyapatite scaffolds fabricated by dispense-plotting and negative mould technique. J Mater Sci: Mater Med 19, 1491–1496. https://doi.org/10.1007/s10856-007-3297-x

Doraiswamy, A., Narayan, R.J., Harris, M.L., Qadri, S.B., Modi, R., Chrisey, D.B., 2007. Laser microfabrication of hydroxyapatite-osteoblast-like cell composites. J. Biomed. Mater. Res. 80A, 635–643. https://doi.org/10.1002/jbm.a.30969

Dorozhkin, S.V., 2012. Calcium orthophosphates and human beings: A historical perspective from the 1770s until 1940. Biomatter 2, 53–70. https://doi.org/10.4161/biom.21340

Dorozhkin, S.V., 2009. Calcium Orthophosphates in Nature, Biology and Medicine. Materials (Basel) 2, 399–498. https://doi.org/10.3390/ma2020399

Dorozhkin, S.V., Epple, M., 2002. Biological and medical significance of calcium phosphates. Angew Chem Int Ed Engl 41, 3130–3146. https://doi.org/10.1002/1521-3773(20020902)41:17<3130::AID-ANIE3130>3.0.CO;2-1

Duan, B., Wang, M., Zhou, W.Y., Cheung, W.L., Li, Z.Y., Lu, W.W., 2010a. Three-dimensional nanocomposite scaffolds fabricated via selective laser sintering for bone tissue engineering. Acta Biomaterialia 6, 4495–4505. https://doi.org/10.1016/j.actbio.2010.06.024

Duan, B., Wang, M., Zhou, W.Y., Cheung, W.L., Li, Z.Y., Lu, W.W., 2010b. Three-dimensional nanocomposite scaffolds fabricated via selective laser sintering for bone tissue engineering. Acta Biomaterialia 6, 4495–4505. https://doi.org/10.1016/j.actbio.2010.06.024

Eliaz, N., Metoki, N., 2017. Calcium Phosphate Bioceramics: A Review of Their History, Structure, Properties, Coating Technologies and Biomedical Applications. Materials 10, 334. https://doi.org/10.3390/ma10040334

Elkhooly, T.A., 2008. Preparation and characterization of calcium phosphate ceramics containing some rare earth oxides for using as biomaterials. https://doi.org/10.13140/rg.2.1.3902.5369

Elliott, J.C., 1994. Structure and chemistry of the apatites and other calcium orthophosphates, Studies in inorganic chemistry. Elsevier, Amsterdam [The Netherlands] : New York.

Ellis, S.K., McNamara, E.P., 1989. Powder synthesis research at CAMP. American Ceramic Society Bulletin; (USA) 68, 988–994.

Eosoly, S., Brabazon, D., Lohfeld, S., Looney, L., 2010. Selective laser sintering of hydroxyapatite/poly-ε-caprolactone scaffolds. Acta Biomaterialia 6, 2511–2517. https://doi.org/10.1016/j.actbio.2009.07.018

Erdem, F., 2013. The effect of binder on chemically precipitated hydroxyapatite during spray drying. Materiali in tehnologije 4.

Farzadi, A., Solati-Hashjin, M., Asadi-Eydivand, M., Abu Osman, N.A., 2014. Effect of Layer Thickness and Printing Orientation on Mechanical Properties and Dimensional Accuracy of 3D Printed Porous Samples for Bone Tissue Engineering. Plos One 9, e108252. https://doi.org/10.1371/journal.pone.0108252

Feng, C., Zhang, K., He, R., Ding, G., Xia, M., Jin, X., Xie, C., 2020. Additive manufacturing of hydroxyapatite bioceramic scaffolds: Dispersion, digital light processing, sintering, mechanical properties, and biocompatibility. J Adv Ceram 9, 360–373. https://doi.org/10.1007/s40145-020-0375-8

Fernandes, J.G., 2019. Development and optimization of a Low Temperature Co-fired Ceramic suspension for Mask-Image-Projection-based Stereolithography (Ph.D. Thesis). TDX (Tesis Doctorals en Xarxa). Universitat de Barcelona.

Ferrage, L., 2018. Elaboration d'un assemblage céramique-métal par fusion/frittage sélectif(ve) d'un lit de poudre à l'aide d'un laser Nd :YAG. Université Toulouse III – Paul Sabatier, Toulouse.

Ferraz, M.P., Monteiro, F.J., Manuel, C.M.M., 2004. Hydroxyapatite nanoparticles: A review of preparation methodologies. Journal of applied biomaterials & biomechanics : JABB 2, 74–80. https://doi.org/10.5301/JABB.2008.1812

Fu, X., Huck, D., Makein, L., Armstrong, B., Willen, U., Freeman, T., 2012. Effect of particle shape and size on flow properties of lactose powders. Particuology 10, 203–208. https://doi.org/10.1016/j.partic.2011.11.003

Fulmer, M., Ison, I., Hankermayer, C., Constantz, B., Ross, J., 2002. Measurements of the Solubilities and Dissolution Rates of Several Hydroxyapatites. Biomaterials 23, 751–5. https://doi.org/10.1016/S0142-9612(01)00180-6

Gao, M.-W., Forssberg, K.S.E., Weller, K.R., 1996. Power predictions for a pilot scale stirred ball mill. International Journal of Mineral Processing, Comminution 44–45, 641–652. https://doi.org/10.1016/0301-7516(95)00072-0

Groot, K.D., 1988. Effect of Porosity and Physicochemical Properties on the Stability, Resorption, and Strength of Calcium Phosphate Ceramics. Ann NY Acad Sci 523, 227–233. https://doi.org/10.1111/j.1749-6632.1988.tb38515.x

Grossin, D., Montón, A., Navarrete-Segado, P., Özmen, E., Urruth, G., Maury, F., Maury, D., Frances, C., Tourbin, M., Lenormand, P., Bertrand, G., 2021. A review of additive manufacturing of ceramics by powder bed selective laser processing (sintering / melting): Calcium phosphate, silicon carbide, zirconia, alumina, and their composites. Open Ceramics 5, 100073. https://doi.org/10.1016/j.oceram.2021.100073

Guo, W., Han, Y., Li, Y., Tang, Z., 2021. Impact of ball filling rate and stirrer tip speed on milling iron ore by wet stirred mill: Analysis and prediction of the particle size distribution. Powder Technology 378, 12–18. https://doi.org/10.1016/j.powtec.2020.09.052

Habraken, W., Habibovic, P., Epple, M., Bohner, M., 2016. Calcium phosphates in biomedical applications: materials for the future? Materials Today 19, 69–87. https://doi.org/10.1016/j.mattod.2015.10.008

Hao, L., Savalani, M.M., Zhang, Y., Tanner, K.E., Heath, R.J., Harris, R.A., 2007. Characterization of selective laser-sintered hydroxyapatite-based biocomposite structures for bone replacement. Proceedings of the Royal Society A: Mathematical, Physical and Engineering Sciences 463, 1857–1869. https://doi.org/10.1098/rspa.2007.1854

Hao, L, Savalani, M.M., Zhang, Y., Tanner, K.E., Heath, R.J., Harris, R.A., 2007. Characterization of selective laser-sintered hydroxyapatite-based biocomposite structures for bone replacement. Proc. R. Soc. A 463, 1857–1869. https://doi.org/10.1098/rspa.2007.1854

Harris, M.L., Doraiswamy, A., Narayan, R.J., Patz, T.M., Chrisey, D.B., 2008. Recent progress in CAD/CAM laser direct-writing of biomaterials. Materials Science and Engineering: C, Proceedings from the Advanced Processing of Biomaterials Symposium, Materials Science and Technology Conference and Exhibition 28, 359–365. https://doi.org/10.1016/j.msec.2007.04.013

He, M., Wang, Y., Forssberg, E., 2006. Parameter Effects on Wet Ultrafine Grinding of Limestone Through Slurry Rheology in a Stirred Media Mill. Powder Technology 161, 10–21. https://doi.org/10.1016/j.powtec.2005.08.026

He, P., Davis, S.S., Illum, L., 1999. Chitosan microspheres prepared by spray drying. Int J Pharm 187, 53–65. https://doi.org/10.1016/s0378-5173(99)00125-8

Hench, L.L., 1991. Bioceramics: From Concept to Clinic. Journal of the American Ceramic Society 74, 1487–1510. https://doi.org/10.1111/j.1151-2916.1991.tb07132.x

Hench, L.L., Best, S.M., 2013. Chapter I.2.4 - Ceramics, Glasses, and Glass-Ceramics: Basic Principles, in: Ratner, B.D., Hoffman, A.S., Schoen, F.J., Lemons, J.E. (Eds.), Biomaterials Science (Third Edition). Academic Press, pp. 128–151. https://doi.org/10.1016/B978-0-08-087780-8.00016-4

Hennart, S., Domingues, M.C., Wildeboer, W.J., Hee, P., Meesters, G., 2010. Study of the process of stirred ball milling of poorly water soluble organic products using factorial design. Powder Technology - POWDER TECHNOL 198, 56–60. https://doi.org/10.1016/j.powtec.2009.10.014

Herbst, J.A., Sepulveda, J.L., 1978. Fundamentals of fine and ultrafine grinding in a stirred ball mill. International Powder and Bulk Solids Handling and Processing: Proceedings held Rosemount Illinois 16, 18.

Ho, H.C.H., Cheung, W.L., Gibson, I., 2002. Effects of graphite powder on the laser sintering behaviour of polycarbonate. Rapid Prototyping Journal 8, 233–242. https://doi.org/10.1108/13552540210441148

Hull, C.W., 1986. Apparatus for production of three-dimensional objects by stereolithography. US4575330A.

Improvement in drying and concentrating liquid substances by atomizing, 1872. . US125406A.

Inam, M.A., Ouattara, S., Frances, C., 2011. Effects of concentration of dispersions on particle sizing during production of fine particles in wet grinding process. Powder Technology 208, 329–336. https://doi.org/10.1016/j.powtec.2010.08.025

Iuliano, A., Wal, E., Ruijmbeek, C.W.B., in 't Groen, S.L.M., Pijnappel, W.W.M.P., Greef, J.C., Saggiomo, V., 2020. Coupling 3D Printing and Novel Replica Molding for In House Fabrication of Skeletal Muscle Tissue Engineering Devices. Adv. Mater. Technol. 2000344. https://doi.org/10.1002/admt.202000344

Jain, M.S., Lohare, G.B., Bari, M., Chavan, R., Barhate, S., Shah, C.B., 2012. Spray Drying in Pharmaceutical Industry: A Review. Research Journal of Pharmaceutical Dosage Forms and Technology. 4, 74–79. https://doi.org/N/A

Japanese Technology Evaluation Center (Loyola College in Maryland), World Technology Evaluation Center (Loyola College in Maryland), Rapid Prototyping Association of SME (Eds.), 1997. JTEC/WTEC panel on rapid prototyping in Europe and Japan: final report. Published and Distributed by Rapid Prototyping Association of the Society of Manufacturing Engineers, in cooperation with International Technology Research Institute, Loyola College in Maryland, Baltimore, MD.

Jung, J.Y., Yoo, S.D., Lee, S.H., Kim, K.H., Yoon, D.S., Lee, K.H., 1999. Enhanced solubility and dissolution rate of itraconazole by a solid dispersion technique. Int J Pharm 187, 209–218. https://doi.org/10.1016/s0378-5173(99)00191-x

Kalita, S.J., Bose, S., Hosick, H.L., Bandyopadhyay, A., 2003. Development of controlled porosity polymer-ceramic composite scaffolds via fused deposition modeling. Materials Science and Engineering: C 23, 611–620. https://doi.org/10.1016/S0928-4931(03)00052-3

Kamitani, T., Yamada, O., Marutani, Y., 2000. Selective laser sintering with heat of formation by using reactive materials, in: Miyamoto, I., Sugioka, K., Sigmon, T.W. (Eds.), . Presented at the First International Symposium on Laser Precision Microfabrication (LPM2000), Omiya, Saitama, Japan, pp. 299–302. https://doi.org/10.1117/12.405683

Kao, F.-C., Chiu, P.-Y., Tsai, T.-T., Lin, Z.-H., 2019. The application of nanogenerators and piezoelectricity in osteogenesis. Science and Technology of Advanced Materials 20, 1103–1117. https://doi.org/10.1080/14686996.2019.1693880

Karapatis, N.P., Egger, G., 1999. Optimization of Powder Layer Density in Selective Laser Sintering. Presented at the 10th Solid Freeform Fabrication Symposium (SFF), AUSTIN, TX, p. 10.

Komissarenko, D., Sokolov, P., Evstigneeva, A., Shmeleva, I., Dosovitsky, A., 2018. Rheological and Curing Behavior of Acrylate-Based Suspensions for the DLP 3D Printing of Complex Zirconia Parts. Materials 11, 2350. https://doi.org/10.3390/ma11122350

Krantz, M., Zhang, H., Zhu, J., 2009. Characterization of powder flow: Static and dynamic testing. Powder Technology 194, 239–245. https://doi.org/10.1016/j.powtec.2009.05.001

Krishnan, S., Kshirsagar, A., Singhal, R., 2005. The use gum Arabic and modified starch in the microencapsulation of a food flavoring. Carbohydrate Polymers 62, 309–315. https://doi.org/10.1016/j.carbpol.2005.03.020

Kusrini, E., Pudjiastuti, A.R., Astutiningsih, S., Harjanto, S., 2012. Preparation of Hydroxyapatite from Bovine Bone by Combination Methods of Ultrasonic and Spray Drying 5.

Kwade, A., 2003. A Stressing Model for the Description and Optimization of Grinding Processes. Chem. Eng. Technol. 26, 199–205. https://doi.org/10.1002/ceat.200390029

Kwade, A., 1999. Wet comminution in stirred media mills — research and its practical application. Powder Technology 105, 14–20. https://doi.org/10.1016/S0032-5910(99)00113-8

Kwade, A., Schwedes, J., 2007. Chapter 6 Wet Grinding in Stirred Media Mills, in: Handbook of Powder Technology. Elsevier, pp. 251–382. https://doi.org/10.1016/S0167-3785(07)12009-1

Lam, C.X., Teoh, S.H., Hutmacher, D.W., 2007. Comparison of the degradation of polycaprolactone and polycaprolactone–(β-tricalcium phosphate) scaffolds in alkaline medium. Polymer International 56, 718–728. https://doi.org/10.1002/pi.2195

Lam, C.X.F., Hutmacher, D.W., Schantz, J.-T., Woodruff, M.A., Teoh, S.H., 2009. Evaluation of polycaprolactone scaffold degradation for 6 months in vitro and in vivo. Journal of Biomedical Materials Research Part A 90A, 906–919. https://doi.org/10.1002/jbm.a.32052

Langrish, T. a. G., Fletcher, D.F., n.d. Spray drying of food ingredients and applications of CFD in spray drying. Chemical Engineering and Processing: Process Intensification 40, 345–354.

Lee, J.W., Ahn, G., Kim, D.S., Cho, D.-W., 2009. Development of nano- and microscale composite 3D scaffolds using PPF/DEF-HA and micro-stereolithography. Microelectronic Engineering, MNE '08 86, 1465–1467. https://doi.org/10.1016/j.mee.2008.12.038

LeGeros, R.Z., 1991. Calcium phosphates in oral biology and medicine. Monogr Oral Sci 15, 1–201.

Li, H., Liu, Yongsheng, Liu, Yansong, Hu, K., Lu, Z., Liang, J., 2020. Effects of Solvent Debinding on the Microstructure and Properties of 3D-Printed Alumina Ceramics. ACS Omega 5, 27455–27462. https://doi.org/10.1021/acsomega.0c03944

Li, M., Azad, M., Davé, R., Bilgili, E., 2016. Nanomilling of Drugs for Bioavailability Enhancement: A Holistic Formulation-Process Perspective. Pharmaceutics 8. https://doi.org/10.3390/pharmaceutics8020017

Littringer, E.M., Mescher, A., Eckhard, S., Schröttner, H., Langes, C., Fries, M., Griesser, U., Walzel, P., Urbanetz, N.A., 2012. Spray Drying of Mannitol as a Drug Carrier—The Impact of Process Parameters on Product Properties. Drying Technology 30, 114–124. https://doi.org/10.1080/07373937.2011.620726

Liu, L.X., Marziano, I., Bentham, A.C., Litster, J.D., E.T.White, Howes, T., 2008. Effect of particle properties on the flowability of ibuprofen powders. International Journal of Pharmaceutics 362, 109–117. https://doi.org/10.1016/j.ijpharm.2008.06.023

Lu, H., Guo, X., Liu, Y., Gong, X., 2015. Effect of Particle Size on Flow Mode and Flow Characteristics of Pulverized Coal. KONA 32, 143–153. https://doi.org/10.14356/kona.2015002

Maa, Y.F., Costantino, H.R., Nguyen, P.A., Hsu, C.C., 1997. The effect of operating and formulation variables on the morphology of spray-dried protein particles. Pharm Dev Technol 2, 213–223. https://doi.org/10.3109/10837459709031441

Melchels, F.P.W., Feijen, J., Grijpma, D.W., 2010. A review on stereolithography and its applications in biomedical engineering. Biomaterials 31, 6121–6130. https://doi.org/10.1016/j.biomaterials.2010.04.050

Mende, S., Stenger, F., Peukert, W., Schwedes, J., 2003. Mechanical production and stabilization of submicron particles in stirred media mills. Powder Technology 132, 64–73. https://doi.org/10.1016/S0032-5910(03)00042-1

Metelkova, J., Kinds, Y., Kempen, K., de Formanoir, C., Witvrouw, A., Van Hooreweder, B., 2018. On the influence of laser defocusing in Selective Laser Melting of 316L. Additive Manufacturing 23, 161–169. https://doi.org/10.1016/j.addma.2018.08.006

Minh, D.P., Rio, S., Sharrock, P., Sebei, H., Lyczko, N., Tran, N.D., Raii, M., Nzihou, A., 2014. Hydroxyapatite starting from calcium carbonate and orthophosphoric acid: synthesis, characterization, and applications. Journal of Materials Science 49, p.4261-4269. https://doi.org/10.1007/s10853-014-8121-7

Misra, D.N., 1984. Adsorption on and Surface Chemistry of Hydroxyapatite. https://doi.org/10.1007/978-1-4757-9012-2_7

Murray, M.G.S., Wang, J., Ponton, C.B., Marquis, P.M., 1995. An improvement in processing of hydroxyapatite ceramics. J Mater Sci 30, 3061–3074. https://doi.org/10.1007/BF01209218

Murtaza, Q., Stokes, J., Ardhaoui, M., 2012. Experimental Analysis of Spray Dryer Used in Hydroxyapatite Thermal Spray Powder. Journal of Thermal Spray Technology 21. https://doi.org/10.1007/s11666-012-9791-9

Nandiyanto, A.B.D., Okuyama, K., 2011. Progress in developing spray-drying methods for the production of controlled morphology particles: From the nanometer to submicrometer size ranges. Advanced Powder Technology 22, 1–19. https://doi.org/10.1016/j.apt.2010.09.011

Ouattara, S., 2010. Nanobroyage d'actifs organiques en suspensions concentrées dans un broyeur à billes agité (Thesis). Toulouse, INPT.

Palmer, L.C., Newcomb, C.J., Kaltz, S.R., Spoerke, E.D., Stupp, S.I., 2008. Biomimetic systems for hydroxyapatite mineralization inspired by bone and enamel. Chem Rev 108, 4754–4783. https://doi.org/10.1021/cr8004422

Pei, X., Ma, L., Zhang, B., Sun, J., Sun, Y., Fan, Y., Gou, Z., Zhou, C., Zhang, X., 2017. Creating hierarchical porosity hydroxyapatite scaffold with osteoinduction by three-dimensional printing and microwave sintering. Biofabrication 9. https://doi.org/10.1088/1758-5090/aa90ed

Peng, T., Chen, C., 2018. Influence of energy density on energy demand and porosity of 316L stainless steel fabricated by selective laser melting. Int. J. of Precis. Eng. and Manuf.-Green Tech. 5, 55–62. https://doi.org/10.1007/s40684-018-0006-9

Pfaffinger, M., Mitteramskogler, G., Gmeiner, R., Stampfl, J., 2015. Thermal Debinding of Ceramic-Filled Photopolymers. MSF 825–826, 75–81. https://doi.org/10.4028/www.scientific.net/MSF.825-826.75

Posner, A.S., Betts, F., 1975. Synthetic amorphous calcium phosphate and its relation to bone mineral structure. Acc. Chem. Res. 8, 273–281. https://doi.org/10.1021/ar50092a003

Prashanth, K.G., Scudino, S., Maity, T., Das, J., Eckert, J., 2017. Is the energy density a reliable parameter for materials synthesis by selective laser melting? Materials Research Letters 5, 386–390. https://doi.org/10.1080/21663831.2017.1299808

Preobrazhenskiy, I.I., Tikhonov, A.A., Evdokimov, P.V., Shibaev, A.V., Putlyaev, V.I., 2021. DLP printing of hydrogel/calcium phosphate composites for the treatment of bone defects. Open Ceramics 6, 100115. https://doi.org/10.1016/j.oceram.2021.100115

Qin, X.-H., Ovsianikov, A., Stampfl, J., Liska, R., 2014. Additive manufacturing of photosensitive hydrogels for tissue engineering applications. BioNanoMaterials 15. https://doi.org/10.1515/bnm-2014-0008

Quan, H., Zhang, T., Xu, H., Luo, S., Nie, J., Zhu, X., 2020. Photo-curing 3D printing technique and its challenges. Bioactive Materials 5, 110–115. https://doi.org/10.1016/j.bioactmat.2019.12.003

Ramesh, S., Aw, K.L., Tolouei, R., Amiriyan, M., Tan, C.Y., Hamdi, M., Purbolaksono, J., Hassan, M.A., Teng, W.D., 2013. Sintering properties of hydroxyapatite powders prepared using different methods. Ceramics International 39, 111–119. https://doi.org/10.1016/j.ceramint.2012.05.103

Ramesh, S., Christopher, P., Tan, C.Y., Teng, W.D., 2004. The effect of cold isostatic pressing on the sinterability of synthesized HA. Biomed. Eng. Appl. Basis Commun. 16, 199–204. https://doi.org/10.4015/S101623720400027X

Ré, M.I., 1998. Microencapsulation by Spray Drying. Drying Technology 16, 1195–1236. https://doi.org/10.1080/07373939808917460

Rey, C., Combes, C., Drouet, C., Grossin, D., Bertrand, G., Soulié, J., 2017. 1.11 Bioactive Calcium Phosphate Compounds: Physical Chemistry☆, in: Ducheyne, P. (Ed.), Comprehensive Biomaterials II. Elsevier, Oxford, pp. 244–290. https://doi.org/10.1016/B978-0-12-803581-8.10171-7

Ronca, A., Ambrosio, L., Grijpma, D.W., 2013. Preparation of designed poly(d,l-lactide)/nanosized hydroxyapatite composite structures by stereolithography. Acta Biomaterialia 9, 5989–5996. https://doi.org/10.1016/j.actbio.2012.12.004

Ruffel, L., Soulié, J., Coppel, Y., Roblin, P., Brouillet, F., Frances, C., Tourbin, M., 2020. Ibuprofen loading into mesoporous silica nanoparticles using Co-Spray drying: A multi-scale study. Microporous and Mesoporous Materials 291, 109689. https://doi.org/10.1016/j.micromeso.2019.109689

Russias, J., Saiz, E., Deville, S., Gryn, K., Liu, G., Nalla, R.K., Tomsia, A.P., 2007. Fabrication and in vitro characterization of three-dimensional organic/inorganic scaffolds by robocasting. Journal of Biomedical Materials Research Part A 83A, 434–445. https://doi.org/10.1002/jbm.a.31237

Sadat-Shojai, M., Khorasani, M.-T., Dinpanah-Khoshdargi, E., Jamshidi, A., 2013. Synthesis methods for nanosized hydroxyapatite with diverse structures. Acta Biomaterialia 9, 7591–7621. https://doi.org/10.1016/j.actbio.2013.04.012

Samavedi, S., Whittington, A.R., Goldstein, A.S., 2013. Calcium phosphate ceramics in bone tissue engineering: a review of properties and their influence on cell behavior. Acta Biomater 9, 8037–8045. https://doi.org/10.1016/j.actbio.2013.06.014

Santos, D., Maurício, A.C., Sencadas, V., Santos, J.D., Fernandes, M.H., Gomes, P.S., 2018. Spray Drying: An Overview, in: Pignatello, R., Musumeci, T. (Eds.), Biomaterials - Physics and Chemistry - New Edition. InTech. https://doi.org/10.5772/intechopen.72247

Schmid, M., Amado, F., Levy, G., Wegener, K., 2013. Flowability of powders for Selective Laser Sintering (SLS) investigated by Round Robin Test, in: da Silva Bártolo, P., de Lemos, A., Pereira, A., Mateus, A., Ramos, C., Santos, C., Oliveira, D., Pinto, E., Craveiro, F., da Rocha Terreiro Galha Bártolo, H., de Amorim Almeia, H., Sousa, I., Matias, J., Durão, L., Gaspar, M., Fernandes Alves, N., Carreira, P., Ferreira, T., Marques, T. (Eds.), High Value Manufacturing: Advanced Research in Virtual and Rapid Prototyping. CRC Press, pp. 95–99. https://doi.org/10.1201/b15961-19

Scipioni Bertoli, U., Wolfer, A.J., Matthews, M.J., Delplanque, J.-P.R., Schoenung, J.M., 2017. On the limitations of Volumetric Energy Density as a design parameter for Selective Laser Melting. Materials & Design 113, 331–340. https://doi.org/10.1016/j.matdes.2016.10.037

Seville, P.C., Li, H., Learoyd, T.P., 2007. Spray-Dried Powders for Pulmonary Drug Delivery. Critical Reviews™ in Therapeutic Drug Carrier Systems 24, 54. https://doi.org/10.1615/CritRevTherDrugCarrierSyst.v24.i4.10

Shen, S.-C., Ng, W.K., Chia, L., Dong, Y.-C., Tan, R.B.H., 2010. Stabilized amorphous state of ibuprofen by co-spray drying with mesoporous SBA-15 to enhance dissolution properties. J Pharm Sci 99, 1997–2007. https://doi.org/10.1002/jps.21967

Shuai, C., Gao, C., Nie, Y., Hu, H., Qu, H., Peng, S., 2010. Structural Design and Experimental Analysis of a Selective Laser Sintering System with Nano-Hydroxyapatite Powder. j biomed nanotechnol 6, 370–374. https://doi.org/10.1166/jbn.2010.1139

Shuai, C., Gao, C., Nie, Y., Hu, H., Zhou, Y., Peng, S., 2011. Structure and properties of nano-hydroxypatite scaffolds for bone tissue engineering with a selective laser sintering system. Nanotechnology 22, 285703. https://doi.org/10.1088/0957-4484/22/28/285703

Shuai, C., Li, P., Liu, J., Peng, S., 2013. Optimization of TCP/HAP ratio for better properties of calcium phosphate scaffold via selective laser sintering. Materials Characterization 77, 23–31. https://doi.org/10.1016/j.matchar.2012.12.009

Singe Gowda, R., Udayagiri, C., Drakshayani, D., 2014. Studies on the Process Parameters of Rapid Prototyping Technique (Stereolithography) for the Betterment of Part Quality. International Journal of Manufacturing Engineering 2014, 1–11. https://doi.org/10.1155/2014/804705

Sofia, D., Barletta, D., Poletto, M., 2018. Laser sintering process of ceramic powders: The effect of particle size on the mechanical properties of sintered layers. Additive Manufacturing 23, 215–224. https://doi.org/10.1016/j.addma.2018.08.012

Sofia, D., Barletta, D., Poletto, M., 2016. Flowability of ceramic powders in the sintering process. Presented at the Powder, Granule and Bulk Solids: Innovations and Applications, Jaipur (Rajasthan), India, Thapar University, p. 8.

Sollohub, K., Cal, K., 2010. Spray drying technique: II. Current applications in pharmaceutical technology. J Pharm Sci 99, 587–597. https://doi.org/10.1002/jps.21963

Sommer, M., Stenger, F., Peukert, W., Wagner, N.J., 2006. Agglomeration and breakage of nanoparticles in stirred media mills—a comparison of different methods and models. Chemical Engineering Science 61, 135–148. https://doi.org/10.1016/j.ces.2004.12.057

Song, S.Y., Park, M.S., Lee, D., Lee, J.W., Yun, J.S., 2019. Optimization and characterization of high-viscosity ZrO2 ceramic nanocomposite resins for supportless stereolithography. Materials & Design 180, 107960. https://doi.org/10.1016/j.matdes.2019.107960

Spierings, A.B., Voegtlin, M., Bauer, T., Wegener, K., 2016. Powder flowability characterisation methodology for powder-bed-based metal additive manufacturing. Prog Addit Manuf 1, 9–20. https://doi.org/10.1007/s40964-015-0001-4

Stanford, M.K., Dellacorte, C., Eylon, D., 2003. Particle Size Effects on Flow Properties of Ps304 Plasma Spray Feedstock Powder Blend, in: Kriven, W.M., Lin, H.-T. (Eds.), Ceramic Engineering and Science Proceedings. John Wiley & Sons, Inc., Hoboken, NJ, USA, pp. 577–585. https://doi.org/10.1002/9780470294802.ch82

Strobel, A., Schwenger, J., Wittpahl, S., Schmidt, J., Romeis, S., Peukert, W., 2018. Assessing the influence of viscosity and milling bead size on the stressing conditions in a stirred media mill by single particle probes. Chemical Engineering Research and Design 136, 859–869. https://doi.org/10.1016/j.cherd.2018.06.040

Suchanek, W., Yoshimura, M., 1998. Processing and properties of hydroxyapatite-based biomaterials for use as hard tissue replacement implants. Journal of Materials Research 13, 94–117. https://doi.org/10.1557/JMR.1998.0015

Sudha, P.N., Kirubanandam, S., Av, J., N, V., Kannan, R., 2018. Corrosion of ceramic materials, in: Fundamental Biomaterials: Ceramics. pp. 223–250. https://doi.org/10.1016/B978-0-08-102203-0.00009-3

Šupová, M., 2015. Substituted hydroxyapatites for biomedical applications: A review. Ceramics International 41, 9203–9231. https://doi.org/10.1016/j.ceramint.2015.03.316

Suryawanshi, J., Prashanth, K.G., Scudino, S., Eckert, J., Prakash, O., Ramamurty, U., 2016. Simultaneous enhancements of strength and toughness in an Al-12Si alloy synthesized using selective laser melting. Acta Materialia 115, 285–294. https://doi.org/10.1016/j.actamat.2016.06.009

Tanaka, T., 1995. Determining the optimum diameter of grinding media used for ultrafine grinding mechanisms. Advanced Powder Technol. 6, 125–137. https://doi.org/10.1163/156855295X00121

Thijs, L., Kempen, K., Kruth, J.-P., Van Humbeeck, J., 2013. Fine-structured aluminium products with controllable texture by selective laser melting of pre-alloyed AlSi10Mg powder. Acta Materialia 61, 1809–1819. https://doi.org/10.1016/j.actamat.2012.11.052

Tolochko, N.K., Khlopkov, Y.V., Mozzharov, S.E., Ignatiev, M.B., Laoui, T., Titov, V.I., 2000. Absorptance of powder materials suitable for laser sintering. Rapid Prototyping Journal 6, 155–161. https://doi.org/10.1108/13552540010337029

Tõnsuaadu, K., Gross, K.A., Plūduma, L., Veiderma, M., 2012. A review on the thermal stability of calcium apatites. J Therm Anal Calorim 110, 647–659. https://doi.org/10.1007/s10973-011-1877-y

Varinot, C., Berthiaux, H., Dodds, J., 1999. Prediction of the product size distribution in associations of stirred bead mills. Powder Technology 105, 228–236. https://doi.org/10.1016/S0032-5910(99)00142-4

Vert, M., Doi, Y., Hellwich, K.-H., Hess, M., Hodge, P., Kubisa, P., Rinaudo, M., Schué, F., 2012. Terminology for biorelated polymers and applications (IUPAC Recommendations 2012). Pure and Applied Chemistry 84, 377–410. https://doi.org/10.1351/PAC-REC-10-12-04

Wdfert, F., 1697. Part of a letter of Mr. Anthony van Leeuwenhoeck. Concerning the Eggs of Snails, Roots of vegetables, teeth, and Young Oysters 10.

Weiner, M.L., Salminen, W.F., Larson, P.R., Barter, R.A., Kranetz, J.L., Simon, G.S., 2001. Toxicological review of inorganic phosphates. Food and Chemical Toxicology 39, 759–786. https://doi.org/10.1016/S0278-6915(01)00028-X

Wen, Y., Xun, S., Haoye, M., Baichuan, S., Peng, C., Xuejian, L., Kaihong, Z., Xuan, Y., Jiang, P., Shibi, L., 2017. 3D printed porous ceramic scaffolds for bone tissue engineering: a review. Biomater. Sci. 5, 1690–1698. https://doi.org/10.1039/C7BM00315C

Wu, Q., Zhang, X., Wu, B., Huang, W., 2013. Effects of microwave sintering on the properties of porous hydroxyapatite scaffolds. Ceramics International 39, 2389–2395. https://doi.org/10.1016/j.ceramint.2012.08.091

Wu, X., Lian, Q., Li, D., Jin, Z., 2019. Biphasic osteochondral scaffold fabrication using multi-material mask projection stereolithography. RPJ 25, 277–288. https://doi.org/10.1108/RPJ-07-2017-0144

Xia, Y., Zhou, P., Cheng, X., Xie, Y., Liang, C., Li, C., Xu, S., 2013. Selective laser sintering fabrication of nano-hydroxyapatite/poly-ε-caprolactone scaffolds for bone tissue engineering applications. Int J Nanomedicine 8, 4197–4213. https://doi.org/10.2147/IJN.S50685

Xiao, K., Dalgarno, K.W., Wood, D.J., Goodridge, R.D., Ohtsuki, C., 2008. Indirect selective laser sintering of apatite—wollostonite glass—ceramic. Proc Inst Mech Eng H 222, 1107–1114. https://doi.org/10.1243/09544119JEIM411

Xing-Bang, L., He, Z., Jing-Xian, Z., Yu-Sen, D., Dong-Liang, J., 2019. Effect of Powder Characteristics on the Rheological Performance of Resin-based Zirconia Suspension for Stereolithography. Journal of Inorganic Materials 13. https://doi.org/10.15541/jim20190091

Yang, H.Y., Wang, M., 2001. Effect of reaction parameters on the thermostability of spray-dried hydroxyapatite powders, in: Processing and Fabrication of Advanced Materials VIII. Presented at the Processing and Fabrication of Advanced Materials VIII, WORLD SCIENTIFIC, Singapore, pp. 307–316. https://doi.org/10.1142/9789812811431_0036

Yi, T., Wan, J., Xu, H., Yang, X., 2008. A new solid self-microemulsifying formulation prepared by spray-drying to improve the oral bioavailability of poorly water soluble drugs. Eur J Pharm Biopharm 70, 439–444. https://doi.org/10.1016/j.ejpb.2008.05.001

Zeng, H., Pathak, J.L., Shi, Y., Ran, J., Liang, L., Yan, Q., Wu, T., Fan, Q., Li, M., Bai, Y., 2020. Indirect selective laser sintering-printed microporous biphasic calcium phosphate scaffold promotes endogenous bone regeneration via activation of ERK1/2 signaling. Biofabrication 12, 025032. https://doi.org/10.1088/1758-5090/ab78ed

Ziaee, A., Albadarin, A.B., Padrela, L., Femmer, T., O'Reilly, E., Walker, G., 2019. Spray drying of pharmaceuticals and biopharmaceuticals: Critical parameters and experimental process optimization approaches. European Journal of Pharmaceutical Sciences 127, 300–318. https://doi.org/10.1016/j.ejps.2018.10.026

Zyzalo, J.R., 2008. Masked projection stereolithography : improvement of the Limaye model for curing single layer medium sized parts (Thesis). Massey University.

Chapter II. Materials, characterization methods, and syntheses.

1. Introduction

This chapter serves as a general description of the materials employed throughout the entire thesis, as well as, the methods used for their characterization and syntheses. After a description of the materials used, an overview of the techniques used to characterize the products is given. Starting with the most used techniques to analyse calcium phosphate (CaP) materials in literature, which are the main protagonists in this work. Since aqueous and organic hydroxyapatite (HA)-filled slurries were prepared during our study, the general principles of suspensions together with the methods used for the evaluation of their stability and rheology are defined. Finally, we offer a description of the procedures followed for the preparation of stoichiometric HA and chlorapatite (ClA) calcium phosphate powders and their examination.

All the equipment used in this thesis were part of two different establishments:

- Analysis and processes service (SAP) which is a shared analytical service of the LGC laboratory. This service brings together essential analysis equipment for this laboratory with dedicated technical staff.
- The CIRIMAT technical competence centre, which involves the equipment of nine different competence centres.

2. Materials

Materials used for this work are presented in Table 1. All the chemicals were used as received and without further purification.

The water used in this study, both for preparing the suspension of reagents and media, and for cleaning the equipment was ultrapure water (18.2 MΩ at 25ºC), dispensed from the equipment “Purelab Ultra” of VWS Ltd. Its density was found to be 0.9952 $g.cm^{-3}$ at 25˚C whereas its pH varied between 6.3 to 6.8 at 25˚C.

185 mm diameter very slow filtering (grade:393), purple dot filter paper discs from SARTORIUS were used for vacuum filtration during this thesis. Composed of 100 % cotton linters with an α-cellulose content of > 98 % have been acid-washed to make the papers ashless and achieve high purity.

All the glassware, beads, alumina crucibles (SCERAM Advanced Ceramics), and planetary mill alumina jar used within this study were, when needed, washed by soaking them in a 10% v/v HNO_3 aqueous solution for at least one day and followed by washing with plenty of ultrapure water. After washed, they were dried at room temperature before being used.

Table 1. Summary of materials used during the thesis.

No.	Chemical name	Chemical structure	MW ($g.mol^{-1}$)	Supplier	Used for
1	Ammonia solution 28%	NH_3	17.031	CARLO ERBA® Reagents	Reagents for HA synthesis (chapter II)
2	Calcium Nitrate 4-hydrate	$Ca(NO_3)_2*4H_2O$	236.150	Dr. Paul Lohmann®	
3	Orthophosphoric Acid, 85%	H_3PO_4	97.994	CARLO ERBA® Reagents	
4	Ethanol, absolute, >= 99%	C_2H_5OH	46.070	Fisher® Scientific	Washing scientific glassware
5	Nitric Acid, 65% Ultra Pure.	HNO_3	63.010	Chem Lab™	pH control, alumina crucible cleaning
6	TIMREX® KS 44 Graphite	C	12.010	Kindly provided by Imerys® Graphite & Carbon	Powder bed selective laser processing feedstock preparation (chapter V)
7	Polyvinyl alcohol (Rhodoviol®)	CH_2CHOH	44.050	Sigma-Aldrich®	Spray drying process (chapter IV)
8	Ammonium polymethacrylate (DARVAN® C-N)	$C_4H_9NO_2$	103.120	Kindly provided by Vanderbilt Minerals®, LLC	HA aqueous suspensions preparation (chapter III and IV)
9	Polyethylene glycol 200 (PEG200)	$H(OCH_2CH_2)_nOH$	190.000	Sigma-Aldrich®	Photosensitive organic resin preparation (chapter VI)
10	Isopropyl alcohol (IPA)	C_3H_8O	60.100	Charbonneaux brabant®	
11	Dentifix HR	N/A	N/A	FunToDo®	
12	Ammonium chloride, 99+%, pure	NH_4Cl	53.490	ACROS Organics™	ClA synthesis (chapter II)
13	Calcium hydroxide	$Ca(OH)_2$	74.100	Merck®	
14	Tris(hydroxymethyl)methylamine	$H_2NC(CH_2OH)_3$	121.140	Electran®	Degradation rate test (chapter VI)
15	Hydroxyapatite commercial powders (300-08-2 & 206.93.003*)	$Ca_5(PO_4)_3(OH)$	3.160	Urodelia® SA	ClA synthesis (chapter II), starting material* (chapter III, VI), and 3D printing feedstock preparation (chapter V)

3. Calcium phosphates characterization

The characterization of bioactive calcium phosphates could be either the easiest or the most complicated task depending on the type of compound and the amount of information needed. The conjoint use of several techniques along with chemical analyses is of foremost importance for the precise characterization of complex CaP materials. This section is an outline of the main methods used to characterize CaP materials. Some of them have been used in future chapters to characterize different products as well as precursors. Rey et al. [1] presented a compilation of the most relevant characterization methods for calcium phosphates. The different techniques can be divided into different categories, chemical analysis methods, followed by diffraction methods, electron microscopy techniques, vibrational spectroscopies, and thermal analyses.

3.1 Chemical analysis

Determining precisely the nature and relative amounts of the chemical elements composing the system is of particular importance for apatitic materials, which can accommodate a large number of ionic vacancies and which can tolerate many ionic substitutions. Such data hence allows decoding the chemical formula of the compound studied.

We can distinguish between three main types of ions in CaPs of biological origin and many synthetic apatites:

- Major ions such as Ca^{2+}, orthophosphates, including PO_4^{3-} and HPO_4^{2-}, CO_3^{2-}, and OH^-;
- Minor ions like Na^+, Mg^{2+};
- Trace elements like Sr^{2+}, Zn^{2+}, F^-.

Table 2, based on the work of Rey et al. [1], summarizes the main techniques used depending on the determination of major and minor ions, and trace elements.

During the thesis the chemical characterization of the CaP products was crucial. Some of these techniques have been used, as FTIR spectroscopy and RAMAN analysis to characterize the CaP powders produced or used during this thesis. Such techniques are detailed in the next sections. Moreover, inductively coupled plasma – atomic emission (ICP-AES) spectroscopy analyses were performed in a Horiba - ULTIMA 2 for the determination of Fe, Zr, and Y ions impurities (cf. chapter III) and the content of Ca^{2+} ion for the dissolution rate analysis of printed parts (cf. chapter VI). We will provide precisely our experimental procedure for the measurements of each material.

Table 2. Main techniques used for the determination of different elements or species in calcium phosphates [1].

Element to determinate	Technique
Calcium	Atomic absorption spectroscopy (AAS)
	Inductively coupled plasma (ICP) emission spectroscopy
	Ionometry (specific electrode)
	Ion chromatography
	Complexometry (e.g., with a complexing agent such as ethylenediaminetetraacetic acid (EDTA)
	X-ray fluorescence or electron microscopy-based techniques (microprobe analyses, energy-dispersive X-ray analyses)
Phosphorus (Orthophosphate ions PO_4^{3-}, HPO_4^{2-}, H_2PO^{4-} and pyrophosphate ions $P_2O_7^{4-}$)	Inductively coupled plasma (ICP)
	Electron microprobe analysis
	Ion chromatography
	Vibrational spectroscopies
	Solid-state NMR
	Spectrophotometry (for the distinction between the different orthophosphate ions)
Carbonate	Coulometry
	Gas chromatography
	CHN classical analysis system
	FTIR spectroscopy
	Thermogravimetric determination
Hydroxide ions (Determination rarely made)	Substitution of OH^- ions by F^- ions (method proposed by Trombe and Montel [2])
	FTIR analysis (OH^- lines at 3570 or 633 cm^{-1})
	Raman analysis (OH^- stretching band at 3570 cm^{-1})
Minor ions and trace elements (eg, Fluoride)	Spectroscopic methods (e.g., AAS)
	ICP-related methods (using emission spectroscopy or mass spectroscopy)
	Neutron activation analysis
	Ionometry

3.2 Ca/P ratio and diffraction method

The atomic Ca/P ratio of calcium phosphates is one of their major characteristics. It is frequently used to characterize the apatite composition. Two cases can be found:

The first case concerns non-stoichiometric apatite with Ca/P ratios lower than that of the stoichiometric composition (Ca/P = 10/6 = 1.667), which occurs when the apatite contains HPO_4^{2-} ions in place of PO_4^{3-} ions. In this case, the Ca/P ratio represents the number of cationic vacancies.

The second case concerns non-stoichiometric apatites with carbonate ions replacing phosphate groups (type B carbonate apatites). In this case, the Ca/P ratio does not represent the number of cationic vacancies and the meaning becomes more complex. Considering that there are only a few vacancies in the trivalent anionic sites of the apatite structure (all six sites are occupied either by phosphate or by carbonate groups), it is the Ca/(P+C) ratio (where C represents the number of carbonate ions replacing phosphate groups) which represents the departure from stoichiometry and the cationic vacancies.

For complex compositions with other cations substituting calcium, for example, Sr^{2+}, in carbonated apatite, the atomic ratio related to cation vacancies is considered as (Ca+Sr)/(P+C). In the same way when silicate or other ions are incorporated in place of phosphate the cationic vacancies possibly present are given by Me/(P+Si), where Me represents all the cations in the apatite structure.

The ratio is usually determined by solution chemical analyses, atomic absorption spectroscopy, or electron-microprobe spectroscopy. These methods have drawbacks like time-consuming, experimental error or they are not accurate. Some special techniques for the determination of Ca/P ratio using XRD have also been developed and standardized in the case of HA ceramics and coatings, which also imply several assumptions. It was further shown that for $1.5 < Ca/P < 1.67$ the XRD method is even more accurate than the classical wet methods [1,3].

XRD is an essential method for the characterization of calcium phosphate materials. These experiments can be performed on monocrystals, polycrystalline bulk ceramics, coatings, or powder samples. The existence of several databases of diffraction patterns makes possible the identification of all crystalline calcium phosphate compounds. Some of these databases are the International Centre for Diffraction Data (ICDD) and the Joint Committee for Powder Diffraction Standards (JCPDS) among others. Some specific intense peaks in the patterns are used to recognize the main CaP phases; they are summarized in Table 3.

Table 3. Useful lines for the identification of main CaP and secondary phases in ceramics and thermal coatings by diffraction techniques (ISO 13779-3)

Phase	JCPDS folder	hkl	d_{hkl} (Å)	2θ (λ_{Cu}=1.54 Å)
α-Tricalcium phosphate (α-TCP)	09-0348	4 4 1	2.905	30.753
β-Tricalcium phosphate (β-TCP)	09-0169	0 2 10	2.880	31.027
Tetracalcium phosphate (TTCP)	25-1137	0 4 0	2.995	29.807
Calcium oxide (CaO)	82-1690	2 0 0	2.405	37.361
Calcium deficient Hydroxyapatite	09-0432	2 1 0	3.080	28.966
Hexagonal Hydroxyapatite	72-1243	2 1 1	2.810	31.820

The identification of the different phases needed for several biological applications has been standardized (Standard ISO 13779-3), mainly related to the high-temperature processing of apatites as coatings or ceramics. The method described is based on the use of reference samples and single peaks integrated intensity ratios and needs the establishment of a standardization curve using known mixtures of phases in presence. It is a very accurate technique, for the determination of the Ca/P ratios between 1.50 and 2. Non-stoichiometric HA are not stable and they decompose on heating at 900-1100°C depending on their Ca/P ratio. If the Ca/P ratio is lower than 1.67, the heated sample is constituted by stoichiometric β-TCP and HA. If the Ca/P ratio is higher than 1.67, a mixture of stoichiometric HA and calcium oxide is observed. For a Ca/P ratio equal to 1.67, no decomposition is observed. The foreign phases (β-TCP and CaO) can be detected with high accuracy by XRD and quantified [1].

In literature, we can find some examples for the calculation of the ratios of HA/ β-TCP and HA/CaO mixtures by XRD like the one proposed by Zyman et al.[4] After the determination of the phase proportion through the main diffraction lines of each phase, the Ca/P atomic ratio of the initial non-stoichiometric powder, subjected to the calcination, can be calculated.

To characterize the composition of the powders treated during this work, calibration lines were obtained from a series of mixtures containing different ratios of HA, β-TCP, and CaO references. Graphs with the calibration lines are shown in Figure 1a (HA/ β-TCP) and Figure 1b (HA/CaO). The lines represent the ratio between the phase's main peaks raw areas (Ra) versus the percentage concentration ratio (%/%) of the phases. The selected diffraction lines for the analysis were taken following the standard ISO 13779-3:2008:

The line (0.2.10) (d=2.88 x 10^{-10} m) of the β-TCP.

The line (2.0.0) (d=2.405 x 10^{-10} m) of the CaO.

The line (2.1.0) and (2.1.1) (d=3.08 x 10^{-10} m and d = 2.81 x 10^{-10} m) of the HA.

The best-fit parameter values of these calibration lines can be found in Table 4.

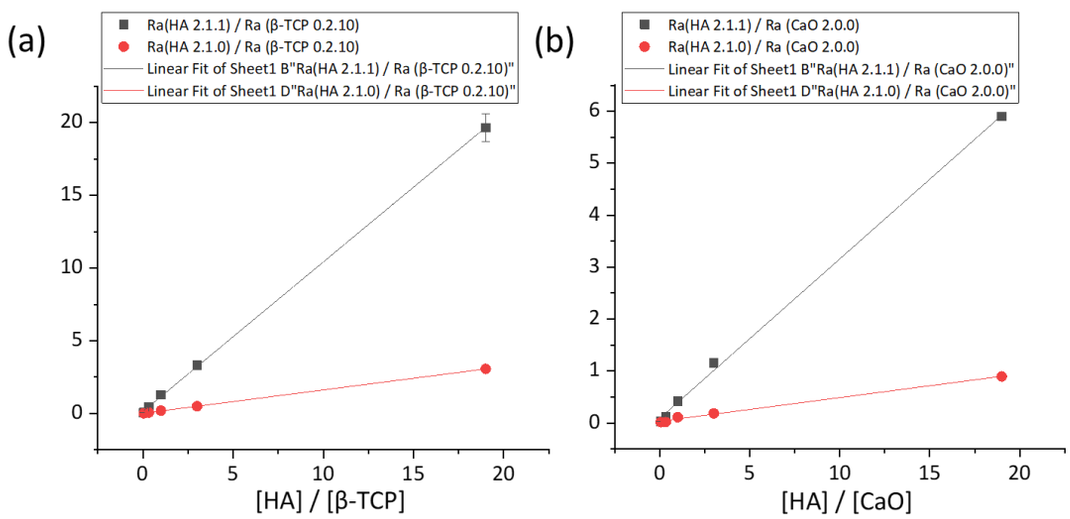

Figure 1. Calibration lines of the different calcium phosphate phases mixtures (a) HA/β-TCP and (b) HA/CaO for quantitative analyses.

Table 4. Best-fit parameter values for calibration lines of the calcium phosphate phases mixtures.

	Intercept		Slope		Statistics
	Value	Std Error	Value	Std Error	Adj. R-Square
Ra (HA 2.1.1) / Ra (β-TCP 0.2.10)	0.14	0.06	1.03	0.01	0.9998
Ra (HA 2.1.0) / Ra (β-TCP 0.2.10)	0.02	0.01	0.16	0.00	0.9990
Ra (HA 2.1.1) / Ra (CaO 2.0.0)	0.09	0.05	0.31	0.01	0.9983
Ra (HA 2.1.0) / Ra (CaO 2.0.0)	0.03	0.01	0.04	0.00	0.9941

The analysis of the samples following the calibration lines allowed us to calculate the percentage concentration ratio of each one of the phases present in the products. Once the weight percent of each phase was known, the Ca/P atomic ratio of the powders containing a mixture of HA and β-TCP (Ca/P < 1.67) was calculated following the formula described by Zyman et al. [4]:

$$\frac{Ca}{P} = \frac{3x+10(100-x)M_{\beta-TCP}/M_{HA}}{2x+6(100-x)M_{\beta-TCP}/M_{HA}} \quad (1)$$

Where M_{HA} and $M_{\beta\text{-}TCP}$ are the molar weights of HA and β-TCP (1004.64 and 310.18 g.mol^{-1}, respectively) and x the weight percent of β-TCP.

In the case of powders containing a mixture of HA and CaO (Ca/P > 1.67), a modified version of the equation shown previously was used:

$$\frac{Ca}{P} = \frac{x+10(100-x)M_{CaO}/M_{HA}}{6(100-x)M_{CaO}/M_{HA}} \quad (2)$$

Where M_{CaO} is the molar weight of CaO (56.08 g.mol^{-1}) and x the weight percent of CaO.

Another method employing the integrated intensity of all the peaks of the phases present in the compound is the Rietveld refinement method developed by Luca Lutterotti [5]. This requires a knowledge of the crystallographic structure, including atomic positions of each crystallized phase and the assumption that the phases are pure, containing only specified atoms. This method was used to estimate the crystalline phase compositions of powders and obtained parts. More details about the procedure followed for the refinement will be offered in chapter V.

A BRUKER's X-ray diffractometers D8 using Cu Kα radiation (wavelength λ = 0.15406 nm), a nickel filter at 40 kV, and 40 mA was employed for the analysis of the phase composition and crystallinity of powders and solid parts produced in this work. Our experimental procedure followed for the measurements will be described in detail in chapters III, IV, V, and VI.

3.3 Electron microscopy techniques

The use of electron microscopy techniques for materials characterization can have several objectives:

- Composition determination using energy dispersive spectrometry (EDS) or wavelength dispersive spectrometry (WDS).

- Determination of the crystal morphology, their size, and organization, including pores distribution in ceramics.

- Analyses of crystal defects through lattice imaging at high resolution.

- Identification of phases at the microscopic level using electron diffraction.

Some CaPs exhibit their own crystal morphology, which can be used for their identification. A classification was proposed based on three major structural types: (1) the apatite-type structure also including apatite-related structures such as octacalcium phosphate (OCP), (2) the glaserite-type structure in which all the TCP polymorphs can be included, and (3) the $CaPO_4$ sheet-containing compounds including dicalcium and monocalcium phosphate phases. However, this classification cannot be used for the determination of the crystal morphology of these compounds, since other parameters like formation conditions can control nucleation and crystal growth of CaPs [1]. Still, some morphologies can be considered as recurrent, some examples of scanning electron microscope (SEM) micrographs are shown in Figure 2.

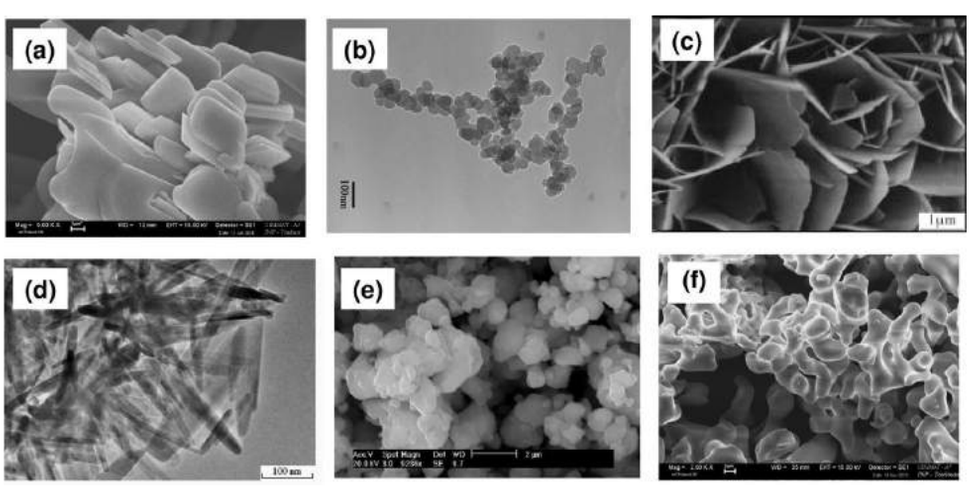

Figure 2. Example of typical morphologies of CaP compounds. (a) SEM image of dicalcium phosphate dihydrate (DCPD) platelet crystals; (b) TEM image of amorphous calcium phosphate (ACP), generally spherical units; (c) SEM image of OCP crystals, it can hydrolyse into apatite keeping the crystal habit; (d) TEM image of apatite crystals, well-crystallized apatites generally exhibit a needle-like morphology; (e) SEM image of β-TCP crystals; (f) SEM image of TTCP crystals. Retrieved from Rey et al. [1].

Upon heating, the morphology of apatite crystals changes considerably: the length is reduced and the width-thickness is increased, resulting in a lower crystal surface energy. The hexagonal shape, however, remains recognizable. Some preparations such as hydrothermal synthesis, slow hydrolysis of more soluble CaP salts (dicalcium phosphate dihydrate (DCPD), TCPs), and reactions in fused salts may give apatite crystals a very high aspect ratio (length/width ratio) that can be considered as fibres [6]. Mostly, the needle-like crystals tend to form dendritic spherical units.

Bone crystals appear as platelet crystals with a quite irregular shape, with an elongation on the c axis of the hexagonal structure but with different perpendicular dimensions along with a and b axis directions. A hexagonal crystal is supposed to possess equivalent a and b directions, it could be an indication of the formation of OCP precursor phases.

One of the main problems with these techniques is beam damage, which can lead to the decomposition of hydrated phases or even volatilize phosphorus. The high vacuum may also alter the hydrated CaP phases; however, environmental microscopes can be used. Calcium phosphates are nonconductive, which it makes necessary to limit the charge effect. For scanning electron microscopy (SEM), several techniques can be used:

- Coating with an electrically conductive layer (preferred for morphology examination)
- Working under altered vacuum
- Working at the low accelerating voltage at short working distances

In the present work, dry powder morphologies and parts surfaces were investigated with scanning electron microscopy (LEO 435 VP) equipped with a Ge detector (Imix-PC, PGT) and metallization of the ceramic surface with a thin film of silver using a Scancoat Six sputter coater. More details will be offered in chapters III, IV, V, and VI. Only in chapter V, an additional microscope was used for the analysis of specific printed samples. In this case, the analyses were performed in an FEI ESEM Quanta™ 450 FEG, an environmental scanning electron microscope (ESEM) used with a large field detector (LFD) in low vacuum (LowVac) mode without previous metallization of the surface of the sample.

3.4 Vibrational spectroscopies

FTIR and Raman spectroscopies are very useful techniques to identify most calcium phosphate phases. It is possible through the analysis of the internal vibrational levels of molecules and ions that can change depending on the short-range environments of these molecules or ions. Phosphate, carbonate, hydroxide ions, and water molecules are the main species detected by FTIR and Raman spectroscopies.

While some calcium phosphate phases cannot be well distinguished by XRD analysis, it is possible using FTIR and Raman spectroscopies. This is the case of OCP, HA, oxyhydroxyapatite (OHA), and amorphous phases. It is also possible to perform phase quantification using standard mixtures and standardization curves based on line intensity ratios. Raman spectroscopy allows also a mapping of the different phases in coatings. The main advantage over XRD is the identification of fine structural details, especially concerning apatites, such as the location of carbonate species on the different sites of the apatite structure, the presence of HPO_4^{2-} species, the quantification of the amount of OH^- ions, or the fine characterization of nanocrystalline apatites.

A detailed presentation of vibrational spectroscopy of CaPs was proposed by Rey et al. [7]. The main line positions of the FTIR and Raman spectra of different CaPs are reported in Table 5, Table 6, and Table 7 showing the four main vibrational domains for PO_4^{3-} group and carbonate ions. FTIR and Raman spectra of the most important CaPs are shown in Figure 3 and Figure 4.

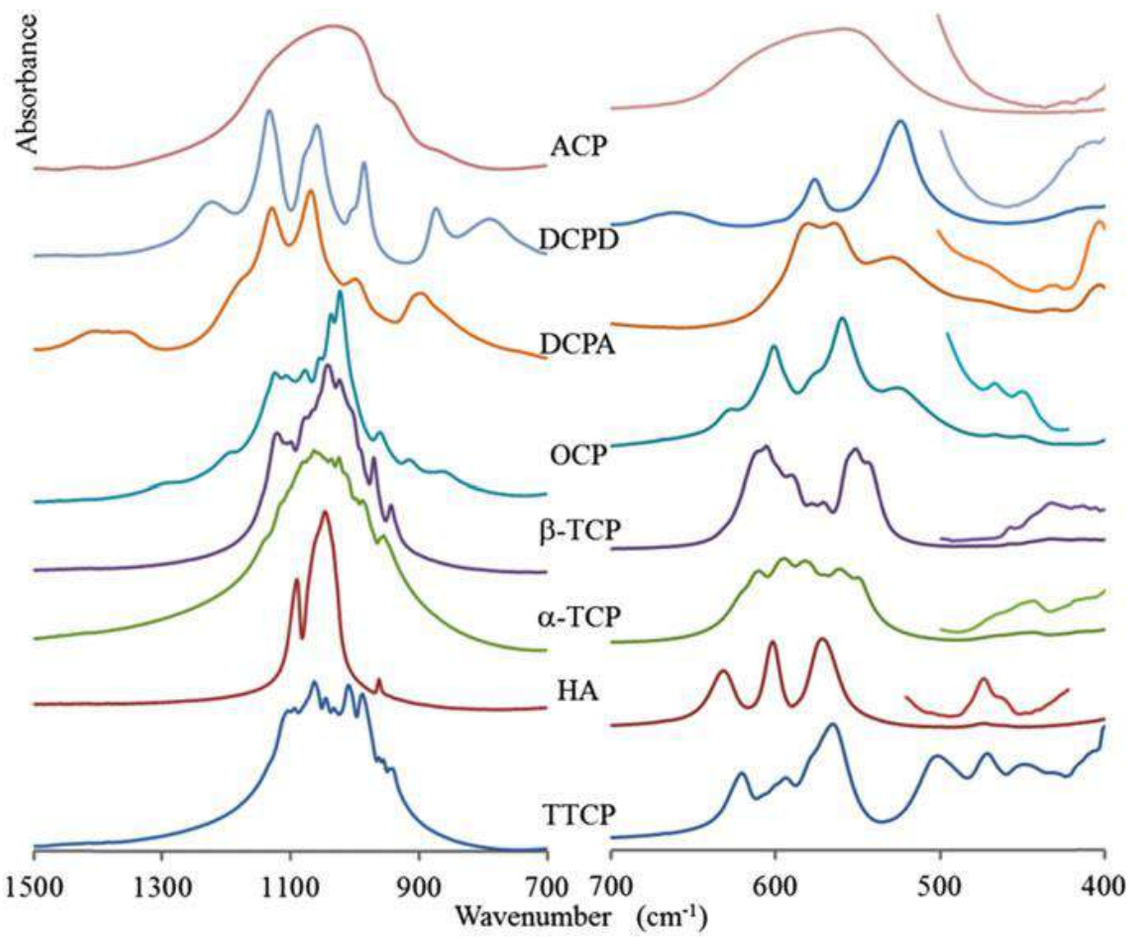

Figure 3. FTIR spectra of calcium phosphates in the domains of internal vibrations of phosphate ions. Retrieved from Rey et al. [7].

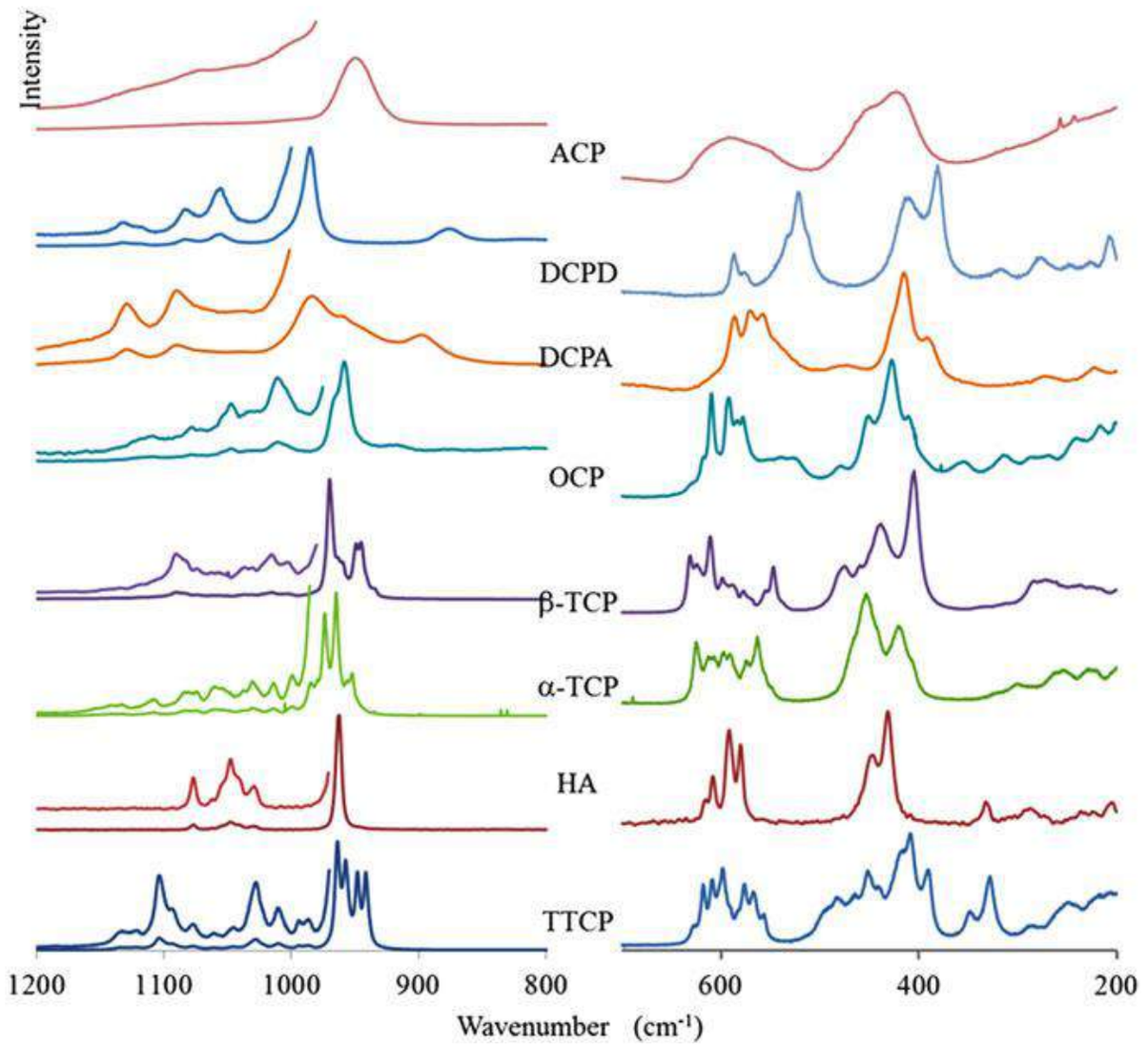

Figure 4. Raman spectra of calcium phosphates in the domains of internal vibrations of phosphate ions (for comparison purposes the wavenumber axis is in reverse order, like for the FTIR spectra). Retrieved from Rey et al. [7].

In the case of OH^- ions, there is only one vibrational domain corresponding to the stretching of the O-H bond (3400-3650 cm^{-1}). However, a vibration line, corresponding to a rotational energy level of the ion in the lattice, is also observed (630–750 cm^{-1}), within the usual wavenumber window of the technique. OH^- bands are essentially detected in apatites and related compounds like partly hydrolysed OCP. The OH^- stretching and vibration movements are very sensitive to hydrogen bonding, and it has been shown in fluoride- and chloride-containing apatites that the OH^- bands can be considerably shifted away from their position in HA. Carbonate ions are always present in biological apatites and can occupy different types of sites labelled as A and B: site A correspond to monovalent anionic sites of the apatite structure and site b corresponds to trivalent anionic sites.

Water molecules exhibit three vibrational modes: the symmetric stretching mode (ν_s) and the antisymmetric stretching mode (ν_{as}) have very close energy and they are difficult to distinguish. They generally give a broad absorption band on FTIR spectra (3000–3700 cm^{-1}). The bending movement around 1640 cm^{-1} gives a narrower band. Like OH, the water molecules are very sensitive to hydrogen bonding. In some calcium phosphates such as DCPD, the lines due to water molecules appear very specific and allow a clear identification. In other calcium phosphates (OCP, HA, ACP), however, the water bands appear rather unspecific [7].

FTIR analyses were employed in chapters III, IV, V, and VI for the characterization of the compounds present in powders and printed samples. A spectrometer Nicolet™ FTIR iS50 was used to perform the analyses together with a sample preparation based on the KBr pellet method. A deeper description of the procedure is offered in the corresponding chapters.

In chapter V a Horiba Jobin Yvon Labram HR 800 was used to perform the RAMAN analyses of the calcium phosphate printed samples. More details will be given in the specific chapter.

Table 5. FTIR line positions of calcium phosphates (cm^{-1}; m medium, s strong, sh shoulder, v very, w weak. DCPA = dicalcium phosphate anhydrous. Retrieved from Rey et al. [7].

	TTCP	HA	α-TCP	β-TCP	OCP	DCPA	DCPD	ACP
v_3 PO_4						1,400 w		
						1,350 w		
					1,295 w		1,215 m	
					1,193 w	1,175 m,sh		
					1,137 vvw	1,128 s	1,132 s	
				1,119 s	1,121 s			
	1,105 w				1,103 s			
	1,093 w	1,092 s		1,094 w,sh				
	1,073 w			1,080 w,sh	1,077 s		1,070 s	
	1,062 s		1,055 s		1,055 s	1,064 s	1,060 s	
	1,046 s	1,040 vs	1,039 s	1,041 vs				1,040 s
	1,033 m		1,025 s		1,037 s			
			1,013 s		1,023 s			
	1,010 s		997 s	1,010 w,sh	1,000 vvw		1,000 w,sh	
	989 s		984 s					
v_1 PO_4				972 s		992 m	984 s	
	962 w	962 w			962 w			
	956 w		954 m					
	946 w			945 m				949 w, sh
	941 w							
P-OH of HPO_4^{2-}					917 w			
					861 w	892 m	872 m	
v_4 PO_4	620 w		613 m		627 vw			
	594 w	601 m	597 m	602 m	601 m			
			585 m	589 w				
	571 s	575 m,sh	563 m		575 w	576 s	577 m	
		561 m	551 m	550 m	560 m	563 s		560 m
	501 w			541 m	524 w	525 m	526 s	
v_2 PO_4	471 m	472 vw	471 w			480		
		462 sh	463 w		466 vw			
			454 w					
	450 w		430 w	432 vw	449 vw	428 vw	418 sh	
	429 w		415 w			405 m	400 m	
	399 m					398 sh		

Table 6. Raman line positions of calcium phosphates (cm^{-1}; m medium, s strong, sh shoulder, v very, w weak). DCPA = dicalcium phosphate anhydrous. Retrieved from Rey et al. [7].

	TTCP	HA	α-TCP	β-TCP	OCP	DCPA	DCPD	ACP
v_3 PO_4						1,131 m	1,132 vw	
	1,119 vw						1,119 vw	1,118 w
	1,101 w				1,112 w			
	1,091 sh	1,077 w	1,077 w	1,090 w	1,079 vw	1,094 m	1,079 w	
	1,076 vw	1,064 w					1,061 m	
		1,057 w	1,058 w		1,052 w			
	1,045 vw	1,048 w			1,048 w			1,050 w
		1,041 w						
		1,034 w			1,036 vw			
	1,026 w	1,029 w	1,027 w		1,027 vw			
	1,008 w		1,012 w	1,015 w	1,011 m			
			998 w		1,005 w,sh			
v_1 PO_4	983 vw		976 s					
	961 vs	964 vs	964 s	970 s	966 s	988 s	986 s	
	956 vs		954 sh	948 s	959 vs			
	946 s							951 s
	940 s							
P-OH of					916 w	900 m		
HPO_4^{2-}					874 w		878 m	
v_4 PO_4	615 vw	614 w	620 w		619 vw			
	608 vw	607 w	610 w	612 w	609 mw			
	597 w	591 w	593 w		591 m	588 m	588 w	594 m
	576 vw	580 w	577 w		577 m	563 m		
	566 sh		563 w					
	556 vw			549 w				
	495 sh				523 w, b		525 w	
v_2 PO_4	481 sh			480 w				
	463 sh	448 w	451 w		451 m			451 m
	449 w	433 w		439 w				
	414 sh		421 w		427 m	420 w		419 m
	407 w			408 w	409 m		411 w	
	389 w				353 w	394 w	381 w	

Table 7. FTIR and Raman spectral characteristics of carbonate ions in different calcium phosphates (wavenumbers in cm^{-1}). Retrieved from Rey et al. [7].

	Type A carbonate		Type B carbonate (in HA)		Type B carbonate (in FA)	Carbonate in ACP
	FTIR	Raman	FTIR	Raman	FTIR	FTIR
ν_3CO_3	1542 s					1490 s
	1465 s		1462 s		1452 s	
			1412 s		1425 s	1425 s
ν_1CO_3		1107 m		1070 m		
ν_2CO_3	883 m	765 w	872 m		862 m	868 m
ν_4CO_3	757 vw	675 w	718 vw		716 vw	
	670 vw		692 vw		695 vw	

3.5 Thermal analysis

Thermal analysis becomes very useful when processing CaP materials. Figure 5 shows the information related to the thermal decomposition of different CaPs. [1]

Considering apatites, there are two types of decompositions depending if the apatites are stoichiometric (reversible decomposition) or not (irreversible decomposition). The irreversible decomposition also occurs in the case of apatites-containing thermally unstable ions such as carbonate and HPO_4^{2-}, for example.

Stoichiometric HA is thermally very stable and is generally sintered at 1200-1250°C without strong alteration. It starts to lose water at 850 °C at a very low H_2O partial pressure and forming oxyapatite (OAP). Then, OCP decomposes into TCP and TTCP at about 1050°C and, at a higher temperature (1720°C), CaO and a liquid phase form. These reactions are theoretically reversible and, on cooling under a certain water partial pressure, HA structure is possible to be reformed [1].

This knowledge on the thermal behaviour of CaP materials has a big interest for the understanding of the processes happening during, for example, a laser-based 3D printing process. The high temperatures can produce the phase transition, so knowing the final phases obtained can give us an idea of the temperatures reached during the process. In addition, it can be helpful when designing a debinding-sintering process for the pyrolysis of the cured resin of the printed green bodies where any phase transition could affect the quality of the parts.

Thermogravimetric analyses (TGA) were performed during the work in chapter VI. A Setsys Evolution 1750 Setaram® was used to carry out the analyses. A deeper explanation of the procedure and temperature ramps is provided in the corresponding chapter.

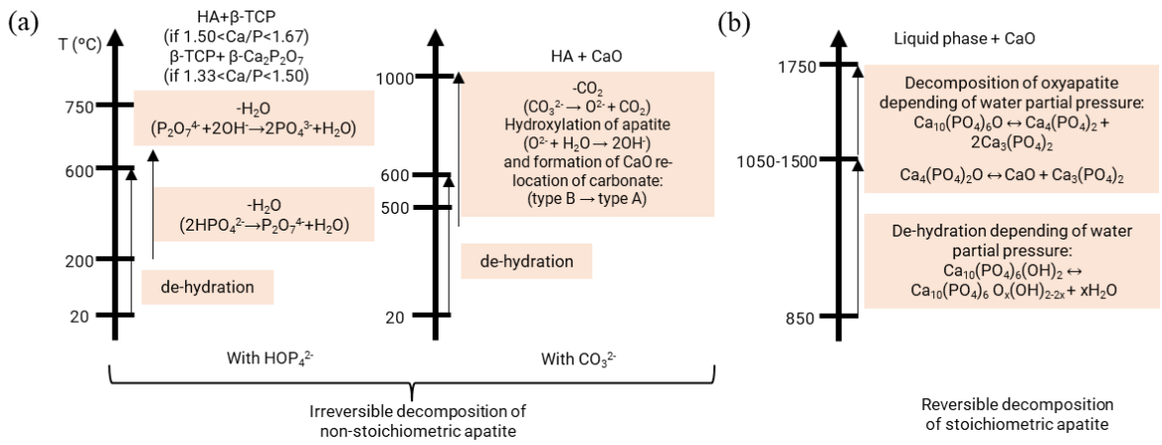

Figure 5. Thermal decomposition of apatites. For non-stoichiometric apatite (a) depending on their composition (HPO_4^{2-} or CO_3^{2-} or both) vacancies-containing apatites decompose differently, these reactions are always irreversible. For stoichiometric apatite (b), at high temperature (above 850°C) it decomposes reversibly into different CaP compounds depending on the temperature and water partial pressure. (Adapted from Rey et al. [1])

4. Suspension characterization

This section will focus on giving a brief explanation of the general principles of suspensions, as well as their classification and characterization methods more relevant for the present study.

A suspension is a "heterogeneous mixture in which some of the particles settle out of the mixture upon standing" [8]. In comparison with a solution, coarse suspensions contain considerably larger particles (over 1000 nm) which are submitted to gravitational forces pulling them out of the dispersion medium. Then, an active mixing is needed to have a uniform distribution of the substances present in the mixture. When particles size is ranging 1-1000 nm the system is called colloidal suspension. Apart from the granulometric types of suspensions (colloidal, coarse) they can be mono-dispersed or poly-dispersed depending if the particles have the same size or not. Based on the solid content, suspensions can be classified as diluted (< 10 wt. %) or concentrated (10-50 wt. %). Then, depending on the nature and behaviour of solids, suspensions can be classified as flocculated (physical bridging forming particle aggregates) and deflocculated (individual solid particles).

During the present work, different suspensions containing ceramic particles will be prepared for their direct consolidation (stereolithography) or further processing operations (milling, spray drying…). Sometimes, particles size will be in the coarse and/or colloidal range depending on the application. To control the behaviour of the particles in suspension it is important to understand the different interactions taking place between the dispersed phase - dispersing medium interface (surface charge, electrical double layer, adsorption…). The total interaction will be the result of particle-particle, fluid-fluid, and particle-fluid interactions [9,10].

4.1 Stability of the suspensions

4.1.1 Interparticle forces

Suspensions are commonly thermodynamically unstable systems. Physical stability is defined as the state in which particles remain uniformly distributed, dispersed, and without showing any sedimentation. For specific applications (ceramics, pharmaceuticals, painting, etc.) reaching the stabilization of the media at least for the required duration of use (it can be hours, days, months, or years) is one of the scientific challenges to surpass. To obtain stable suspensions two conditions should be fulfilled, the size of the particle should prevent the effects of gravity, and repulsive interactions should predominate between the different interparticle forces. Four types of interparticle interactions can be identified in concentrated suspensions:

- "Hard-sphere" interactions from where attractive and repulsive forces are distinguished.
- "Soft" or electrostatic interactions are affected by double-layer repulsion.
- Steric repulsion from the interaction between grafted or adsorbed polymeric and surfactant layers.
- Van der Waals attraction is mostly caused by London dispersion forces.

A more detailed explanation of each of the four types of interparticle interactions was offered by Tadros [10].

Concerning colloidal suspensions, Brownian motion produces the collision between particles and if the attraction forces govern, particles agglomerate after the collision. Instead, if the repulsive forces are higher, the particles remain separated after the collision. The authors Derjaguin, Landau, Verwey, and Overbeek developed the DLVO theory allowing the electrostatic stability of a suspension to be established relatively easy [11–13]. It consists in superimposing the Van der Waals attractive potential and the electrostatic repulsive potential. The minimum of the resulting total potential fixes the equilibrium distance between the particles. Four different cases can be expected:

- Stable suspensions (low risk of agglomeration): the total interaction potential stays positive for any distance between particles.
- Suspensions in which particles tend to form agglomerates (agglomerates of feasible redispersion): total interaction profile shows a secondary minimum for long-range repulsive forces.
- Agglomerated suspensions: the total interaction energy is negative. The repulsive energy barrier is surpassed leading to the formation of agglomerates. These are reversible physicochemical interactions.
- Aggregated suspensions: Electrical double layers have covered themselves and non-reversible chemical bonds have been formed between particles. It is usual in short separation distances between particles of the same nature.

Electrolytes or macromolecules can be added to the suspension modifying the electric double layer repulsive force controlling the coagulation/dispersion state of particles [14].

4.1.2 Sedimentation

The phenomenon inducing a certain velocity to the Brownian particles by the action of an external field is called sedimentation. This translational velocity is also referred to as settling velocity. The stabilization of ceramic suspensions has been largely studied intended for a wide variety of applications [15–17].

For low concentrated suspensions (0.5-2 wt. %) with non-cohesive particles, the particles settle individually. In this case, the rate of sedimentation of particles can be expressed by Stoke's law following the formula:

$$v_{Stokes} = v_{\infty} = \frac{(\rho_p - \rho_1) g d^2}{18 \eta_{medium}} \quad (3)$$

Where ρ_p is the density of the particles with diameter d, ρ_1 the density of the liquid of viscosity η, and g refers to the gravity acceleration. Different factors can affect the rate of sedimentation [18]:

- Smaller the particle size the slower the sedimentation rate. Particle-particle interaction can induce the formation of aggregates or flocs which will increase the sedimentation rate.
- Closer the densities of solid particles and dispersion medium slower the rate of sedimentation. The density of the medium can be changed through the addition of, for example, non-ionic substances. When the density of the particles is lower than the medium density, the creaming phenomenon occurs instead of sedimentation.
- Higher the viscosity of the suspension slower the sedimentation rate. Suspending agents or thickening agents can be added to increase the viscosity. However, a too high viscosity can bring disadvantages such as making suspension handling difficult.

4.1.3 Agglomeration of particles in suspension

The agglomeration of particles suspended in a fluid is a method frequently used to speed up their sedimentation. This strategy is regularly utilized in water potabilization and wastewater treatment processes. Conversely, the agglomeration of particles might be inconvenient in specific fields like materials, cosmetics, or paints. For this situation, the ideal objective is frequently to develop a homogeneous and stable slurry. Furthermore, the change of the particle size, due to agglomeration, can alter the viscosity of the medium. In the field of ceramics or particulate composites, the agglomeration of fillers should be controlled to guarantee the handling and performance of these materials. Mastering the mechanisms dominating the agglomeration

is important to ensure stable behaviour. The different particles agglomeration mechanisms in the presence or none of the surfactants will be briefly discussed below.

A micron particle suspended in water becomes charged, either by dissociation of functional groups from the surface of the solid, surrounding itself with the interphase of other ions or by forming an electric double layer by adsorption of ions present in water [19]. The particle in suspension interacts with three types of forces: electrostatic pressure, gravitational force, and osmotic pressure caused by the non-uniform distribution of ions in the aqueous medium (Figure 6).

When two charged particles approach each other in aqueous media, their electrical double layers interact by electrostatic forces. Adding a polyelectrolyte or a salt to a suspension containing negatively charged particles, the positive ions are displaced to the surface of the particles neutralizing the net charge of the particle. The diffuse layer is compressed and the particle collision energy barrier becomes weak. The particles can therefore cross this barrier and agglomerate. Moreover, if macromolecules are added, agglomeration can occur according to other types of mechanisms: agglomeration by depletion, and/or agglomeration by bridging [20].

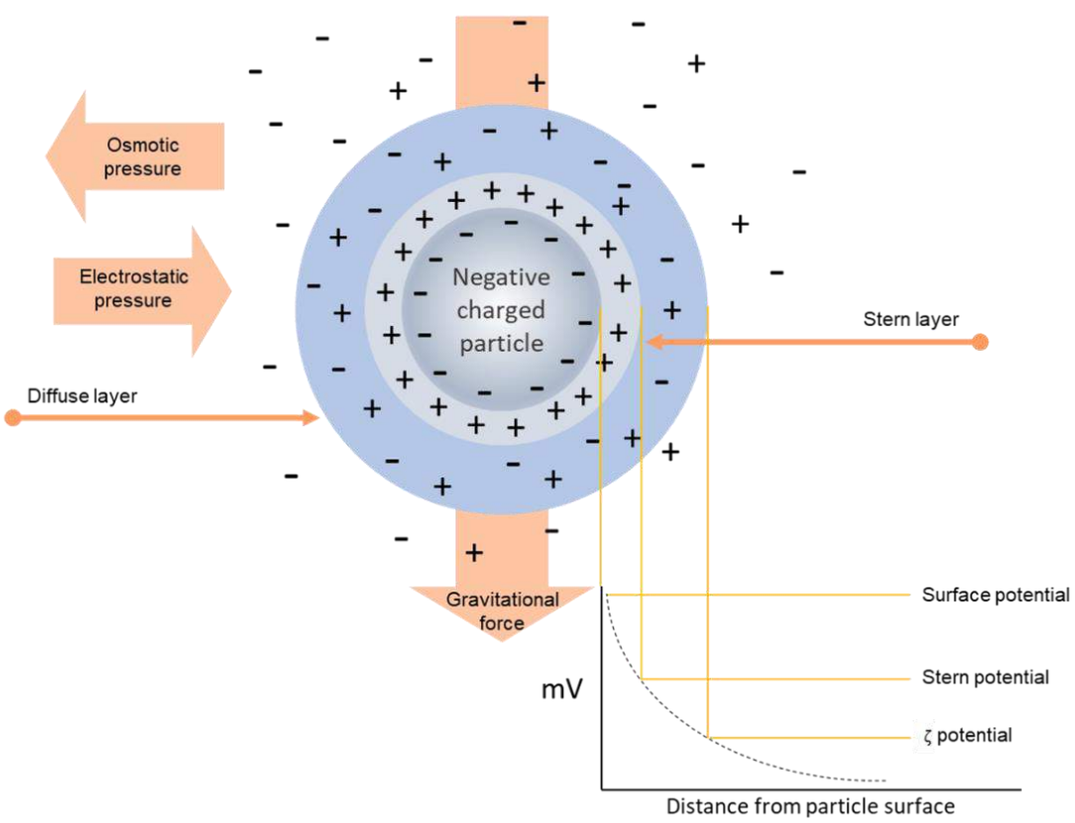

Figure 6. Schematic illustration of the electric double layer and the three types of forces interacting on the particle.

4.1.4. Characterization of the stability

A brief explanation of each of the different characterization methods employed during this thesis to evaluate the dispersion stability of the suspensions is given below:

Preliminary tests: The explanation of the first method was offered by Garcia et al.[21] in their study on the agglomeration phenomena in ultrafine particles and the use of polyelectrolyte additives as a dispersing agent. This common preliminary test is used to evaluate the dispersion ability of a dispersant. It consists of the preparation of several test tubes containing the same amount of suspension (~30 wt. %) composed of fine particles. Different quantities of polymer are then added to each tube varying their final concentration. The tubes are then agitated for several hours at ambient temperature and after equilibration, a qualitative evolution of the suspension is followed. The separation particle sedimentation rate and the sedimentary volume are evaluated. This final sedimentary volume indicates the dispersion state of the suspension. It is dependant on the nature and the intensity of the interparticle forces as is illustrated in Figure 7. We could distinguish three different states: (i) Interparticle forces are highly attractive, large and loose-packed flocs are formed and the resulting sedimentary volume is important and not dense. (ii) The interactions are less attractive; the constitutive aggregates are smaller and the density of the sedimentary volume becomes higher. (iii) Interparticle interactions are repulsive maintaining the particles in a well-dispersed state and giving a maximum density of the sedimentary volume.

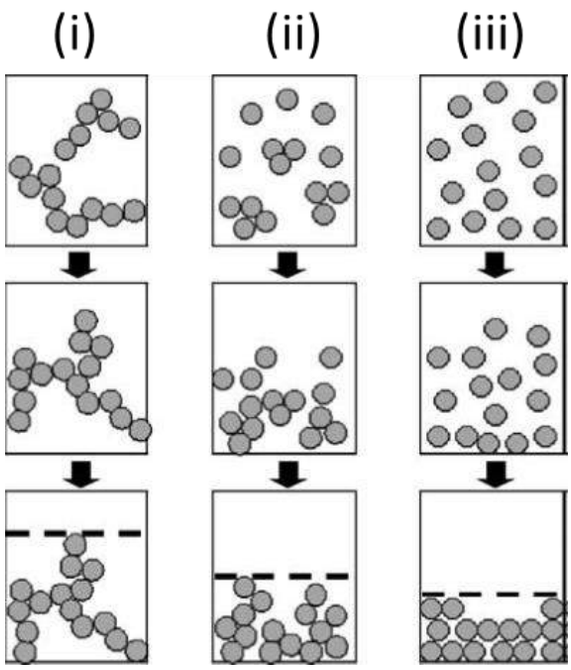

Figure 7. Effect of the dispersion state on the sedimentary volume. Retrieved from Garcia et al. [21]. (i) Highly attractive interparticle forces, (ii) less attractive, and (iii) repulsive interparticle interactions.

Turbiscan^{LAB} (Formulaction) optical suspension analyser (Figure 8a): This apparatus consists of 3 parts, an optical part called the read head, a mechanical part, and a software part called Turbisoft. This equipment, based on multiple light scattering, enables the analysis of suspension stability in its native state

without dilution. After placing the sample contained in a cylindrical cell (16x125 mm) inside of the apparatus, a read head, moved by the stepper motor, scans it vertically. Every 40 μm, a diode emits a light beam in the near-infrared (λ = 860 nm) and it is diffused by the sample. At 135º and 0º there are placed two detectors to collect the backscattered and transmitted light beams (Figure 8b).

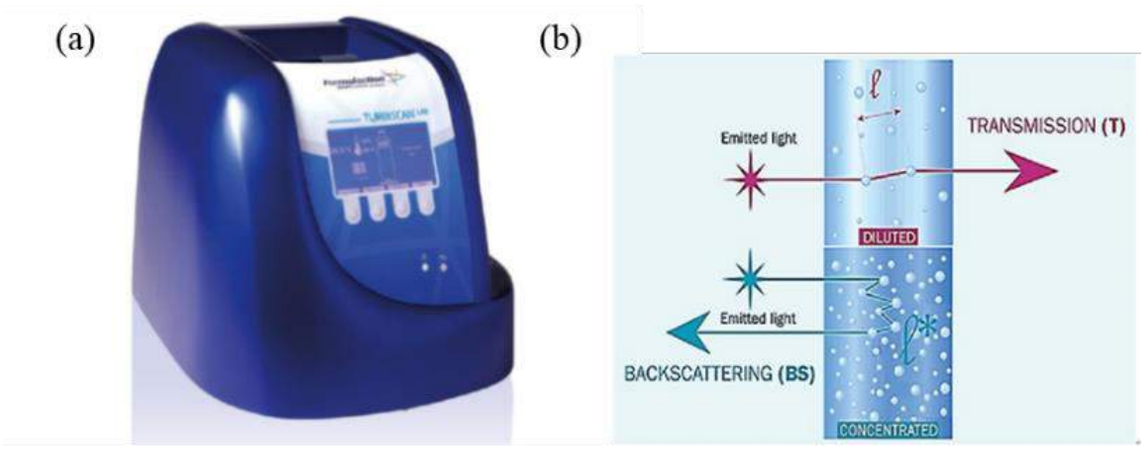

Figure 8. (a) Turbiscan^{LAB} (Formulacton) optical suspension analyser and (b) scheme of the Turbiscan^{LAB} measurement principle. (Adapted from equipment user guide).

Backscattered and transmitted profiles are registered to establish an image of the current state of the sample allowing the qualitative analysis of the phenomena due to destabilization (creaming, sedimentation, agglomeration…) (Figure 9). Destabilization kinetics and destabilization phenomena can be recognized and quantitatively assessed from these profiles.

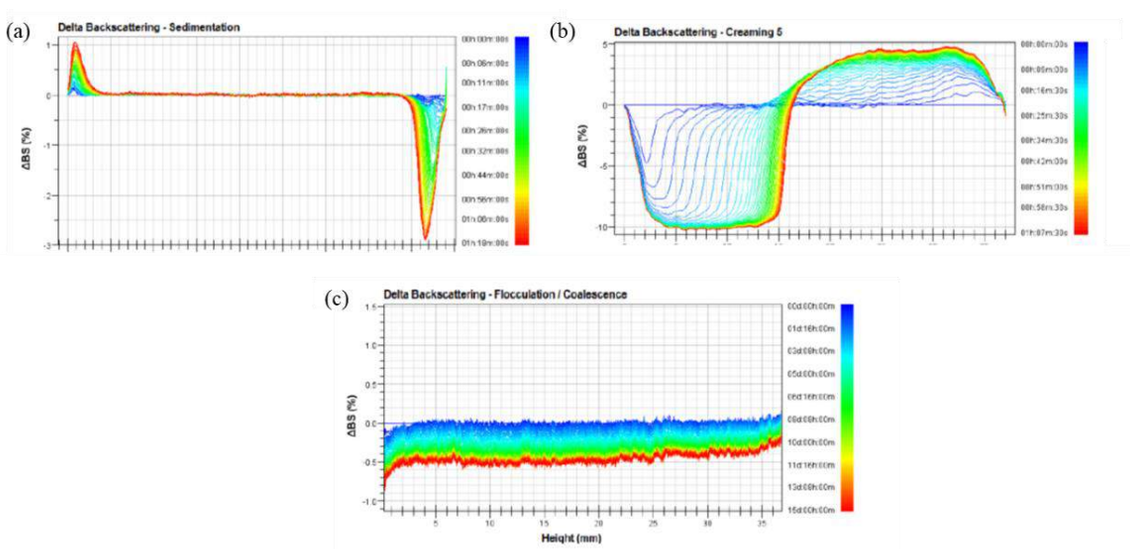

Figure 9. Delta backscattering examples of (a) sedimentation, (b) creaming, and (c) flocculation/coalescence suspension phenomena. (Adapted from equipment user guide).

Measurement of zeta (ζ) potential: The zeta (ζ) potential of particles in suspensions can be measured by Laser Doppler Velocimetry (LDV). A laser is used as a source of light, which is split into incident and reference beams. The incident beam passes through the sample cell and a detector detects the attenuated scattered light at angle 173º. When an electric field is applied, the particles move towards the electrodes and create a fluctuation of the scattered light. The intensity of the fluctuating scattered light will be converted to particle speed and then further computed into zeta potential thanks to the expression of the electrophoretic mobility:

$$U_E = \frac{V}{E} \quad (4)$$

Being V the particles speed and E the electric field.

Then the zeta potential ζ can be obtained applying the Henry law:

$$U_E = \frac{2\,\varepsilon\,\zeta\,f\,(\kappa a)}{3\eta} \quad (5)$$

Or

$$\zeta = \frac{3U_E\eta}{2\,\varepsilon\,f\,(\kappa a)} \quad (6)$$

Where ε is the dielectric constant of the medium, κ is the Debye parameter, κa corresponds to the ratio between the particle diameter a and the thickness of an electrical double layer, and η is the viscosity of the medium. The function $f(\kappa a)$ changes with the concentration or the polarity of the suspension or the presence of salts. It lies between 1 and 1.5.

The analyses of the suspension stability were crucial during this PhD work, as it will be presented in chapters III, IV, and VI to obtain a proper performance during the milling, spray drying, and masked stereolithography processes. Different types of analyses were performed to compare the stability of suspensions (e.g., containing different dispersant dosages, particle sizes, solid concentrations…).

The preliminary sedimentation test was carried out to evaluate the use of a polyelectrolyte additive in chapter III.

The zeta (ζ) potential of HA particles in aqueous suspensions with different additives concentrations was measured in chapters III and IV. A zetasizer nano-ZS from Malvern Instrument was used for the measurements at a temperature of 25ºC.

A Turbiscan^{LAB} (Formulacton) was used to compare the dispersion stability of organic photocurable suspensions containing HA powders of different characteristics. A deeper description of the backscatter and transmission profiles will be given as well as the definition of the Turbiscan stability index (TSI) (a Turbiscan® specific parameter) in chapter VI.

4.2 Rheological behaviour of suspensions

Rheology is the science studying the relation between the forces (stress) applied to a material and its response as deformation or shear rate. Its application is crucial to understand the complex physics dominating the behaviour of a suspension.

The "suspension viscosity" η [Pa.s] is an intrinsic property that represents the behaviour between external applied forces (shear stress τ [Pa]), and the internal response through deformation rate (shear rate $\dot{\gamma}$ [s^{-1}]). The viscosity η (φ) is an essential function of φ, the volume concentration of particles in the suspension.

Then, rheometry is the group of experimental techniques employed to determine the rheological properties of materials. Two types of rheometers exist, the shear rheometers and the extensional ones. Inside of shear rheometers, two groups are distinguished, drag flows (shear produced between a moving and a fixed solid surface) and pressure-driven flows (shear generated by a pressure difference over a closed channel). A more extended description of the different experimental artifacts and the calculation of the rheological parameters were provided by Macosko [22].

From a rheological point of view, suspensions are classified according to their behaviour to the amplitude of the shear. Thus, we can distinguish:

- Newtonian suspensions whose viscosity is constant whatever the shear,
- shear-thinning suspensions (or pseudoplastic fluids) whose viscosity decreases with increasing shear rate,
- stress threshold suspensions (or Bingham plastic fluids) which do not begin to flow only from a certain so-called threshold constraint and whose viscosity decreases with increasing shear,
- shear-thickening (or dilating) suspensions whose viscosity increases with the shear rate.

This simple classification is observed only in limited ranges of shear and the described behaviours change when the volume fraction increases [23].

In this manuscript, a two-parallel-disk geometry (Figure 10) installed on a shear rheometer (TA Instruments AR2000) was used for the characterization of the viscosity of the HA-filled suspensions. More details will be given about the measurement's conditions in the next chapters.

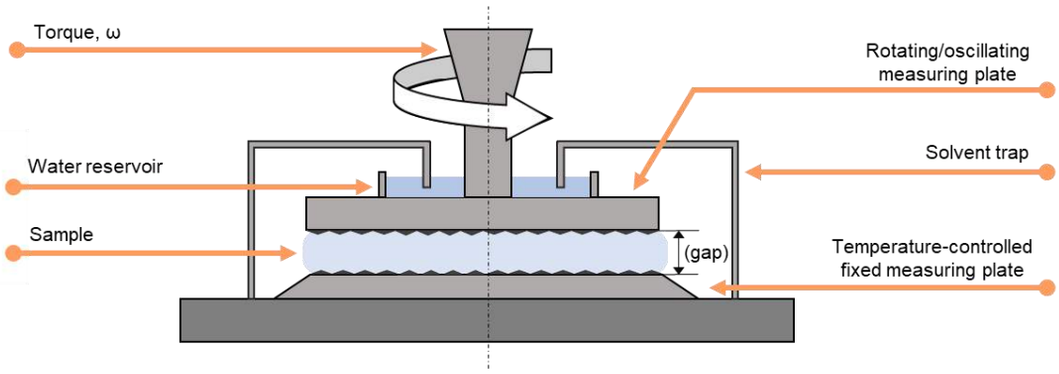

Figure 2. Schematic drawing of the rheometer parallel plate geometry with positioning of the solvent trap.

In chapters III and IV aqueous HA-filled suspensions were prepared and characterized for their correct processing by milling and spray drying processes. Then, in chapter VI HA-filled organic suspensions (photosensible resin) were produced and analysed to study their processability in a masked stereolithography equipment.

5. 3D-printed parts characterization

New emergent technologies need to develop a series of international standards based on a set of consistent documents compiling terminology, test methods, and data exchange. It is needed to offer recommendations and advice to machine manufacturers, feedstock suppliers, machine users, part providers, and customers, as well as to improve communication between these stakeholders concerning test methods. Table 8 shows the structure of AM standards including terminology, process/materials, test methods, and design/data formats of AM models.

Table 8. Summary of AM international standards for ceramics. (Retrieved from European Committee for Standardization CEN/TC 438)

Additive manufacturing general standards			
Terminology	**Processes/Materials**	**Test Methods**	**Design/Data Formats**
ASTM F2792-12a ISO 17296-1 ISO/ASTM 52921-13 ISO/ASTM 52900	ISO 17296-2 NF E67-010	ISO 17296-3	ISO 17296-4 ISO/ASTM 52915-13
Main quality characteristics and corresponding recommended test standards for ceramics (ISO 17296-3)			
Feedstock			
Bulk raw material requirements	Powder particle size and distribution	ISO 13319 ISO 13320 ISO 24235 ISO 14703	
	Morphology	ISO 9276-6	
	Surface	ISO 18757 ISO 9277	
	Density (tap and apparent)	ISO 18753 ISO 23145-1 ISO 23145-2	
	Flowability/pourability	ISO 14629	
Parts			
Surface requirements	Appearance	ISO 16348	
	Surface texture	ISO 1302 (specification) ISO 4288 (measurement)	
	Colour	ISO 11664-1 ISO 11664-2 ISO 11664-4 ISO 11664-5	
Geometric requirements	Size, length and angle dimensions, dimensional tolerances	ISO 129-1 ISO 286-1 ISO 14405-1 (specification) ISO 1938-1 (measurement) ISO 2768-1	
	Geometrical tolerancing (deviations in shape and position)	ISO 1101 (specification) + Isostatism ISO 2768-2	
Mechanical requirements	Shear resistance	ISO 14129	
	Crack extension	ISO 15732 ISO 18756 ISO 24370	

		ISO 23146
	Hardness	ISO 14705
	Tensile strength	ISO 15490
	Impact strength	ISO 11491[a]
	Compressive strength	ISO 17162
	Flexural strength	ISO 14704 ISO 14610
	Fatigue strength	ISO 22214 ISO 28704
	Creep	ISO 22215
	Frictional coefficient	ISO 20808
Build material requirements	Density	ISO 18754

[a] *Specific to implants for surgery.*

Chapters V and VI include several characterizations of printed parts obtained by either PBSLP and MSLA 3D printing techniques.

First to study the quality of the parts as implants for surgery the standard ISO-13175 was followed for two specific types of characterization methods:

To compare the mechanical properties between parts printed by a different set of parameters the compressive strength test was employed. The maximum amount of compressive load the parts could bear before fracturing was measured. Two different presses were used for the measurements depending on the sensibility of the load cell needed. A universal mechanical testing press HOUNSFIELD - Tinius Olsen Series- H25KS and an MTS Criterion® Model 42 electromechanical universal test system was used for the measurements.

The measurements of the in vitro dissolution rate of the bone substitutes parts and pH change of the dissolution medium were also performed. Calcium ions concentrations in the dissolution medium versus the soaking time (three days) were determined.

For the determination of the apparent solid densities two methods were followed (ISO 18754): Liquid displacement (Archimedes method) and geometric calculation (measurement of dimensions and mass).

µ-CT imaging, also referred to as X-ray microtomography was as well employed to evaluate the quality of the printed parts. This technique involves the use of rotating x-ray equipment, combined with a digital computer, to obtain images of the parts. Using µ-CT imaging, cross-sectional images of parts can be produced without sacrificing clarity. It was also used to measure parts density and to detect defects to internal architecture.

A more detailed description of the followed procedures will be offered in the corresponding chapters.

6. Complementary characterization techniques

In this section, other techniques used in this work for the characterization of powders, suspensions, and parts are listed and briefly described:

- **Mercury porosimetry**: it is an analytical technique used to determine the material's porous structure of powders and parts. It is determined by applying different pressure levels to a sample soaked in mercury. The pressure required by the mercury to enter pores is inversely proportional to the size of the pores. The analyses were carried out in a Micromeritics, Autopore™ IV.

- **Laser diffraction analysis** is the most common technique among optical techniques for the characterization of the particle size distribution of powders and suspensions. It is based on the principle of diffraction and scattering of a laser (or a coherent and monochromatic light beam) by the particles. The diffraction pattern obtained depends only on the radius of the particle and can be expressed as a size distribution in area, volume, or number. A Mastersizer MS3000 Malvern Panalytical apparatus was used in this work. The wavelengths of the light-emitting diodes equipped in the Mastersizer are 632.8 nm (red laser) and 470.0 nm (blue light).

- Specific surface area analysis by **nitrogen adsorption**, following the Brunauer-Emmett-Teller (BET) theory. The BET theory allows to determine the pressure resulting from the adsorption or condensation of a gas (e.g., nitrogen, helium), called the absorbent, that do not chemically react with material surfaces as adsorbates to quantify specific surface area. The calculation of the specific surface area is based on the theory of multilayer adsorption. Assuming that the first layer of gas molecules absorbed on the particle surface depends only on the adsorbent/substrate interaction energy and the subsequent layers condensing are only a function of the energy of vaporization (or condensation) adsorbent/adsorbent [24]. A Micromeritics, model ACCUPYC 1330 equipment was used to measure the surface area during this work.

- **UV-Visible/NIR spectrophotometer** equipped with integrating spheres accessory was used to measure the total reflectance of powder samples. The absolute transmittance and reflectance can be measured directly with high accuracy and the absorptance can be obtained from these by a simple calculation. The radiation, which is reflected by the powder sample and integrated by the sphere, arrives at the photo-receiver detector. The photo-receiver output signal varies proportionally with the intensity of the reflected radiation. It is registered by a digital processing oscilloscope. A predetermined photometry calibration was made using specimens with known reflectance. The study of a powder absorptance at a certain laser wavelength is of particular interest for the PBSLP process (Chapter V) because it allows one to determine the processing window suitable for sintering or melting without pronounced evaporation. A double beam spectrophotometer AGILENT UV/Visible/NIR and integration sphere accessory of 110 mm were used for the measurement.

- **Powder moisture**, is the loss in weight (%) after a drying process at 110ºC until constant weight is obtained. The water content analyses were carried out on powdered samples in chapter IV with a commercial moisture analyser (MBT model from VWR®).

- **Powder flowability**: many techniques are available to characterize the flow properties of powders. Krantz et al. [25] provide a comprehensive description of different techniques, considering static and dynamic powder state conditions. Depending on the method used is possible to obtain a different kind of information. Techniques that reflect an aired state as the bed expansion ratio are appropriate to predict the fluidization performance, while methods with externally charged and compacted powder suggest static stability and compressibility ratio. Some of these methods are easy to access and can be simply accomplished (Angle of repose/ Bulk & Tap density). Others need higher sophisticated apparatus and corresponding investments (Ring Shear Cell, revolution powder analyser). However, any of these specific methods have been established for PBSLP powders. It is not completely clear which one of these methods provides reliable analytical data for PBSLP powders currently. In our work different methods were used to assess the powder flowability. The angle of repose, compressibility percentage, and Hausner ratio were obtained in a Hosokawa Micron's powder characteristics tester PT-X. The flow rate was analysed in discrete samples by measuring the time it took for 50g of powder to pass through the orifice to the nearest tenth of a second. Finally, the flow factor (ffc) of the powders, a flowability index according to the classification by Jenike [26] was measured in the previously mentioned universal mechanical testing press (HOUNSFIELD - Tinius Olsen Series- H25KS) following the procedure described by Parrella et al. [27]. More details of the parameters evaluated and procedures followed for the characterization of powders flowability will be given in chapter IV.

- **pH measurements**: The pH of the solutions and suspensions was measured by Hach Sension+ PH3 Basic laboratory pH meter, which was calibrated with standards pH 4, 7, and 10 each time before measurement.

7. Synthesis of calcium phosphate powders

7.1 Previous studies on hydroxyapatite (HA) and chlorapatite (ClA) syntheses

Orthopaedic joint replacement, prosthesis, and dental restoration employing bioceramic materials have been investigated since the 1960s; its interest is due to the many advantages compared to other materials. Currently, metallic prostheses are the most developed bone substitutes, and a hydroxyapatite (HA) coating, with chemical formula $Ca_{10}(PO_4)_6OH)_2$, is used to improve the bone-implant interface. Thus, enhancing the osteointegration properties, shortening the surgery time, and obtaining better durability of the prosthesis over time. The quality of the coating is highly influenced by the characteristics of the HA powder used and its production has been exhaustively studied to be adjusted for the coating processing step. Consequently, numerous research laboratories, such as the "Centre Inter-universitaire de Recherche et d'Ingénierie des Matériaux" (CIRIMAT), the "Laboratoire de Génie Chimique" (LGC), and small and medium companies (SMEs) have investigated the production of HA powders for biomedical applications during many years.

Numerous methods to produce HA powder already exist: Wet chemical precipitation, hydro/solvothermal processing, solid-state, sol-gel…[28,29]. However, the simplicity and the possibility of variation related to the shape, size, and phase of the samples make the wet chemical precipitation an interesting method [30]. The collaboration of the previously mentioned academic laboratories (CIRIMAT and LGC) and an industrial partner (Urodelia® S.A.) made possible the realization of a deeper study on the HA precipitation and the scale-up of the process into a pilot scale, keeping a continuous procedure [31]. During this study, the influence of the operating conditions on the stoichiometric hydroxyapatite powder properties such as, morphology, crystallinity, and phase composition was evaluated. It was discovered that the most crucial step was the beginning of the process, during the formation of the large agglomerates. Some advantages observed comparing to the conventional processes were the improvement of the reproducibility, and the energy saving. After this initial study, the pilot-scale development of the process (1-5 tons / year) continued by members of the project in terms of know-how transfer and a start-up creation.

After this, the adaptation of the production process parameters to produce hydroxyapatite powders with suitable properties for additive manufacturing (AM) started with the present work. Finally, the tailoring of the HA powder properties for masked stereolithography (MSLA) and powder bed selective laser processing (PBSLP) techniques required more steps than only the synthesis. The impossibility of producing hydroxyapatite microspheres (giving a level of flowability to the dry powder required for a PBSLP process) directly from the synthesis makes the tailoring of the powder properties dependent on consequent processes. For this reason, and the need for important quantities of powder for future studies (such as, processes optimization), it was decided that powder produced commercially by Urodelia® S.A company, which share same properties (composition and morphology) with the powder produced in-house will be acquired as starting material. However, during this work, some preliminary syntheses were performed following the already optimized procedure to fully understand the HA production process. It was possible then to obtain

a general view of all the steps involved in the production of HA powder intended for AM technologies. Starting with the synthesis described in this chapter and followed by the milling, spray-drying, and additive mixing steps detailed in the next chapters.

The synthesis of an additional calcium phosphates powder is also detailed in the present section. Chlorapatite (ClA) with chemical formula $Ca_{10}(PO_4)_6Cl_2$, results from the chloride-substitution of the hydroxyl group in the hydroxyapatite structure. ClA feedstock powder was prepared for performance comparison against HA in a PBSLP apparatus. Interestingly, ClA was never been tested in a PBSLP despite its ability to melt without decomposition unlike HA, which could be one important advantage [32]. In addition, it has demonstrated highly enhanced bioactivity and osteoconductive compared with HA making it a very promising material for its use as a bone grafting material [33]. The production of ClA from hydroxyapatite chloride-substitution was previously studied by Demnati et al. [34] so a similar procedure was followed and only the HA powder used as precursor was changed.

As explained before, stoichiometric-HA and ClA synthesis methods were already optimized by previous works. In the case of the HA precipitation process, the optimal set of operating parameters described by Tourbin et al. [31] was followed. Only slight and scale-up oriented variations were imposed on the processes. A complete powders characterization was performed to ensure that the obtained powders share the same properties that the powders produced in previous studies.

7.2 Methods of characterization for in-house produced HA and ClA powders

The PSD of the particles in suspension and dry powders was measured by laser diffraction using a Mastersizer 3000 (Malvern Instruments Ltd.). In addition, the quality of the products was examined in terms of structural and chemical composition. A scanning electron microscope (SEM) LEO 435 VP equipped with a Ge detector (Imix-PC, PGT) was used to study the morphology of the powders through metallization of the ceramic surface with a thin film of silver using a Scancoat Six sputter coater. PSD of the commercial Hydroxyapatite microspheres (HAm) and SEM micrographs of the granules, can be observed in Figure 11.

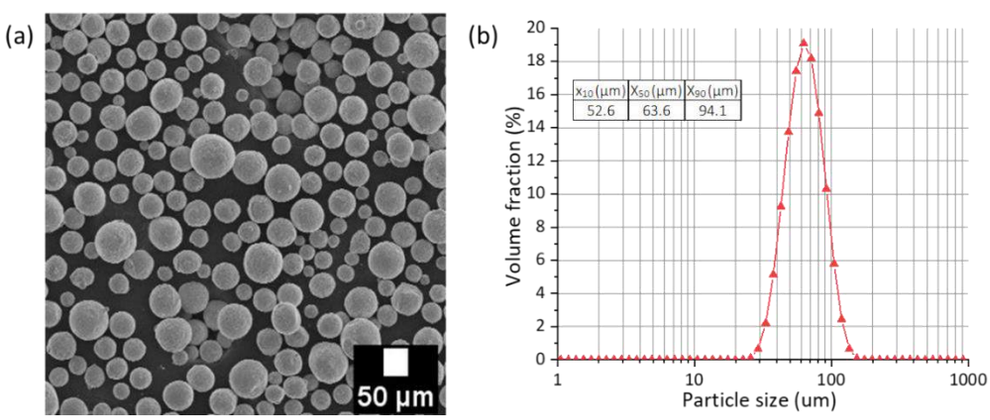

Figure 11. Morphology and microstructural analysis of the commercial HAm used for the production of ClA powder. (a) SEM micrograph, (b) Particle size distribution.

The analyses of the composition of initial and resulting powders were carried out by Fourier transform infrared spectroscopy (FTIR) performed by transmission using KBr pellets in a spectrometer FTIR iS50. The sample preparation consisted in weighing and transferring of about 9 mg of sample powder to a clean mortar. The sample was homogeneously mixed with dry KBr powder (300±5 mg). A compression at 6000 kg was used to produce the analysed sample pellets. FTIR spectra was measured from the pellet in a 4000-400 cm^{-1} wavenumber range with a step width of 0,48 cm^{-1}.

In addition, X-ray diffraction (XRD) analyses were performed by BRUKER's X-ray diffractometer D8-2 by using Cu Kα radiation (wavelength λ = 0.15406 nm) with a nickel filter at 40 kV and 40 mA. A chosen 2θ range between 20º and 90º, a step of 0.03º 2θ, and a time per step of 0.2 s were used to record the diffractograms.

The quality of the precipitated HA was then evaluated since only the powders with a stoichiometric ratio Ca/P=1.67 are stable after calcination. Powders with a higher Ca/P ratio decompose into a mixture of HA and calcium oxide (CaO) phases while powders with a lower ratio decompose into HA and β-TCP phases. Calibration curves of HA powder combined with β-TCP and CaO at different weight fractions were produced to perform quantitative analyses of the calcium phosphate phases present in the produced powder. Data analysis, line fitting, and calculation of parameter values were performed using OriginLab 2018 software. A stoichiometric HA powder purity higher than 95% was pursued. In the case of the chlorination process, the main purpose was to obtain a total conversion of the HAm into ClA microspheres by complete chloride-substitution of the hydroxyl groups of HA.

7.3 Synthesis of HA suspensions and powders

7.3.1 Stoichiometric-HA synthesis procedure (wet-chemical precipitation)

The wet chemical precipitation synthesis of stoichiometric-HA follows the overall global equation:

$$10Ca(NO_3)_2, 4H_2O + 6(NH_4)_2HPO_4 + 8(NH_4)OH \rightarrow Ca_{10}(PO_4)_6(OH)_2 + 20NH_4NO_3 + 6H_2O \quad (7)$$

The synthesis process was slightly adapted from the procedure described by Tourbin et al. [31]. The main reactor of 1L of capacity was used previously to perform the precipitation but, in the present work, there was a slight change on the scale of the process, and a reactor of 4 L was used instead to produce a higher amount of HA in the same batch. The quantities for the reagents were increased and the pumps speed was adjusted in accordance. Figure 12 shows the scheme of the set-up used for the precipitation process.

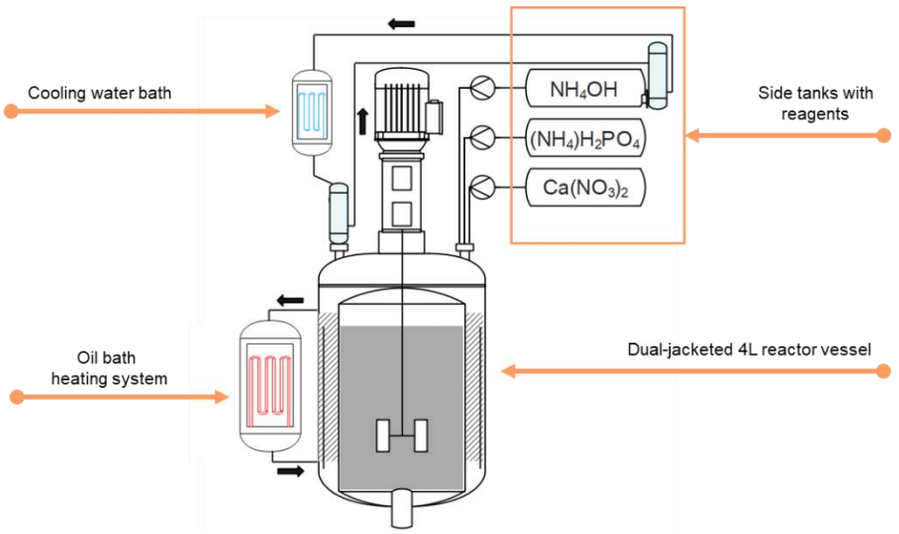

Figure 12. Schematic illustration of the stoichiometric-HA wet chemical precipitation synthesis set-up.

The main dual-jacketed 4L reactor vessel is equipped with an oil bath heating system for controlled heating during the process. Then it is connected to three side tanks containing aqueous ammonia (NH_4OH), ammonium dihydrogen phosphate ($(NH_4)H_2PO_4$), and calcium nitrate ($Ca(NO_3)_2$) reagents solutions. The reactor is also equipped with a mechanical agitator with a three blades Lightning A310 axial stirrer of 6 cm in diameter, placed at one-third of the height of the reactor.

At the beginning of the process, an initial volume of calcium nitrate aqueous solutions is poured into the reactor and stirred at 1000 rpm, while the temperature of the reactor is raised reaching and keeping a temperature of 80ºC during the rest of the process. The feeding of the three solutions contained in the side tanks is controlled employing peristaltic pumps set at fixed flow rates. The total pumped volume ratio of reagents during the precipitation was 1:1.7:1.4 for NH_4OH, $(NH_4)H_2PO_4$, and $Ca(NO_3)_2$ solutions respectively. The three side tanks are kept at room temperature. A refrigerant connected to the reactor and a cooling water bath is used to condense the ammonia vapor in a close circuit.

First, the ammonia solution is pumped into the main reactor to adjust the pH of the solution to 7.5 to avoid the formation of non-stoichiometric HA. Once the desired pH is reached (15 minutes), the precipitation starts with the continuous feeding of the three solutions. After 1 hour of synthesis, the reagents feeding is stopped but the stirring and the temperature of the reactor are kept constant during a further maturation step for 15 minutes. The final suspension is vacuum filtered, and the agglomerates are washed with distilled water. The filtration cake is then frozen overnight and then freeze-dried to obtain poorly crystallized apatite powder. Finally, this powder is calcined at 1000ºC for 15 hours into an oven to obtain a completely dried and free of impurities crystallized HA powder.

Suspension samples were collected during the whole process to characterize the particle size distribution (PSD) evolution during the process.

7.3.2 Characterization of precipitated HA powders

Since the wet chemical precipitation process parameters were already optimized no further effort was employed on changing the process conditions. The stirring rate was varied since a scale-up of the process was performed from a reactor of 1 L of capacity to one of 4 L. Since the amounts of reagents were increased to obtain higher quantities of product, an increase in the stirring rate was needed for correct homogenization. Then from the 600 rpm of stirring rate defined previously it was increased to 1000 rpm for proper mixing of the compounds inside the process reactor. Aliquots were taken at different times during the process giving the PSD evolution shown in Figure 13a. A decrease of the particle size is observed with time, as well as a change in the number of particles populations from 1 to 3. It is remarkable the no variation in the PSD during the maturation phase. The SEM micrograph shown in Figure 13b confirms the presence of coarse and dendritic agglomerates with diverse proportions. A closer look at one of the agglomerates is shown in Figure 13c. They are composed of an assembly of crystallites with characteristic acicular morphology.

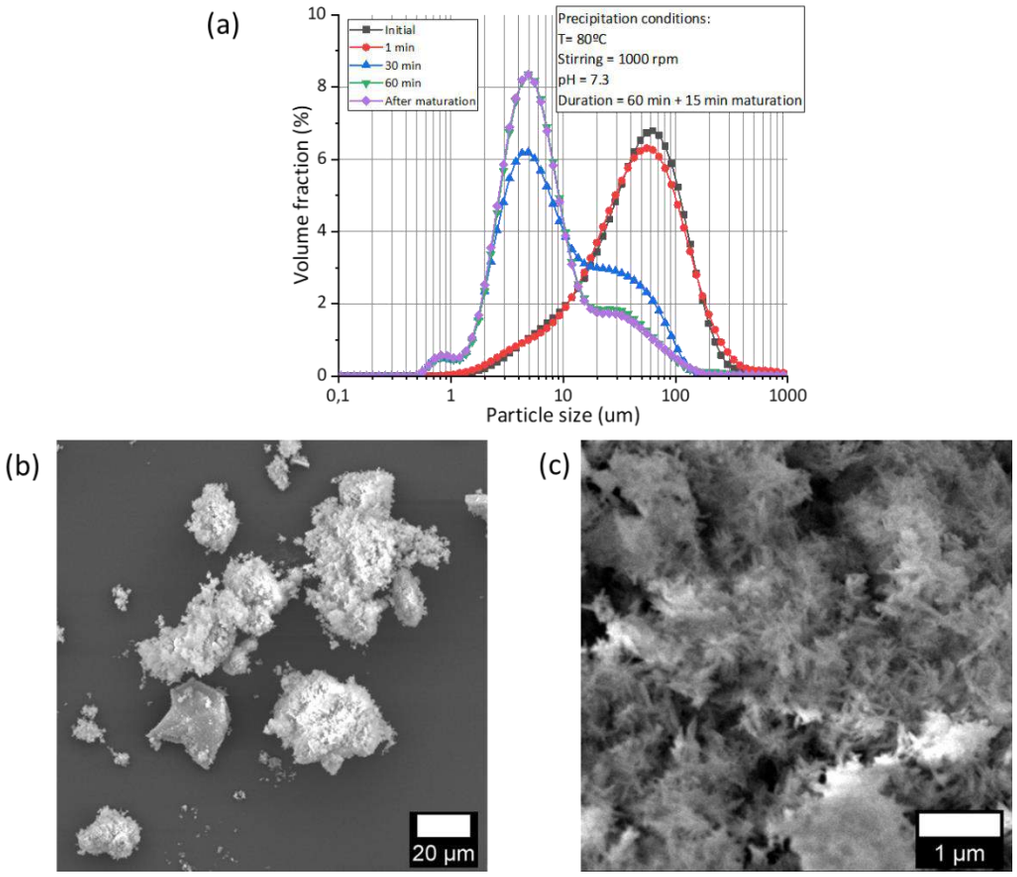

Figure 13. (a) HA powders PSD evolution during the wet precipitation process. SEM micrographs of HA powders produced showing (b) large agglomerates composed of (c) smaller needle-like particles.

For the quality analysis of the precipitation product, FTIR and XRD spectra were obtained of the produced powders before and after calcination. To determine the product quality, the standard ISO 13779-3:2008 was followed regarding the powder chemical composition (Ca/P ratio), and phase composition. A comparison between the XRD spectra of the powders obtained (before and after calcination) is shown in Figure 14. A clear increase in the crystallinity of the powder is observed for the powder after calcination. Crystallinity is understood as the degree of completeness of a crystal in the sense of crystallography. Normally, the bigger the crystal is, the better the crystallinity, and narrower and more isolated the XRD reflections. For example, a broad XRD peak means low crystallinity, and a sharper XRD peak indicates an increase in crystallinity [35]. Even if the crystallinity degree was not quantified, the differences between the XRD spectra denote an influence of the temperature on the HA powder crystallinity.

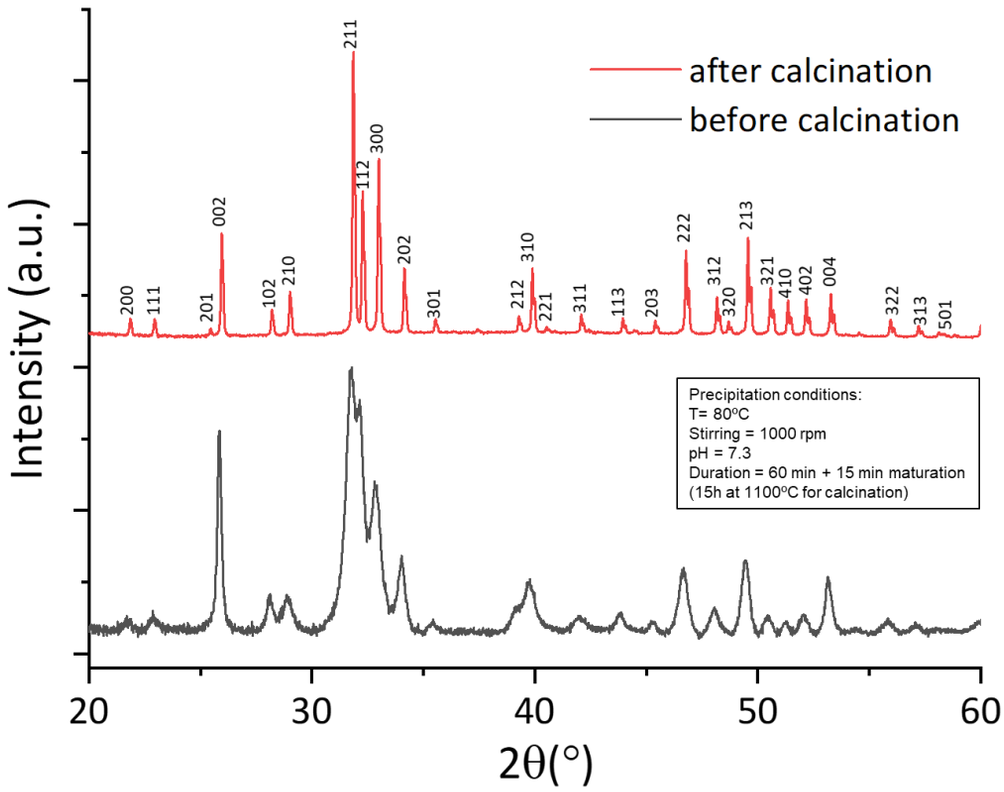

Figure 14. XRD analyses of the products obtained after the wet chemical precipitation process. Before and after the calcination process. All the diffraction peaks correspond to stoichiometric hydroxyapatite (JCPDS 00 009 0432).

The Ca/P ratio of stoichiometric HA is equal to 1.67, then a value considered acceptable for this ratio was in the range between 1.658 (which corresponds to a HA powder containing 5% of β-TCP) and 1.824 (HA powder + 5% CaO). It was found, through the comparison with the calibration lines obtained previously (Figure 1) that none of the powders produced in this study surpassed the mentioned limits of Ca/P ratio, so the composition was confirmed to be stoichiometric HA.

For a deeper analysis of the powder composition, FTIR analysis was performed before and after the calcination process. The spectra comparison can be observed in Figure 15. The broader peaks in the no-calcined powder spectrum to the calcinated one indicate a lower degree of crystallinity. It can be also observed that the calcination treatment results in the production of powder completely free of impurities from the precipitation process such as $CaNO_3$. No secondary phases were detected by FTIR analysis. The vibration bands corresponding to PO^4 are visible at 1092 cm^{-1}, 1040 cm^{-1}, 962 cm^{-1}, 601 cm^{-1}, 575 cm^{-1}, 561 cm^{-1}, as well as the band belonging to OH^- at 650 cm^{-1} 3600 cm^{-1} [7].

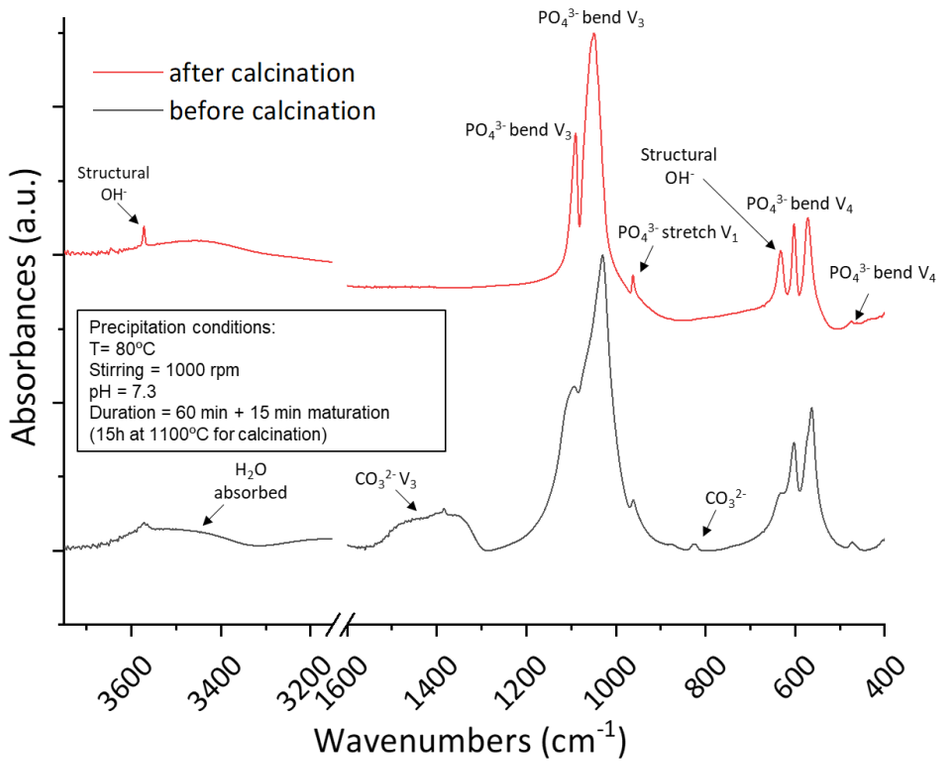

Figure 15. FTIR spectra of the product obtained after the wet chemical precipitation process. For comparison spectra before and after the calcination process are shown.

A SEM micrograph of the HA powder after calcination is shown in Figure 16. An increase in the size of the agglomerates is observed compared to the agglomerates of the powder before the thermal treatment. With the increase in temperature, the morphology of apatite crystals changes considerably: the width-thickness is increased, resulting in a lower crystal surface energy, and the length of the particles is reduced.

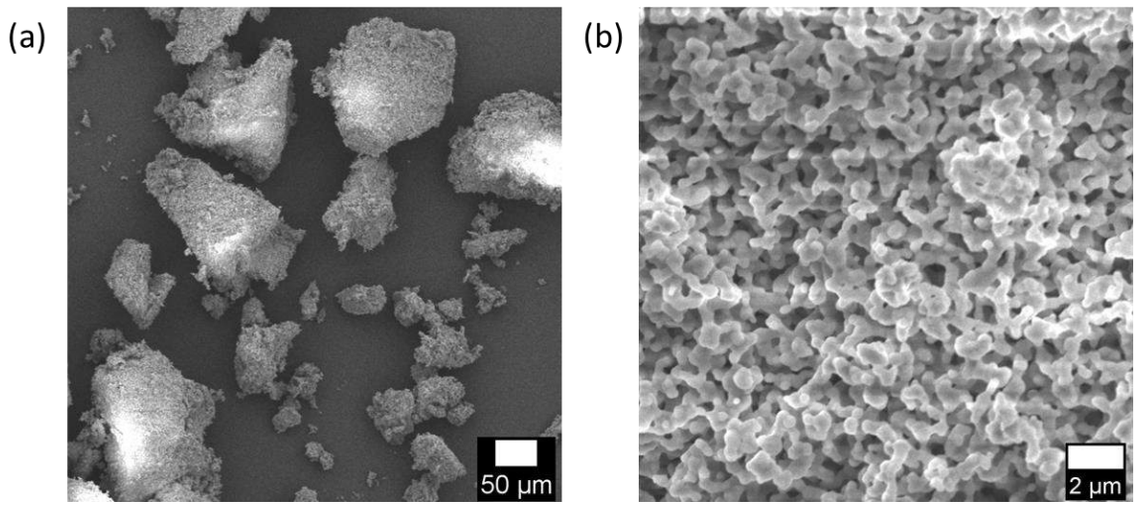

Figure 16. SEM micrographs of calcined HA powder showing (a) large agglomerates composed of (b) smaller partially sintered particles.

In conclusion, the production of pure stoichiometric-HA powder was confirmed by physical-chemical analysis. A calcination process was required to obtain completely free of impurities powder. In addition, the changes in particles morphology due to the thermal treatment were illustrated by the comparison of SEM analyses of powders before and after calcination.

7.4 Synthesis of ClA powders

7.4.1 Chlorapatite synthesis procedure (chlorination)

The ClA powder was produced from the chloride substitution of the commercial HA microspheres (HAm) provided by the company Urodelia® S.A. (ref. 300-08-2) by using ammonium chloride (NH_4Cl) through a solid-gas reaction. The synthesis was performed in a tubular furnace under inert gas (ALPHAGAZ™ 2 Argon) flow (Figure 17) at 900ºC following the reaction:

$$Ca_{10}(PO_4)_6(OH)_2 + 2NH_4Cl \rightarrow Ca_{10}(PO_4)_6Cl_2 + 2NH_3 + 2H_2O \quad (8)$$

The reagents were placed in alumina crucibles. HAm powder was placed in the middle of the tube where the maximum temperature (900ºC) is reached while the NH_4Cl was placed in a region of the tube where the temperature reaches a value close to its sublimation value (400ºC). The temperature pattern followed during the process can be seen in Figure 18. A first purge phase is performed to remove the presence of air inside of the tube. Then, the temperature increases following a heating rate of 5ºC/min and followed by an isotherm step of 1 hour at 950ºC before the cooling phase of the furnace. A mass proportion of powders of 1:1.85 between the HAm and the NH_4Cl was used. An excess of NH_4Cl was used to ensure a complete chloride substitution of the powder.

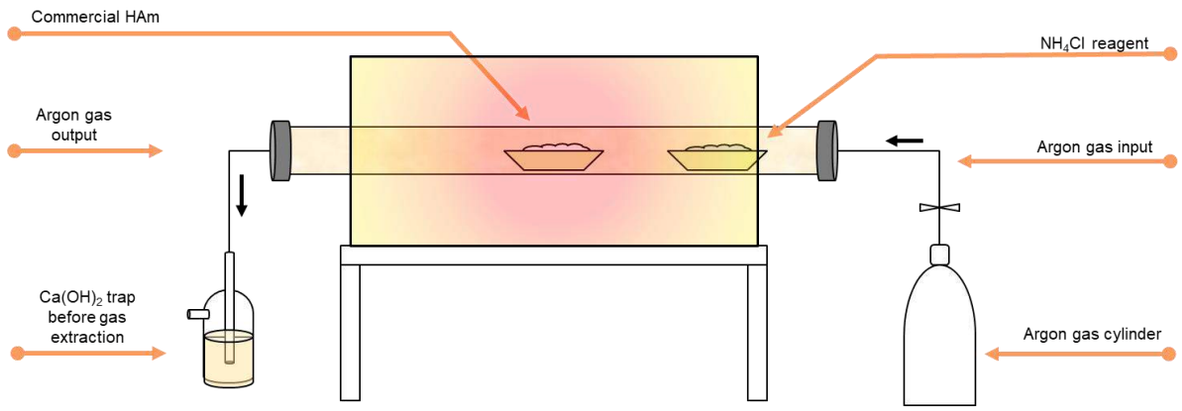

Figure 17. Schematic illustration of the ClA synthesis setup.

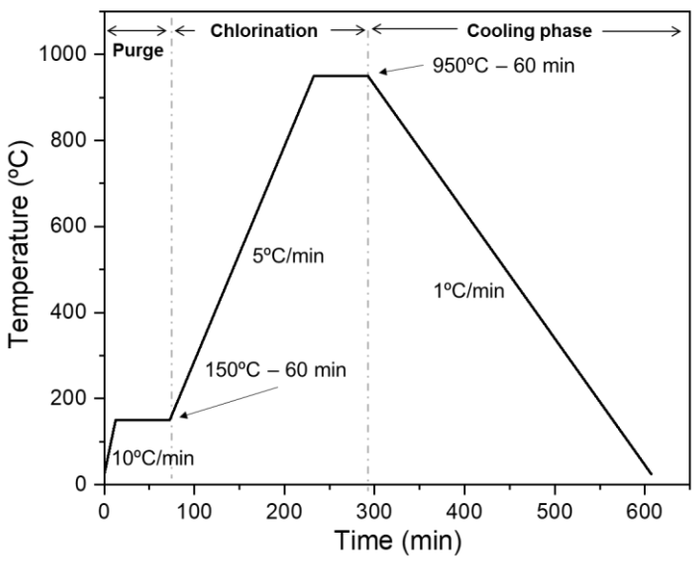

Figure 18. Temperature pattern for chlorination process.

A calcium hydroxide ($Ca(OH)_2$) and water trap was placed before the extraction of the argon gas output which contains the chlorine (Cl_2) produced during the reaction. The conversion of chlorine into calcium hypochlorite ($Ca(OCl)_2$), less hazardous liquid bleach, eliminates the risk of a chlorine gas leak during the process. Chlorine treatment with calcium hydroxide follows the equation below:

$$2Ca(OH)_2 + 2Cl_2 \rightarrow Ca(OCl)_2 + CaCl_2 + 2H_2O \quad (9)$$

Several reactions were performed to produce the amount of ClA powder needed for the tests in a PBSLP apparatus.

7.4.2 Characterization of synthesized ClA powder

The production of ClA powder was based on the chloride substitution of commercial HA microspheres (HAm). Since this commercial powder already demonstrated correct suitability to be used in a PBSLP process (in terms of powder flowability) it was important to perform complete chlorination of the powder avoiding any modification of the particle morphology. Once the reaction finished, the powder obtained was analysed to confirm the obtention of pure ClA microspheres.

First, to analyse the final product purity a comparison between XRD spectra of the initial HAm and the produced ClA powder was carried out (Figure 19). We can observe a difference in the degree of crystallinity between both powders being higher on the powder treated at high temperatures during chlorination. After the diffraction lines identification, the absence of peaks from the HA phase on the final product means that the chloride substitution was complete and pure ClA powder was obtained. We could point out a partial phase of ClA during the chlorination. ClA undergoes a phase change from hexagonal to monoclinic upon heating at 200-300 ºC [16].

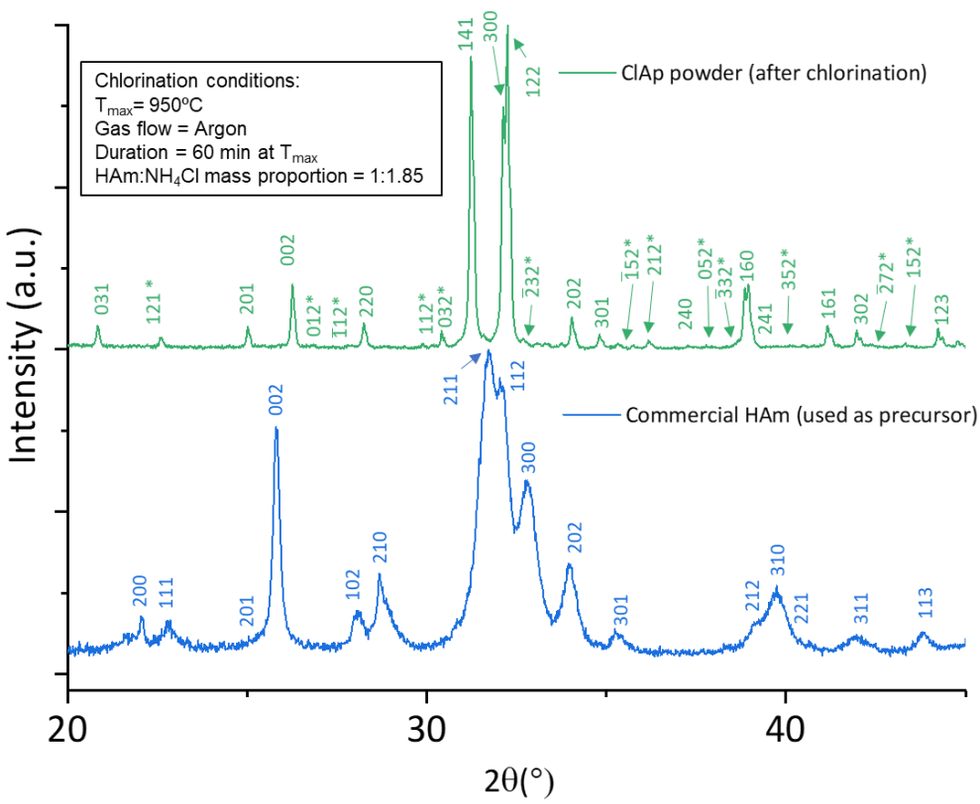

*Figure 19. XRD powder patterns of commercial HAm and ClA produced by chlorination. Diffraction peaks correspond to (below) stoichiometric hydroxyapatite (JCPDS 00 009 0432) and (above) hexagonal chlorapatite (JCPDS 00-33-0271) [36]. *Monoclinic lines for ClA.*

FTIR analyses of the initial HAm and the obtained ClA powder were as well carried out. The comparison between both spectra is shown in Figure 20. The disappearance of the structural carbonate impurities located at the A and B sites (hydroxyl and phosphate sites, respectively) of apatite structure in the initial powder was confirmed after the chlorination. The absence of peaks corresponding to the structural hydroxyl OH^- in the final product at 650 cm^{-1} and 3600 cm^{-1} confirms complete chlorination of the initial HAm. No secondary phases were detected by FTIR analysis. The vibration bands corresponding to PO_4^{3-} are visible at 1092 cm^{-1}, 1040 cm^{-1}, 962 cm^{-1}, 601 cm^{-1}, 575 cm^{-1}, 561 cm^{-1} [7].

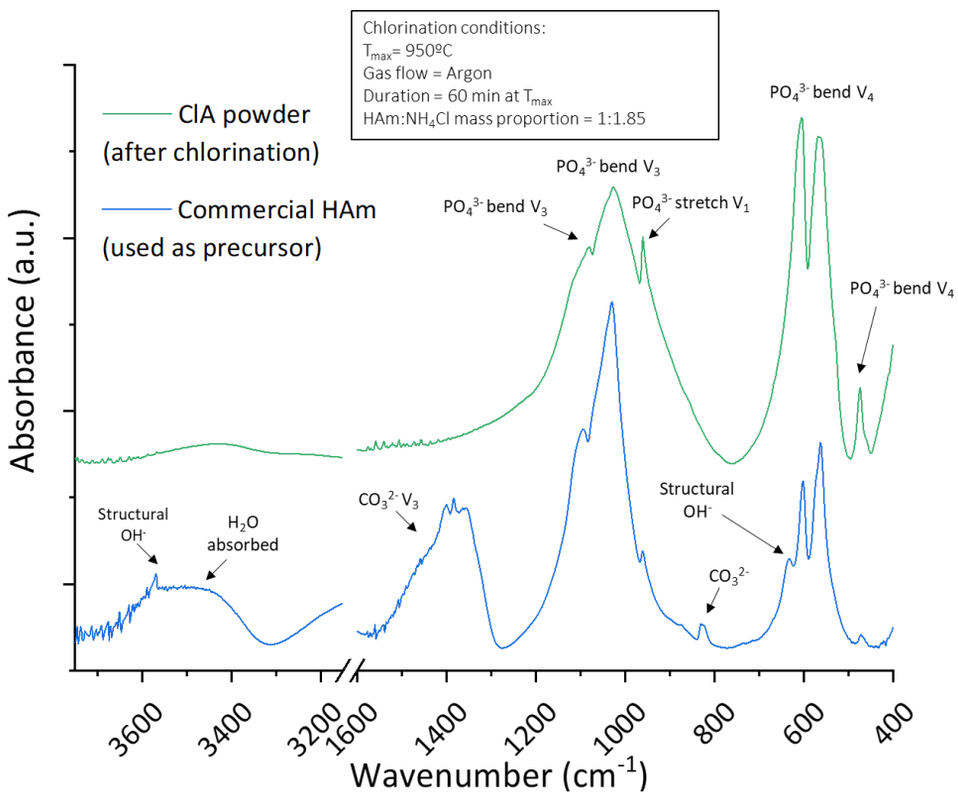

Figure 20. FTIR spectra comparison between the commercial HAm used as a precursor and the obtained ClA powder after chloride substitution.

The morphology of the ClA microspheres was examined to check that no modification of the particle shape occurred during their production. The SEM micrograph shown in Figure 21a proves the no alteration of the particles during its conversion in comparison with the HAm particles used as precursors. A closer look at the particle morphology can be seen in Figure 21b. Small rough spherical dense particles shape has been kept intact after chlorination.

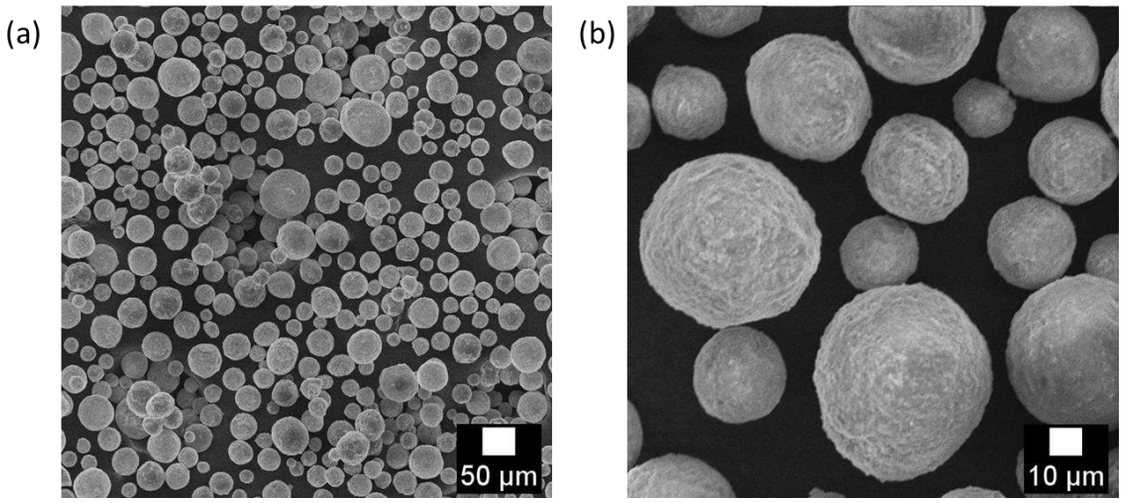

Figure 21. (a) A SEM micrograph of ClA microspheres produced after chlorination. (b) SEM micrograph at higher magnification of (a).

As a conclusion, complete chlorination of HAm particles to produce ClA microspheres was demonstrated to be feasible through FTIR and XRD analyses. A study on particles morphology by SEM approved the absence of morphological alterations on the microspheres after the process. This study established that the use of a tubular furnace to perform a solid-gas chlorination reaction of HA powder to produce pure ClA can be suitable.

8. Conclusions

In this chapter, the materials, equipment, methods, and syntheses procedures used have been presented.

A complete list of the materials employed was compiled to facilitate access to their characteristics and supplier information. A battery of complementary characterization techniques focused on the analyses of CaP powders was presented and exhaustively described. It is a piece of basic and essential knowledge for the correct understanding of the next chapters of this work. Then, a basic description of suspensions principles and their properties was offered accompanied by the techniques used in this thesis for their assessment. The analyses carried out to evaluate the 3D printed parts quality were exposed too. The standards that have been agreed upon by experts and followed to perform our analyses were also mentioned.

And finally, two different processes were re-evaluated for the production of pure stoichiometric-HA and ClA powders. The relevance of these studies on the production of calcium phosphate powders intended for PBSLP and other AM techniques made this section one interesting contribution for the completion of this chapter.

The next chapter (chapter III) is dedicated to the study of the stirred bead milling process of HA powder. The different factors influencing the HA ground product characteristics (suspension formulation, operating parameters…) will be evaluated. The objective will be the production of two different products: (i) a suspension containing sub-micron-sized particles intended for a posterior spray-drying process to produce spherical agglomerates and (ii) a suspension composed of micron-sized particles that, after filtering and drying steps, could be used in VAT photopolymerization technologies.

9. REFERENCES

[1] C. Rey, C. Combes, C. Drouet, D. Grossin, G. Bertrand, J. Soulié, Bioactive Calcium Phosphate Compounds: Physical Chemistry, in: Reference Module in Materials Science and Materials Engineering, Elsevier, 2017. https://doi.org/10.1016/B978-0-12-803581-8.10171-7.

[2] J.C. Trombe, G. Montel, Some features of the incorporation of oxygen in different oxidation states in the apatitic lattice—I On the existence of calcium and strontium oxyapatites, Journal of Inorganic and Nuclear Chemistry. 40 (1978) 15–21. https://doi.org/10.1016/0022-1902(78)80298-X.

[3] J.M. Toth, W.M. Hirthe, W.G. Hubbard, W.A. Brantley, K.L. Lynch, Determination of the ratio of HA/TCP mixtures by x-ray diffraction, Journal of Applied Biomaterials. 2 (1991) 37–40. https://doi.org/10.1002/jab.770020106.

[4] Z. Zyman, D. Rokhmistrov, K. Loza, Determination of the Ca/P ratio in calcium phosphates during the precipitation of hydroxyapatite using X-ray diffractometry, Processing and Application of Ceramics. 7 (2013) 93–95. https://doi.org/10.2298/PAC1302093Z.

[5] L. Lutterotti, S. Matthies, H. Wenk, MAUD: a friendly Java program for material analysis using diffraction, UCr: Newsletter of the CPD. 21 (1999) 14–15.

[6] K. Ioku, Hydrothermal preparation of fibrous apatite and apatite sheet, Solid State Ionics. 151 (2002) 147–150. https://doi.org/10.1016/S0167-2738(02)00593-3.

[7] C. Rey, O. Marsan, C. Combes, C. Drouet, D. Grossin, S. Sarda, Characterization of Calcium Phosphates Using Vibrational Spectroscopies, in: B. Ben-Nissan (Ed.), Advances in Calcium Phosphate Biomaterials, Springer Berlin Heidelberg, Berlin, Heidelberg, 2014: pp. 229–266. https://doi.org/10.1007/978-3-642-53980-0_8.

[8] J.S. Gaffney, N.A. Marley, Chemistry of environmental systems: fundamental principles and analytical methods, First edition, Wiley, Hoboken, NJ, 2020.

[9] R. Moreno, Colloidal processing of ceramics and composites, Advances in Applied Ceramics. 111 (2012) 246–253. https://doi.org/10.1179/1743676111Y.0000000075.

[10] T. Tadros, Interparticle interactions in concentrated suspensions and their bulk (rheological) properties, Adv Colloid Interface Sci. 168 (2011) 263–277. https://doi.org/10.1016/j.cis.2011.05.003.

[11] B. Derjaguin, On the repulsive forces between charged colloid particles and on the theory of slow coagulation and stability of lyophobe sols, Trans. Faraday Soc. 35 (1940) 203–215. https://doi.org/10.1039/TF9403500203.

[12] B. Derjaguin, L. Landau, Theory of the stability of strongly charged lyophobic sols and of the adhesion of strongly charged particles in solutions of electrolytes, (1941). https://doi.org/10.1016/0079-6816(93)90013-L.

[13] E.J.W. Verwey, J.T.G. Overbeek, K. van Nes, Theory of the Stability of Lyophobic Colloids: The Interaction of Sol Particles Having an Electric Double Layer, Elsevier Publishing Company, 1948.

[14] S. Lu, R.J. Pugh, E. Forssberg, eds., Chapter 10 Dispersion of particles in liquids, in: Studies in Interface Science, Elsevier, 2005: pp. 517–558. https://doi.org/10.1016/S1383-7303(05)80011-0.

[15] J.C. Fariñas, R. Moreno, J.-M. Mermet, Effect of colloidal stability of ceramic suspensions on nebulization of slurries for inductively coupled plasma atomic emission spectrometry, J. Anal. At. Spectrom. 9 (1994) 841–849. https://doi.org/10.1039/JA9940900841.

[16] W. Liu, M. Li, J. Nie, C. Wang, W. Li, Z. Xing, Synergy of solid loading and printability of ceramic paste for optimized properties of alumina via stereolithography-based 3D printing, Journal of Materials Research and Technology. 9 (2020) 11476–11483. https://doi.org/10.1016/j.jmrt.2020.08.038.

[17] P. Höhne, B. Mieller, T. Rabe, Slurry development for spray granulation of ceramic multicomponent batches, Journal of Ceramic Science and Technology. 9 (2018) 327–336. https://doi.org/10.4416/JCST2018-00022.

[18] M. Nutan, I. Reddy, General Principles of Suspensions, in: Pharmaceutical Suspensions: From Formulation Development to Manufacturing, 2009: pp. 39–65. https://doi.org/10.1007/978-1-4419-1087-5_2.

[19] N. Maximova, O. Dahl, Environmental implications of aggregation phenomena: Current understanding, Current Opinion in Colloid & Interface Science. 11 (2006) 246–266. https://doi.org/10.1016/j.cocis.2006.06.001.

[20] L. Guérin, C. Frances, A. Liné, C. Coufort-Saudejaud, Fractal dimensions and morphological characteristics of aggregates formed in different physico-chemical and mechanical flocculation environments, Colloids and Surfaces A: Physicochemical and Engineering Aspects. 560 (2019) 213–222. https://doi.org/10.1016/j.colsurfa.2018.10.017.
[21] F. Garcia, N. Le Bolay, J.-L. Trompette, C. Frances, On fragmentation and agglomeration phenomena in an ultrafine wet grinding process: the role of polyelectrolyte additives, International Journal of Mineral Processing. 74 (2004) S43–S54. https://doi.org/10.1016/j.minpro.2004.07.001.
[22] C.W. Macosko, ed., Rheology: principles, measurements, and applications, VCH, New York, 1994.
[23] D. Quemada, Rheological modelling of complex fluids. I. The concept of effective volume fraction revisited, Eur. Phys. J. AP. 1 (1998) 119–127. https://doi.org/10.1051/epjap:1998125.
[24] P.W. Atkins, Physical chemistry, 3. ed., repr. with corr, Oxford Univ. Pr, Oxford, 1988.
[25] M. Krantz, H. Zhang, J. Zhu, Characterization of powder flow: Static and dynamic testing, Powder Technology. 194 (2009) 239–245. https://doi.org/10.1016/j.powtec.2009.05.001.
[26] A.W. Jenike, Storage and flow of solids. Bulletin No. 123 of the Utah Engineering Experiment Station; Vol. 53, No. 26, November 1964, Utah Univ., Salt Lake City (United States), 1976. https://doi.org/10.2172/5240257.
[27] L. Parrella, D. Barletta, R. Boerefijn, M. Poletto, Comparison between a Uniaxial Compaction Tester and a Shear Tester for the Characterization of Powder Flowability, KONA. 26 (2008) 178–189. https://doi.org/10.14356/kona.2008016.
[28] S. Cox, Synthesis Method of Hydroxyapatite, (2014) 11.
[29] M. Okada, T. Furuzono, Hydroxylapatite nanoparticles: fabrication methods and medical applications, Sci Technol Adv Mater. 13 (2012). https://doi.org/10.1088/1468-6996/13/6/064103.
[30] A. Yelten, S. Yilmaz, Wet chemical precipitation synthesis of hydroxyapatite (HA) powders, Ceramics International. 44 (2018). https://doi.org/10.1016/j.ceramint.2018.02.201.
[31] M. Tourbin, F. Brouillet, B. Galey, N. Rouquet, P. Gras, N. Abi Chebel, D. Grossin, C. Frances, Agglomeration of stoichiometric hydroxyapatite: Impact on particle size distribution and purity in the precipitation and maturation steps, Powder Technology. 360 (2020) 977–988. https://doi.org/10.1016/j.powtec.2019.10.050.
[32] K. Tõnsuaadu, K.A. Gross, L. Plūduma, M. Veiderma, A review on the thermal stability of calcium apatites, J Therm Anal Calorim. 110 (2012) 647–659. https://doi.org/10.1007/s10973-011-1877-y.
[33] J. Cho, D. Su Yoo, Y.-C. Chung, S.-H. Rhee, Enhanced bioactivity and osteoconductivity of hydroxyapatite through chloride substitution, Journal of Biomedical Materials Research. Part A. 102 (2014). https://doi.org/10.1002/jbm.a.34722.
[34] I. Demnati, D. Grossin, C. Combes, M. Parco, I. Braceras, C. Rey, A comparative physico-chemical study of chlorapatite and hydroxyapatite: from powders to plasma sprayed thin coatings, Biomed. Mater. 7 (2012) 054101. https://doi.org/10.1088/1748-6041/7/5/054101.
[35] H. Wang, L. Yuan, J. An, Crystallographic Characteristics of Hydroxylapatite in Hard Tissues of Cololabis saira, Crystals. 7 (2017) 103. https://doi.org/10.3390/cryst7040103.
[36] J.C. Elliott, Structure and chemistry of the apatites and other calcium orthophosphates, Elsevier, Amsterdam [The Netherlands] : New York, 1994.

Chapter III. Powder bed fusion and VAT photopolymerization hydroxyapatite powder feedstock obtained by stirred bead milling

Powder bed fusion and VAT photopolymerization hydroxyapatite powder feedstock obtained by stirred bead milling

Pedro Navarrete-Segado,[a,b] David Grossin,[a] Mallorie Tourbin,[b] Christine Frances[b,*]

[a] CIRIMAT, Université de Toulouse, CNRS, 4 Allée Émile Monso, 31432 Toulouse Cedex 4, France

[b] Laboratoire de Génie Chimique, Université de Toulouse, CNRS, 4 Allée Émile Monso, 31432 Toulouse Cedex 4, France

Abstract. This paper focuses on the preparation of ceramic hydroxyapatite (HA) powder feedstock for additive manufacturing (AM) technologies. For VAT photopolymerization technologies the use of calcium phosphate particles within the size range of 1-20 µm and irregular shape have been demonstrated to be suitable. While powder bed fusion (PBF) material feedstock generally involves the use of spherical powders that could be obtained by atomisation of particles within a 0.2-1.5 µm particle size range. Since as-synthesized powders usually do not meet these required sizes, in this work the use of stirred bead milling process to tune the HA particle size distribution adjusting the process parameters was investigated. A wide variety of parameters was evaluated such as the slurry formulation and milling operating conditions. Ground HA-filled slurries were analysed in terms of stability and rheological behaviour to ensure their suitability for the process. A Darvan C dispersant agent dosage of 2.1 $mg.m^{-2}$ (active component) to the specific surface of the ceramic was found to be the most outstanding dosage for the stabilization of the dispersion. Milling chamber, bead wear, and energy consumption were evaluated and minimized finding the most efficient operating parameter setting for the milling process of hydroxyapatite particles depending on the application. It was found that for the studied material, the use of a fast stirrer speed, smaller grinding media size, and higher solids concentration shorten the grinding time and increased the energy efficiency. In conclusion, the laboratory-scale milling used in the present work can be considered a promising method for studying material processability and energy requirements for the production of hydroxyapatite powder feedstock in the additive manufacturing industry.

Keywords: hydroxyapatite, slurry, stirred bead milling, 3D-Printing, photopolymerization, powder bed fusion

*****Corresponding author: christine.frances@ensiacet.fr

1. Introduction

Additive manufacturing (AM) technologies have demonstrated the feasibility of the production of ceramic parts for tissue engineering and implantology by different categories such as VAT photopolymerization [1,2], or powder bed fusion (PBF) [3,4]. This group of techniques might produce convenient, fast, and individualized implants, shortening the production period of patient-matched tissue engineering scaffolds from a bio-ceramic powder feedstock, as hydroxyapatite (HA) [5,6]. HA is already a well-known calcium phosphate-based bio-ceramic material, frequently used in bone tissue engineering because of its ideal properties for bone tissue reparation [7]. Its bioactivity and biocompatibility ensure the osseointegration of the implants while keeping their mechanical properties [8].

At the time of tailoring the powder feedstock properties, it is necessary to know the needs for the technique in which it will be used. In the VAT photopolymerization category different ceramic particle characteristics have been demonstrated to affect the rheology and stability of the photocurable resins as well as the posterior debinding-sintering process [9]. Calcium phosphate particles with median particle size, x_{50}, in the range of 1 µm to 20 µm have been demonstrated to be suitable for the preparation of ceramic slurries avoiding dispersion and stabilization issues [10]. Indeed, these larger particles show an appropriate debinding-sintering behaviour evading the formation of cracks in the printed structures [11]. In the case of PBF techniques, a homogeneous powder bed is preferably achieved by flowable spherical particles with median particle size, x_{50}, between 10 and 100 µm [6]. Various material studies [12–16] have shown how the larger size and spherical shape improve the flowability of powders. A Hausner ratio lower than 1.25 (high flowability) should be obtained for the powder, which is recommended for PBF powders [17]. Thus the production of an optimal PBF powder feedstock should involve a previous process step like spray drying to shape the ceramic particles into spherical granules [18]. In a spray-drying process, it is known that the size of the primary particles present in the liquid suspension feedstock has an effect on the spray formation, morphology and internal structure of the produced granules. Several studies have demonstrated that higher heat transfer efficiency (resulting in the lowest moisture content of the granules) and more solid, spherical and dense granules are obtained when using ceramic primary particles having an x_{50} commonly in the range of 0.2 to 1.5 µm [19–22]. Thus, the tailoring of the particle size of powders is preferred before its utilisation as feedstock in a spray drying process.

In ceramic powders synthesis, the particle size distribution (PSD) of the as-synthetized powders rarely corresponds to process requirements and frequently a milling process is carried out to tune their PSD. In a spray drying process, a high concentration of solutes in the liquid (thus reducing the volume of liquid to evaporate) is desirable to increase dryer thermal efficiency [23]. However, the higher the concentration, the higher the viscosity of a slurry. If the viscosity is too high, it can cause the grinding media to be stuck on the surface of the grinding chamber affecting the comminution of the particles and the fineness of the obtained particles [24]. It could also bring handling difficulties during the spray drying process itself,

especially during the pumping and mixing of the slurry [25]. The successful spray drying of ceramic slurries having viscosities exceeding the 0.1 Pa.s has been reported previously [19].

The most important factors influencing a grinding process could be grouped into four main categories: formulation properties, operating parameters, operating mode of the mill, and mill geometry. There is a variety of works in the literature using different methods to perform the comminution of HA powders to reduce their particle size (Table 1).

Kwade et al. [26] pointed out the interest of having a large number of stress events and stress intensity in a stirred bead milling (SBM) process compared to those present in other ball-milling processes (mechanical, tumbling, vibrating, high energy ball mills…). The grindability of materials is not so easy to evaluate concerning ultrafine wet grinding processes, so according to the recent review analysis by Taylor et al. [27], the most practical method to define optimum conditions and specific energy requirements for a stirred bead milling process is to perform tests on a laboratory-scale mill.

The purpose of the present study is to produce HA-filled suspensions with properties meeting the requirements depending on the intended 3D printing technology:

For PBF techniques, before 3D printing, a preliminary spray drying process of the suspensions is preferred to obtain a suitable spherical and flowable HA powder. Thus, our objective will be to find the SBM conditions able to produce highly loaded (HA solid mass fraction, w_{HA}, equal or higher than 0.50) and stabilized HA-filled slurries for their use as spray drying process feedstock. The produced HA-filled suspensions should contain dispersed particles with an x_{50} in the range of 0.2 to 1.5 µm and show a viscosity lower than 0.1 Pa.s during the whole process.

The targeted HA-filled suspensions intended for the VAT photopolymerization technique should contain particles with a final x_{50} in the range of 1-20 µm.

By evaluating the effect of the formulation and operating parameters on the HA particles and HA-filled suspensions properties, the different combinations of formulation and process parameters producing HA-suspensions meeting our objectives will be found. Then, between this wide range of parameter combinations the optimal set of operating conditions for the process, thus meaning less energy consumption to reach the same targeted powders properties, will be determined.

Table 1. Report of previous bibliographic studies on the grinding of hydroxyapatite powders using different milling processes. N/A will be written when data was not indicated by the authors in the publication. (wp:w_{GM} = powder/grinding media weight ratio, x_{GM} = grinding media size, x_i= initial median particle size, x_f= final median particle size)

No.	Reference	Kind of mill, wet or dry conditions	Operating conditions	Crushed material, initial and final particle sizes
1	[28]	Agitator bead mill, wet	t = 1h, w_p:w_{GM} = N/A x_{GM} = 200 µm, zirconia beads, additive BYK 151	Si, Ti, HA (Alfa aesar), x_i = <325 mesh, x_f = 0.06 µm
2	[29]	Vibration ball milling, high-energy ball milling, dry	t = 1h, w_p:w_{GM} = 1:40 x_{GM} = N/A	HA (Wako, 99.5%), x_i = 250 µm, x_f = 0.04-0.07 µm
3	[30]	Ball milling, high-energy ball milling, dry	t = 1h, w_p:w_{GM} = N/A x_{GM} = N/A inert atmosphere,	Ti-20%HA, $x_f \approx$ 100 µm
4	[31]	Ball milling, dry	t = 3h w_p:w_{GM} = N/A x_{GM} = N/A	Synthesized (Wet method) then calcinated HA, $x_i \approx$ 30 µm, x_f = 5 µm
5	[32]	Agitator bead mill, moliNEx system (Netzsch), wet	t = N/A, w_p:w_{GM} = N/A x_{GM} = 1850 µm, zirconia beads, water & ethanol	Synthesized (Wet method) then calcinated HA, $x_i \approx$ 30 µm, x_f = 5 µm
6	[33]	Agitator bead mill, moliNEx system (Netzsch), wet	t = 8h, w_p:w_{GM} = N/A x_{GM} = 1850 µm, zirconia beads, ethanol/water	Synthesized (Wet method) then calcinated HA, $x_i \approx$ 30 µm, x_f = 1 µm (ethanol), x_f = 3-10 µm (water)
7	[34]	Shaker–mixer, tubular, dry	t = 3-6-24-96h, w_p:w_{GM} = N/A x_{GM} = 2000 µm, zirconia beads	Calcium phosphate powders, x_i = 3 µm, x_f = 2-1.5-0.75-0.3 µm resp.

2. Material and methods

2.1 Materials

The starting stoichiometric HA powder used during the present study was produced by Urodelia (SA Company, Saint-Lys, France) via wet precipitation process (product reference 206.93.003). More details about the synthesis procedure can be found in a previous work [35]. Ultrapure water served as a dispersion medium in the suspensions prepared in this work. It was obtained from the equipment "Purelab Ultra" of VWS (UK) Ltd. Its density was found to be 0.9952 g.cm^{-3} at 25˚C whereas its pH varied between 6.3 to 6.8 at 25˚C. A commercial dispersant Darvan® C (DC) was used for better stabilization of the prepared HA-filled slurries. It is an anionic polyelectrolyte (ammonium poly(methacrylate)) provided by R. T. Vanderbilt Co. (Norwalk, CT, USA) consisting of an aqueous solution with an active matter of 25 wt. %, 0.075 Pa.s of viscosity, a volumetric mass density of 1.11 ± 0.02 g.cm^{-3}, a pH of 7.5 to 9, and an average molecular weight of 10,000 to 16,000 Da, with a low tendency to foam.

2.2 Characterization of HA powders and HA-filled slurries

2.2.1 Particle size distributions and morphology

The PSD of the starting HA powder and HA-filled ground suspensions collected during the SBM process was determined by laser diffraction method (Mastersizer MS3000 Malvern Panalytical). A total number of replicate measurements (N) of five was performed for each suspension to calculate the resulting sample mean and sample standard deviation. Obtained values will be given as follows: mean ± standard deviation. Refractive indices of 1.632 and 1.330 were used for HA particles and water, respectively, and a particle absorption index of 0.1. For dry powders, a venturi pressure of 0.1 bar was used for the measurement. Figure 1a shows the PSD of the starting dry HA powder, which has an x_{50} of 21.20 ± 1.65 µm. Initial and ground powder morphologies were investigated by scanning electron microscopy (LEO 435 VP) equipped with a Ge detector (Imix-PC, PGT). In the case of the ground powders, the slurries were freeze-dried overnight and the resulting dry powder was metallized with a thin film of silver using a Scancoat Six sputter coater. Figure 1b shows the scanning electron microscope (SEM) micrographs of the starting powder, it is composed of aggregates of smaller particles with irregular shapes.

Powders specific surface areas were measured by nitrogen adsorption, following the Brunauer-Emmett-Teller (BET) method. A Micromeritics® TriStar II Plus 3.00 equipment was used for the physisorption analysis of powders (N=3, mean ± standard deviation). The specific surface area of the starting HA powder was found to be 0.77±0.02 $m^2.g^{-1}$. Ground powders were freeze-dried overnight before the measurement. All samples were previously degassed at 40ºC overnight in a VacPrep™ 061. The specific surface of ground powder was found to be 23.81±6.00 m^{-2}.g. This value will be used as a reference for the calculation of the dispersant concentration during the analyses.

The particle density of the starting HA powder was analysed by measuring the pressure change of helium in a calibrated volume in an AccuPyc 1330 Pycnometer (N=10, mean ± standard deviation). The obtained true density of the initial powder was 3.10±0.01 $g.cm^3$, close to the density of microscale hydroxyapatite powder reported in the literature (3.16 $g.cm^3$) [36].

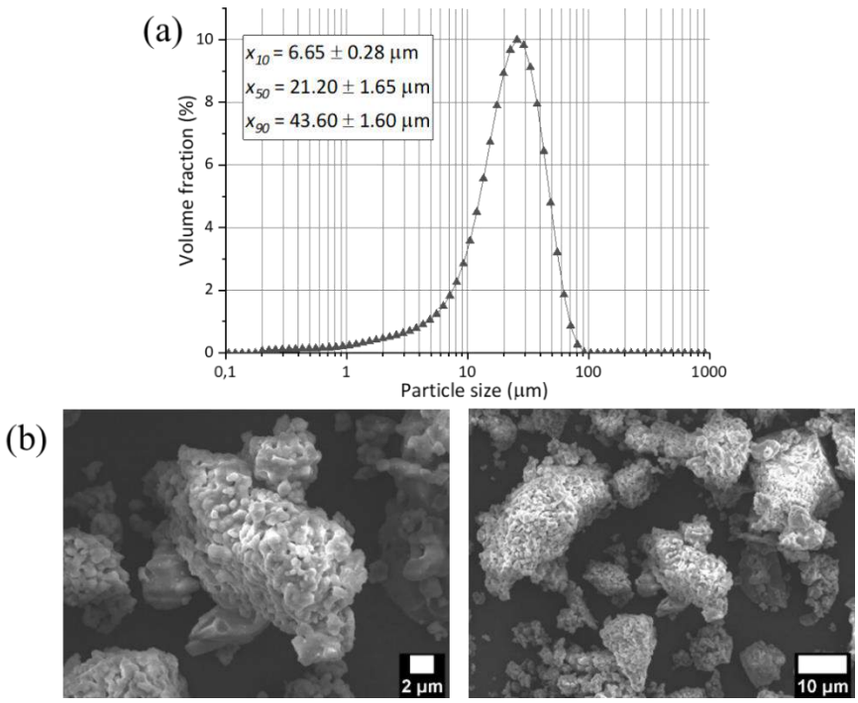

Figure 1. (a) PSD and (b) SEM micrographs of as-received hydroxyapatite powder.

2.2.2 Chemical and structural analyses

Fourier transform infrared spectroscopy (FTIR) analyses performed in a spectrometer Nicolet™ FTIR iS50 (Thermo Scientific™) were used to determine the chemical composition of the initial HA powder as well as the freeze-dried ground HA powder. KBr pellet method was used for the sample preparation.

X-ray diffraction (XRD) analyses of dry starting and ground HA powders were performed in a BRUKER's X-ray diffractometer D8 by using Cu Kα radiation (wavelength λ = 0.15406 nm) with a nickel filter at 40 kV and 40 mA. A step of 0.03º 2θ, and a time per step of 0.2 s were used to record the diffractograms in a 2θ range between 20º and 60º for the analysis and comparison of phase composition and crystallinity of powders.

Analysis of the species produced due to the milling chamber and grinding media wear (Fe, Zr, and Y) during the SBM process was carried out by inductively coupled plasma atomic emission spectrometry (ICP-AES, Ultima2R HORIBA). Slurry aliquots collected during and after the SBM process were freeze-dried to obtain a dried powder. One gram of each sample was accurately weighed and introduced in a mineralization tube, then dissolved by acid digestion, adding 12 ml HNO_3 65%, 3 ml HCl 36.5-38%, and 2 ml ultrapure water, and then heated at 95ºC during 1h. After cooling, ultrapure water was added to all solutions until a total of 50 ml before being injected into the plasma. One of the three SBM runs analysed (Table 2-Run 2) was performed and analysed three times to obtain the mean value and the standard error of the measurement.

2.2.3 HA-filled slurries rheological and electrophoretic measurements

A TA Instruments AR2000 rheometer equipped with a temperature control Peltier plate was used for the rheological analysis of the HA-filled suspensions. A 40mm crosshatched parallel plates system and a gap between plates of 1300 µm were chosen as configuration. A conditioning step was applied before the measurements at a shear rate of 200 s^{-1} during 30.0 s and an equilibration time of 30.0 s.

The geometry with roughened surfaces allowed us to prevent wall slip effects. In addition, the gap of 1300 µm was chosen for being at least 10 times higher than the largest particle size understudy, which corresponds to an x_{50} of 100 µm in the starting HA powder, thus also avoiding wall effects (slip) [37]. However, one practical limitation of this geometry-gap configuration was the lowering of the highest shear rate limit that some samples can reach before being ejected out of the gap due to centrifugal forces. For this reason, the suspensions were compared in an equal shear rate range of 10-100 s^{-1}. To produce the flow curve of each sample a constant plate temperature of 25ºC and an increasing shear rate (steady-step flow step) was used taking ten points by decade. At least three measurements of each slurry were performed to obtain the standard error of the mean.

Even though prepared suspensions are intended for a posterior spray drying process with typically high shear rates (10^5 to 10^6 s^{-1}), the step of the process that could bring more handling problems (higher viscosity) is during the pumping and mixing of the suspensions, which produce lower shear rate (10 to 10^3 s^{-1}) [38].

The influence of different w_{HA} and DC dosages on the rheological behaviour of ceramic suspensions was investigated. HA slurries were prepared by gradually pouring the corresponding amounts of DC and starting HA powder (before milling) in water. Samples were stirred at 600 rpm for 10 min to ensure the homogeneity of the suspensions before the rheological analyses.

Several rheological mathematical models are usually applied to rheograms to transform them into the information of the steady shear fluid rheological behaviour. In this work, data were fitted to the Power Law model (Equation 1), which is a two-parameter rheological model describing a pseudoplastic fluid, i.e., a fluid whose viscosity decreases as the shear rate increases. Power-law fluids can be described mathematically as follows:

$$\tau = K(\dot{\gamma})^n \qquad (1)$$

Where τ [Pa] is the shear stress, $\dot{\gamma}$ [s^{-1}] the shear rate, K [$Pa.s^n$] is the consistency index, and n [-] is the flow behaviour index. Data analysis, curve fitting, and calculation of parameter values were performed using OriginLab 2016 software.

The stabilization of a suspension may be evaluated by the zeta potential of the suspended particles. The potential refers to the electrical potential difference between the particle surface and the liquid beyond the charge cloud of ions. A zeta potential value outside the limits of −30 mV to +30 mV is generally considered to have sufficient repulsive force to attain better physical suspension stability. The electrophoretic mobility of the HA particles in slurries containing different DC dispersant concentrations was determined in a Zetasizer Nano-ZS (Malvern Panalytical) at 25ºC. Different samples of 20 ml at w_{HA} = 0.20 were prepared by adding the corresponding HA powder amount and different dosages of DC (active component) from 0 to 2.100 $mg.m^{-2}$ (to the ceramic powder surface) before being stirred for 2 hours. Samples were diluted before the analysis to avoid the multiple diffusion phenomena and adjusted to a solids concentration of 4 $mg.mL^{-1}$. Zeta potential was obtained from electrophoretic mobility measurements. Each zeta potential value reported was calculated from the mean of five measurements as well as the standard error.

The pH of the water and HA-filled suspensions was measured by Hach Sension+ PH3 Basic laboratory pH meter, which was calibrated with standards pH 4, 7, and 10 each time before the repetition of at least five different measurements. The pH of an HA-filled suspension at w_{HA} = 0.50 was found to be 9.5±0.2 at 25ºC due to the basic properties of HA particles. Padilla et al.[39] already offered a study of the influence of the pH and dispersants on the zeta potential of HA particles. They found that the most constant and highest zeta potential values were always obtained at pH ≥ 8. For this reason, no further analyses neither alteration of the pH of the HA-filled suspensions was followed during our study.

2.3 Stirred bead milling (SBM) experiments

Several SBM runs (Table 2) were carried out in commercial equipment Labstar manufactured by NETZSCH (Germany) to reduce the size of the HA particles present in the slurries. For each experiment, firstly, the suspension was prepared in a stirrer tank before being pumped to the milling chamber. The corresponding dispersant agent DC volume was added to water followed by the addition of the weighted HA powder amount. The total batch size was approximately 2 kg for each of the runs. All dispersions were agitated for 10 minutes at 600 rpm at 25ºC before starting the pumping and grinding process. The duration of the run and the DC and HA amounts used at each run are indicated in Table 2.

*Table 2. List of experiments performed, including the experimental conditions, final specific energy, particle size obtained at the end, and purpose of the run. * Run was performed three times for the repeatability study.*

Run no.	x_{GM} [mm]	φ_{GM} [-]	V_r [m.s^{-1}]	w_{HA} [-]	DC dosage [mg.m^{-2}]	Grinding time [min]	Ending E_m [kJ.kg^{-1}]	x_{10} [µm]	x_{50} [µm]	x_{90} [µm]	Operating condition studied
1	0.6	0.85	7.7	0.20	0	120	2880	0.62 ± 0.04	1.70 ± 0.16	3.74 ± 0.76	DC dosage
2*	0.4	0.75	5.7	0.20	2.1	120	5760	0.27 ± 0.01	0.42 ± 0.01	0.62 ± 0.01	V_r
3	0.4	0.75	3.8	0.20	2.1	135	3240	0.39 ± 0.00	0.69 ± 0.03	2.63 ± 0.49	
4	0.4	0.75	11.5	0.20	2.1	15	1800	0.41 ± 0.00	0.59 ± 0.00	0.86 ± 0.00	
5	1.0	0.85	7.7	0.10	2.1	60	2571	0.47 ± 0.05	0.86 ± 0.02	2.61 ± 0.17	x_{GM}
6	0.4	0.85	7.7	0.10	2.1	60	1600	0.40 ± 0.01	0.61 ± 0.02	1.02 ± 0.07	
7	0.4	0.75	11.5	0.10	2.1	7	3360	0.34 ± 0.03	0.54 ± 0.05	1.36 ± 0.13	w_{HA}
8	0.4	0.75	11.5	0.30	2.1	15	1714	0.48 ± 0.00	0.77 ± 0.02	1.85 ± 0.12	
9	0.4	0.75	11.5	0.50	2.1	15	720	0.47 ± 0.02	0.89 ± 0.04	2.00 ± 0.15	
10	0.4	0.75	5.7	0.50	2.1	120	654	0.46 ± 0.00	0.88 ± 0.02	2.06 ± 0.04	PSD evolution with grinding time
11	0.6	0.85	7.7	0.30	2.1	60	720	0.44 ± 0.01	0.94 ± 0.10	2.35 ± 0.37	

A detailed scheme of the experimental setup is provided in previous work [40]. This SBM Labstar equipment is a laboratory-scale model with a grinding chamber volume of 0.62 l. The horizontal configuration of this circulation Zeta® grinding system ensures uniform exposure of the product through the media-intensive grinding zone within the mill as well as a high product throughput rate. A pin grinding system, of 7.2 cm in diameter, as a media mill stirrer, provides a high grinding intensity while a multi-zone cooling system prevents overheating of the product. The equipment has a stirrer speed (V_r) limit range of 1000-4000 rpm corresponding to a tip stirrer speed range of 3.8-17.3 m.s^{-1}. The bead wear was reduced by using high resistant Yttrium Stabilized Zirconia 95% (YSZ, ZrO2) micro grinding beads (Zirmil® Y from WAB-Group) (ρ_{GM} = 6020 kg.m^{-3}, bulk density: 3700 kg.m^{-3}). Different grinding media sizes (x_{GM}) ranging from 400 to 1000 µm were used to study their effect on the final product quality. The nominal and laser diffraction measured xGM values for the grinding media used are described in Table 3. Refractive and absorption indices of 2.148 and 1.000 respectively were used for the measurements.

Table 3. Vendor provided nominal and measured grinding media sizes. The measured values show the average and the standard deviation obtained from three measurements.

Nominal x_{GM} value *(mm)*	Measured x_{10} value *(mm)*	*Measured* x_{50} value *(mm)*	*Measured* x_{90} value *(mm)*
0.35-0.45 (0.4)	0.32 ± 0.00	0.39 ± 0.00	0.45 ± 0.00
0.6	0.55 ± 0.00	0.71 ± 0.00	0.93 ± 0.00
1.0	0.76 ± 0.00	1.15 ± 0.00	1.85 ± 0.03

Once comminution has occurred in the grinding chamber, the dispersion leaves through a steel (Cr-Ni-steel) separating cartridge of 100 µm installed at the outlet of the grinding chamber to separate the product returning to the feeding tank and keep the beads inside the chamber. In this way, the circulation mode (multi-passes) was selected as the operating mode. The product flow rate was kept constant at 8.8 x 10^{-6} $m^3.s^{-1}$ and its analysis was kept out of the scope since it was already demonstrated that it does not have a significant effect on the product quality [41].

According to the literature [42,43], the specific energy (E_m) is more relevant than the grinding time to quantify the effect of operating parameters in SBM processes to reach a certain product fineness. E_m is the ratio of the total energy supplied to the grinding chamber to the mass of solid processed. The determination of E_m for a demanded product quality also depends among others on the mode of the milling operation [44]. Details on its calculation can be found in a previous experimental study [41].

3. Results and discussion

In this section, the influence of different factors on the final suspension quality and the particle dispersion stability is analysed. In between the groups of factors already discussed in the Introduction of this article, we focused our work on the formulation of the initial suspensions (Section 3.1) and the operating parameters of the mill (Section 3.2). The section dealing with the formulation of the suspensions refers to the study of the impact of w_{HA} and dispersant Darvan C dosage on the properties of the initial suspension before being treated by SBM. The effect of the milling operating parameters, including the stirrer speed, grinding media size, and solid concentration, is then discussed in (Section 3.2) analysing the particle size distribution during the SBM process. Finally, the comparison of the chemical and structural analysis of the product before and after been treated in the milling process is detailed in Section 3.3.

3.1 Initial suspension formulation

3.1.1 Influence of solid mass fraction (w_{HA}) on suspension viscosity

Since the production of an optimal fluid feedstock for a subsequent spray drying process was within the scope of this work, it was important to find the HA concentration that gives a balance between process effectiveness and suspension stability for optimal performance in a spray drying process as well as in an SBM process.

Figure 2a shows the shear stress versus shear rate diagram of the initial suspensions at different w_{HA}. The best-fit parameter values of these rheograms can be observed in Table 4. Suspensions from w_{HA} = 0.40 to w_{HA} = 0.50 exhibited a Newtonian behaviour over the whole shear rate range, also confirmed by the flow behaviour indexes very close to 1, whereas the flow behaviour of the slurry at w_{HA} = 0.55 changes to a pseudoplastic (shear-thinning) behaviour for the measured shear rate range. It is important to note that the coefficient of determination (R^2) indicates that the Power Law model fits the measurements well, better for lower HA concentrations. Suspensions with w_{HA} higher than 0.55 showed handling difficulties and adverse phenomena produced by the suspension instability, such as sedimentation. For this reason, it was not possible to perform their measurement.

Figure 2b shows the viscosity of the suspension at different w_{HA}. It can be observed that the higher the solid loading, the higher the slurry viscosity is, with a slight increase between w_{HA} = 0.40 and w_{HA} = 0.50 compared with the pronounced rise observed at w_{HA} = 0.55. Within a similar volume, the high solids content increases the resistance to gradual deformation by shear stress due to the higher number of entities with a reduced space to move. The suspension at w_{HA} = 0.50 showed the most suitable behaviour as a highly loaded suspension in terms of experimental handling for the SBM process and the subsequent spray drying process. This concentration was kept constant for the rest of the work.

Additionally, a shear-thickening behaviour is observed at a high shear rate for the samples with higher concentrations. (This behaviour will be also observed in the next rheological analyses although our explanation will be only offered in this section.) This phenomenon was already observed by Bergström [45] in his study on the rheological behaviour of concentrated ceramic suspensions. He observed that concentrated aqueous silicon carbide (SiC) suspensions showed a strong, sometimes discontinuous, shear thickening. He attributed this behaviour to a possible hydrodynamic clustering, where anisotropic particles will be strongly affected by flow changing the suspension structure. Thus, altering the resistance to flow at some critical shear rate. This shear thickening behaviour seemed to increase with the suspension concentration. This transition to shear-thickening is sample-specific and other factors like particle size (distribution) and particle shape can control it [46].

Table 4. Parameters fitted to Power Law model for suspensions with different hydroxyapatite solid mass fraction before milling and in absence of dispersant in steady-state conditions during the shear stress-shear rate test (imposed shear range 10-100 s^{-1}).

		Solid mass fraction (w_{HA})			
Sample		0.40	0.45	0.50	0.55
Consistency index K (10^{-3} Pa.s^n)	Value	8	9	10	16
	Standard Error	0.30	0.20	0.50	3.00
Flow index n	Value	1.02	0.97	0.98	0.92
	Standard Error	0.01	0.01	0.01	0.04
R^2		0.99	0.99	0.99	0.98

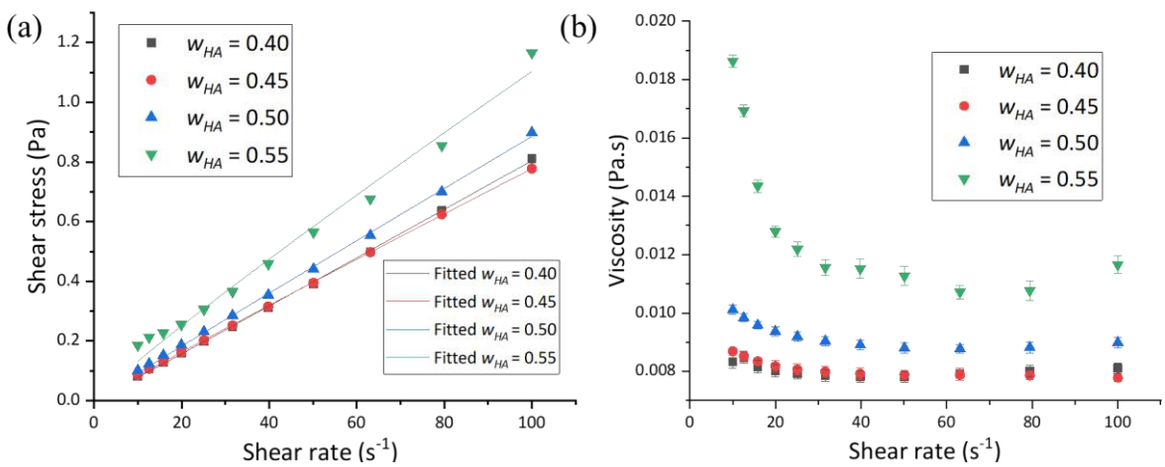

Figure 2. (a) The flow data for several suspensions containing different solid mass concentrations fitted to the Power Law model and (b) viscosity-shear rate curves.

3.1.2 Dispersing agent content

The amount of dispersing agent DC needed to obtain well-stabilized suspensions was determined through different preliminary analyses.

First, the zeta-potential evolution of the initial HA particles in an aqueous suspension was analysed. The changes in the zeta potential at different DC concentrations can be observed in Figure 3a. In the range studied, a concentration ≥ 2.100 mg.m^{-2} of DC the zeta-potential value exceeded the targeted limit of -30 mV, thus indicating that there is a sufficient number of negatively charged particles that could trigger their repulsion and prevent the flocculation.

Secondly, the influence of the dispersant DC concentration on the x_{50} of the HA particles in a ground suspension (Table 2– run 1) at w_{HA} = 0.20 was evaluated. The evolution of the x_{50} of the HA particles at different DC concentrations is shown in Figure 3b. For concentrations higher than 0.84 mg.m^{-2} of DC the x_{50} of grounded particles was reduced until enter in our targeted range of particle size values (0.2 µm < x_{50}

< 1.5 µm) at a DC dosage of 2.100 mg.m^{-2}. An initial increase of the particle size is noticed at low dispersant concentrations, which leads us to hypothesize that a particle-binding bridge process between the HA particles is taking place due to an insufficient dispersant covering degree. Then, by increasing the dispersant concentration, the coverage is increased and the repulsion of the particles could be triggered. The third study was the evaluation of the sedimentation behaviour of these suspensions, which contain different DC dosages. The suspensions were magnetically stirred for 10 min and different aliquots of 10 ml of suspension were poured on nine different test tubes. To evaluate the sedimentation behaviour, photographs of the tubes after 48 hours and after 4 weeks were taken for comparison (Figure 3c). It can be observed how at very low DC concentrations the sedimentation behaviour shows minor changes compared with the absence of dispersant. Instead, for the concentration range from 0.042 to 0.210 mg.m^{-2} faster sedimentation is observed and at the end of the experiment, the final sedimentary volumes of these samples were more important than for the rest of the tubes. It is indicative of the dispersion state, when the interparticle forces are highly attractive, large and loose-packed flocs are formed resulting in a more important sedimentary volume and not dense [24]. From a DC concentration of 0.420 mg.m^{-2} the dispersant starts triggering the deflocculation of the particles showing a slower settling velocity and producing a minor but dense sedimentary volume.

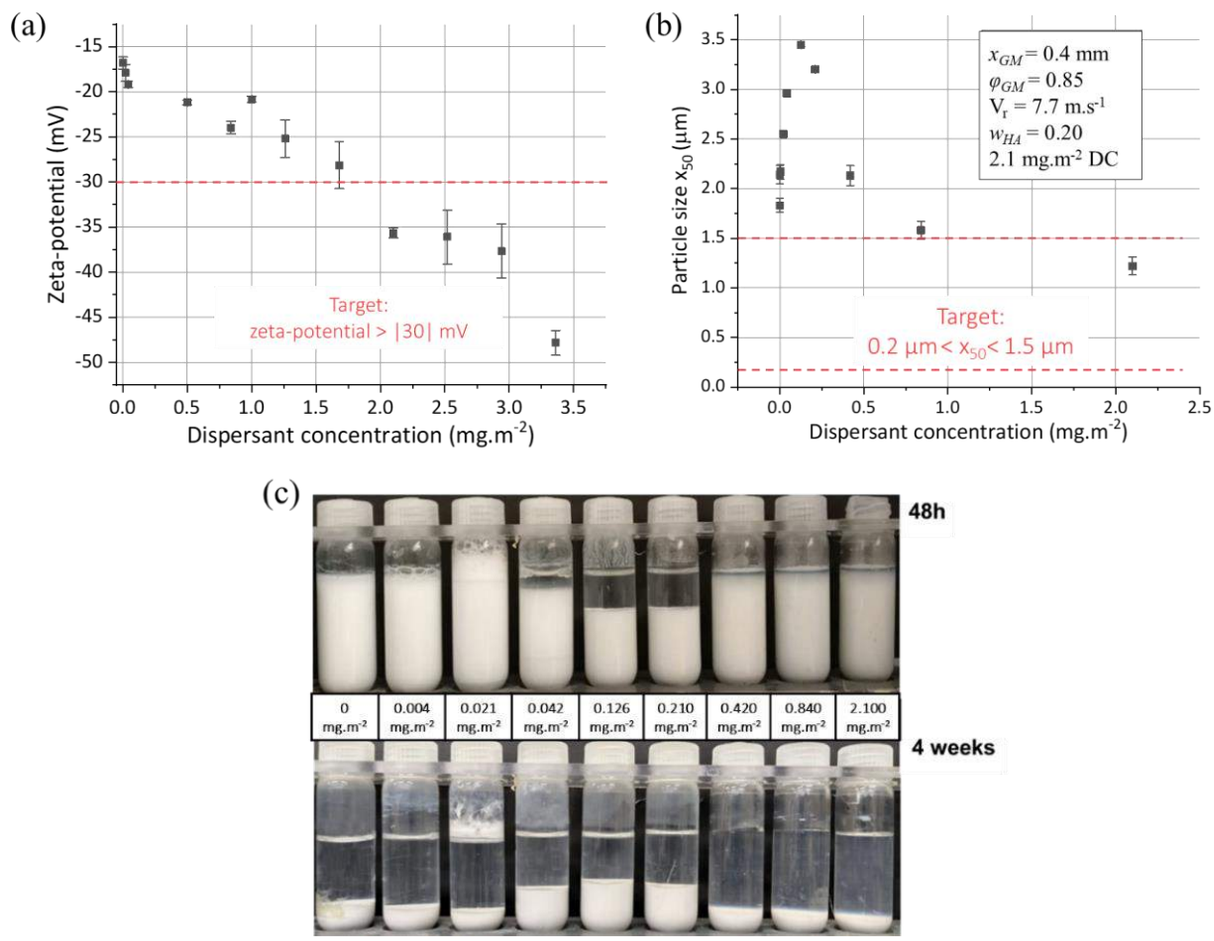

Figure 3. Effect of DC concentration on the (a) suspended particles zeta potential, (b) powder median size (x_{50}) and (c) the settlement after 48 hours and after 4 weeks of a slurry ground at E_m = 2880 kJ.kg^{-1} with a HA solid mass fraction of 0.20.

The effect of the DC dosage on the rheological behaviour of the suspensions containing initial HA powder (w_{HA} = 0.50) was evaluated. The rheograms obtained together with the fitting to the Power Law model can be observed in Figure 4a. The best-fit parameter values of these rheograms can be found in Table 4. It was observed that in presence of dispersant, the suspensions show a Newtonian behaviour over the shear rate ranging from 10 s^{-1} to 100 s^{-1}, with flow index values close to 1. It is less evident for the sample without dispersant, having a lower flow index value (0.96).

Figure 4b shows the flow curves obtained for the samples containing different amounts of DC. The first decrease in viscosity is observed at low DC concentration (0.42 $mg.m^{-2}$), then the viscosity tends to increase gradually as the DC concentration is increased beyond 0.42 to 2.10 $mg.m^{-2}$. This phenomenon was already studied by Khan et al. [47] in their work focused on the mechanism followed by Darvan C as a ceramic dispersant. They explained this behaviour as a result of the aggregates in the suspension breaking down into smaller flow units. By adsorption isotherm measurements, they could confirm that the DC concentration giving the lowest viscosity of their alumina suspensions corresponds to all the dispersant molecules being adsorbed on the particles. Then, when more dispersant is added, the attractive interactions between the particles are reduced and gradually the interactions become repulsive. It is not easy to find a clear explanation for the mode of stabilization that could be due to steric interactions between the adsorbed DC layers and/or to electrostatic interactions, due to an increase in the surface charge.

Additionally, the viscosity of the commercial DC (aqueous solution) was studied showing a higher viscosity than pure water ($7.5*10^{-2}$ Pa.s at 25ºC) and the increase of viscosity at shear rate 100 s^{-1} with the concentration in a Darvan C-Water system was found to follow (R^2 = 0.98) the equation below:

$$\ln \eta = -5.03 + 0.12\, C_{DC} \quad (2)$$

where η (Pa.s) is the viscosity of the system and C_{DC} ($mg.m^{-2}$) the DC concentration in an aqueous solution.

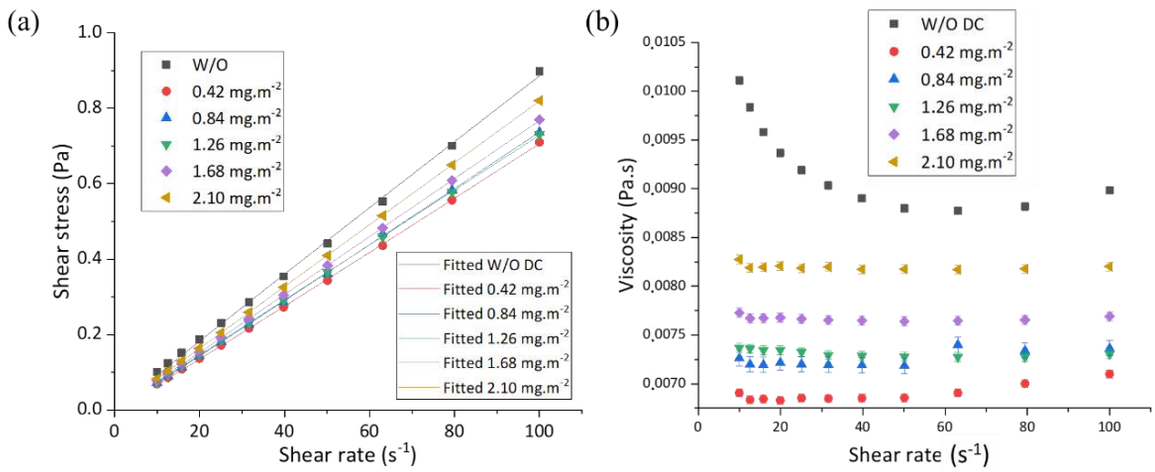

Figure 4. (a) The flow data for several suspensions at w_{HA} = 0.50 before grinding process containing different amounts of dispersant DC fitted to the Power Law model and (b) viscosity-shear rate curves.

Table 5. Parameters fitted to Power Law model for w_{HA}= 0.50 hydroxyapatite suspensions with different Darvan C concentrations before milling in steady-state conditions during the shear stress-shear rate test (shear range 10-100 s^{-1}).

		Darvan C concentration ($mg.m^{-2}$)					
Sample		0	0.42	0.84	1.26	1.68	2.10
Consistency index K (10^{-3} $Pa.s^n$)	Value	9.64	6.20	6.81	7.33	7.57	8.15
	Standard Error	0.50	0.14	0.15	0.05	0.05	0.04
Flow index n	Value	0.96	1.02	1.01	1.00	1.00	1.00
	Standard Error	0.01	0.01	0.01	0.00	0.00	0.00
R^2		0.99	0.99	0.99	0.99	0.99	0.99

3.2 Effect of grinding operating parameters

Firstly, the repeatability of the process for the particle size of the product obtained can be noted in Figure S1 (supplementary material) where the mean value and standard error for the same run (Table 2 – runs 2) performed three times under identical conditions are reported.

In this section, grinding operating parameters (stirrer speed, grinding media size and solid concentration) have been investigated to find the combination of parameters able to produce suspensions fulfilling the as mentioned targeted characteristics (particle size, viscosity…) depending on the application (spray drying and VAT photopolymerization processes). The resulting PSD and the required specific energy input will be examined for their evaluation. To do not overextend the present paper the study of the impact of the rest of the operational parameters was relegated outside of the scope. An example is the grinding media filling degree (φ_{GM}) which was settled to values between 75-85% of the total volume of the chamber

for the experiments performed. It has been recently demonstrated by Guo et al [48], using a vertical stirred media mill, that the PSD uniformity is generally independent on the φ_{GM}, although a higher φ_{GM} produces finer particle size at the same specific energy input. The increase of the grinding media filling rate increases in turn the collision frequency leading to a higher frequency of impacts on the material during the ball-ball collision [49].

3.2.1 Stirrer speed (V_r)

The rotation speed of a stirred mill is considered one of the most important factors affecting the grinding performance. It affects the collision intensity between beads, and hence the interactions with material particles to be ground. To study the influence of the stirrer speed on the SBM process results runs with different stirrer speeds (V_r = 3.8, V_r = 5.7, and V_r = 11.5 m.s^{-1}) were performed (Table 2 – runs 2, 3, 4) keeping the rest of the conditions identical between runs. These V_r correspond to 1000, 1500, and 3000 rpm respectively. Figure 5a shows the evolution of the particle means size versus the grinding time. Increasing the stirrer speed increases the breakage kinetics and smaller particle size is reached for the same grinding time. This phenomenon agrees well with those reported on the impact of stirrer speed for YSZ beads [50]. Indicating that increasing stirrer speed results in a faster apparent breakage rate. The increase in stirrer speed increases the stress intensity in the mill, thus influencing the interaction between beads and suspension, being an important operating variable in the stirred mill operation. The stirrer speed increases the stress intensities which eventually increases the breakage kinetic due to the high probability of bead to particle collisions [50–52].

Figure 5a shows the relation between the particle size x_{50} and the specific energy E_m at different stirring speeds V_r. If we compare both graphs the difference of amplitude between curves is significant. It indicates that higher stirrer speed consumes lower energy to reduce the desired product particle size. This observation differs from the observed in literature where the energy consumption increases at higher stirrer speed to reach a defined particle size. Indeed, for constant specific energies, the product becomes finer with the speed. It could be explained by the nature of the initial powder, which is composed of aggregates made of smaller particles [53]. The HA powder used in our study could then be defined as a weak material because of its capability to be ground [54]. When a certain value of specific energy is surpassed, the aggregates break rapidly into particles with a much smaller size than the initial aggregates. That could explain the verticality of the curves reaching relatively fast the final plateau in which adding higher energies do not decrease the particle size. Increasing the stirrer speed, the number of collisions and the stress intensity both increases however for weak materials the milling process depends more of the collision probability than the energy needed to break particles. The supplied energy needs to be at least equal to the required for the breakage of the aggregates. In addition, the operating time should be long enough for all the aggregates have the opportunity to be bead-stressed or on the other hand the collision probability should be boosted by increasing the stirrer speed [55].

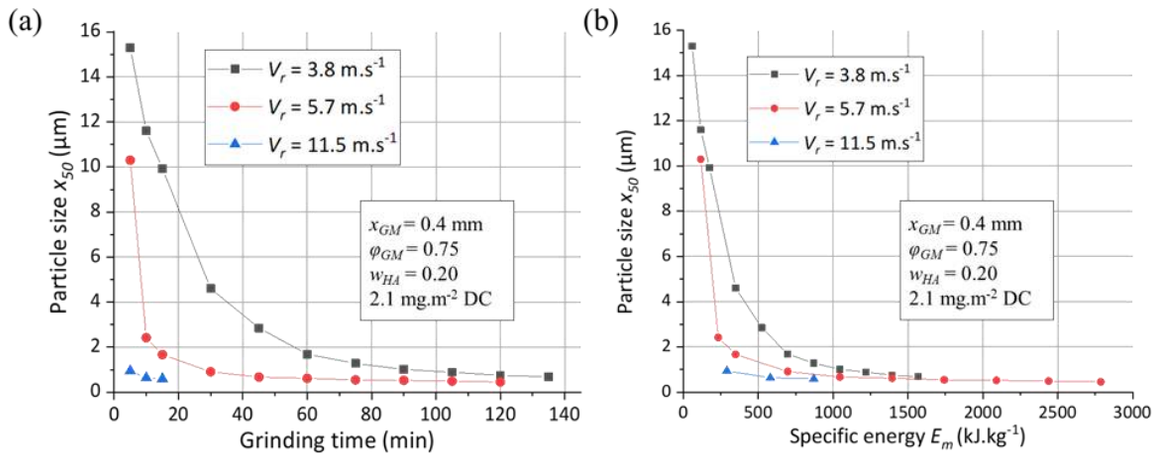

Figure 5. Influence of stirrer speed on SBM product quality. a) Particle mean size versus grinding time. b) Particle mean size versus specific energy.

A comparison of the whole size distribution at similar specific energies for the runs performed at different stirred speeds is shown in Figure 6. At 660 kJ.kg^{-1} (Figure 6a), it can be observed how a contraction of the size distribution is more rapidly reached by increasing the agitation speed. For this E_m *value*, the PSDs of the suspensions show different grinding stages, being the grinding of suspensions from V_r = 3.8 m.s^{-1} and V_r = 5.7 m.s^{-1} still incomplete. It is not until higher specific energies (Figure 6b) that the suspensions at lower stirrer speeds experience a PSD transformation from bimodal to unimodal to finally all suspensions have nearly similar PSDs reaching the complete grinding stage. The obtention of finer particle size at the same specific energy input supports the importance of using a higher stirrer speed for a more efficient and time-effective milling process. A similar tendency was observed in suspensions at w_{HA} = 0.50.

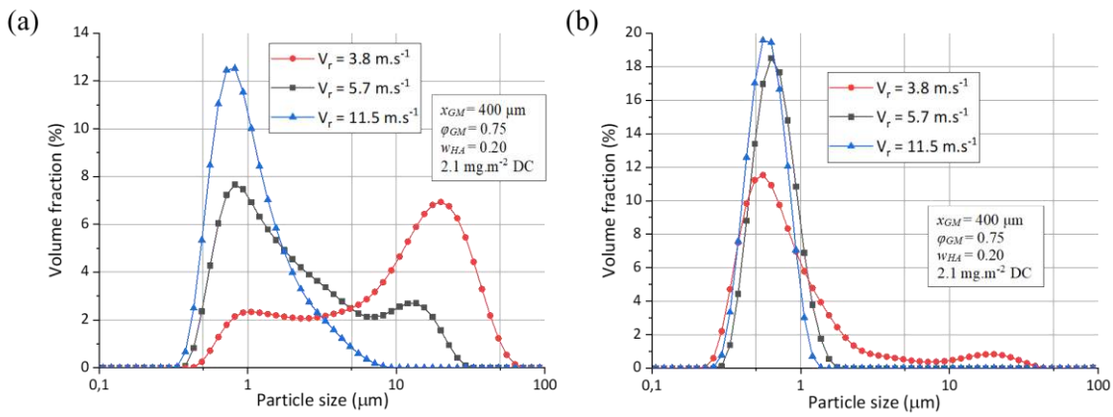

Figure 6. (a) Effect of stirrer speed on the PSD of ground suspensions at 660 kJ.kg^{-1}. (b) PSD of ground suspensions at the moment of obtaining uniform and unimodal distribution, equivalent to 3240 kJ.kg^{-1}, 2160 kJ.kg^{-1}, and 1800 kJ.kg^{-1} for V_r = 3.8 m.s^{-1}, V_r = 5.7 m.s^{-1}, and V_r = 11.5 m.s^{-1} respectively.

3.2.2 Grinding media size (x_{GM})

There are different factors to consider at the time of choosing the right type of grinding media like size, beads filling degree, contamination, cost, shape… depending on the application. The diameter of the grinding media will define the efficacy of the milling process since it can output diverse PSDs of the material supplied to the mill for the same duration. Tanaka [56] derived an empirical equation to calculate the optimum diameter in ultrafine wet milling processes under given conditions (i.e. particle size and strength and ball or bead density and hitting speed). Since the inherent strength of the material is not precisely known, these indications cannot be easily applied but it gives one idea of the influence of bead size in a wet stirred milling process.

Two different mean grinding media sizes (x_{GM} = 1000 µm and x_{GM} = 400 µm) were used on different runs (Table 2 – runs 5, 6) of the SBM process by keeping the rest of the operational parameters identical and the median particle sizes and PSDs obtained are compared in Figure 7. For a given specific energy, faster production of finer particle size and a monomodal distribution occurs when using x_{GM} = 400 µm, thus yielding a different product quality. A similar decrease of the median particle size and the width of the size distribution decreasing the bead size was also reported on TiO_2 dispersion [57] while a quite different effect was observed on the grinding of talc [54]. For this lamellar material, the minimum fineness was reached for intermediate bead size, and an increase of the width of the distribution was obtained using the largest beads [54]. More recently, Li et al. [58] concluded that optimal bead size decreased upon an increase in the stirrer speed. It was explained by the two counter-acting effects of bead size: more bead-bead collisions (more stressing events) with less energy/force (lower stress intensity) upon a decrease in bead size. Strobel et al. [59] also observed that the bead size affects the flow pattern of the suspension through the milling chamber. They found that for small bead size (0.5 mm in their study), different milling bead packing densities arise in the mill chamber resulting in different flow rates through those zones. The suspension evades regions with high bead concentrations inside the mill. It results in a large fraction of non-stressed particles and at the same time many impacts on stressed particles which could help to explain the multimodal profile of the PSDs.

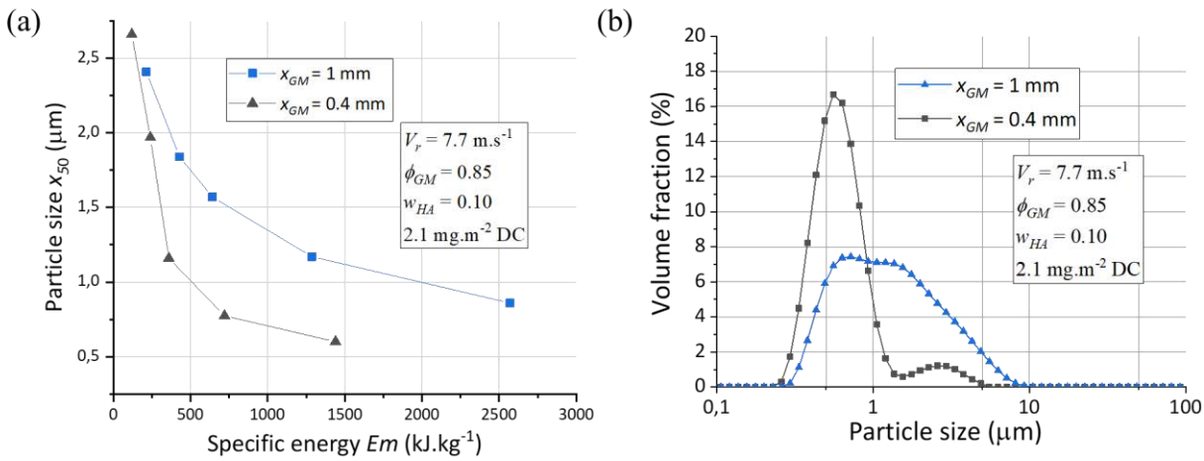

Figure 7. Effect of the (YSZ, ZrO_2) grinding media size on the (a) particle median size and (b) PSD (x_{GM} = 1 mm and 0.4 mm, at 1350 kJ.kg^{-1}) of a hydroxyapatite slurry during the stirred bead milling process. Each distribution is the average of five measurements on the same sample.

3.2.3 Solid mass fraction (w_{HA})

Suspensions solid mass fraction can also influence the evolution of the PSD during a milling process. A comparison of the effect of the suspension solid concentration on the quality of the product during the milling process is shown in Figure 8. To analyse this effect, runs (Table 2 – runs 7, 8, 9) with different concentrations (w_{HA} = 0.10, w_{HA} = 0.30, and w_{HA} = 0.50) were performed keeping the rest of the conditions (V_r, x_{GM}, DC dosage…) identical between runs. This w_{HA} range (w_{HA} = 0.10 to w_{HA} = 0.50) comprises all concentrations used during the runs carried out for the present study.

Figure 8a shows the evolution of the particle mean size (x_{50}) versus the grinding time. It is observed that for the same process duration finer mean particle size is obtained when the solid concentration is lower. However, when comparing the particle mean size versus the specific energy, the effect of the solid concentration can be truly followed. It can be deducted that for an equal specific energy input spent, the higher is the load of the suspension the finer is the mean particle size obtained. It indicates that a higher process energy efficiency is reached in highly loaded suspensions. Similar results were observed on the dispersion of TiO_2 [57] but an opposite effect was reported on other materials [40,59] for which an inverse proportion between milling efficiency (capturing efficiency of the product particles by milling beads collisions) and suspension viscosity was observed. In the present study, such an effect was not noticeable. It could be explained by the smaller difference magnitude between suspensions viscosities (cf. next section) within the w_{HA} range in our work compared with the above-mentioned studies.

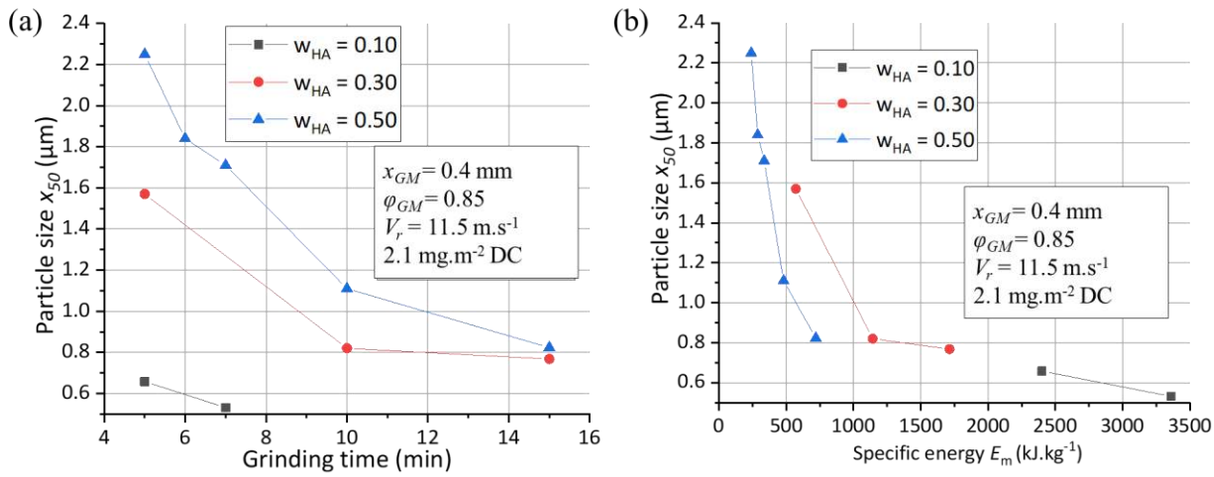

Figure 8. Influence of w_{HA} on SBM product quality. a) Particle mean size versus grinding time. b) Particle mean size versus specific energy.

We could then conclude that the importance of the control of the suspension formulation (Darvan C dosage, and HA solid mass fraction) and the operational conditions of the mill (stirrer speed, grinding media size, ...) has been proved through the studies performed in Sections 3.1 and 3.2. In addition, we were able to adjust these conditions to tune the final HA product quality depending on the application of the resultant suspensions. Highly loaded stabilized suspensions with finely ground HA particles in an x_{50} range of 0.2-1.5 µm could be prepared for its use as liquid feedstock in a spray drying process. Alternatively, the production of suspensions containing HA powder with a particle size in the micron range (x_{50} = 1-20 µm) was also feasible. In this case, additional drying steps should be carried out for the use of the dry powder in VAT photopolymerization. Other authors have studied the use of other milling methods such as the planetary mill and ball mill for the grinding of particles suspended in photocurable resins with milling times that can reach several days of duration [60]. An additional step in the research of industrial photocurable ceramic suspension production would be their direct milling in an SBM process thus shortening, even more, the time needed for their preparation. However, special care should be given to the viscosity of the suspensions to make it feasible.

A wide range of operating parameters gave a product meeting the targeted characteristics; however, it was demonstrated that by using a faster V_r, smaller x_{GM}, and higher w_{HA} is possible to reduce the energy consumption in the process reaching a higher energy efficiency.

3.3 Characterization of slurries and powder products

In this section, the HA product chemic composition is analysed before and after the SBM process. These analyses become relevant since during a milling process is possible to induce chemical structural modifications on the HA mineral phase that could significantly compromise the integrity, function, and aesthetic quality of the product. The rheology of the ground suspensions concerning the milling time is also analysed as well as its PSD evolution during the process since as mentioned in the introduction, a too high increase of the viscosity (> 0.1 Pa.s) of the suspensions could affect negatively the process.

3.3.1 Physico-chemical properties of ground powders

To discard any kind of alteration of the physico-chemical properties of the powder after the SBM process different analyses were performed. Figure 9 shows the XRD and FTIR spectra of ground powders (Table 2 – runs 6, 10 respectively) to the initial powder. After the experiment of the SBM process, the suspensions were freeze-dried and the powder obtained was submitted to the KBr pellet method in the case of FTIR analyses. For XRD sample preparation the dry powder was manually crushed using a mortar and pestle.

Through the XRD analysis (Figure 9a) of the powders, the maintenance of the calcium phosphate phase (stoichiometric hydroxyapatite (JCPDS 00-009-0432)) and crystallinity state can be verified as unaltered, as well as no secondary phases were detected [7]. The FTIR analysis (Figure 9b) also confirmed the absence of relevant changes in the chemical composition of the HA powder after the SBM process. The vibration bands corresponding to PO_4 are visible at 1092 cm^{-1}, 1040 cm^{-1}, 962 cm^{-1}, 601 cm^{-1}, 575 cm^{-1}, 561 cm^{-1}, as well as the band belonging to OH^- at 650 cm^{-1} 3600 cm^{-1} [7,61]. The band at 1400 cm^{-1} was attributed to the vibrational band of the dispersant DC [62]. Thus pointing out the need for filtering and washing steps of the particles before drying if the powder is intended for VAT photopolymerization. Whether or not the presence of DC affects the posterior spray-drying step will be discussed in chapter IV although it is expected that it will thermally degrade during the process.

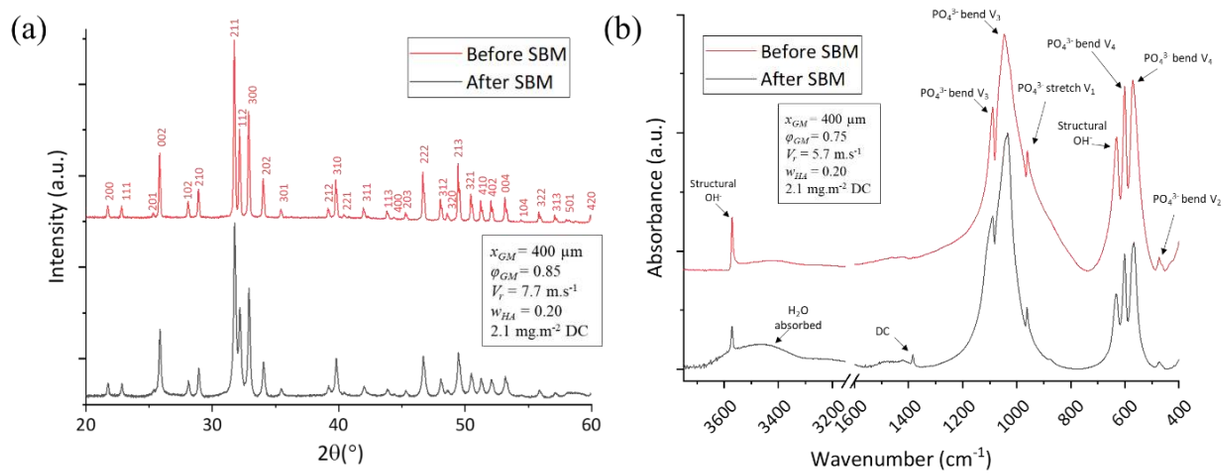

Figure 9. XRD (a) and FTIR (b) analyses of the hydroxyapatite powder before and after a stirred bead milling process. All the diffraction peaks correspond to stoichiometric hydroxyapatite (JCPDS 00 009 0432).

SEM micrographs of the freeze-dried powder after the SBM process (Table 2 – run 5) are shown in Figure S2. The size of the particles observed would confirm the PSD measured by laser diffraction. The ground powder density was found to be 2.97±0.00 g.cm^{-3} showing a slight alteration of the density of the particles to the ones in the initial powder (3.10±0.01 g.cm^{-3}).

The chemical analysis of the product with ICP-AES equipment allowed us to characterize accurately the presence of species coming from the grinding chamber and grinding media wear. The species analysed were Fe, Zr, and Y, and an example of how an operational parameter, such as the stirrer speed V_r, can influence its production is illustrated in Figure S3. To reach the same particle size, three different runs (Table 2 – runs 2, 3, 4) were performed at three different speeds (3.8, 5.7, and 11.5 m.s^{-1}), then samples were collected at different times (135 min, 30 min, and 5 min respectively) once an objective median particle size (x_{50} = 0.8 µm) was reached. In this study, the generation of the grinding media and chamber wear was minimized using the highest stirrer speed.

It is known that grinding media wear can be minimized by applying optimal media diameter, specific energy input, and stirrer speed [63]. However, since the nature and amount of these elements were not too relevant for our goal, a deeper study on the selection, operation and optimization of the process to minimize the grinding media wear was out of the scope of this paper. Indeed, a simple solution could be the changing of the material of the grinding chamber and/or stirrer from stainless steel into ceramic or polymer, avoiding or minimizing the generation of these species.

3.3.2 PSD evolution with grinding time

The evolutions of the PSDs during SBM runs (Table 2 – runs 10, 11) with two different sets of parameters are shown in Figure 10 . Initial particle population having a median size of x_{50} = 22 µm experiments a gradual reduction during the SBM process. Final populations of micron and submicron particles can be obtained for different grinding times. In addition, a different combination of parameters can have diverse effects on the uniformity of the PSDs. SBM process parameters could be tuned to pursuit a determinate PSD depending on the application.

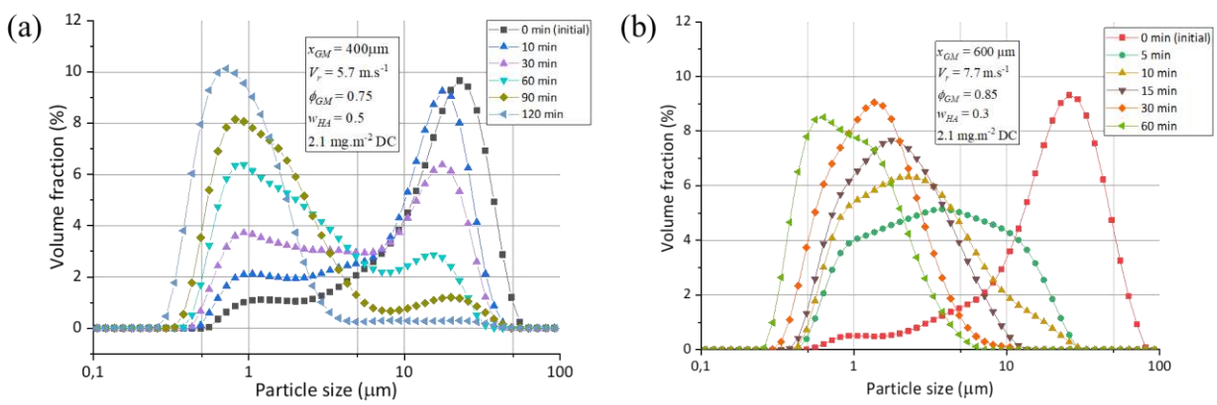

Figure 10. Evolution of PSD of a HA slurry with the grinding time for two different sets of parameters. (a) run 11 and (b) run 12

3.3.3 Rheological behaviour of the ground suspension

The effect of the grinding time on the rheological behaviour of the suspensions was evaluated by taking aliquots at different times during an SBM process. The parameters of this SBM experiment (Table 2 – run 11) together with the rheograms and fitting to the Power Law model can be observed in Figure 11a. The best-fit parameter values of these rheograms can be found in Table 6. It is observed a clear tendency of the rheological behaviour to turn into shear thinning with the grinding time since the flow index decreases from about 1 to 0.88 with the grinding time, therefore for a given solid concentration, this effect is more pronounced for suspensions with smaller particles.

Table 6. Parameters fitted to Power Law model for w_{HA}= 0.50 hydroxyapatite suspensions at different grinding times in steady-state conditions during the shear stress-shear rate test (shear range 10-100 s^{-1}).

		Grinding time (min)					
Sample		0	10	30	60	90	120
Consistency index K (10^{-3} Pa.s^n)	Value	7.22	7.00	8.50	9.06	11.30	14.88
	Standard Error	0.08	0.12	0.27	0.32	0.66	0.62
Flow index n	Value	1.01	1.01	0.97	0.95	0.92	0.88
	Standard Error	0.00	0.00	0.01	0.01	0.01	0.01
R^2		0.99	0.99	0.99	0.99	0.99	0.99

Figure 11b shows the viscosity-shear rate curves obtained for suspensions ground at different times. After 10 min of the process, an increase of the viscosity is observed at low shear rates with the increase of the grinding time (or decrease of the particle size). For a given solid mass fraction and the same volume, the smaller the particle size the higher the number of particles present. Thus, the particle surface area can be several orders of magnitude higher. Very small particles show Brownian motion acting against an applied shear force [64]. A clear shear-thinning behaviour is observed for the suspensions containing particles of smaller sizes. It could be due to a more favourable rearrangement of small particles to the flow direction. A higher grinding time increases the PSD span, increasing the maximum packing density as space can be filled more efficiently.

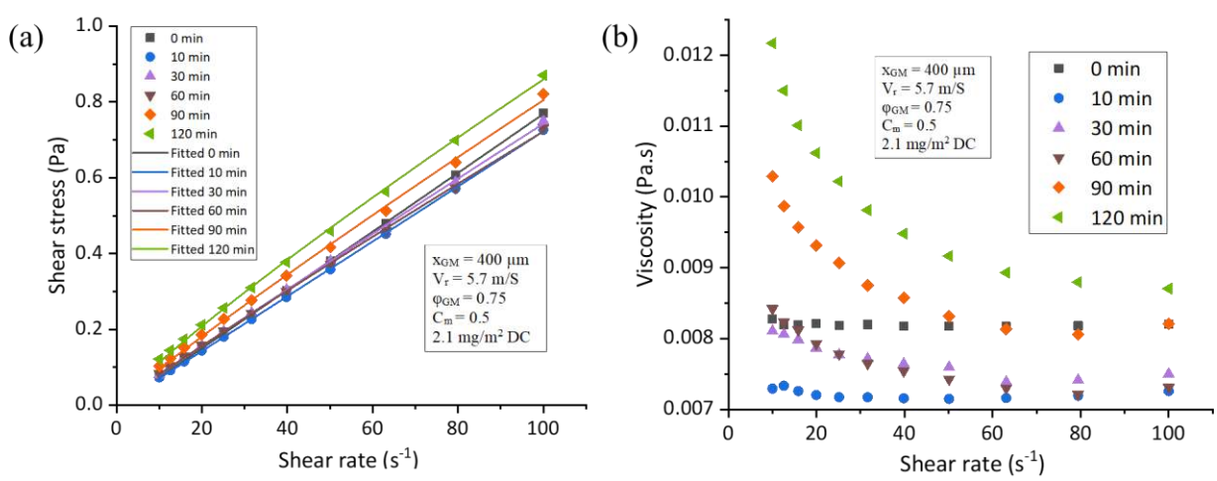

Figure 11. (a) The flow data for several suspensions ground at different grinding times fitted to the Power Law model and (b) viscosity-shear rate curves.

4. Conclusions

This investigation toward the production of HA feedstocks for additive manufacturing techniques revealed that its production is possible by SBM. The choice of the suspension formulation and operating parameters set within the process has been demonstrated to be of high importance for the feasibility of the process, the quality of the final product, and the energy efficiency.

Highly loaded suspensions were successfully ground and the additive DC was demonstrated to be an efficient dispersant additive altering the zeta potential of the particles and thus stabilizing the suspensions, better at a concentration of 2.1 $mg.m^{-2}$. For this specific material, the operating parameters were demonstrated to influence the product quality as well as the process energy efficiency. Hence, for the same specific energy values, faster stirrer speed, smaller grinding media size, and higher HA solid concentration shorten grinding times obtaining finer particles. Indeed, the increase in stirrer speed showed a lower generation of grinding chamber and media wear during the process. The explanation for the low specific energy spent to perform the milling of the product comes from the weakness of the initial HA aggregates and the relative low viscosities of the ground HA products even in fairly loaded suspensions. No high increases in viscosity were observed for the suspensions in the conditions studied, thus keeping their processability.

The production of suspensions with characteristics and properties adapted for either a subsequent spray drying step ($w_{HA} \geq 0.50$; x_{50} = 0.2-1.5 µm; viscosity < 0.1 Pa.s) or as dried powder in VAT photopolymerization (x_{50} = 1-20 µm) was possible by SBM process. And this was possible without major alteration of the composition or the structural phase of the initial HA product. The specific energy cost reduction and shortening of the processing time compared with other beads milling processes make the SBM an interesting technique for the production of hydroxyapatite powder feedstock for additive manufacturing technologies.

5. Acknowledgments

This project has received funding from the European Union's Horizon 2020 research and innovation programme under the Marie Skłodowska-Curie grant agreement No 764935.

We would like to express our acknowledgment to R. T. Vanderbilt Co. for the supplied Darvan C samples.

6. REFERENCES

[1] F. Scalera, C. Esposito Corcione, F. Montagna, A. Sannino, A. Maffezzoli, Development and characterization of UV curable epoxy/hydroxyapatite suspensions for stereolithography applied to bone tissue engineering, Ceramics International. 40 (2014) 15455–15462. https://doi.org/10.1016/j.ceramint.2014.06.117.

[2] M. Dehurtevent, L. Robberecht, J.-C. Hornez, A. Thuault, E. Deveaux, P. Béhin, Stereolithography: A new method for processing dental ceramics by additive computer-aided manufacturing, Dental Materials. 33 (2017) 477–485. https://doi.org/10.1016/j.dental.2017.01.018.

[3] C. Shuai, P. Li, J. Liu, S. Peng, Optimization of TCP/HAP ratio for better properties of calcium phosphate scaffold via selective laser sintering, Materials Characterization. 77 (2013) 23–31. https://doi.org/10.1016/j.matchar.2012.12.009.

[4] S. Eosoly, D. Brabazon, S. Lohfeld, L. Looney, Selective laser sintering of hydroxyapatite/poly-ε-caprolactone scaffolds, Acta Biomaterialia. 6 (2010) 2511–2517. https://doi.org/10.1016/j.actbio.2009.07.018.

[5] J.W. Lee, G. Ahn, D.S. Kim, D.-W. Cho, Development of nano- and microscale composite 3D scaffolds using PPF/DEF-HA and micro-stereolithography, Microelectronic Engineering. 86 (2009) 1465–1467. https://doi.org/10.1016/j.mee.2008.12.038.

[6] L. Ferrage, G. Bertrand, P. Lenormand, D. Grossin, B. Ben-Nissan, A review of the additive manufacturing (3DP) of bioceramics: alumina, zirconia (PSZ) and hydroxyapatite, J Aust Ceram Soc. 53 (2017) 11–20. https://doi.org/10.1007/s41779-016-0003-9.

[7] C. Rey, C. Combes, C. Drouet, D. Grossin, G. Bertrand, J. Soulié, Bioactive Calcium Phosphate Compounds: Physical Chemistry, in: Reference Module in Materials Science and Materials Engineering, Elsevier, 2017. https://doi.org/10.1016/B978-0-12-803581-8.10171-7.

[8] Y. Xia, P. Zhou, X. Cheng, Y. Xie, C. Liang, C. Li, S. Xu, Selective laser sintering fabrication of nano-hydroxyapatite/poly-ε-caprolactone scaffolds for bone tissue engineering applications, Int J Nanomedicine. 8 (2013) 4197–4213. https://doi.org/10.2147/IJN.S50685.

[9] L. Xing-Bang, Z. He, Z. Jing-Xian, D. Yu-Sen, J. Dong-Liang, Effect of Powder Characteristics on the Rheological Performance of Resin-based Zirconia Suspension for Stereolithography, Journal of Inorganic Materials. (2019) 13. https://doi.org/10.15541/jim20190091.

[10] S.Y. Song, M.S. Park, D. Lee, J.W. Lee, J.S. Yun, Optimization and characterization of high-viscosity ZrO2 ceramic nanocomposite resins for supportless stereolithography, Materials & Design. 180 (2019) 107960. https://doi.org/10.1016/j.matdes.2019.107960.

[11] M. Pfaffinger, G. Mitteramskogler, R. Gmeiner, J. Stampfl, Thermal Debinding of Ceramic-Filled Photopolymers, MSF. 825–826 (2015) 75–81. https://doi.org/10.4028/www.scientific.net/MSF.825-826.75.

[12] A. Lüddecke, O. Pannitz, H. Zetzener, J.T. Sehrt, A. Kwade, Powder properties and flowability measurements of tailored nanocomposites for powder bed fusion applications, Materials & Design. 202 (2021) 109536. https://doi.org/10.1016/j.matdes.2021.109536.

[13] H. Lu, X. Guo, Y. Liu, X. Gong, Effect of Particle Size on Flow Mode and Flow Characteristics of Pulverized Coal, KONA. 32 (2015) 143–153. https://doi.org/10.14356/kona.2015002.

[14] L.X. Liu, I. Marziano, A.C. Bentham, J.D. Litster, E.T.White, T. Howes, Effect of particle properties on the flowability of ibuprofen powders, International Journal of Pharmaceutics. 362 (2008) 109–117. https://doi.org/10.1016/j.ijpharm.2008.06.023.

[15] X. Fu, D. Huck, L. Makein, B. Armstrong, U. Willen, T. Freeman, Effect of particle shape and size on flow properties of lactose powders, Particuology. 10 (2012) 203–208. https://doi.org/10.1016/j.partic.2011.11.003.

[16] M.K. Stanford, C. Dellacorte, D. Eylon, Particle Size Effects on Flow Properties of Ps304 Plasma Spray Feedstock Powder Blend, in: W.M. Kriven, H.-T. Lin (Eds.), Ceramic Engineering and Science Proceedings, John Wiley & Sons, Inc., Hoboken, NJ, USA, 2003: pp. 577–585. https://doi.org/10.1002/9780470294802.ch82.

[17] M. Schmid, F. Amado, G. Levy, K. Wegener, Flowability of powders for Selective Laser Sintering (SLS) investigated by Round Robin Test, in: P. da Silva Bártolo, A. de Lemos, A. Pereira, A. Mateus, C. Ramos, C. Santos, D. Oliveira, E. Pinto, F. Craveiro, H. da Rocha Terreiro Galha Bártolo, H. de Amorim Almeia, I. Sousa, J. Matias, L. Durão, M. Gaspar, N. Fernandes Alves, P.

Carreira, T. Ferreira, T. Marques (Eds.), High Value Manufacturing: Advanced Research in Virtual and Rapid Prototyping, CRC Press, 2013: pp. 95–99. https://doi.org/10.1201/b15961-19.
[18] F. Erdem, The effect of binder on chemically precipitated hydroxyapatite during spray drying, Materiali in Tehnologije. (2013) 4.
[19] A. Tsetsekou, C. Agrafiotis, I. Leon, A. Milias, Optimization of the rheological properties of alumina slurries for ceramic processing applications Part II: Spray-drying, Journal of the European Ceramic Society. 21 (2001) 493–506. https://doi.org/10.1016/S0955-2219(00)00232-6.
[20] P. Ramavath, R. Papitha, M. Ramesh, P. Babu, R. Johnson, Effect of primary particle size on spray formation, morphology and internal structure of alumina granules and elucidation of flowability and compaction behaviour, PAC. 8 (2014) 93–99. https://doi.org/10.2298/PAC1402093R.
[21] J.S. Reed, J.S. Reed, Principles of ceramics processing, 2nd ed, Wiley, New York, 1995.
[22] L. Pawlowski, P. Blanchart, Industrial chemistry of oxides for emerging applications., Wiley, Laboratory SPCTS, University of Limoges, France, 2018.
[23] R. Wisniewski, Spray Drying Technology Review, in: 45th International Conference on Environmental Systems, Washington, 2015. https://ttu-ir.tdl.org/handle/2346/64598 (accessed August 14, 2021).
[24] F. Garcia, N. Le Bolay, J.-L. Trompette, C. Frances, On fragmentation and agglomeration phenomena in an ultrafine wet grinding process: the role of polyelectrolyte additives, International Journal of Mineral Processing. 74 (2004) S43–S54. https://doi.org/10.1016/j.minpro.2004.07.001.
[25] C. Onwulata, Encapsulated and Powdered Foods, 1st Edition, Boca Raton, 2005. https://doi.org/10.1201/9781420028300.
[26] A. Kwade, Determination of the most important grinding mechanism in stirred media mills by calculating stress intensity and stress number, Powder Technology. 105 (1999) 382–388. https://doi.org/10.1016/S0032-5910(99)00162-X.
[27] L. Taylor, D. Skuse, S. Blackburn, R. Greenwood, Stirred media mills in the mining industry: Material grindability, energy-size relationships, and operating conditions, Powder Technology. 369 (2020). https://doi.org/10.1016/j.powtec.2020.04.057.
[28] D. Holzmann, D. Holzinger, G. Hesser, T. Schmidt, G. Knör, Hydroxyapatite nanoparticles as novel low-refractive index additives for the long-term UV-photoprotection of transparent composite materials, Journal of Materials Chemistry. 19 (2009) 8102–8106. https://doi.org/10.1039/B912116A.
[29] A.E. Hannora, A.S. Mukasyan, Z.A. Mansurov, Nanocrystalline Hydroxyapatite/Si Coating by Mechanical Alloying Technique, Bioinorganic Chemistry and Applications. 2012 (2012) 1–14. https://doi.org/10.1155/2012/390104.
[30] S. Tsipas, P. Goodwin, H.B. McShane, R.D. Rawlings, Effect of high energy ball milling on titanium-hydroxyapatite powders, Powder Metallurgy. 46 (2003) 73–77. https://doi.org/10.1179/003258903225010523.
[31] R.T. Candidato, Jr, P. Sokołowski, L. Łatka, S. Kozerski, L. Pawłowski, A. Denoirjean, Plasma spraying of hydroxyapatite coatings using powder, suspension and solution feedstocks, Przegląd Spawalnictwa. 87 (2015). https://doi.org/10.26628/ps.v87i10.491.
[32] R. Jaworski, C. Pierlot, L. Pawlowski, M. Bigan, M. Quivrin, Synthesis and Preliminary Tests of Suspension Plasma Spraying of Fine Hydroxyapatite Powder, J Therm Spray Tech. 17 (2008) 679–684. https://doi.org/10.1007/s11666-008-9220-2.
[33] R. Jaworski, C. Pierlot, L. Pawlowski, M. Bigan, M. Martel, Design of the synthesis of fine HA powder for suspension plasma spraying, Surface and Coatings Technology. 203 (2009) 2092–2097. https://doi.org/10.1016/j.surfcoat.2008.10.036.
[34] A. Bignon, J. Chevalier, G. Fantozzi, Effect of ball milling on the processing of bone substitutes with calcium phosphate powders, Journal of Biomedical Materials Research. 63 (2002) 619–626. https://doi.org/10.1002/jbm.10379.
[35] M. Tourbin, F. Brouillet, B. Galey, N. Rouquet, P. Gras, N. Abi Chebel, D. Grossin, C. Frances, Agglomeration of stoichiometric hydroxyapatite: Impact on particle size distribution and purity in the precipitation and maturation steps, Powder Technology. (2019) S0032591019308733. https://doi.org/10.1016/j.powtec.2019.10.050.
[36] Y. Wu, S. Bose, Nanocrystalline Hydroxyapatite: Micelle Templated Synthesis and Characterization, Langmuir. 21 (2005) 3232–3234. https://doi.org/10.1021/la046754z.

[37] H.A. Barnes, Measuring the viscosity of large-particle (and flocculated) suspensions — a note on the necessary gap size of rotational viscometers, Journal of Non-Newtonian Fluid Mechanics. 94 (2000) 213–217. https://doi.org/10.1016/S0377-0257(00)00162-2.

[38] N.J. Alderman, Non-Newtonian Fluids: Guide to Classification and Characteristics., ESDU Data Item 97034 (1997) 30.

[39] S. Padilla, Hydroxyapatite suspensions as precursors of pieces obtained by gelcasting method, Journal of the European Ceramic Society. (2004) 10.

[40] M.A. Inam, S. Ouattara, C. Frances, Effects of concentration of dispersions on particle sizing during production of fine particles in wet grinding process, Powder Technology. 208 (2011) 329–336. https://doi.org/10.1016/j.powtec.2010.08.025.

[41] S. Ouattara, C. Frances, Grinding of calcite suspensions in a stirred media mill: Effect of operational parameters on the product quality and the specific energy, Powder Technology. 255 (2014) 89–97. https://doi.org/10.1016/j.powtec.2013.11.025.

[42] A. Kwade, A Stressing Model for the Description and Optimization of Grinding Processes, Chem. Eng. Technol. 26 (2003) 199–205. https://doi.org/10.1002/ceat.200390029.

[43] S. Breitung-Faes, A. Kwade, Use of an Enhanced Stress Model for the Optimization of Wet Stirred Media Milling Processes, Chem. Eng. Technol. 37 (2014) 819–826. https://doi.org/10.1002/ceat.201300686.

[44] A. Kwade, J. Schwedes, Chapter 6 Wet Grinding in Stirred Media Mills, in: Handbook of Powder Technology, Elsevier, 2007: pp. 251–382. https://doi.org/10.1016/S0167-3785(07)12009-1.

[45] L. Bergström, Shear thinning and shear thickening of concentrated ceramic suspensions, Colloids and Surfaces A: Physicochemical and Engineering Aspects. 133 (1998) 151–155. https://doi.org/10.1016/S0927-7757(97)00133-7.

[46] J.J. Stickel, R.L. Powell, Fluid Mechanics and Rheology of Dense Suspensions, Annual Review of Fluid Mechanics. 37 (2005) 129–149. https://doi.org/10.1146/annurev.fluid.36.050802.122132.

[47] A.U. Khan, P.F. Luckham, S. Manimaaran, Probing the mechanism by which ceramic dispersants act, J. Mater. Chem. 7 (1997) 1849–1853. https://doi.org/10.1039/a701170i.

[48] W. Guo, Y. Han, Y. Li, Z. Tang, Impact of ball filling rate and stirrer tip speed on milling iron ore by wet stirred mill: Analysis and prediction of the particle size distribution, Powder Technology. 378 (2021) 12–18. https://doi.org/10.1016/j.powtec.2020.09.052.

[49] A. Kwade, J. Schwedes, Breaking characteristics of different materials and their effect on stress intensity and stress number in stirred media mills, Powder Technology. 122 (2002) 109–121. https://doi.org/10.1016/S0032-5910(01)00406-5.

[50] A. Afolabi, O. Akinlabi, E. Bilgili, Impact of process parameters on the breakage kinetics of poorly water-soluble drugs during wet stirred media milling: a microhydrodynamic view, Eur J Pharm Sci. 51 (2014) 75–86. https://doi.org/10.1016/j.ejps.2013.09.002.

[51] S.K. Singh, K.K. Srinivasan, K. Gowthamarajan, D.S. Singare, D. Prakash, N.B. Gaikwad, Investigation of preparation parameters of nanosuspension by top-down media milling to improve the dissolution of poorly water-soluble glyburide, Eur J Pharm Biopharm. 78 (2011) 441–446. https://doi.org/10.1016/j.ejpb.2011.03.014.

[52] Y. Tanaka, M. Inkyo, R. Yumoto, J. Nagai, M. Takano, S. Nagata, Nanoparticulation of probucol, a poorly water-soluble drug, using a novel wet-milling process to improve in vitro dissolution and in vivo oral absorption, Drug Dev Ind Pharm. 38 (2012) 1015–1023. https://doi.org/10.3109/03639045.2011.637051.

[53] A.W. Weimer, ed., Carbide, Nitride and Boride Materials Synthesis and Processing, Springer Netherlands, Dordrecht, 1997. https://doi.org/10.1007/978-94-009-0071-4.

[54] K. Ohenoja, M. Illikainen, Effect of operational parameters and stress energies on stirred media milling of talc, Powder Technology. 283 (2015) 254–259. https://doi.org/10.1016/j.powtec.2015.05.036.

[55] H. Bel Fadhel, C. Frances, Wet batch grinding of alumina hydrate in a stirred bead mill, Powder Technology. 119 (2001) 257–268. https://doi.org/10.1016/S0032-5910(01)00266-2.

[56] T. Tanaka, Determining the optimum diameter of grinding media used for ultrafine grinding mechanisms, Advanced Powder Technol. 6 (1995) 125–137. https://doi.org/10.1163/156855295X00121.

[57] K. Ohenoja, M. Illikainen, J. Niinimäki, Effect of operational parameters and stress energies on the particle size distribution of TiO2 pigment in stirred media milling, Powder Technology. 234 (2013) 91–96. https://doi.org/10.1016/j.powtec.2012.09.038.

[58] M. Li, P. Alvarez, E. Bilgili, A microhydrodynamic rationale for selection of bead size in preparation of drug nanosuspensions via wet stirred media milling, International Journal of Pharmaceutics. 524 (2017) 178–192. https://doi.org/10.1016/j.ijpharm.2017.04.001.

[59] A. Strobel, J. Schwenger, S. Wittpahl, J. Schmidt, S. Romeis, W. Peukert, Assessing the influence of viscosity and milling bead size on the stressing conditions in a stirred media mill by single particle probes, Chemical Engineering Research and Design. 136 (2018) 859–869. https://doi.org/10.1016/j.cherd.2018.06.040.

[60] J.G. Fernandes, Development and optimization of a Low Temperature Co-fired Ceramic suspension for Mask-Image-Projection-based Stereolithography, Ph.D. Thesis, Universitat de Barcelona, 2019. http://www.tdx.cat/handle/10803/667478.

[61] H. Gheisari, E. Karamian, M. Abdellahi, A novel hydroxyapatite –Hardystonite nanocomposite ceramic, Ceramics International. 41 (2015) 5967–5975. https://doi.org/10.1016/j.ceramint.2015.01.033.

[62] A.M. Popa, J. Vleugels, J. Vermant, O. Van der Biest, Influence of Surfactant Addition Sequence on the Suspension Properties and Electrophoretic Deposition Behavior of Alumina and Zirconia, Journal of the European Ceramic Society. 26 (2006) 933–939. https://doi.org/10.1016/j.jeurceramsoc.2004.12.023.

[63] M. Juhnke, D. Märtin, E. John, Generation of wear during the production of drug nanosuspensions by wet media milling, European Journal of Pharmaceutics and Biopharmaceutics. 81 (2012) 214–222. https://doi.org/10.1016/j.ejpb.2012.01.005.

[64] R. Newburgh, J. Peidle, W. Rueckner, Einstein, Perrin, and the reality of atoms: 1905 revisited, American Journal of Physics - AMER J PHYS. 74 (2006). https://doi.org/10.1119/1.2188962.

7. Supplementary material

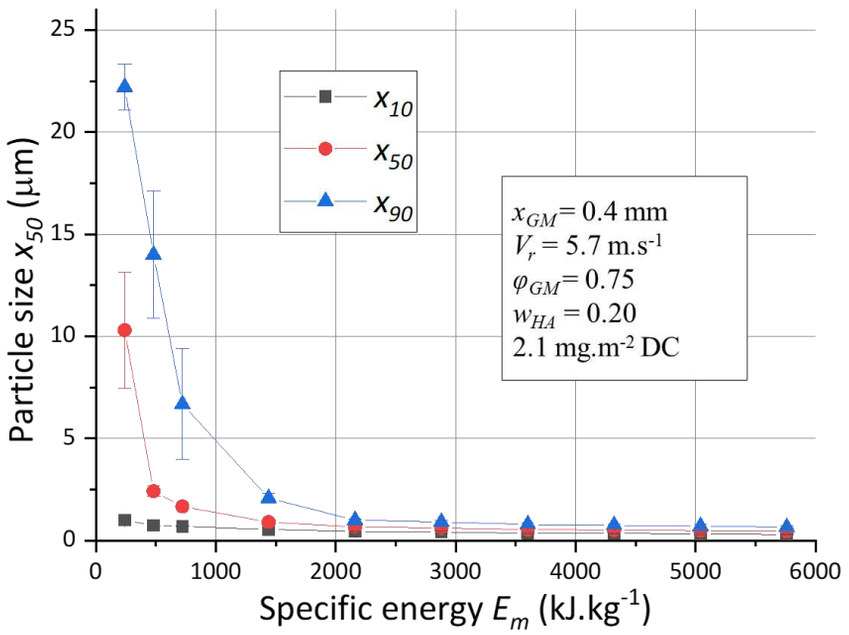

Figure S1. Study of repeatability of the process

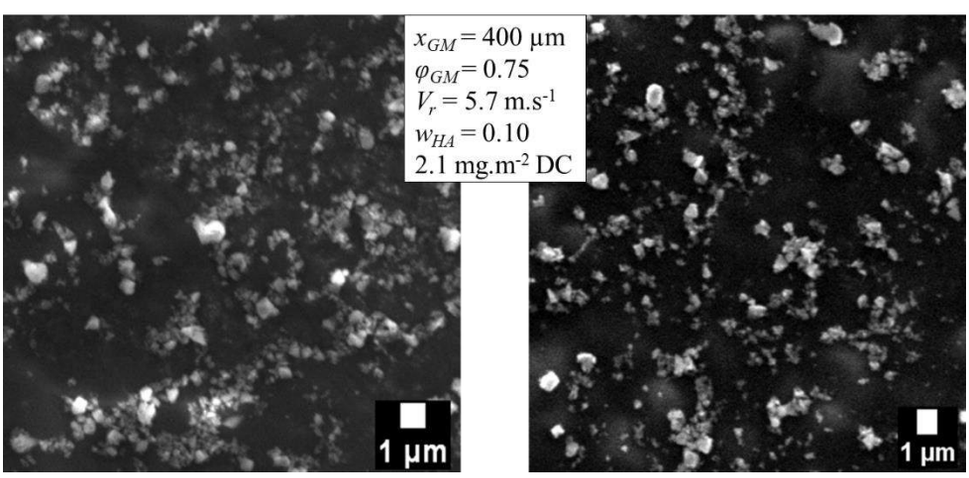

Figure S2. SEM micrographs of freeze-dried HA powder after the milling process.

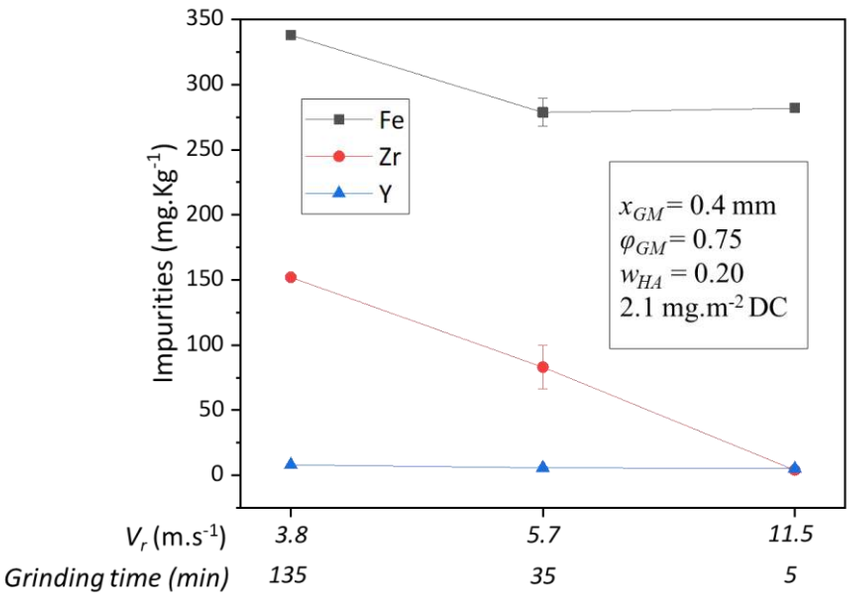

Figure S3. ICP-AES elemental analysis of Fe, Zr, and Y of the final product obtained by three different SBM process runs (Table 2– runs 2,3,4). Samples were collected once the same particle size objective (x_{50} = 0.8 µm) was reached.

Chapter IV. Production of hydroxyapatite microspheres via spray drying for powder bed selective laser processing (sintering/melting)

Production of hydroxyapatite microspheres via spray drying for powder bed selective laser processing (sintering/melting).

Pedro Navarrete-Segado,[a,b] Christine Frances,[b] David Grossin,[a] Mallorie Tourbin,[b,*]

[a] CIRIMAT, Université de Toulouse, CNRS, 4 Allée Émile Monso, 31432 Toulouse Cedex 4, France

[b] Laboratoire de Génie Chimique, Université de Toulouse, CNRS, 4 Allée Émile Monso, 31432 Toulouse Cedex 4, France

Abstract. The present work deals with a study on the physical characteristics of hydroxyapatite microspheres produced by spray-drying process through different operating conditions. Obtained hydroxyapatite microspheres will be used as powder feedstock in powder bed selective laser processing additive manufacturing technologies where the flowability and the particle size distribution of the powder feedstock is of special importance. Spray air pressure and solid content of the slurries were the most influent parameters to control the final particle size distribution, while higher air pressure and temperatures gave the higher process recovery rate. The use of polyvinyl alcohol as organic binder increased the granules strength. The produced hydroxyapatite microspheres were found to fulfil the powder bed selective laser processing feedstock requirements, keeping the physico-chemical properties of the material. These promising results confirm the use of a spray dryer as an efficient method for the production of hydroxyapatite microspheres for powder bed selective laser processing.

Keywords: hydroxyapatite, microspheres, spray-drying, 3D printing, flowability, powder bed fusion,

***Corresponding author: mallorie.tourbin@ensiacet.fr

1. Introduction

Spray drying (SD) process is one of the many methods proposed for the production of ceramic particles with controllable morphology, from which we can distinguish bottom-up (precipitation, supercritical fluid…) and top-down (mechanical milling, freeze-drying…) processes [1]. While with SD is possible to produce and/or tailor already existing particles into high-purity spherical shape ceramic agglomerates in an economical, continuous, and rapid way [2]. SD technique leads to the transformation of fluid state feed into dried particulate form by spraying the feed into a hot drying medium. The feed can be constituted of a suspension, emulsion, or a solution. In addition, it is common the use of additives, such as, dispersants and binders to control the stability of the particles against flocculation as well as the hardness of the resulting particles. The final product morphology depends of several factors including the physical and chemical properties of the feed formulation, process conditions, and the equipment geometry [2,3].

The advantages of a SD process, such as particle size distribution (PSD) and morphology control, make it an interesting option for the production of microspheres composed of hydroxyapatite (HA), a very well-known bio-ceramic material in bone tissue engineering because of its ideal properties for bone tissue reparation [4–6]. It has chemical similarity to bone and its high bioactivity, biocompatibility, and stability ensures good osseointegration of the implants while keeping good mechanical and chemical resistance [7]. The recent application of Additive Manufacturing (AM) technologies to process ceramic materials open new ways for the production of ceramics for many diverse applications (healthcare, aerospace…). Precisely the Powder Bed Selective Laser Processing (PBSLP) method uses a laser to sinter/melt selectively regions of a ceramic powder bed fabricating parts from previously designed 3D models [8]. The production of HA parts for tissue engineering and implantology has been possible through the use of composites comprising biocompatible polymers such as poly-L-lactic acid (PLLA), polycaprolactone (PCL), and poly(3-hydroxybutyrate-co-3-hydroxyvalerate (PHBV)) as the main component [9–12]. However, still some research is needed on the direct use of pure HA as powder feedstock, or at least as main component, for the production of parts which could wholly benefit from the ideal properties for bone tissue reparation of this calcium phosphate-based bio-ceramic [13–15].

At the time of tailoring the powder feedstock properties for PBSLP method it is important to know the needs required for an optimal performance during the process. Microstructural composition, physico-chemistry rheology, thermal, and optical properties should be tailored to improve printed parts quality [16,17]. One of the PBSLP method steps make use of a recoater to repeatedly spread the powder in a homogeneous way on the building platform creating thickness-controlled powder beds before the laser scanning. Powder feedstock flowability and packing density are then crucial properties for their processability, and these can be tuned by modifying the powder morphology (shape and size) and size distribution. One measurement method for the flowability of powder is the ratio of tap and bulk density (Hausner ratio) [18]. A PBSLP powder feedstock should yield a Hausner ratio of less than 1.25**.** This is

better achieved by flowable spherical agglomerates particles within the micron range (x_{50} > 20 µm) [19–22]. In addition, the use of polydisperse size distribution (span > 1) has demonstrated to improve their flowability and packing density, with the smaller particles filling the interstitial void between larger particles [23–25]. It makes the SD an excellent process for the production of hydroxyapatite microspheres (HAm) intended for PBSLP, since the possibility of controlling their PSD as well as the morphology allow the tailoring of powders properties such as flowability and packing density.

A growing interest for the production and employment of HAm on diverse applications, including AM technologies [26–28] and biomedical fields [29–32] can be observed in an increase of the number of research works focused on these materials during the most recent years. Though, it can be observed that not many studies are focused on the production of HAm through SD, neither on the evaluation of the experimental conditions on the final dried HAm properties. Some recent examples have been offered by Bastan [5], Erdem [33], Yang and Wang [34], and Chow [35], however, these works do not cover completely the large variety of parameters affecting the final powder properties (slurry formulation, operating conditions, apparatus geometry…) for hence, there is still then a need to extend the research in this topic.

The goal of the present study would be, first, the preparation of the HA slurries meeting the expected properties in terms of rheology and stability for their processing by SD (this part was mainly covered in chapter III). Then, we will focus on the evaluation of the effect of the slurry formulation and operating parameters during the SD process on the final HAm powder properties. The main objective will be then the production of HAm powder with a targeted particle size in the micron range (30 µm < x_{50} < 70 µm) and a certain size polydispersity (span > 1) to fulfil the flowability requirements (e.g., Hausner ratio < 1.25) for its use in a PBSLP process.

2. Materials and method

2.1 Materials

Stoichiometric hydroxyapatite (HA) aqueous slurries used during the present study were produced by precipitation and stirred bead milling process following the conditions already discussed during previous works (chapter II and chapter III, respectively). Once the objective initial particle size range (x_{50} = 0.2 – 1.5 µm) was reached by wet milling, the influence of the HA load and the dispersant dosage in the viscosity of the slurry was studied since the higher is the load content of a suspension the less is the amount of water needed to be dried, thus increasing the process efficiency. First, a suitable dispersant able to produce the deflocculation of the HA particles and hence increase the suspension stability was found. The ammonium polymethacrylate dispersant, named Darvan C and provided by R. T. Vanderbilt Co. (Norwalk, CT, USA) was assessed. The optimum dispersant dosage was determined in terms of viscosity, zeta potential, and sedimentation speed measurements. It was a concentration of 2.1 mg/m^2 of dispersant active matter respect to the ceramic surface or what is the same, a 5 wt. % respect to the ceramic powder mass. Secondly, the

highest processable HA load in a suspension was found to be a solid mass fraction (w_{HA}) of 0.5, that is to say the 50% of the total mass of the suspension. Following this previous study, all suspensions used in the present work contain a 5 wt. % of dispersant DC and a solid content of HA w_{HA} = 0.5 was preferred even if the influence of lowering the load content on the final HAm properties was assessed. Thus, in this work only the effect of the binder addition on the slurry stability was studied. A deeper description of the dispersant and the studies about the influence of HA and dispersant concentrations on slurries stability and rheology can be found in chapter III.

Polyvinyl alcohol (PVA), Rhodoviol® 8/140 was obtained from VWR Chemicals® and was used as an organic binder during the spray drying process for its excellent granulation properties. PVA granules were dissolved in water at 90ºC (20 wt. % granules, 80 wt. % distilled water) to prepare a homogeneous solution before adding it to the respective HA powder slurries.

Two additional powders were evaluated for flowability comparison with the spray-dried powder produced in the present work:

- First, a commercial HA powder from the company Urodelia® S.A (ref. 300-08-2) was used as reference material of powder that already showed good results in terms of flowability in a PBSLP apparatus.
- The HA powder of the initial slurries was filtered and dried at 70ºC overnight to obtain an initial HA powder for comparison of flowability.

2.2 Characterization of the powders and slurries

2.2.1 Morphological and structural properties of the particles

All PSD of HA suspensions and dry powders were performed with a Mastersizer MS 3000 (Malvern Panalytical®) laser particle size analyser (refractive indexes: 1.63 and 1.33 for particles and water, respectively; dispersion pressure of 0.1 bar and a standard stainless steel venturi disperser for dry powders). A total number of replicate measurements (N) of five was performed for each measurement to calculate the resulting sample mean and sample standard deviation. Obtained values will be given as follows: mean ± standard deviation.

The morphology of powders present in this work was investigated with a scanning electron microscope (SEM) LEO 435 VP (Leica®) equipped with a Ge detector (Imix-PC, PGT) and metallization of the ceramic surface was performed with a thin film of silver using a Scancoat Six sputter coater. Particle size distribution of the initial HA slurry and SEM micrographs of the particles (dried) constituting of the initial suspension, can be observed in Figure 1.

The specific surface of these initial particles was found to be 23.81±6.00 m^{-2}.g. Determined in a Micromeritics® TriStar II Plus 3.00 equipment through physisorption analysis of overnight freeze-dried powder (N=3). Ultrapure water used as dispersion medium was produced by the equipment "Purelab Ultra" of VWS (UK) Ltd. The water density was measured at 25˚C obtaining 0.99 $g.cm^{-3}$, whereas its pH varied between 6.3 to 6.8 at 25˚C.

2.2.2 Chemical and structural analyses

Fourier transform infrared spectroscopy (FTIR) analysis performed with a spectrometer FTIR iS50 and the KBr pellet method was used to determine the composition of the powder before and after the spray drying process. About 9 mg of sample powder were homogeneously mixed in a clean mortar to mix it with dry KBr powder (300±5 mg). A compression at 6000 kg was used to produce the analysed sample pellets. FTIR spectra was measured from the pellet in a 4000-400 cm-1 wavenumber range with a step width of 0,48 cm-1.

Thereafter, X-ray diffraction (XRD) analysis was performed by BRUKER's X-ray diffractometer D8 by using Cu Kα radiation (wavelength λ = 0.15406 nm) with a nickel filter at 40 kV and 40 mA. Samples diffractograms were recorded in a 2θ range between 20º and 90º, with a step of 0.03º 2θ, and a time per step of 0.2 s.

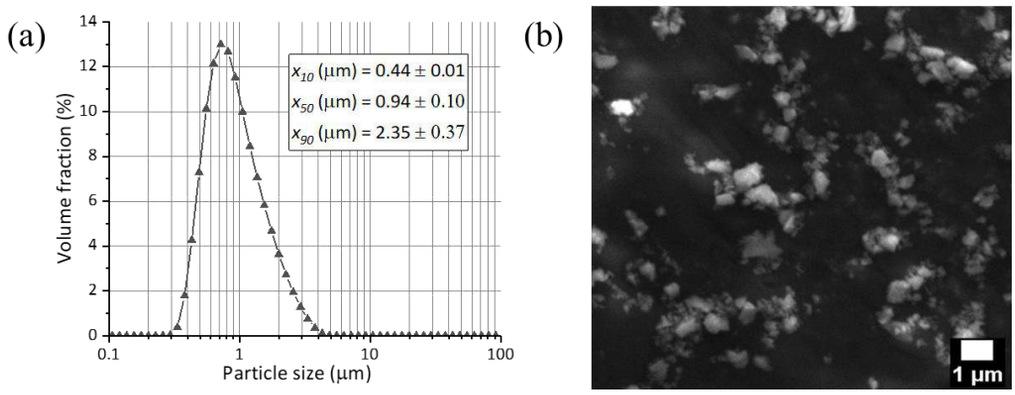

Figure 1. (a) PSD of the primary stoichiometric hydroxyapatite powder measured in dispersion. (b) SEM micrograph of the same dried powder.

2.2.3 Rheological behaviour

Rheological analyses were undertaken to study the PVA binder influence on HA slurries viscosity and stability. These analyses were performed in a TA Instruments® AR2000 rheometer using a 40mm crosshatched parallel plates system with a gap equal to 1300 µm and a Peltier plate. The measurements were performed with a conditioning step at a shear rate of 200 s^{-1} during 30.0 s and an equilibration time of 30.0 s. Steady-step shear flow curves were then obtained for each sample at a constant plate temperature of 25ºC

and an increasing shear rate in the range of 1–1000 s^{-1} by taking ten data points by decade. It includes the pumping and mixing processes typical ranges of shear rate [36]. Power Law model was found to fit properly the rheological analyses data.

2.2.4 Suspension stability analyses

Additionally, to support our study on the HA slurries stability before drying, electrophoretic analyses were performed to determine their zeta-potential depending on the amount of PVA binder. A Zetasizer Nano-ZS (Malvern Panalytical®) was employed for the analyses at a constant temperature of 25ºC. Samples were diluted and adjusted to a concentration of 4 $mg.ml^{-1}$ before the analysis to avoid the multiple diffusion phenomena.

2.2.5 Powder flow experiments

Powder flow experiments of initial, spray-dried, and commercial powders were conducted following the standardized methods, specifications, and comments raised by the European Pharmacopoeia Chapter 2.9.36. A brief explanation for each of the five different flowability tests used in this work is presented below:

- Angle of repose, is the angle formed by the pile powder (relative to the horizontal) when it is poured through a funnel. It is a characteristic related to interparticle friction or resistance to movement between particles. Some variation in the qualitative description of powder flow using the angle of repose exists, however authors seem to agree with the classification given by Carr [37], which is shown in Table S1. According to this classification, for good or even excellent flowability, the powder must present an angle of repose between 25° to 35°.
- Compressibility index and Hausner ratio are closely related and both have become the most simple, fast, and popular methods to predict the powder flow behaviour. Both are determined by measuring the bulk (ρ_0) and tapped (ρ_f) densities of powders. They are calculated as follows:

$$Compressibility\ index = 100 * \left(\frac{\rho_0 - \rho_f}{\rho_0}\right) \quad (1)$$

$$Hausner\ ratio = \frac{\rho_0}{\rho_f} \quad (2)$$

The largely accepted scale of flowability is given in Table S1. For good or even excellent flowability, the compressibility index of the powder must be lower or equal to 15% and the Hausner index must be under 1.25 [16].

- The flow through an orifice, has been proposed as the best measure of flowability of free-flowable powders [38]. It is measured as the mass per time flowing from any of a number of types of containers (cylinders, funnels, hoppers). There is no general flowability scale available since the flow rate is dependent on the method used to measure it. Comparison between different published results is then difficult. Experimental studies have detected a significant influence of orifice height on powder mass flow rate, thus for better comparison of the experimental results information regarding the orifice height used should always be referred [38].
- The flow function of powders (ff_c) is used as a flowability index according to the classification by Jenike [39] shown in Table S2. The flowability of a bulk solid can be characterized by its unconfined yield strength, f_c, in dependence on consolidation stress, σ_1. Usually, the ratio ff_c of consolidation stress, σ_1, to unconfined yield strength, f_c, is used to characterize flowability numerically. The larger the ff_c is, the better a bulk solid flows. For easy or free flowing of the powder, the flow function must be higher than 4.

The following paragraphs contain more detailed information about the procedures followed and the equipment used for each of the five flowability tests performed:

- The angle of repose, compressibility index, and Hausner ratio (ratio of tapped density to aerated density) of the powders were evaluated on a powder characteristics tester PT-S (Hosokawa Micron B. V®).
- The flow rate of the different powders was measured in discrete samples by measuring the time it took for 100g of powder to pass through the orifice of a stemless funnel (truncated cone) to the nearest tenth of a second. A glass funnel with an inner diameter of 15.5 cm, 13.5 cm height and a circular orifice diameter of 3.2 cm was used as container. Then, the orifice was circular and free of any vibration. The use of a stemless funnel was preferred instead of one with stem to avoid any effect of the friction between the stem and the flowing powder.
- The ff_c ratio was measured in a universal mechanical testing press HOUNSFIELD H25KS (Tinius Olsen®, USA) following the procedure described by Poletto et al. [40]. Once the cylindrical mould (diameter of 8.3 mm) was filled with 1 gram of powder sample, the piston is moved downwards applying a normal load, N_c, of 75 MPa with a speed of 20 mm/min. The compression step is carried with the piston moving downwards with a speed of 1 mm/min onto the consolidated sample increasing the normal force, until reaching the normal force at specimen failure, N_f. The flow function (ff_c) is then calculated as the ratio between the major principal stress at steady state, $\sigma 1$, and the unconfined yield strength, f_c. Both calculated in turn following the equations below:

$$\sigma_1 = \frac{N_c}{A_{UCT}} \quad (3)$$

$$f_c = \frac{N_f}{A_{UCT}} \quad (4)$$

Where A_{UCT} is the cross-sectional area of the mould (54.11 mm^2).

At least six measurements (N=6, mean ± standard deviation) were recorded to obtain the standard deviations of the means for the angle of repose, compressibility index, Hausner ratio, and flow rate, then at least three measurements (N=3, mean ± standard deviation) to obtain the standard deviation of the mean for *ffc* of each powder.

2.3. Spray drying experiments

The spray drying process was carried out in an APV Anhydro (SPX Flow®, USA) 1-meter diameter chamber pilot spray drying plant (Figure 2), model PSD 52 in 316 stainless steel. The process starts with the HA slurry being pumped from the bottom of the chamber by means of a BOYSER® peristaltic pump (model AMP-10/B) while stirred with a Heidolph instruments® mechanical stirrer equipped with a straight-blade impeller at 150 rpm. Then, the slurry was finely sprayed into the chamber through a SU04 two-fluid external mixing nozzle (Fluid Cap 60100 + Air Cap 120) from Spraying Systems Co. ® with round spray pattern in a 17-19º spray angle. An air duct heater produces a stable heating of the chamber drying the drops into powder, then a flow is created by an aspirator, to lead the powder reaching the cyclone where the solid particles are separated from the air flow and settled into a collection jar. Once the powder is separated, the air loaded with very fine particles passes through a filter bag in order to minimize the fine particles emissions. The list of experimental runs performed for the present study together with the slurry formulation, experimental conditions, and results information can be found in Table 1.

The experimental runs were carried out following the methodology below:

- Run 1: The objective of this run was to evaluate using "standard" experimental conditions the steady state regime of the equipment, as well as, the global performance of the process (recovery rate, residual powder moisture, PSD…) and the operation time needed for the rest of the study.
- Runs 2-14: Through these runs, we could examine the influence of the slurry formulation and the experimental conditions on the final powder properties. It also allowed us to find the set of parameters producing the powder that better meet the properties needed for its use in a PBSLP process.

The procedure followed for the runs started with the operating parameters of the SD process being settled by using water as feed. Thus, reaching an estimated temperature of the chamber before start pumping the suspension. After this preliminary step, the pumping of the suspension starts together with the chronometer. The powder produced during the spraying of the suspension starts to be gathered through the cyclone into the collection jar. Once the process finished the powder inside of the jar was extracted and stocked for analysis. In the case of the Run 1 (operation time study) the cyclone valve was closed every ten minutes and the powder inside of the container was collected and stocked for analysis. Then, the recipient was returned to the cyclone and the valve was reopened to continue collecting the product.

Powders obtained were weighted for recovery rate studies and analysed for their water content with a commercial moisture analyser (MBT 64 M-C model from VWR®). A standard drying profile was used to dry the powder to constant weight at 110 ºC.

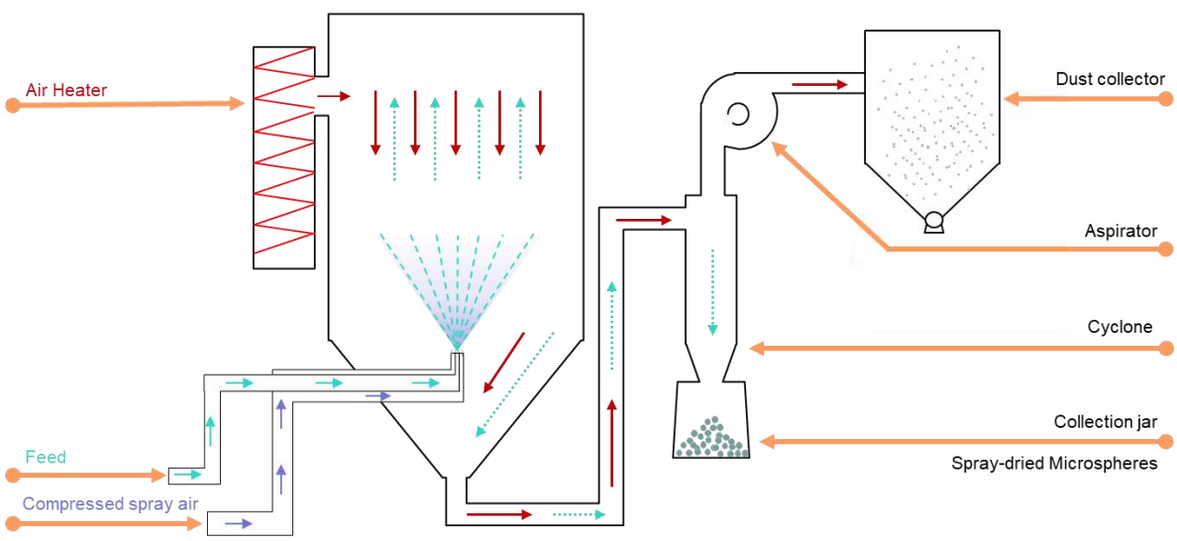

Figure 2. Schematic representation of the pilot-scale spray dryer.

Table 1. List of spray drying experiments performed, including the slurry formulation, experimental conditions, and resulting powder properties.

	Formulation			**Experimental conditions**			**Result**						
Run Nº	w_{HA} (-)	DC conc. (wt. % of active matter)	PVA conc. (wt. %)	T_{int} (ºC)	P (bar)	Qs (kg.h^{-1})	x_{10} (µm)	x_{50} (µm)	x_{90} (µm)	Recovery rate (%)	Span (-)	Moisture content (%)	**Parameters effect studied**
1	0.5	5	0	250	0.25	3.2	25 ± 7	64 ± 4	123 ± 1	37	1.77	1.5	Qs, P, w_{HA}, Steady-state regime, PVA conc., repeatability, T_{int}, flowability
2	0.1	5	0	250	0.25	3.2	10 ± 2	27 ± 2	61 ± 2	32	1.78	1.1	w_{HA}
3	0.3	5	0	250	0.25	3.2	16 ± 3	47 ± 2	88 ± 0	22	1.38	1.3	w_{HA}
4	0.5	5	0	250	0.25	4.9	56 ± 4	88 ± 3	137 ± 2	23	0.81	1.6	Qs
5	0.5	5	0	250	0.25	5.8	72 ± 2	101 ± 2	140 ± 5	19	0.64	1.8	Qs
6	0.5	5	0	250	1	3.2	29 ± 4	58 ± 2	101 ± 2	24	1.56	1.6	P
7	0.5	5	0	250	2	3.2	16 ± 3	45 ± 1	88 ± 2	46	1.93	1.4	P, Qs+T_{int}
8	0.5	5	3	250	0.25	3.2	44 ± 4	78 ± 5	131 ± 6	20	1.15	3.8	PVA conc.
9	0.5	5	5	250	0.25	3.2	30 ± 3	65 ± 4	117 ± 6	19	1.37	4.6	PVA conc.
10	0.5	5	0	275	0.25	3.2	27 ± 8	66 ± 2	122 ± 2	16	1.21	1.4	T_{int}
11	0.5	5	0	300	0.25	3.2	30 ± 8	87 ± 10	221 ± 12	18	1.99	1.2	T_{int}
12	0.5	5	0	250	2	4.9	8 ± 0	31 ± 0	75 ± 1	79	2.15	2.0	Qs+T_{int}
13	0.5	5	0	300	2	9.7	9 ± 0	38 ± 1	101 ± 3	76	2.34	2.3	Qs+T_{int}
14	0.5	5	0	320	2	11.3	10 ± 1	40 ± 1	100 ± 2	75	2.17	1.9	Qs+T_{int}

3. Results and discussion

3.1 Preparation of HA slurry properties

It was already mentioned in section 2 that the preparation of the aqueous HA slurries already started in a previous work with the diminution of the particle size in a sub-micron range (x_{50} = 0.2-1.5 µm) by wet grinding of the suspensions (chapter III). This process was necessary since the use of initial particles with too large size affect the formation of the sprayed droplets making impossible the production of the spherical agglomerates.

Depending on the application, spray-dried spherical granules with controlled hardness and deformability may be required. We can find some works studying the effect of adding different organic binders to the ceramic suspension on the final granule characteristics [41,42]. However, the use of a binder can induce an increase in the slurry viscosity and produce the destabilization of an already dispersant-stabilized suspension. In a PBSLP process the importance of having coherent granules or not has not been studied yet. Some PBSLP apparatus are equipped with a cylindrical recoater part that is able to produce a compression of the powder bed once it has been spread. Further research is needed to know if the packing density of the powder bed is improved by using easy-deformable granules or not at the moment of compress it. In the present study, suspensions with and without binder in their composition were spray-dried and its influence on the final HAm characteristics (morphology and strength) was analysed.

The effect of the addition of the binder PVA on the dispersant-stabilized slurries was determined through viscosity and zeta-potential measurements. Three similar volumes of aqueous solutions, two of them containing 3 and 5 wt. % of binder PVA (respect to the ceramic powder) were prepared and poured to three different samples of a HA suspension at w_{HA} = 0.3 to study the binder influence on the viscosity. Figure 3a shows the shear stress versus shear rate diagram of the HA suspensions at different PVA concentrations. The best-fit parameter values of these rheograms by a power-law of type $\tau = K(\dot{\gamma})^n$ with τ the shear stress [Pa] and γ the shear rate [s^{-1}] can be observed in Table 2. All suspensions analysed exhibited pseudoplastic behaviour over the whole shear rate range, also confirmed by the flow behaviour indexes (n being less than 1). It is important to note that the correlation ratios indicate that the Power Law model fits the measurements well. The viscosity of aqueous suspensions with different PVA concentrations is compared in Figure 3b. As expected, the higher the PVA concentration, the higher the slurry viscosity is. However low viscosity values were observed, even for high binder concentration (< 0.1 Pa.s for the whole shear rate range). These results are in agreement with those of Tsetsekou et al. [43] who observed that the addition of PVA binder into alumina slurries exhibited a slight increase of the viscosity. A higher PVA content may increase the resistance to deformation by shear stress due to the presence of more entities in the suspension reducing the free space for individual particles to move around.

Table 2. Parameters fitted to Power Law model for HA suspensions with different PVA concentrations in steady-state conditions during the shear stress-shear rate test (imposed shear range 1-1000 s^{-1}).

		PVA conc. (wt. %)		
Sample		0	3	5
Consistency index K [10^{-3} Pa.s^n]	Value	9	18	21
	Standard Error	0.90	2.24	2.47
Flow index n	Value	0.69	0.66	0.67
	Standard Error	0.01	0.02	0.02
Correlation ratio R^2		0.99	0.98	0.99

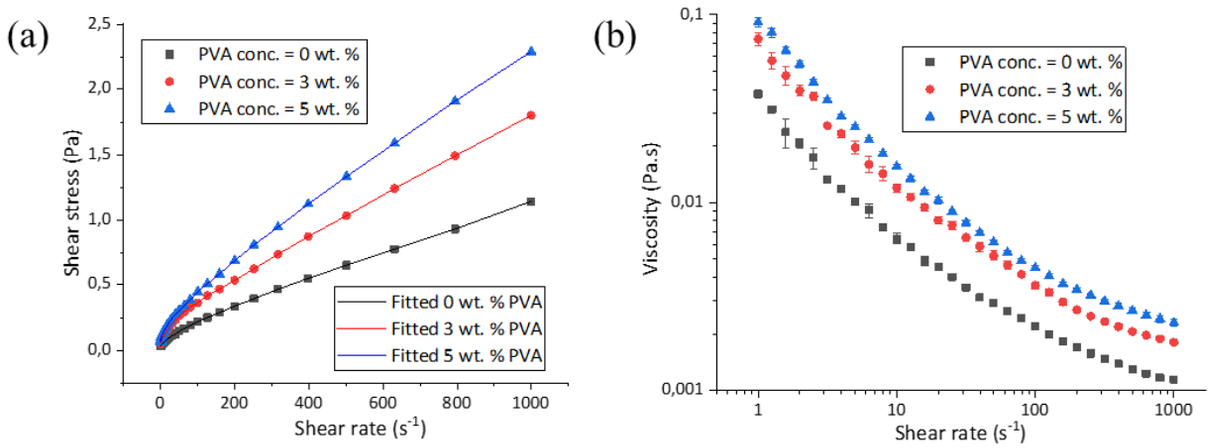

Figure 3. (a) Flow data for several suspensions containing different binder concentrations fitted to the Power Law model and (b) viscosity-shear rate curves.

In addition, the zeta-potential evolution of the HA suspensions was analysed in the PVA dosage range of 0-5 wt. % relative to the HA content. The addition of PVA can alter the slurry stability, reducing the zeta-potential of the slurries and producing the pre-agglomeration of the particles in suspension that could preclude a correct formation of the dry agglomerates during the SD process. An absolute zeta-potential value higher than 30 mV would indicate a good stabilization of the suspension [44]. Then, it was important to avoid the alteration and diminution of the zeta potential of the suspension under this limit value. Figure 4 shows the average of the zeta-potential values from a set of five measurements for each of the three analysed suspensions. It can be observed how the suspension was already well stabilized due to the previous addition of DC. Between the suspensions containing PVA, the one with a 5 wt. % of PVA respect to the ceramic showed a higher absolute value for the zeta potential of the suspension indicating a lower alteration of the initial stability of the slurry.

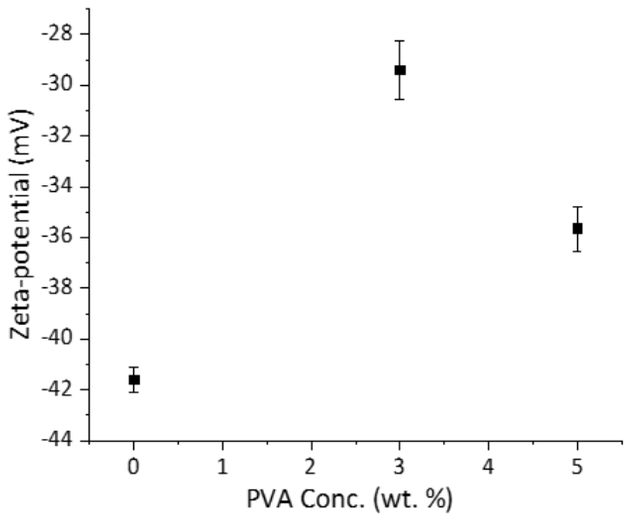

Figure 4. Effect of PVA dosage on HA dispersant-stabilized slurries zeta-potential.

In this section it was demonstrated that the addition of PVA to the slurries prior to the SD process induced a higher but controlled slurry's viscosity. In addition, comparing these concentrations, a concentration of 5 wt. % of PVA respect to the ceramic kept a higher stability of the suspensions with a higher zeta-potential absolute value.

3.2 Spray drying of the HA suspension

Below, the time to reach a steady-state regime and the effect of the operating parameters of the SD continuous process on the final HAm properties are analysed. Different experiment runs where performed with diverse parameters combinations. These operating parameters were the feed rate, solid mass fraction, spray air pressure, inlet temperature, and the binder dosage. The influence of these parameters has been investigated in terms of resulting PSD and particles shape through SEM micrographs analyses of the produced HAm and residual moisture content of the powder after drying.

3.2.1 Steady-state regime

Firstly, the time to reach the steady-state process regime in which the variables remain constant as time changes was evaluated in the conditions described for the run 1. Figure 5a shows the average particle size obtained at different process times. A certain variation of the particle size is observed within the time of the experiment but not a clear tendency can be perceived. Assuming that the time required to bring the equipment up to operating capability under these conditions is no more than two hours (time over which the

process has been monitored), it would indicate that the steady-state of the process is reached rapidly at the beginning of the experiment and that not important variations for the particle size of the powder obtained are expected. As was already indicated in Table 1, the average x_{10}, x_{50}, and x_{90} of the whole process are 25 µm, 64 µm, and 123 µm with standard deviations of ± 7 µm, ± 4 µm, and ± 1 µm respectively. This variation of the product quality with the process time is also observed in the evolution of the PSD of the powders shown in Figure 5b. A certain difference is perceived between distributions but neither here a clear variation tendency depending on the process time is observed. All powders showed a roughly similar PSD span.

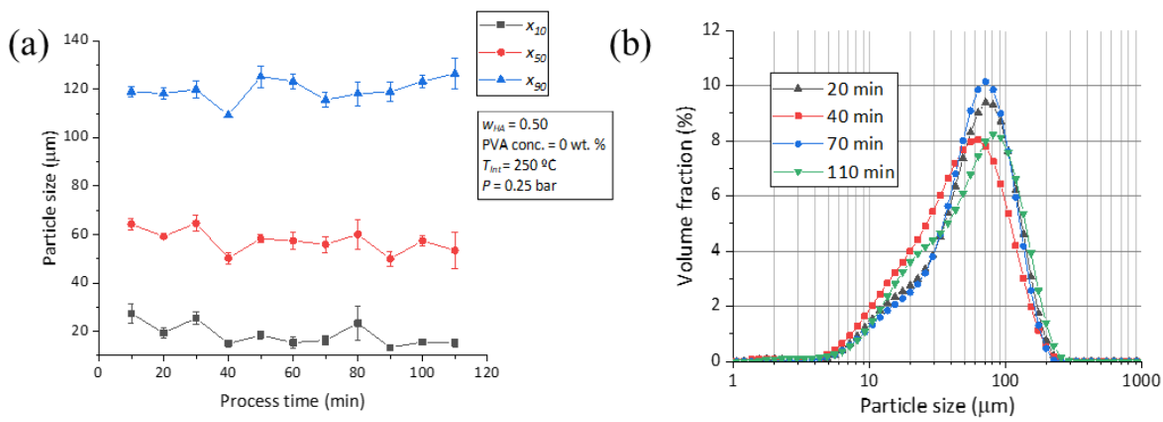

Figure 5. (a) Average particle size (x_{10}, x_{50}, and x_{90}) of powders obtained at different process times and (b) PSD of the powders obtained at 20, 40, 70, and 110 minutes.

HAm morphologies at different process time can be seen on Figure 6. The majority of the particles had small rough spherical and dense morphology, produced by the use of submicronic particles (much smaller than the size of droplets) as starting material. The spherical particles have almost no external visible porosity in their structure. Other particle morphologies can also be observed in the SEM micrographs but in a very lesser extent (Figure 7). These are doughnut, convex, and mushroom particle morphologies produced by the hydrodynamics, the structural stability, and the behaviour of the droplets transforming the spherical droplet into other forms [2,45]. This droplet-transformation phenomenon happens at specific process conditions (e.g., too high temperature process, presence of surfactants…). Okuyama et al. [2] found in their study that doughnut type particles had higher surface area, lower density and more than a 30% of porosity than spherical dense particles.

Formation mechanisms of dense small rough spherical dense particles, as well as, mushroom, convex, and doughnut particles are illustrated in Figure 7a and Figure 7b, respectively. In addition, the SEM micrographs of individual spray-dried HAm, doughnut HA particle, and the cross-section of a HAm showing the initial HA particles can be observed from Figure 7c to Figure 7f.

Regarding the residual moisture of powders obtained at different times, the moisture percentage values oscillated in a range between 1.5% and 0.6%. This tolerable variation of less than 1% on the powder humidity led us to assume that the steady-state regime of the process is rapidly reached and no longer operation times are required.

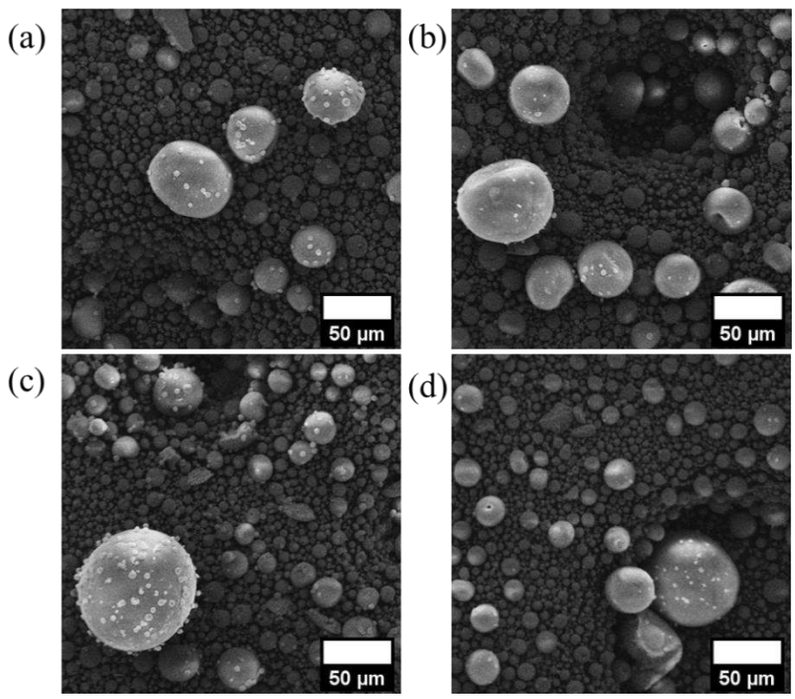

Figure 6. SEM micrographs of spray-dried HAm at (a) 20 min, (b) 60 min, (c) 90 min, and (d) 110 min of process time.

To conclude this preliminary study of the SD process time influence on particles morphology, not important differences between the obtained HAm morphologies, sizes and humidities at different process times were found during the first two hours; demonstrating that the steady-state regime of the process is rapidly reached. Thus, it was chosen to characterize the following experimental runs performed in this study at a same duration time of 20 min for better comparison. Since the presence of a small percentage of mushroom/convex/doughnut particles in a PBSLP powder feedstock has not been demonstrated to have an unfavourable effect, the variables involved in their production have not been further investigated.

Once the time required to reach the steady-state of the process has been evaluated, the effect of the different operating conditions on the product quality was carried out. For hence, the following study was focused on the analysis of HAm morphology in terms of particle size and their PSD only.

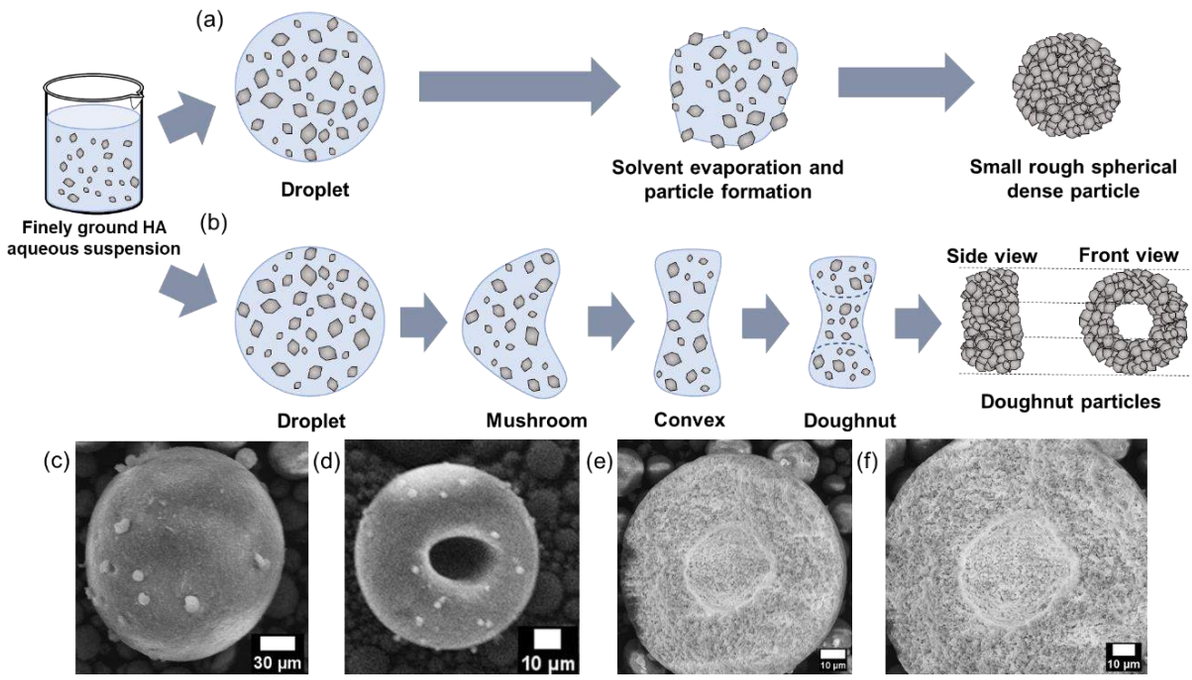

Figure 7. Formation mechanism of (a) small rough spherical dense particles and (b) mushroom, convex, and doughnut particles (based on Okuyama et al. [2]). SEM micrographs of spray-dried (c) small rough HAm, (d) doughnut HA particle produced at specific conditions, (e) cross-section of a HAm showing the initial HA particles forming the agglomerate and (f) at higher magnification.

3.2.2 Influence of the parameters of the spray drying process on the properties of the powders

First, experiments with different combinations of operating parameters, such as, feed rate, solid mass fraction, spray air pressure, and inlet temperature were performed and the powder obtained was analysed for comparison of average particle size (Figure 8) and PSD (Figure 9).

It can be observed from both, average particle size and PSD analyses results that the different SD process conditions have an important effect on the final powder size distributions. The most influential effect observed in the parameters studied ranges came from the increase of the feed rate (runs 1, 4 and 5) and the temperature of the process (runs 1, 10 and 11).

At similar SD conditions, an increase of feed rate from 3.2 $kg.h^{-1}$ (run 1) to 5.8 $kg.h^{-1}$ (run 5) means almost the double of matter sprayed per hour and in consequence, bigger droplets are formed producing larger average particle size. Same reasoning could have the increase of the average particle size with a higher solid mass fraction on the suspension. A higher amount of HA precursor particles per droplet produces the increase of the final particle size. This direct proportional relation between the droplet size and the feed rate/solid mass fraction operating parameters was already mentioned in literature [45,46]. It is also clearly observed that a higher spray air pressure produces finer droplets reducing the average particle size [45–47].

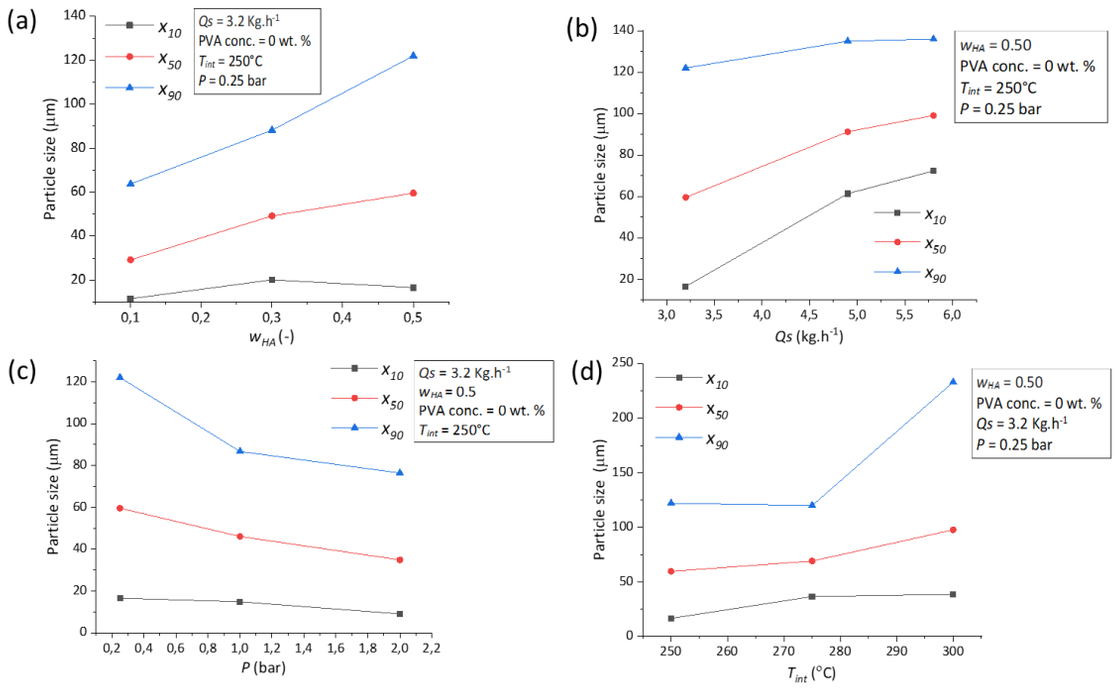

Figure 8. Main spray-dryer operating parameters effect on HAm average particle size (x_{10}, x_{50}, and x_{90}). (a) Solid mass fraction (runs 1-2-3), (b) feed rate (runs 1-4-5), (c) spray air pressure (runs 1-6-7), and (d) inlet temperature (runs 1-10-11).

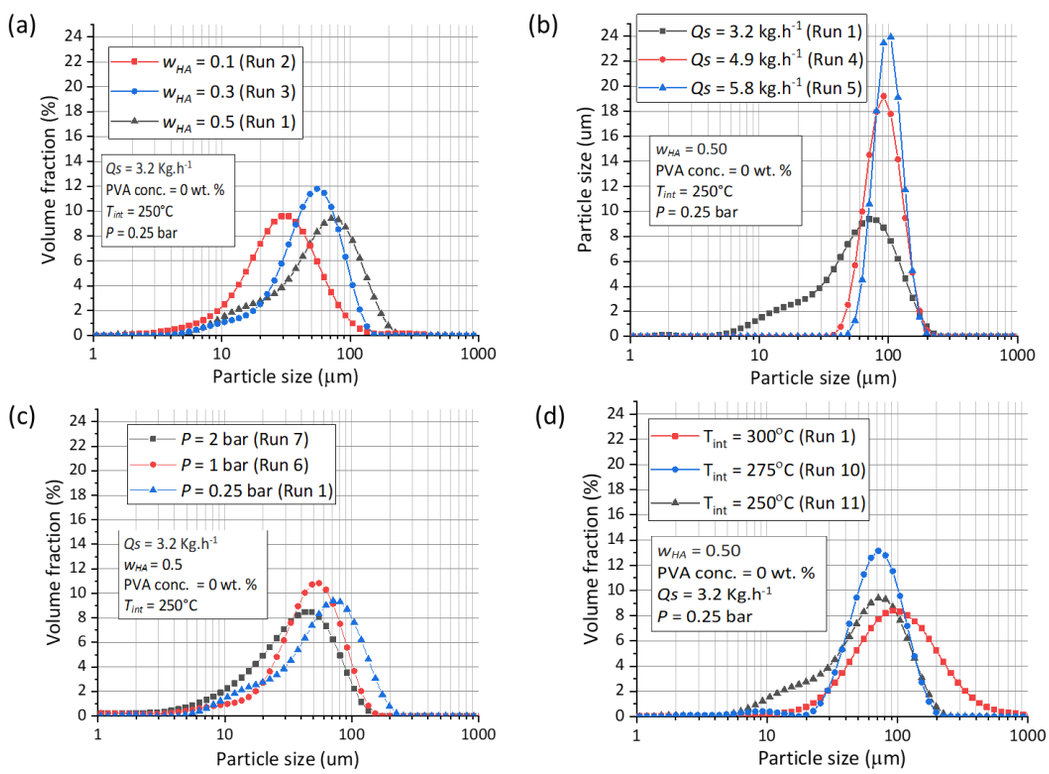

Figure 9. PSD of hydroxyapatite powders depending on the operating parameters: (a) Solid mass fraction (runs 1-2-3), (b) feed rate (runs 1-4-5), (c) spray air pressure (runs 1-6-7), and (d) inlet temperature (runs 1-10-11).

The inlet temperature is known to affect the final particle size in different ways [46,48]. A rise of the temperature reduces the slurry surface tension, expanding in consequence the droplets and dried particles size. The runs 1, 10, and 11 performed at different inlet temperatures from 250ºC to 300ºC showed an increase of the average particle size. However, the SEM analysis performed on these powders (Figure 10) showed the apparition of large particles with irregular shape when the inlet temperature was too high (Figure 10b, run 11). A higher temperature, and therefore a shorter drying time do not allow the correct organization of the particles forming the agglomerates. Thus, inducing an irregular shape as well as an increase of the agglomerates size, then in the runs 1 and 10 the critical temperature value was not exceeded and the formation of particles with irregular shape was avoided giving as result the production of HAm (Figure 10a).

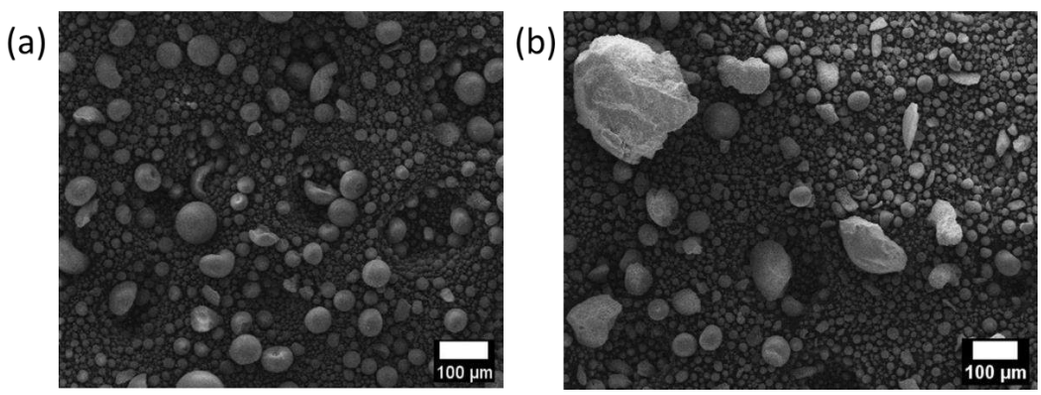

Figure 10. SEM micrographs of (a) HAm formed at inlet temperature of 275ºC (run 10), (b) powder at inlet temperature of 300ºC (run 11) with irregular shape particles.

The addition of PVA to the suspensions did not suppose a high increase of the suspension viscosity (< 0.1 Pa.s for the whole evaluated shear rate range). A too high viscosity could lead to handling problems during the spray drying process, especially during the pumping and mixing of the slurry [49]. However, even at higher viscosities than 0.1 Pa.s the successful spray drying processing of ceramic suspensions has been previously observed [43]. Then, together with the previous rheological study it was demonstrated that the use of PVA as binder during the granule formation in a SD process was possible. The addition of PVA (runs 1, 8 and 9) acting as binder in a range of 0-5 wt. % did not show any clear effect on the median particle size of the spray-dried HAm (Figure 11a). However, the addition of PVA seems to reduce the population of particles with a x_{50} = 15-20 µm. This could indicate a favouring of the formation of the HAm of larger size during the SD process or the enhancement of their hardness. A preliminary analysis of the mechanical properties of the HAm obtained was possible by using different dispersion pressures during the particle size analysis by laser diffraction in a dry way. It was observed that the granules spray-dried with a slurry free of PVA were more fragile and were more affected by the increase of the dispersion pressure reducing their

particle size (Figure 11b). More than a 50% of average particle size diminution was observed for the powder without PVA when the dispersion pressure was increased from 0.1 bar to 4 bar, while the powders containing PVA decreased their size a 25%.

A higher residual moisture was observed on spray-dried powders in presence of PVA (Runs 8 and 9) showing moisture content values in between 4-5%. While in absence of PVA, (rest of experimental runs) lower moisture content values ranging 1-2% were observed. This could be due to a higher water retaining in the structure of the agglomerates by the polymeric binder, but this increase of residual moisture should not affect their performance in a PBSLP apparatus. We could conclude that the addition of a binder such as PVA can improve the granules breakage resistance if the intended application requires it without an important alteration of the powder properties such as, PSD.

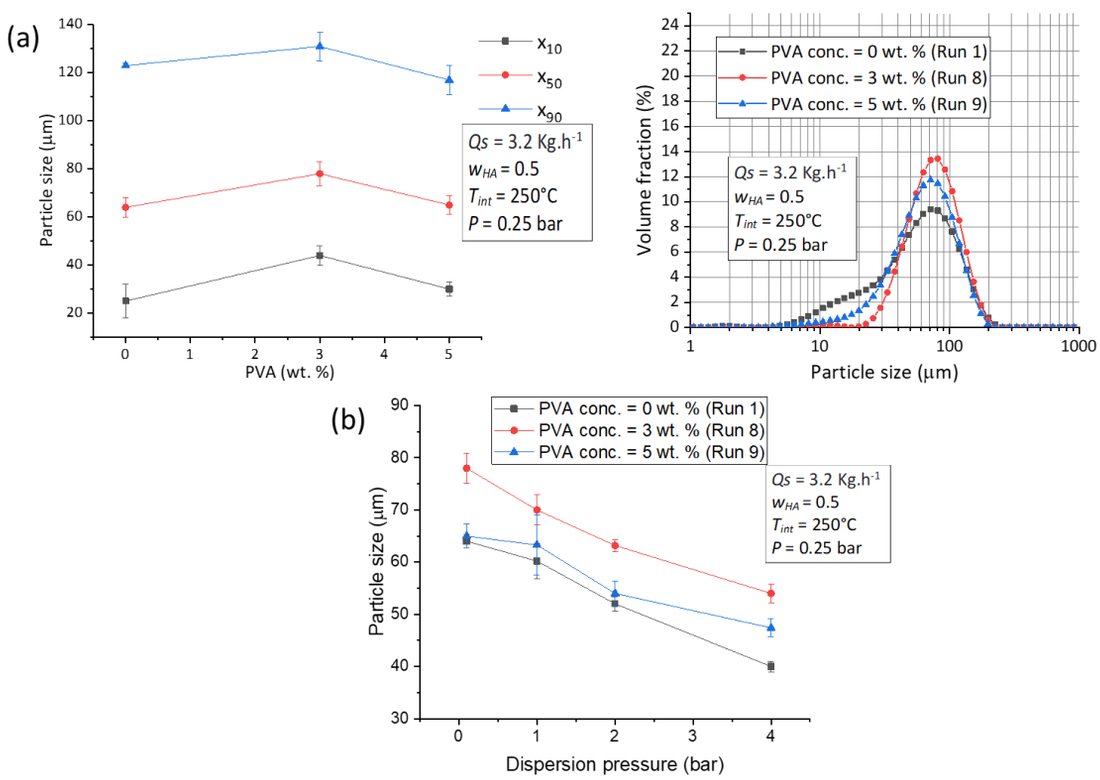

Figure 11. (a) Average particle size and PSD of spray-dried HA powders depending on slurry PVA binder concentration (Runs 1, 8, and 9). (b) Average particle size evolution of previous spray-dried powders at different dispersion pressures during the particle size analysis.

3.2.3 Spray drying operating parameters optimization

An additional study was performed to find a more optimal SD operating parameters combination for better process efficiency, what is to say, reaching a higher recovery rate (process performance) and evaporation capacity of the equipment. An increase of the feed rate could make difficult the atomization of too large droplets, since it could cause an insufficient drying rate when the inlet temperature is not high enough, reducing the recovery rate. For this reason, several experiments (runs 12, 13 and 14) were performed at experimental conditions where both, the feed rate and the inlet temperature were increased accordingly. Figure 12a shows the PSD and average particle size comparison between the three runs at different SD operating parameters sets (feed rates and temperatures). A slight increase of the average particle size is observed on the runs using higher feed rate and inlet temperature. In terms of particles morphology there were no big differences between them, showing all of them a predominance of the already seen HAm, also defined as, small rough spherical dense particles. SEM micrographs were obtained from runs 13 and 14 and they can be observed in Figure 12b and Figure 12c, respectively, showing no important differences in terms of particles morphology.

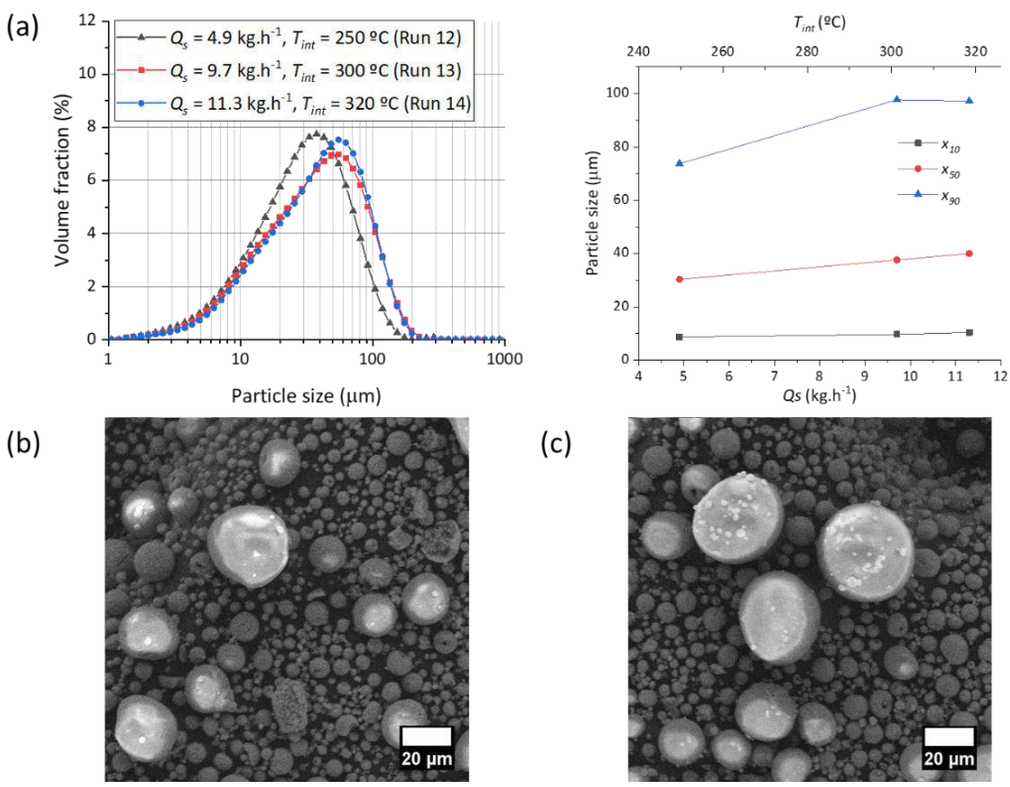

Figure 12. (a) PSD and average particle size of HA powders produced with the most efficient SD operating parameters sets (Runs 12, 13, and 14). SEM micrographs of HA powders produced at different combinations of feed rate and inlet temperature (a) Qs=9.7 kg.h^{-1}, T_{int}=300ºC (run 13) and (b) Qs= 11.3 kg.h^{-1}, T_{int}=320ºC (run 14).

For all the experiments, the recovery rate is understood as the yield of dry HA powder recovered in the collection jar at the end of the process respect to the solid mass within the spray-dried slurry. It was observed that the operating parameters of the SD process have an influence on the recovery percentage. Recovery rates of all experiment runs are summarized in Figure 13. A clear tendency to obtain higher recovery rate is observed when using higher spray air pressure (Runs 6 and 7). In addition, feed rate and inlet temperature play an important role to obtain a higher recovery rate. The highest recovery rates were obtained when, at high spray air pressure, the feed rate and the inlet temperature were increased accordingly (Runs 12, 13, and 14), thus reaching also the highest evaporation rate (amount of slurry evaporated per hour). Run 12 reached the highest recovery rate value of this study.

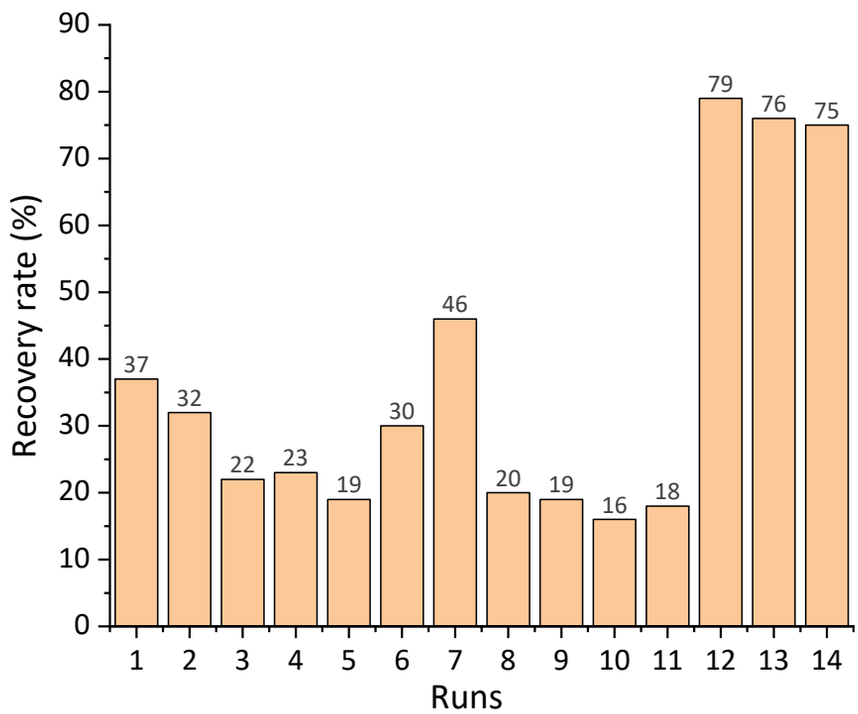

Figure 13. HA powder recovery rate of runs at different SD operating parameters.

In this section, several studies were performed to evaluate the SD process and the influence of its operating parameters on the final product quality. First, the time to reach the steady-state regime of the process was assessed and we concluded that it was relatively fast for the standard conditions used in the study. Then, in this case the time of the process was determined as not a relevant factor for the granule's formation and their final morphology at least as other operating conditions. Small rough dense particles or HAm was the predominant morphology in the SEM analyses of the majority of spray-dried powders with a lower presence of more irregular shape particles. Subsequently, the effect of the different operating parameters on the final product quality was evaluated. Feed rate and solid mass fraction showed the highest

effect obtaining larger average particle size when they are increased. It was demonstrated that there is a permissible limit value for the inlet temperature and when it is surpassed the morphology of the particles is affected producing particles with irregular shape. PVA addition to the slurries did not show a clear influence on the morphology of the powders obtained, neither at high a concentration of 5 wt. % although its presence improved the agglomerates breakage resistance. Spray air pressure seemed to be the parameter that affect the most the powder recovery rate obtaining higher values when it is increased.

3.3 Powders characterization

3.3.1 Flowability of powders

In this section, powders flowability, packing density, and physico-chemical properties were evaluated before and after the SD process to ensure that their flowability is improved and their material integrity remains unaltered during the process.

The importance of having a good powder flow behaviour is due to its direct impact on the homogeneity of a spread powder bed in a PBSLP apparatus. The quality of the powder bed influences the density of the printed parts. A deeper description of the different powder flowability measurement techniques (static and dynamic) to determine the flow behaviour of powders was offered by Spierings et al. [17]. It does not exist a single technique suitable for a complete characterization of a powder flow, for hence different techniques have to be used. The method used should match as much as possible the powder dynamics during its application to have the closest approximation to the reality [50]. The minimum limits for the flowability requirements are highly influenced by the PBSLP apparatus design and the type of layer creation device.

PSD and morphology of powders have an important effect on flowability of powders. In literature, different works have exposed that for powders of narrow PSD the most spherical and larger the particles, the better they flow [19–22]. Between powders with different level of PSD dispersion, a higher dispersion improves the flowability and packing density of the powder. In bimodal size distributions, the smaller particles fill the interstitial voids between the larger particles. A weight fraction of coarse particles about 70% is the condition showing maximum packing density [23–25].

In this study, three different powders were evaluated in terms of flowability. Initial HA powder before the SD process, spray-dried HAm produced following the conditions described in the run 1, and commercial HA powder 300-08-2 from Urodelia®. SEM micrographs of the spray-dried HAm were already shown previously (Figure 6) while the micrographs of the commercial and initial powders can be seen in Figure 14. Both commercial HA and the HAm produced in the present study have spherical shape due to the spray drying step carried out as part of their production process. This is not the case of the initial (and

pre-spray-dried) dry powder which shows an irregular shape. This last powder has a tendency to agglomerate when dry and an additional hand-crushing step was needed to homogenize it.

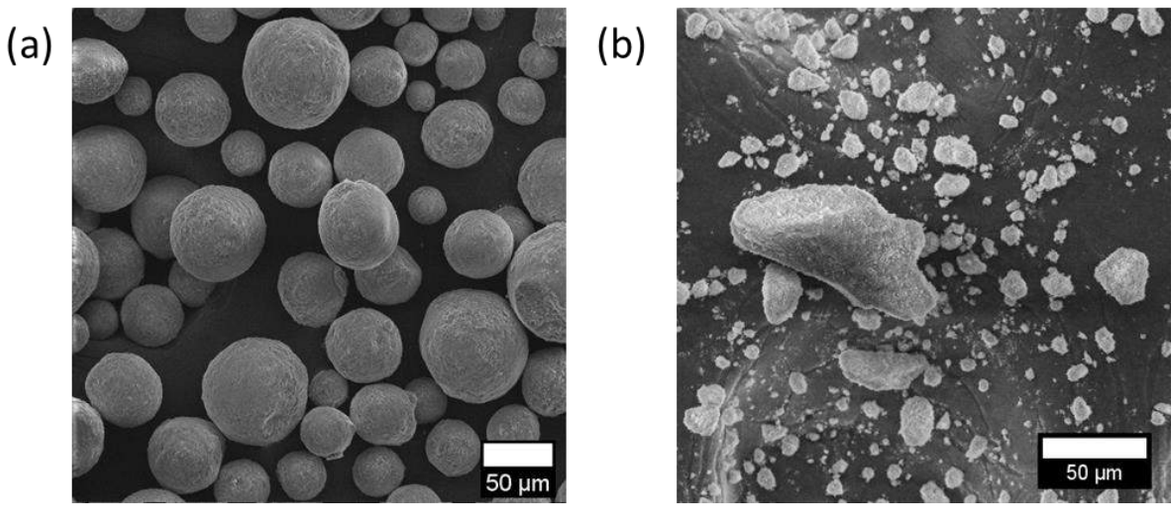

Figure 14. (a) Commercial Urodelia® 300-08-2 powder and (b) dry initial HA powder SEM micrographs.

Table 3 shows a summary of the properties of the three powders (Initial HA, spray-dried HAm, and commercial HA powder) that were evaluated with the different flowability tests. Between both spray-dried powders, the one produced during the run 1 in the present study and the powder from Urodelia®, the differences in flowability are less notorious and the powder that shows the best flowability is dependant of the flowability test. The results obtained from the angle of repose and flow rate tests indicate that the spray-dried powder from the present study could have a better performance than the commercial powder. However, the Hausner ratio indicates that these two are very close in flowability, slightly better in the commercial one. Only in the case of the flow function analysis, the initial powder takes the first position as the most flowable, although the three of them are classified as free flowing powders.

If we take into account that static and dynamic characterization techniques do not necessarily agree, for example, powders showing good fluidization performance can also show agglomeration. It means that flow properties are dependent upon the stress state and that there is no a unique technique suitable for a full characterization of a powder. Both types of techniques, static (e.g., flow function, compressibility, and Hausner ratio) and dynamic (e.g., flow rate) should be used to fully understand the flow behaviour of a powder. In the case of the angle of repose technique, it combines both static and dynamic elements and it is a common test for quality control allowing a quick comparison between flow properties of powders [52]. In this case, the flow rate technique has a closer powder dynamic to the recoating process in a PBSLP additive manufacturing apparatus, and then we could consider it as the most accurate method to evaluate the performance of the powders for a use as PBSLP powder feedstock.

Table 3. Flowability measurements of HA powders in the present study for comparison. Standardized methods according to the European Pharmacopoeia Chapter 2.9.36.

	Powder characteristics		Flowability tests results				
HA Powder sample	x_{50} (µm)	Span	Angle of repose α (°)	Compressibility index (%)	Hausner ratio *HR* (-)	Flow rate ($kg.h^{-1}$)	ff_c (-)
Initial HA (filtered and dry)	43.7	12.77	41.1 ± 1.9	27.62 ± 1.20	1,380 ± 0.021	86.9 ± 17.53	22,3 ± 2.4
Spray-dried HAm (Run 1)	59.6	1.78	26.5 ± 2.3	10.95 ± 0.56	1.123 ± 0.007	344.6 ± 27.7	21,4 ± 2.3
Urodelia® 300-08-2	63.6	0.81	30.9 ± 0.9	10.68 ± 1.67	1.120 ± 0.021	274.9 ± 21.8	15,9 ± 2.4

3.3.2 Physico-chemical properties of powders

To discard any possible alteration in the properties of the product, for example due to a phase transition or to any kind of contamination during the process, different physico-chemical analyses of the products were performed. Figure 15 shows the XRD spectra comparison between the initial HA powder and the powder once it has been spray-dried (run 1). A certain increase of the powder crystallinity (narrower peaks) was observed for the powder after the SD process. No phase transition was observed of the initial calcium phosphate phase (stoichiometric hydroxyapatite (JCPDS 00- 009-0432)) on the spectrum after the process [51].

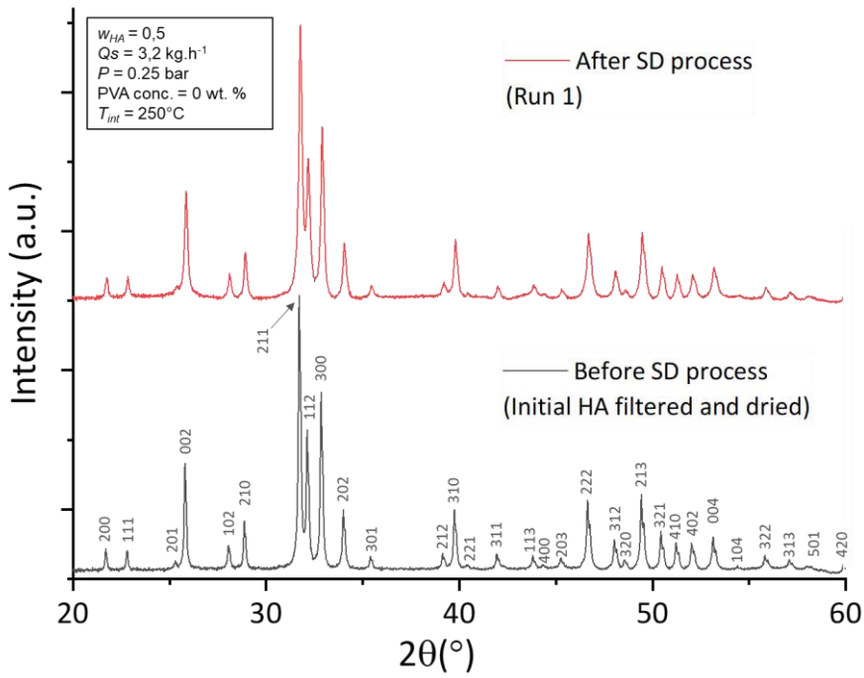

Figure 15. XRD spectrum analysis of the HA before and after the SD process. All the diffraction peaks correspond to stoichiometric hydroxyapatite (JCPDS 00 009 0432).

The FTIR spectra of the powder before and after the SD process are shown in Figure 16. There was no presence of side compounds that could be produced during the SD process. Then, as for XRD analysis, the FTIR method confirmed that the physico-chemical integrity of the material remains nearly unaltered.

PO_4 and OH^- vibration bands are visible at 1092 cm^{-1}, 1040 cm^{-1}, 962 cm^{-1}, 601 cm^{-1}, 575 cm^{-1}, 561 cm^{-1}, and at 650 cm^{-1} 3600 cm^{-1} respectively [51,52]. In the spray-dried powder spectrum, a weak, almost invisible band corresponding to water absorbed (3400 cm^{-1}) is observed confirming the low moisture present powder. A very weak band can be observed at 1400 cm^{-1} in pre-spray-dried HA powder which could correspond with a low presence of dispersant DC used in the suspension feedstock [53]. Then, the filtering and washing steps to obtain the initial dry powder could not be enough for a complete removal of the dispersant. However, after the SD process this band becomes nearly invisible indicating a more evident elimination of the dispersant during the process, which could be due to a thermal degradation.

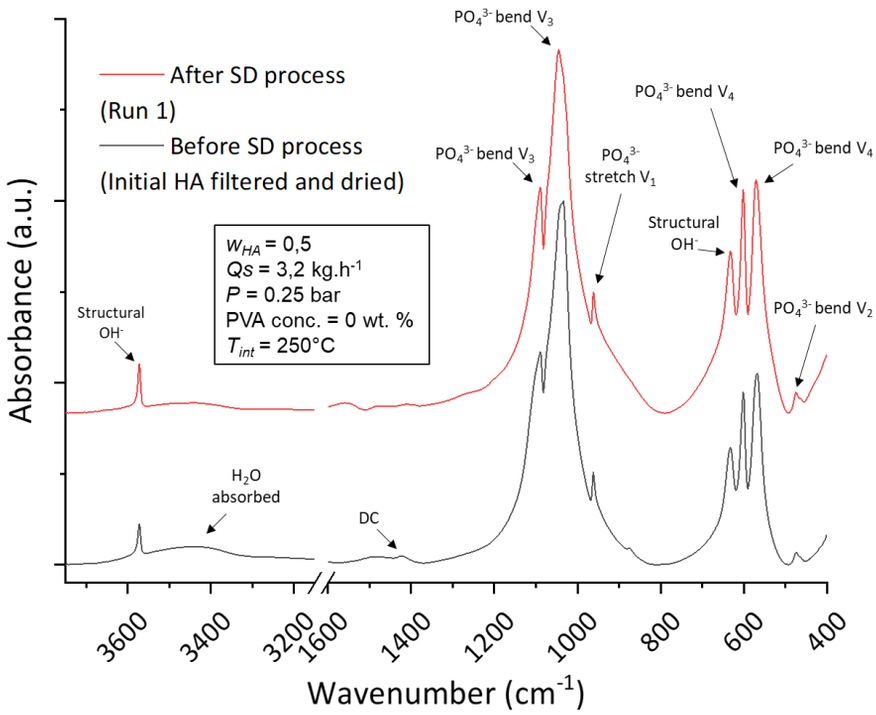

Figure 16. FTIR spectrum analysis of the HA before and after the SD process.

This section allowed us to emphasize the purpose of using a SD process to obtain HAm composed powder able to fulfil the flowability requirements in a PBSLP process. The comparison of the produced powder with the starting powder and an already commercial flowable powder made possible to evaluate the quality of our final product. The production of powder with a suitable flowability was then possible by SD process while the physico-chemical properties of the material remained unaltered and no presence of relevant contamination was observed.

4. Conclusions

In this paper, the effect of the SD process conditions concerning the slurry formulation and experimental parameters on the HAm size and morphology was discussed. PVA was demonstrated to be effective as binder improving the agglomerates breakage resistance without significant increase of suspension viscosity. The results indicated that the feed rate and solid mass fraction showed the highest effect on spray-dried particles morphology obtaining larger average particle size when they are increased. It exists a permissible limit value for the inlet temperature respect to the feed rate and when it is surpassed it alters the morphology of the particles producing particles with irregular shape. For temperatures under this limit, HAm was the main morphology obtained during the process. Several parameters set allowed us to obtain the targeted HAm particle size of 30 µm < x_{50} < 70 µm with a size distribution span higher than 1.

However, highest powder recovery rate values were obtained when using high spray air pressure together high temperature. It was demonstrated that the targeted powder properties help to fulfil the flowability requirements for its use as PBSLP powder feedstock through comparison with different powders. Physico-chemical properties of the powder were not altered during the process, demonstrating that SD process is a non-invasive method. This study allowed us to develop a quantitative relationship between powder morphology and SD process conditions while confirming that this is a promising process for the production of HAm with suitable properties for its use in a PBSLP process.

5. Acknowledgments

This project has received funding from the European Union's Horizon 2020 research and innovation programme under the Marie Skłodowska-Curie grant agreement No 764935.

6. REFERENCES

[1] A. Stunda-Zujeva, Z. Irbe, L. Berzina-Cimdina, Controlling the morphology of ceramic and composite powders obtained via spray drying – A review, Ceramics International. 43 (2017) 11543–11551. https://doi.org/10.1016/j.ceramint.2017.05.023.

[2] A.B.D. Nandiyanto, K. Okuyama, Progress in developing spray-drying methods for the production of controlled morphology particles: From the nanometer to submicrometer size ranges, Advanced Powder Technology. 22 (2011) 1–19. https://doi.org/10.1016/j.apt.2010.09.011.

[3] R.P. Patel, Spray drying technology: an overview, IJST. 2 (2009) 44–47. https://doi.org/10.17485/ijst/2009/v2i10.3.

[4] E. Kusrini, A.R. Pudjiastuti, S. Astutiningsih, S. Harjanto, Preparation of Hydroxyapatite from Bovine Bone by Combination Methods of Ultrasonic and Spray Drying, (2012) 5.

[5] F.E. Bastan, G. Erdogan, T. Moskalewicz, F. Ustel, Spray drying of hydroxyapatite powders: The effect of spray drying parameters and heat treatment on the particle size and morphology, Journal of Alloys and Compounds. 724 (2017) 586–596. https://doi.org/10.1016/j.jallcom.2017.07.116.

[6] Q. Murtaza, J. Stokes, M. Ardhaoui, Experimental Analysis of Spray Dryer Used in Hydroxyapatite Thermal Spray Powder, Journal of Thermal Spray Technology. 21 (2012). https://doi.org/10.1007/s11666-012-9791-9.

[7] N. Eliaz, N. Metoki, Calcium Phosphate Bioceramics: A Review of Their History, Structure, Properties, Coating Technologies and Biomedical Applications, Materials. 10 (2017) 334. https://doi.org/10.3390/ma10040334.

[8] D. Grossin, A. Montón, P. Navarrete-Segado, E. Özmen, G. Urruth, F. Maury, D. Maury, C. Frances, M. Tourbin, P. Lenormand, G. Bertrand, A review of additive manufacturing of ceramics by powder bed selective laser processing (sintering / melting): Calcium phosphate, silicon carbide, zirconia, alumina, and their composites, Open Ceramics. 5 (2021) 100073. https://doi.org/10.1016/j.oceram.2021.100073.

[9] Y. Xia, P. Zhou, X. Cheng, Y. Xie, C. Liang, C. Li, S. Xu, Selective laser sintering fabrication of nano-hydroxyapatite/poly-ε-caprolactone scaffolds for bone tissue engineering applications, Int J Nanomedicine. 8 (2013) 4197–4213. https://doi.org/10.2147/IJN.S50685.

[10] S. Eosoly, D. Brabazon, S. Lohfeld, L. Looney, Selective laser sintering of hydroxyapatite/poly-ε-caprolactone scaffolds, Acta Biomaterialia. 6 (2010) 2511–2517. https://doi.org/10.1016/j.actbio.2009.07.018.

[11] F. Cruz, Fabrication of HA/PLLA Composite Scaffolds for Bone Tissue Engineering Using Additive Manufacturing Technologies, in: M. Elnashar (Ed.), Biopolymers, Sciyo, 2010. https://doi.org/10.5772/10264.

[12] B. Duan, M. Wang, W.Y. Zhou, W.L. Cheung, Z.Y. Li, W.W. Lu, Three-dimensional nanocomposite scaffolds fabricated via selective laser sintering for bone tissue engineering, Acta Biomaterialia. 6 (2010) 4495–4505. https://doi.org/10.1016/j.actbio.2010.06.024.

[13] C. Colin, J.-D. Bartout, E. Shaker, Osseomatrix patent - WO2014154901A1, WO2014154901A1, 2014.

[14] C. Shuai, P. Li, J. Liu, S. Peng, Optimization of TCP/HAP ratio for better properties of calcium phosphate scaffold via selective laser sintering, Materials Characterization. 77 (2013) 23–31. https://doi.org/10.1016/j.matchar.2012.12.009.

[15] K. Zeng, D. Pal, B. Stucker, A review of thermal analysis methods in laser sintering and selective laser melting, 23rd Annual International Solid Freeform Fabrication Symposium - An Additive Manufacturing Conference, SFF 2012. (2012) 796–814.

[16] M. Schmid, F. Amado, G. Levy, K. Wegener, Flowability of powders for Selective Laser Sintering (SLS) investigated by Round Robin Test, in: P. da Silva Bártolo, A. de Lemos, A. Pereira, A. Mateus, C. Ramos, C. Santos, D. Oliveira, E. Pinto, F. Craveiro, H. da Rocha Terreiro Galha Bártolo, H. de Amorim Almeia, I. Sousa, J. Matias, L. Durão, M. Gaspar, N. Fernandes Alves, P. Carreira, T. Ferreira, T. Marques (Eds.), High Value Manufacturing: Advanced Research in Virtual and Rapid Prototyping, CRC Press, 2013: pp. 95–99. https://doi.org/10.1201/b15961-19.

[17] A.B. Spierings, M. Voegtlin, T. Bauer, K. Wegener, Powder flowability characterisation methodology for powder-bed-based metal additive manufacturing, Prog Addit Manuf. 1 (2016) 9–20. https://doi.org/10.1007/s40964-015-0001-4.
[18] G.V. Barbosa-Cánovas, ed., Food powders: physical properties, processing, and functionality, Kluwer Academic/Plenum Publishers, New York, 2005.
[19] H. Lu, X. Guo, Y. Liu, X. Gong, Effect of Particle Size on Flow Mode and Flow Characteristics of Pulverized Coal, KONA. 32 (2015) 143–153. https://doi.org/10.14356/kona.2015002.
[20] L.X. Liu, I. Marziano, A.C. Bentham, J.D. Litster, E.T.White, T. Howes, Effect of particle properties on the flowability of ibuprofen powders, International Journal of Pharmaceutics. 362 (2008) 109–117. https://doi.org/10.1016/j.ijpharm.2008.06.023.
[21] X. Fu, D. Huck, L. Makein, B. Armstrong, U. Willen, T. Freeman, Effect of particle shape and size on flow properties of lactose powders, Particuology. 10 (2012) 203–208. https://doi.org/10.1016/j.partic.2011.11.003.
[22] M.K. Stanford, C. Dellacorte, D. Eylon, Particle Size Effects on Flow Properties of Ps304 Plasma Spray Feedstock Powder Blend, in: W.M. Kriven, H.-T. Lin (Eds.), Ceramic Engineering and Science Proceedings, John Wiley & Sons, Inc., Hoboken, NJ, USA, 2003: pp. 577–585. https://doi.org/10.1002/9780470294802.ch82.
[23] D. Sofia, D. Barletta, M. Poletto, Flowability of ceramic powders in the sintering process, in: Jaipur (Rajasthan), India, Thapar University, 2016: p. 8.
[24] D. Sofia, R. Chirone, P. Lettieri, D. Barletta, M. Poletto, Selective laser sintering of ceramic powders with bimodal particle size distribution, Chemical Engineering Research and Design. 136 (2018) 536–547. https://doi.org/10.1016/j.cherd.2018.06.008.
[25] N.P. Karapatis, G. Egger, Optimization of Powder Layer Density in Selective Laser Sintering, in: AUSTIN, TX, 1999: p. 10.
[26] D. Yan, B. Zeng, Y. Han, H. Dai, J. Liu, Y. Sun, F. Li, Preparation and laser powder bed fusion of composite microspheres consisting of poly(lactic acid) and nano-hydroxyapatite, Additive Manufacturing. 34 (2020) 101305. https://doi.org/10.1016/j.addma.2020.101305.
[27] A. Krokos, A. Bondyra, R. Kwiatkowski, P. Gruber, M. Olejarczyk, B. Stępak, P. Dzienny, B. Kryszak, M. Gazińska, A. Antończak, Comparison of thermal, structural and morphological properties of poly(l-lactide) and poly(l-lactide)/ hydroxyapatite microspheres for laser sintering processes, Polimery. 65 (2020) 605–612. https://doi.org/10.14314/polimery.2020.9.2.
[28] C. Esposito Corcione, F. Gervaso, F. Scalera, S.K. Padmanabhan, M. Madaghiele, F. Montagna, A. Sannino, A. Licciulli, A. Maffezzoli, Highly loaded hydroxyapatite microsphere/ PLA porous scaffolds obtained by fused deposition modelling, Ceramics International. 45 (2019) 2803–2810. https://doi.org/10.1016/j.ceramint.2018.07.297.
[29] Y. Wang, W. Xu, Y. Lu, W. Xu, H. Yin, G. Xiao, Investigation of nature of starting materials on the construction of hydroxyapatite 1D/3D morphologies, Materials Science and Engineering: C. 108 (2020) 110408. https://doi.org/10.1016/j.msec.2019.110408.
[30] S. Mishra, T.R. Rautray, Silver-incorporated hydroxyapatite–albumin microspheres with bactericidal effects, J. Korean Ceram. Soc. 57 (2020) 175–183. https://doi.org/10.1007/s43207-020-00018-z.
[31] S.H. Daryan, A. Khavandi, J. Javadpour, Surface engineered hollow hydroxyapatite microspheres: Hydrothermal synthesis and growth mechanisms, Solid State Sciences. 106 (2020) 106301. https://doi.org/10.1016/j.solidstatesciences.2020.106301.
[32] H. Huang, M. Du, J. Chen, S. Zhong, J. Wang, Preparation and characterization of abalone shells derived biological mesoporous hydroxyapatite microspheres for drug delivery, Materials Science and Engineering: C. 113 (2020) 110969. https://doi.org/10.1016/j.msec.2020.110969.
[33] F. Erdem, The effect of binder on chemically precipitated hydroxyapatite during spray drying, Materiali in Tehnologije. (2013) 4.
[34] H.Y. Yang, M. Wang, Effect of reaction parameters on the thermostability of spray-dried hydroxyapatite powders, in: Processing and Fabrication of Advanced Materials VIII, WORLD SCIENTIFIC, Singapore, 2001: pp. 307–316. https://doi.org/10.1142/9789812811431_0036.
[35] L.C. Chow, L.M. Sun, B. Hockey, Properties of nanostructured hydroxyapatite prepared by a spray drying technique, J. Res. Natl. Inst. Stand. Technol. 109 (2004) 543. https://doi.org/10.6028/jres.109.041.

[36] H. Ji, H.M. Lim, Y.-W. Chang, H. Lee, Comparison of the Viscosity of Ceramic Slurries using a Rotational Rheometer and a Vibrational Viscometer, Journal of the Korean Ceramic Society. 49 (2012). https://doi.org/10.4191/kcers.2012.49.6.542.

[37] D18 Committee, Test Method for Bulk Solids Characterization by Carr Indices, ASTM International, n.d. https://doi.org/10.1520/D6393-14.

[38] Z. Sklubalova, Z. Zatloukal, The influence of orifice height on flow rate of powder excipients, Pharmazie. (2011) 953–955. https://doi.org/10.1691/ph.2011.1074.

[39] A.W. Jenike, Storage and flow of solids. Bulletin No. 123 of the Utah Engineering Experiment Station; Vol. 53, No. 26, November 1964, Utah Univ., Salt Lake City (United States), 1976. https://doi.org/10.2172/5240257.

[40] L. Parrella, D. Barletta, R. Boerefijn, M. Poletto, Comparison between a Uniaxial Compaction Tester and a Shear Tester for the Characterization of Powder Flowability, KONA. 26 (2008) 178–189. https://doi.org/10.14356/kona.2008016.

[41] S. Baklouti, P. Coupelle, T. Chartier, J. Baumard, Compaction Behaviour of Alumina Powders Spray-Dried with Organic Binders, Journal de Physique III. 6 (1996) 1283–1291. https://doi.org/10.1051/jp3:1996186.

[42] V. Naglieri, D. Gutknecht, V. Garnier, P. Palmero, J. Chevalier, L. Montanaro, Optimized Slurries for Spray Drying: Different Approaches to Obtain Homogeneous and Deformable Alumina-Zirconia Granules, Materials. 6 (2013) 5382–5397. https://doi.org/10.3390/ma6115382.

[43] A. Tsetsekou, C. Agrafiotis, I. Leon, A. Milias, Optimization of the rheological properties of alumina slurries for ceramic processing applications Part II: Spray-drying, Journal of the European Ceramic Society. 21 (2001) 493–506. https://doi.org/10.1016/S0955-2219(00)00232-6.

[44] M. Larsson, A. Hill, J. Duffy, Suspension Stability; Why Particle Size, Zeta Potential and Rheology are Important, Transactions of the Nordic Rheology Society. 20 (2012) 7.

[45] P. Luo, T.G. Nieh, Preparing hydroxyapatite powders with controlled morphology, Biomaterials. 17 (1996) 1959–1964. https://doi.org/10.1016/0142-9612(96)00019-1.

[46] F. Erdem, The effect of binder on chemically precipitated hydroxyapatite during spray drying, (2016) 7.

[47] B. Yu, Y.J. Feng, L.S. Wohn, C. Huang, Y.F. Li, Z. Jia, Spray-drying of alumina powder for APS: effect of slurry properties and drying conditions upon particle size and morphology of feedstock, Bull Mater Sci. 34 (2011) 1653–1661. https://doi.org/10.1007/s12034-011-0373-0.

[48] X.Q. Cao, R. Vassen, S. Schwartz, W. Jungen, F. Tietz, D. Stöever, Spray-drying of ceramics for plasma-spray coating, Journal of the European Ceramic Society. 20 (2000) 2433–2439. https://doi.org/10.1016/S0955-2219(00)00112-6.

[49] C. Onwulata, Encapsulated and Powdered Foods, 1st Edition, Boca Raton, 2005. https://doi.org/10.1201/9781420028300.

[50] M. Krantz, H. Zhang, J. Zhu, Characterization of powder flow: Static and dynamic testing, Powder Technology. 194 (2009) 239–245. https://doi.org/10.1016/j.powtec.2009.05.001.

[51] C. Rey, C. Combes, C. Drouet, D. Grossin, G. Bertrand, J. Soulié, Bioactive Calcium Phosphate Compounds: Physical Chemistry, in: Reference Module in Materials Science and Materials Engineering, Elsevier, 2017. https://doi.org/10.1016/B978-0-12-803581-8.10171-7.

[52] C. Rey, O. Marsan, C. Combes, C. Drouet, D. Grossin, S. Sarda, Characterization of Calcium Phosphates Using Vibrational Spectroscopies, in: B. Ben-Nissan (Ed.), Advances in Calcium Phosphate Biomaterials, Springer Berlin Heidelberg, Berlin, Heidelberg, 2014: pp. 229–266. https://doi.org/10.1007/978-3-642-53980-0_8.

[53] A.M. Popa, J. Vleugels, J. Vermant, O. Van der Biest, Influence of Surfactant Addition Sequence on the Suspension Properties and Electrophoretic Deposition Behavior of Alumina and Zirconia, Journal of the European Ceramic Society. 26 (2006) 933–939. https://doi.org/10.1016/j.jeurceramsoc.2004.12.023.

7. Supplementary material

Table S1. Flow properties based on angle of repose, compressibility index, and Hausner ratio.

Angle of repose (º)	*Compressibility index (%)*	*Hausner ratio HR (-)*	*Flow properties*
25-30	*<10*	*1.00-1.11*	*Excellent*
31-35	*11-15*	*1.12-1.18*	*Good*
36-40	*16-20*	*1.19-1.25*	*Fair*
41-45	*21-25*	*1.26-1.34*	*Passable*
46-55	*26-31*	*1.35-1.45*	*Poor*
56-65	*32-37*	*1.46-1.59*	*Very poor*
>66	*>38*	*>1.60*	*Very very poor*

Table S2. Classification of flow function used by Jenike [39].

$ff_c < 1$	*not flowing*
$1 < ff_c < 2$	*very cohesive*
$2 < ff_c < 4$	*cohesive*
$4 < ff_c < 10$	*easy flowing*
$10 < ff_c$	*free flowing*

Chapter V. Powder bed selective laser processing (sintering/melting) applied to tailored calcium phosphate-based powders

Powder bed selective laser process (sintering/melting) applied to tailored calcium phosphate-based powders

Pedro Navarrete-Segado,[a,b] Christine Frances,[b] Mallorie Tourbin,[b] C. Tenailleau[c], B. Duployer[c], David Grossin[a,*]

[a] CIRIMAT, Université de Toulouse, CNRS, 4 Allée Émile Monso, 31432 Toulouse Cedex 4, France

[b] Laboratoire de Génie Chimique, Université de Toulouse, CNRS, 4 Allée Émile Monso, 31432 Toulouse Cedex 4, France

[c] CIRIMAT, Université de Toulouse, CNRS, 118, Route de Narbonne, 31062 Toulouse cedex 9, France.

Abstract. This paper focuses on the tailoring of calcium phosphate powders for their use as powder bed selective laser process feedstock. Hydroxyapatite and chlorapatite were used as starting powders for the preparation of different blends through the addition of graphite as a laser absorptance additive. A methodical study was conducted to compare the processing windows of the blends containing different amounts of graphite through the laser patterning of circular samples. It was found that the addition of graphite increases the process window of the powder blends being the powder without additive non processable. Hydroxyapatite showed a clear phase transition (decreased when using higher volumetric energy density) into other calcium phosphate phases while chlorapatite was demonstrated to be thermally stable during the whole process (examined through X-ray diffraction and vibrational spectroscopies). In parallel, the study evaluating the powder blend composed of hydroxyapatite and graphite for the production of solid and complex parts was carried out although it required long printing times. The productivity of the process was improved by modification of printing parameters. Then, a series of solid samples were produced for the analysis of the microstructure and mechanical properties. High interconnected porosity was observed in the samples which could improve the bioactivity of the bioceramic scaffolds. A post-treatment of the parts increased their proportion in the hydroxyapatite phase and their mechanical properties. These results are expected to contribute to the application of powder bed selective laser processing of calcium phosphates powders toward bone tissue engineering.

Keywords: hydroxyapatite, chlorapatite, powder bed fusion, selective laser sintering, selective laser melting

***Corresponding author: david.grossin@ensiacet.fr

1. Introduction

The use of powder bed fusion selective laser processing (PBSLP) (sintering/melting) additive manufacturing (AM) technology for the production of calcium phosphate scaffolds has been largely studied [1]. The printed bioactive scaffolds would serve as the starting point for the growth of new bone for bone replacement applications. Three main strategies have been followed by researchers for the shaping of bioceramic powders through PBSLP.

The first strategy consisting of the use of polymeric powders (e.g., polyethylene, poly-ϵ-caprolactone, and poly (L-lactic acid)) filled with calcium phosphate powders has been widely studied [2–5]. The polymer as the main component in the powder feedstock is melted through the laser irradiation giving as result the printed polymer/ceramic composite scaffold. Since these polymers are not removed after the PBSLP process the time of implantation can have some adverse effects on them losing some of their properties.

A second strategy is based on the use of a more similar ratio of polymer /ceramic components to print green body (polymer/ceramic composite) scaffolds. These are then submitted to pyrolysis (of the sacrificial polymer) and sintering steps to obtain the final sintered bioceramic scaffold free of the polymer [6].

The third strategy is the use of the bioceramic powder directly as the main component in the PBSLP process feedstock [7]. In this case, the material interacting with the laser is the ceramic powder whose response will be highly influenced by the type of laser-equipped in the PBSLP apparatus. The laser beam energy has to be absorbed and transformed into heat to trigger the sintering/melting of the powder. Different materials show different absorptance levels depending on the wavelength of the laser used. It is known that ceramic insulators (e.g. calcium phosphates) mainly absorb the light energy emitted by CO_2 lasers (λ = 10600 nm) however it is not the case when using a fiber laser source (λ = 1070 nm). The second one is the most common laser-equipped in PBSLP apparatus since it is greatly absorbed by metals, which are the most explored material feedstock in PBSLP technology. For this reason and because of the high cost of the PBSLP equipment there is a significant demand for the development of ceramics adapted to this kind of laser increasing the number of suitable materials feedstock for the same printer. The addition of absorptance additives has been studied as a method to deal with the observed low absorptance by oxide ceramic materials of fiber laser energy needed for their processing. Carbon graphite-based filler has been demonstrated to increase the fiber laser absorptance by adding small amounts in the material feedstock making possible the printing of oxide ceramics [8,9].

The energy input of the process is defined as volumetric energy density (E_d) ($J.cm^{-3}$) and different formulations have been considered for its calculation [1]. Most of the current research on process optimization considers the equation (1) for its calculation, which will be used in the present study. However, caution should be given when using E_d since recent works already showed that this equation gives only an

approximate estimation and further analyses on the hatch parameters and material properties should be done for a correct evaluation of the energy density [10].

$$E_d = \frac{P_{laser}}{v_{scan} \cdot h_{space} \cdot t_{layer}} \quad (1)$$

Where P_{laser} is the laser power (W), v_{scan} the scanning speed (cm.s^{-1}), h_{space} is the hatching distance (cm), and t_{layer} is the layer thickness (cm). Recently, Leo et al. [11] remarked the importance of the laser defocus (positive and negative sense) for the process since it has a significant effect on the final microstructure by varying the spot size and for hence the E_d. In particular, when working at low laser power (~38 W), they found that small variations in the defocus value induced significant changes in the part properties. It is then of vital importance the study of the different PBSLP parameters for each material feedstock to find a processing window showing better sintering/melting phenomena of the powder, thus obtaining high-quality parts.

Thus, the goal of the present work was to evaluate the performance of different graphite-filled calcium phosphate powders (HA & ClA) as PBSLP process feedstock. Our study started with the preparation of calcium phosphate powders feedstock through the addition of different amounts of graphite as an absorptance additive. Then the performance of the different feedstock was evaluated in a PBSLP process at different printing conditions to evaluate the influence of the E_d in the final sample properties. The comparison between the different powders and parameters was possible through the examination of the chemical and structural composition, morphology, and mechanical properties of the printed samples.

2. Materials and method

2.1 Materials

Hydroxyapatite (HA) microspheres powder was used as the main component for the production of the powder blends that will be used as material feedstock for the PBSLP process. This initial powder was produced by Urodelia (SA Company, Saint-Lys, France) via wet-chemical coprecipitation and a posterior spray-drying process (product reference 300.08.2). More information about the wet-chemical approach followed was offered in previous work [12]. The spray drying process of hydroxyapatite powders was covered previously with a deeper examination of the HA microspheres flowability in chapter IV. The spray drying step was crucial to produce the flowable HA powder composed of spherical agglomerates.

In addition, pure chlorapatite (ClA) powder was produced through a solid-gas reaction (chlorination) of the initial HA powder in a tubular furnace. The procedure followed (based on the work of Demnati et al. [13]) was already described in chapter II of the present work. This ClA powder was also used as the main component for the preparation of blends employed as PBSLP process feedstock.

Different powder blends were produced by mixing graphite as an absorptance additive with HA and ClA powders as main components. TIMREX® KS 44 Graphite by Imerys is a carbon graphite-based filler that acts as a near-infrared absorptance additive improving the laser-material interaction of the powders. The preparation of the blends was carried out by pouring the previously weighted amounts of powders in a mixing jar, then the powders were mechanically blended using a Turbula shaker mixer for 1 hour. A list of the acronyms referring to the raw and prepared powder blends is given in Table 1.

Table 1. Acronyms for different raw materials and blends feedstock used during our study.

Powder/blend acronym	Description
HA	Hydroxyapatite microspheres used as raw material.
ClA	Chlorapatite microspheres used as raw material.
G	Graphite flakes used as raw material (absorptance additive).
HA_5G	Powder blend composed of hydroxyapatite and a 5 wt. % of graphite.
HA_10G	Powder blend composed of hydroxyapatite and a 10 wt. % of graphite.
ClA_5G	Powder blend composed of chlorapatite and a 5 wt. % of graphite.

TA6V discs with one side coated by plasma spray with pure HA (0.1 mm coating thickness) were used as a substrate to improve the attachment of the first printing layers to the building platform surface. The dimensions of the discs were 10 cm in diameter, 2 mm of TA6V thickness. They were produced by the company 2PS (Projection Plasma Système, Montbazens, France), which is specialized in plasma projection coating of orthopedic implants.

2.2 Characterization methods

2.2.1 Chemical and structural analyses

Different characterization techniques were used to confirm the chemical and structural composition of the raw and produced materials. X-ray diffraction (XRD) analyses of both powders and printed samples were performed in a BRUKER's X-ray diffractometer D8 Advance system with Cu Kα radiation (wavelength $\lambda = 0.15406$ nm), a nickel filter at 40 kV and 40 mA, and a LYNXEYE XE-T detector (energy resolution of 0.38 keV). Samples were analysed using a 6 mm x 2 mm slit in a 2θ range between 20º and 90º, a step of 0.03º 2θ, and a time per step of 0.2 s.

Rietveld refinement method was applied to estimate the crystalline phase compositions of the different printed samples containing a multiphase calcium phosphate mixture of hydroxyapatite (HA) $Ca_{10}(PO_4)_6(OH)_2$, alpha-tricalcium phosphate (α-TCP) ($Ca_3(PO_4)_2$, tetracalcium phosphate (TTCP) $Ca_4(PO_4)_2O$, and graphite (C) phases. MAUD (Material Analysis Using Diffraction) software (written by Luca Lutterotti [14]) was used for the diffraction analyses. The following methodology was followed to estimate the phase compositions of the multiphase samples. Rietveld refinements were performed in a 2θ range between 21º and 36º. This range was chosen to include the main reflections of each phase. All samples were refined assuming the possible presence of the four phases, and the crystallographic information frameworks (CIF) of the standard single-phase standards were employed for the refinement (phase/database/code: HA/AMCSD/0002281; Graphite/AMCSD/0000049; α-TCP/COD/2106194 TTCP/ICSD/2631). Seven background points were settled for the calculation of the complete background curve via linear interpolation.

Fourier transform infrared spectroscopy (FTIR) analyses were performed to determine the chemical composition of powders using a spectrometer FTIR iS50 and the KBr pellet preparation method. About 9 mg of powdered sample was transferred to a clean mortar, then a weighed amount of dry KBr powder (300±5 mg) was added and homogenously mixed. A compression at 6000 kg was employed to produce the sample disk used for the analysis. FTIR spectra were recorded in the 4000-400 cm^{-1} wavenumber range using a step width of 0,48 cm^{-1}.

A Horiba-Jobin Yvon Labram HR 800 Raman spectrometer provided with 633 nm laser excitation was used to obtain the Raman spectra of the samples during our study. For reference, standard Raman spectra have been obtained from the RRUFF™ Project database for pure HA (RRUFF id: R100225, 780 nm), and ClA (RRUFF id: R060192, 780 nm). Raman spectra from TTCP and α-TCP were obtained through the analyses of pure ceramic samples in the laboratory.

2.2.2 Morphological and structural properties

The particle size distribution (PSD) of the different powders used in this work was analysed in dry conditions with a Mastersizer MS 3000 (Malvern Panalytical®) laser particle size analyser. For the analyses, the powder was dispersed at a venturi pressure of 0.1 bar. Refractive indexes for the different powders were taken as 1.63 (HA), 1.65 (ClA), 2.70 (graphite) while the absorption indexes were 0.01 (HA), 0.01 (ClA), 1 (graphite). The morphology of powders was investigated with a scanning electron microscope (SEM) LEO 435 VP (Leica®) equipped with a Ge detector (Imix-PC, PGT) after metallization of the ceramic surface with a thin film of silver using a Scancoat Six sputter coater. Printed samples were analysed in a FEI ESEM Quanta™ 450 FEG, an environmental scanning electron microscope (ESEM) used with a large field detector (LFD) in low vacuum (LowVac) mode without previous metallization of the surface of the sample. ImageJ was used for the processing of the images [15].

High-resolution X-ray micro-computed tomography (CT) analyses of the HA cylinders were performed in a phoenix nanotom® equipped with a 180 kV / 15 W high-power nanofocus X-ray tube (9 µm voxel size, resolution). A 3D perspective of the cylinders was reconstructed and it was possible to examine their total porosity. VGStudio MAX 4.4 software was used to reconstruct the data sets and visualize the objects three-dimensionally.

The geometrical density of the cylinders was calculated from the mass and dimensions of at least ten samples. For comparison, the density of the parts was also measured by Archimedes' method in distilled water as liquid.

2.2.3 Laser absorptance of powders

Diffuse reflectance spectra were collected using a double beam spectrophotometer AGILENT® Cary 5000 UV/Visible/NIR and integration sphere accessory of 110 mm. Before the measurements, predetermined photometry calibration was made using specimens with known reflectance. Experimental data were collected within the 900-1200 nm range with 1 nm step and 0.5 s integration time. Powders were compacted in the sample holder and were approximatively 3 mm thick. The absolute transmittance and reflectance can be measured directly with high accuracy and the absorptance can be obtained from these by a simple calculation:

$$A = 1 - R - T \qquad (2)$$

Where A represents absorptance, R is reflectance and T is transmittance (which is considered equal to zero). A predetermined photometry calibration was made using specimens with known reflectance. Three different samples (N=3) were taken for each blend and were measured obtaining the mean value and the standard deviations (mean ± standard deviation) evaluating their homogeneity.

2.2.4 Mechanical properties of HA cylinders

The procedure followed for the analysis of the compression strength of the HA cylinders is described in ISO 13175-3:2012 [16]. The compression strength of the printed cylinders before and after thermal post-treatment was measured in an MTS Criterion® Model 42 electromechanical universal test system. An MTS load cell model LSB.203, with a capacity of 2000 N was used to measure the shear force at a crosshead speed of 0.085 mm/s at room temperature. Samples were submitted to a pre-stress of -3N to avoid any irregularity due to the state of the sample surface before starting the compression test. The measurements were stopped manually once the cylinder collapsed. The samples were set in the middle of the plate vertically inverted to the printing orientation. Since it was a preliminary study, a low number of measurement

repetitions were performed: three post-treated cylindric samples (N=3, mean ± standard deviation) and one as-printed.

2.3 PBSLP process

PBSLP process of the blend powders was performed in a 3D Systems ProX® DMP 200. Parts are built up layer by layer sintering/melting the powder particles by a laser which is directed to the powder particles. The laser follows the pre-loaded 3D model building selectively the subsequent horizontal layers. The manufacturing process is then carried out by joining each new layer to the previous one.

The main components present in the manufacturing chamber of the printer are illustrated in Figure 1. A roller (with 110 mm of diameter) which can move in a straight line using a carriage (speed of 400 mm/s, accuracy <1 mm) and rotate (with speed 3.7 turns per second, accuracy <5º) carry out the actions of layering such as spreading, smoothing, and compacting. The layer thickness of powder can differ depending on the material properties (particle size, flowability…). A scraper enables to carry the powder from the feeding piston to the sintering piston. The feeding piston contains the powder reservoir used for sintering (140 x 140 mm, powder volume: 3.85 liters). Parts are manufactured on the TA6V discs coated with HA (which are glued onto the sintering plate which is positioned on plate support on the sintering piston (140 x 140 mm). A collecting tank recovers all non-sintered powders and residues that can be treated for recycling. Since no material is removed, waste is reduced significantly. It is a Class I Laser System. The main optical devices are a fiber laser source (continuous operation, single-mode, power at the collimator output 300W, wavelength in the shortwave infrared range (approx. 1070 nm), a collimator (outlet beam diameter at $1/e^2$ 15 mm), a scanner head, and a flat field F-Theta lens (420 mm focus length). This configuration gives a beam diameter of the focal spot of 38.1 µm. A preliminary trial-and-error study of the powders' processability allowed us to enclose the parameters range used in the present study. These are described in Table 2.

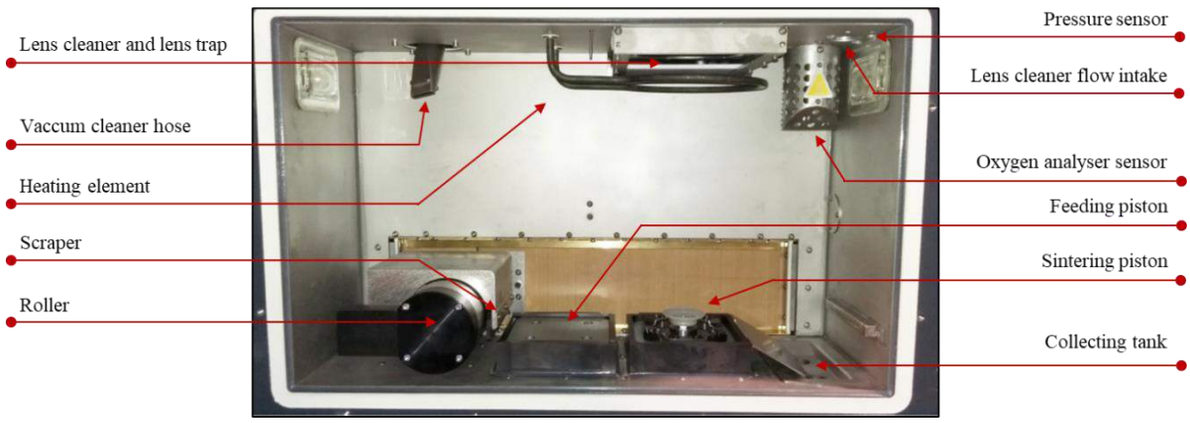

Figure 1. Photograph showing main components present in the manufacturing chamber of a 3D Systems ProX® DMP 200 printer (Adapted from equipment user guide).

Table 2. Fixed and studied parameters for the determination of the processing window of the PBSLP process in the present work.

	Parameter	Value
Studied	Fiber laser power (W)	30-54
	Scan speed (mm/s)	25-125
	Laser scan strategy	Hexagonal & Zig-Zag (5 laser passes) (90° rotation between layers)
Fixed	Hatching distance (mm)	0.05
	Layer thickness (mm)	0.10
	Atmosphere	Air
	Powder compression (%)	300
	Laser defocus	3 cm downward of the focus plane
	Printing substrate	HA-coated TA6V disc
	Chamber preheating	No

Three different approaches were performed in parallel to study the influence of the printing parameters and feedstock formulation. For each of the approaches different 3D models were used for the printing of the samples, also they were printed with two different laser scanning strategies. These two laser scanning strategies are illustrated in Figure 2.

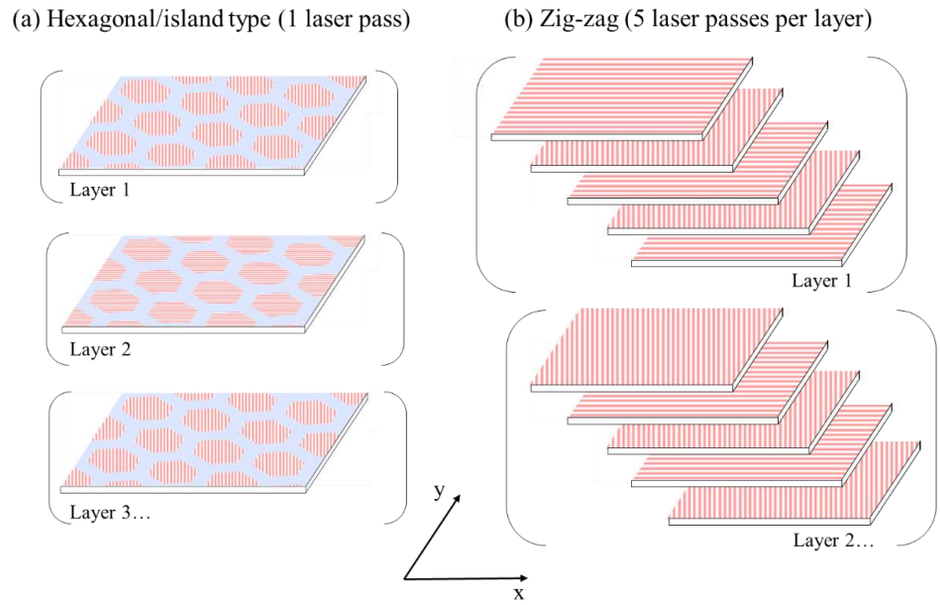

Figure 2. Schematic diagram of the two laser scanning strategies used during the three approaches: (a) Hexagonal/island type scanning (1 laser pass per layer) and (b) zig-zag scanning (5 laser passes per layer). In red the pattern followed by the laser scans and the blue regions refer to the overlap between hexagons.

The three kinds of samples together with the strategies followed for each approach are described below:

- The first approach, laser-induced circular patterns: The 3D model consisted of a short cylinder of 8 mm of diameter and 0.8 mm of height. In this case, the laser scan strategy used was a hexagonal (island type) strategy (Figure 2a). The continuous hexagons had 0.2 mm of diameter and overlap between them of 0.1 mm. The orientation of the hexagons was rotated 90º between layers. This kind of sample was conceived to study the influence of the printing parameters (or E_d) and evaluate the process window of the different powder blends. This specific sample design allowed us to shorter the printing times and to perform different characterization techniques (XRD, Raman, SEM…) directly on the substrate. Once the samples were produced, compressed air was used to clean the surface of the disk to remove the raw material particles settled on the samples.
- The second approach, HA complex shape: In parallel to the previous approach, the printing of two different 3D models with increased shape complexity was evaluated. One model consisted of a cylindrical scaffold (20 x 17 mm) with controlled internal porosity while the second one was based on a trapezoid with a toothed bottom surface (8 x 25 x 13 mm). The same hexagon-based laser scan strategy as in the first approach was used (Figure 2a). However, only one combination of laser parameters was tested (laser power: 30 W, scanning speed: 25 mm/s, E_d: 240 J.cm^{-3}) for both parts. The model used for these samples was designed to test the printing

feasibility of 3D complex parts with a set of printing parameters. After printing, a homemade endless diamond wire saw was used to detach the scaffold from the substrate while for the trapezoid it was not necessary thanks to its toothed bottom surface.

- The third approach, HA cylinders: A cylinder of 10 mm of diameter and 15 mm of height was used as a 3D model (taking into account the dimensions needed for mechanical tests which are described in ISO 13175-3:2012). The E_d and laser parameters combination used for the printing was obtained from the results of the first approach studying the process window (laser power: 36 W, scanning speed: 75 mm/s, E_d: 96 J.cm^{-3}). Due to the low building rate of the hexagonal-based laser strategy for the printing of solid parts (second approach), a new laser scan strategy of zig-zag was used to increase it (Figure 2b) (the building rates obtained for the second and third approaches will be discussed in the next section). Because the overlapping of laser passes in the same region seemed to enhance the final result, an overlapping of 5 laser passes per layer over the same irradiated region was used. The orientation of the laser tracks was rotated between both passes and layer steps. The model used for these samples was designed to perform a posterior compression strength test as well as chemical and structural characterization. After printing, it was possible to detach the HA cylinders from the substrate by hand without modifying their surface.

A list of the acronyms referring to the printed samples corresponding to each of the three different approaches followed is given in Table 3.

Table 3. Acronyms for different printed samples in each of the three approaches followed during our study

Approach	Printed sample acronym	Description
First approach	HA_5G_96	Laser-induced circular pattern produced at 96 J.cm^{-3} with a powder blend composed of hydroxyapatite and a 5 wt. % of graphite.
	HA_10G_57.6 / 96 / 288	Laser-induced circular patterns were produced at 57.6, 96, and 288 J.cm^{-3} with a powder blend composed of hydroxyapatite and a 10 wt. % of graphite.
	ClA_5G_96 / 336	Laser-induced circular pattern produced at 96, and 336 J.cm^{-3} with a powder blend composed of chlorapatite and a 5 wt. % of graphite.
Second approach	HA_Scaffold	Calcium phosphate scaffold complex part produced at 240 J.cm^{-3} with a powder blend composed of hydroxyapatite and a 5 wt. % of graphite.
	HA_Trapezoid	Calcium phosphate trapezoid complex part produced at 240 J.cm^{-3} with a powder blend composed of hydroxyapatite and a 5 wt. % of graphite.
Third approach	HA_Cyl	Calcium phosphate cylinders produced at 96 J.cm^{-3} with a powder blend composed of hydroxyapatite and a 10 wt. % of graphite.
	HA_Cyl_PT	Sample HA_Cyl after thermal post-treatment.

2.4 Thermal post-treatment

A posterior thermal post-treatment was performed at air presence for the HA cylinders to study the changes in their chemical and structural properties as well as in their mechanical properties. The cylinders were placed between two alumina crucibles which were set in the middle of the muffle Nabertherm® LT 9/13 furnace chamber favouring a more homogeneous heat distribution. The temperature programme consisted of a heating ramp of 2ºC/min till a temperature of 1250ºC. This temperature was kept constant for 2 hours before starting the cooling phase (-1ºC/min).

3. Results and discussion

3.1 Characterization of raw/prepared powders and substrate

The PSD and the SEM micrographs of each of the three raw powders (HA, ClA, and graphite) used for the preparation of the PBSLP feedstock materials are illustrated in Figure 3. It can be observed how the ClA and the HA powders have almost similar properties. It demonstrates that the chlorination of the HA powder to obtain ClA powder does not modify their morphology keeping unaltered the PSD and the spherical shape of the agglomerates. The graphite powder is composed of flakes with smaller median particle size and a more dispersed distribution.

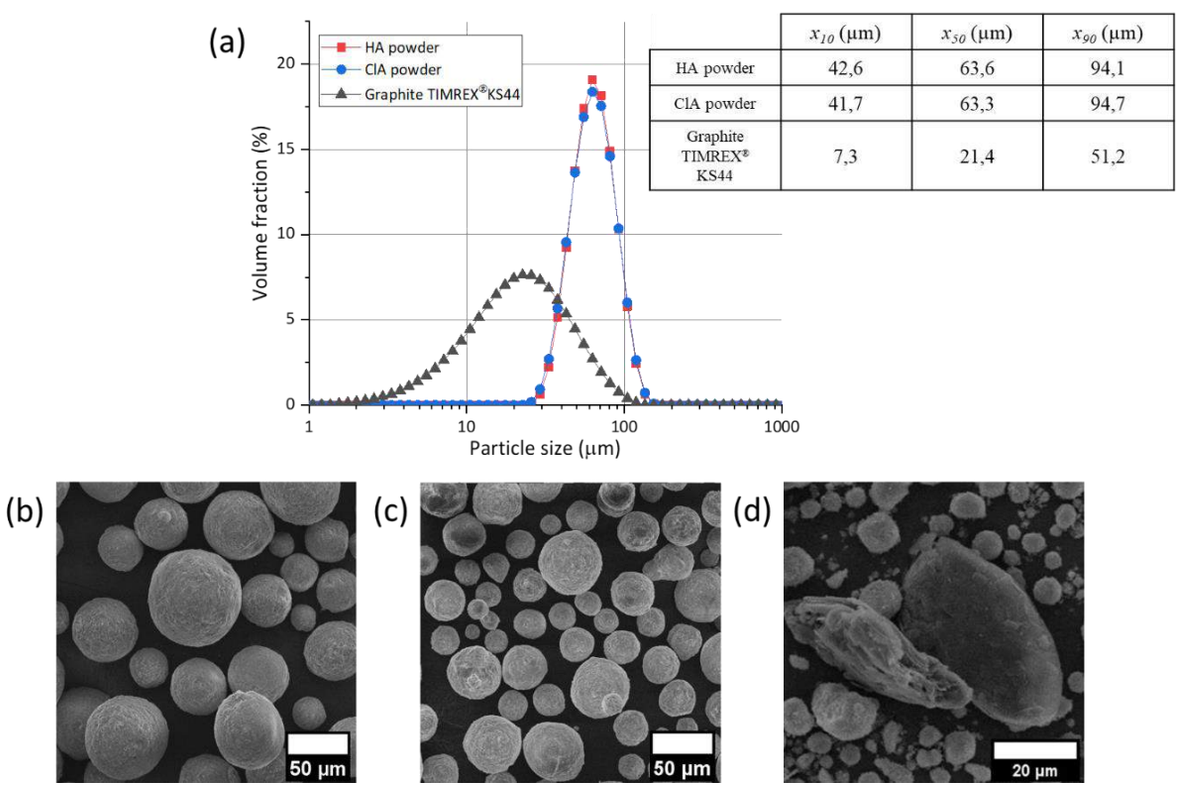

	x_{10} (µm)	x_{50} (µm)	x_{90} (µm)
HA powder	42,6	63,6	94,1
ClA powder	41,7	63,3	94,7
Graphite TIMREX® KS44	7,3	21,4	51,2

Figure 3. (a) Particle size distributions and SEM micrographs of (a) HA, (b) ClA microspheres, and (d) graphite flakes (in a blend) used as raw materials

The obtained Raman spectra and X-ray diffractograms of the initial ceramic powders are offered in Figure 4 and Figure 5, respectively. For reference, standard Raman spectra have been obtained for HA (RRUFF id: R100225), and ClA (RRUFF id: R060192) from the RRUFF™ Project database. The chemical and structural composition of each of the initial powders was confirmed. We can point out the presence of both monoclinic and hexagonal phases in the ClA diffractogram. This partial phase change could be produced during its synthesis since it is known that ClA undergoes a phase change from hexagonal to monoclinic upon heating at 200-300 ºC [17].

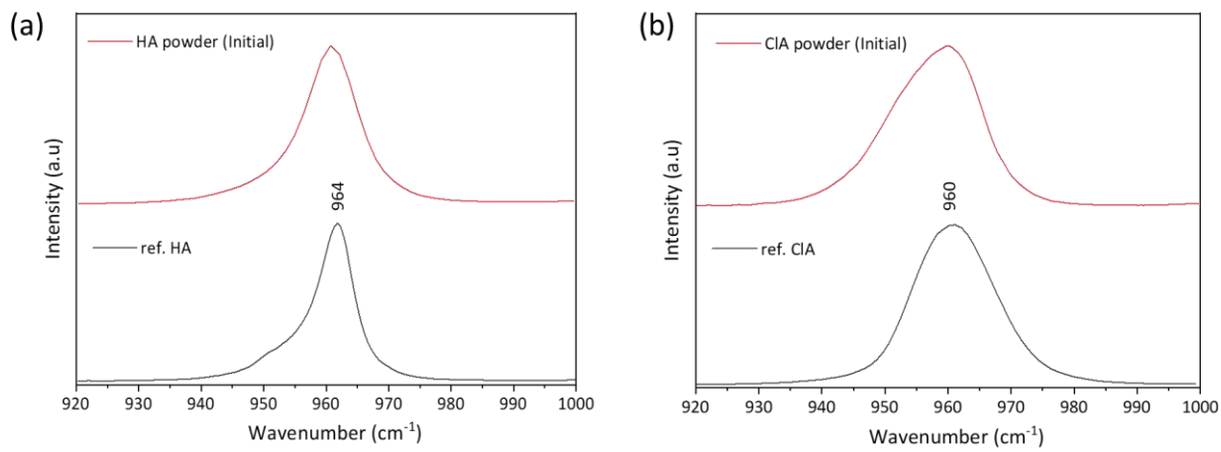

Figure 4. Raman spectra were obtained for the initial ceramic powders used in our study. For reference Raman spectra for (a) HA (RRUFF id: R100225), and (b) ClA (RRUFF id: R060192) were obtained from the RRUFF™ Project database.

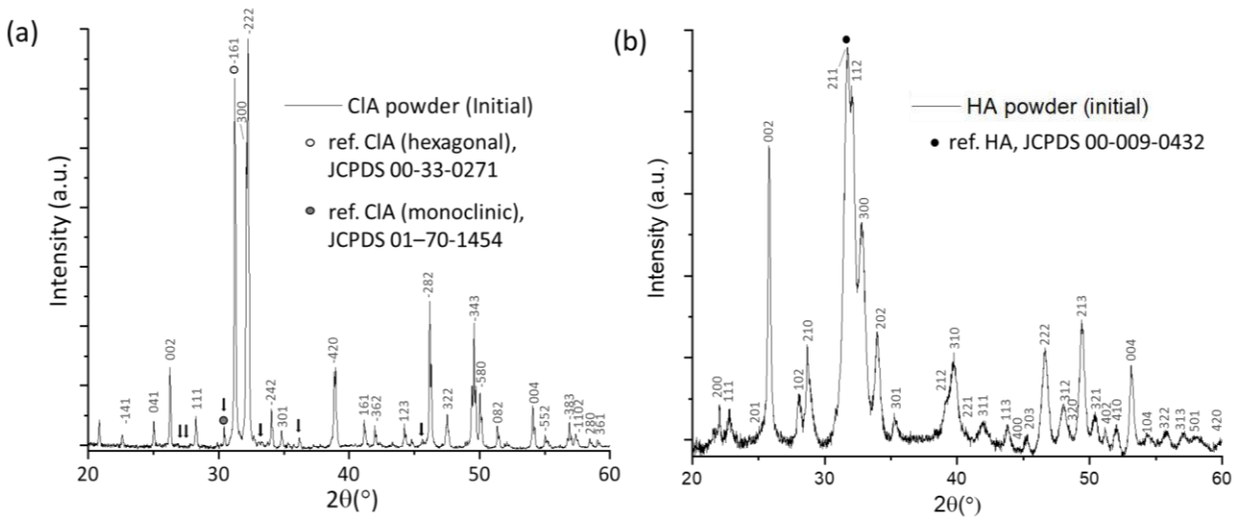

Figure 5. XRD diffractograms obtained for the initial (a) ClA and (b) HA ceramic powders used in our study. Reference patterns: ClA (hexagonal) JCPDS 00-33-0271, ClA (monoclinic) JCPDS 01-70-1454, and HA JCPDS 00-009-0432. Superlattice lines on ClA pattern are shown by arrows.

The study of the powdered material absorptance at a certain laser wavelength is of particular interest for the PBSLP process because it allows one to determine the processing window suitable for sintering or melting. Tolochko et al. [18] carried out an exhaustive study on the laser absorption of different materials stating that the absorption mechanism has a complex character and it depends on the kind of material (metals, ceramics…). Even for the same material, it can vary from one spectral region to another. They explained that the laser sintering of a single-component powder is a complicated process since the sintering processing window can be very narrow. The particles either do not sinter staying as loose powder or undergo a complete melting at high power density that leads to the formation of resolidified droplets due to the liquid surface melt contraction. They also studied the addition of water-soluble powders such as $NaNO_3$ and NaCl to metal/ceramic powders as absorption additives. After laser sintering of the blend, the sintered parts could be immersed in water to dissolve the added substance, controlling the porosity of the part by adding different additive volume fractions. They concluded that the greater the absorptance of a powder, the less the laser energy density needed for the sintering. For this reason, absorption additives have gained special relevance in PBSLP, while they should be carefully selected for the improvement of the product properties.

For the present study, powdered graphite was chosen as the second component in our blends. Its application as an absorption additive has also been evaluated previously showing promising results [8,19,20]. It highly absorbs the laser beam energy emitted at the fiber laser near-infrared wavelength (λ = 1.070 μm) equipped in our printer and can transform it into heat to sinter/melt the powder feedstock. The mechanism expected for its burnout and removal will be detailed below.

The absorptance of the different pure and powder blends used in this work was determined before their use. The absorptance values obtained are shown in Table 4. Different clear changes in powder colour were observed since HA was initially white but after its chlorination, it produced a yellowish ClA powder increasing its laser absorptance from 2.37% to 12.51%. Then, after the addition of graphite to produce the blends, powders became light grey (darker with the increase of graphite proportion). Results showed an increase of the powder absorptance from 2.37% of pure HA to 66.83% and 73.73% when containing 5% and 10% wt. of graphite, respectively, demonstrating its capacity as absorption additive.

Table 4. Determined absorptance at the emitted wavelength (1070 nm) of the fiber laser light for the powders used as PBSLP feedstock. (N=3, mean ± standard deviation)

Material	Absorptance at λ = 1070 nm (%)
HA	2.4±0.1
HA_5G	66.8±0.1
HA_10G	73.7±1.1
ClA	12.5±0.1
ClA_5G	69.2±0.0
G	80.5±0.1

Figure 4 shows the SEM micrographs of the HA coating surface on TA6V discs used as a substrate during the printing process. The HA coating homogeneity is observed for the whole disc surface and surface roughness can be also appreciated at higher magnification, which is common for the atmospheric plasma spray (APS) process [21,22]. For example, high roughness average (Ra) values in between 4.4 and 5.4 µm have been observed for the same kind of HA coatings produced by APS in previous works [23].

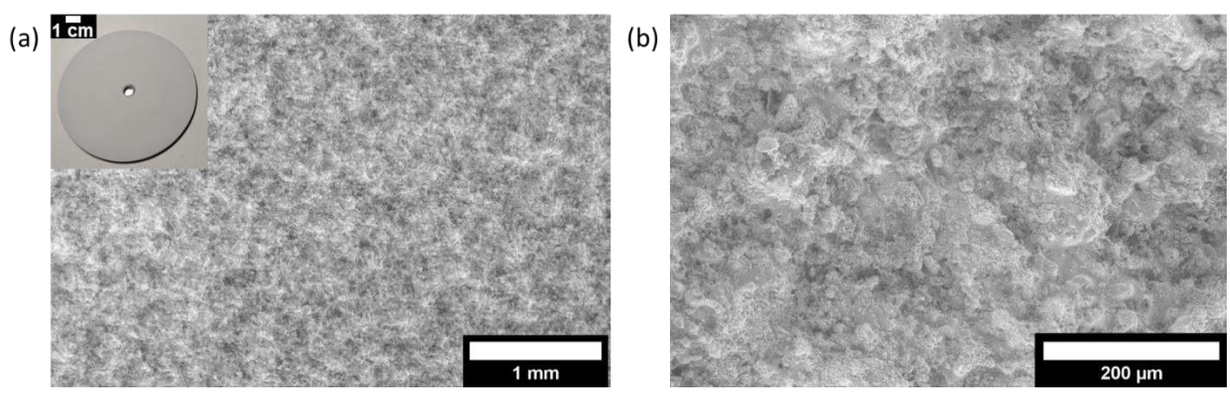

Figure 6. SEM micrographs of HA coating surface on TA6V discs used as a printing substrate.

3.2 Analyses and evaluation of PBSLP samples

3.2.1 First approach: Laser-induced circular patterns.

The printing of circular patterns was used as a faster method to evaluate the performance of the printing parameters as well as the influence of the powder feedstock formulation. The printed single circular patterns obtained with different powder feedstock and E_d can be observed in Figure 7. The corresponding PBSLP process windows are shown in Figure 8. The surrounding circles indicate the samples that will be characterized more in detail for comparison of powder feedstock and E_d (HA_5G_96 / HA_10G_57.6 / HA_10G_96 / HA_10G_288 / ClA_5G_96 / ClA_5G_336). Three quality criteria were used to identify and evaluate macroscopically the different parameters performance at each assigning point: no densification, sintered/melted powder, and thermal cracking. When the laser energy is not enough it does not produce densification of the powder, in absence of sintering/melting phenomena it results in loose particles. Instead, too much energy can induce different adverse effects on the powder bed such as thermal cracks (due to high thermal gradients and stresses) with the impossibility of forming solid parts.

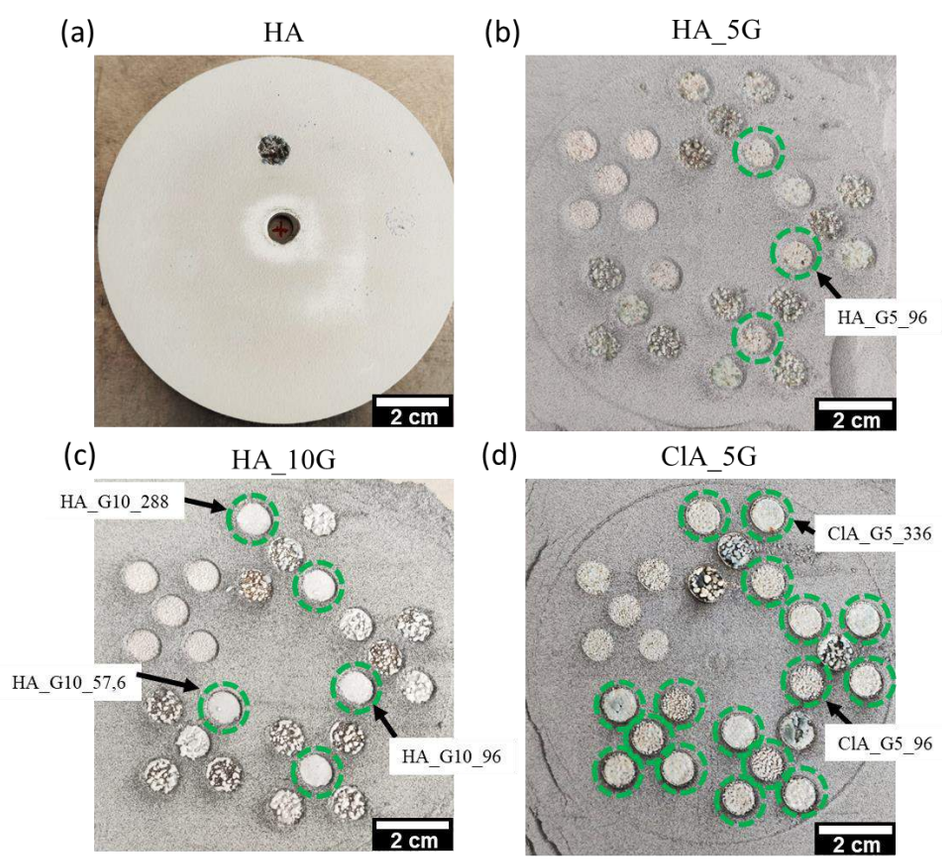

Figure 7. The single circular patterns were obtained for different powder feedstock and printing parameters: (a) HA, (b) HA_G5, (c) HA_10G, (d) ClA_5G. (Process window study)

In the case of pure HA powder, no densification was observed for the whole range of parameters studied. The majority of the set of parameters did not show any kind of interaction between the powder and

the laser. Only at the highest laser power and lowest scanning speed (432 J.cm^{-3}), the powder bed was spattered and the HA coating was removed from the substrate.

Between the process windows obtained for HA_5G and HA_10G, we could observe that the range of parameters in which a correct powder sintering/melting occurred was relatively narrow. However, for the powder containing a higher amount of graphite the process window seemed to be enlarged, thus indicating that a higher number of laser parameters (E_d range) can properly sinter/melt the powder. As we mentioned above, the higher the amount of graphite in the blend the better the interaction of the laser with the powder blend thus leading to a better surface finishing.

It is also important to point out that for the same HA_10G powder blend, we could observe some cases in which samples treated at constant energy density the result depends on the laser speed and laser power used. It is the case for the samples produced with 36 W, 75 mm.s^{-1} and 48 W, 100 mm.s^{-1}. Both produced the same energy density (96 J.mm^{-3}) however only the first sample showed a proper sintering/melting of the powder. Even if the energy density remains constant, it is known that the combination of laser hatch distance, laser scanning speed, and laser power has a significant influence [10]. These three tuneable laser parameters do not have the same effect in the printed parts. Laser scanning has the lowest effect, followed by the hatching distance, and the laser power having the highest influence [24]. These different degrees of influence are not considered in the concept of laser energy density. For this reason, the energy density should not be the only criterion in the optimisation of the process parameters and additional parameters should be indicated (e.g. laser scanning strategy, laser defocus…) [10].

The enlargement of the process window is even more notorious when changing the calcium phosphate powder to ClA. It is known that ClA is more stable than HA. This higher thermal stability is given by the anion substitution in the hexagonal axis of the apatite structure [17]. ClA melts at 1530ºC while HA powders are reported to be sintered up to a theoretical density at 1000–1200 °C. The drawback is that the processing (sintering/melting) of HA is difficult due to the presence of the OH content, which decomposes to form TCP and anhydrous calcium phosphates at ~1200–1450 °C leading to grain growth. Indeed, the water present in the sintering atmosphere can inhibit HA densification and accelerates grain growth. The decomposed phases will trigger different dissolution rates, when present in physiological conditions [25]. For this reason, ClA has been studied as a substitute for HA in other manufacturing processes involving high temperatures (e.g. plasma spraying) [26].

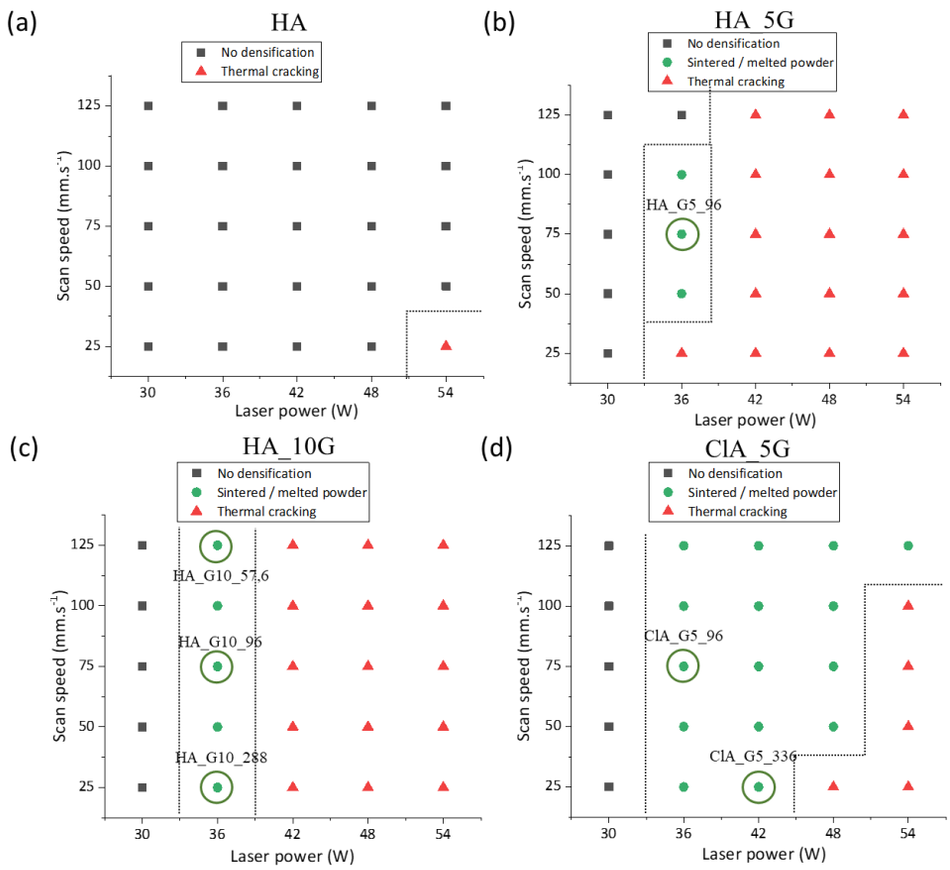

Figure 8. PBSLP process window comparison of the different powder feedstock: (a) HA, (b) HA_5G, (c) HA_10G, and (d) ClA_5G. The surrounding circles indicate the posteriorly characterized samples for comparison.

The SEM analyses of the circular pattern microstructures produced at the same E_d (96 J.cm^2) and using different powder feedstock blends are shown in Figure 11. The three different laser-induced circular pattern samples showed a balling effect. It is a common unfavourable defect in laser processing of both ceramics and metallic materials which has been widely studied [27,28]. Gu et al. [29] defined two different types of balling phenomena:

- The first type of balling phenomenon is defined by coarsened balls giving an interrupted dendritic structure having an inherent structural weakness. It gives as results a rough surface and is caused by a limited liquid formation and low undercooling degree of the melt because of a low laser input. A schematic representation of the process forming this first type of balling phenomenon is illustrated in Figure 9.

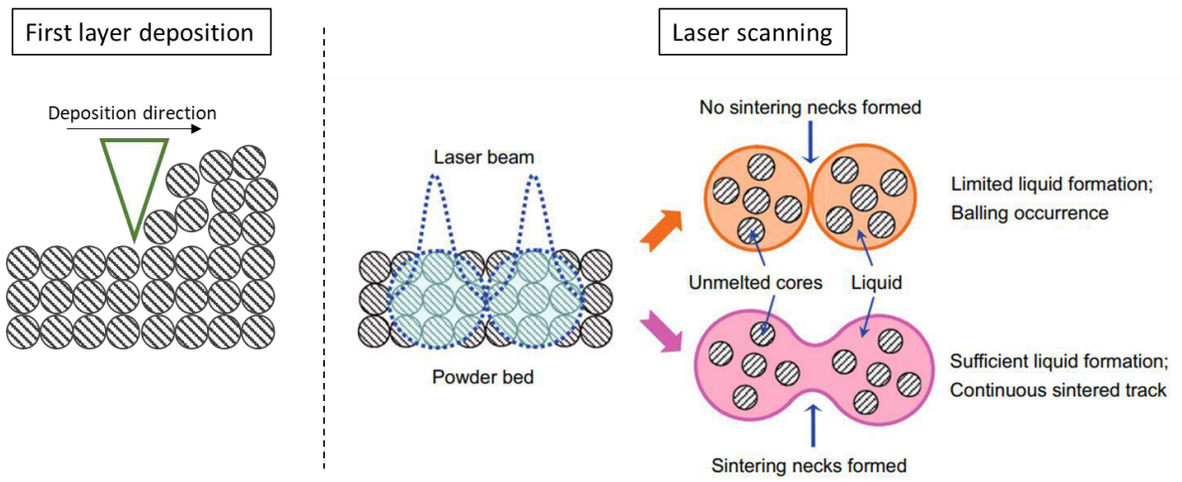

Figure 9. Schematic representation of the formation of the first type of balling phenomenon featured by coarse spherical-shaped sintered agglomerates caused by limited liquid formation. Adapted from Gu et al. [29].

- The second type is defined by numerous micrometric balls over the region irradiated by the laser. These balls should not be confused with the HA or ClA microspheres used as raw material which had a smaller size. In addition, the smoother surface of the balls is an indication that these are produced as a product of a melting process. Its initiation is attributed to the melt splashes due to a high capillary instability of the melt [30].

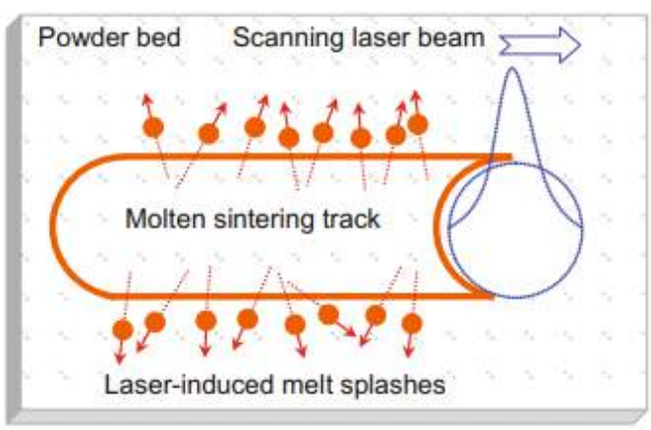

Figure 10. Schematic representation of the formation of the second type of balling phenomenon featured by laser-induced melt splashes. Adapted from Gu et al. [29].

For the sample defined as HA_10G_96, the second type of balling phenomenon can be identified due to the presence of numerous micrometric balls on the surface. In this case, the surface irradiated remained flat apart from the presence of the balls. The ClA_5G_96 sample showed instead signals of the first type of balling effect having a higher surface roughness but the number of micrometric balls was lower. Finally, the sample HA_5G_96 showed a combination of both kinds of phenomena. The differences in laser absorptance and powder stabilities could produce different melting behaviours resulting in different surface finishing.

At higher magnification, pinholes (about 20 µm diameter) can be observed randomly distributed over the whole surface of the samples. We could hypothesize that the formation of these pinholes could be due to the formation of micro gas bubbles of *CO* and CO_2 as a product of the graphite burnout which diffuses leaving a space. The reasons supporting this idea are that the size of the graphite flakes (x_{50} = 21.4 µm) fits well with the size of the observed pinholes and their number is increased when higher amounts of graphite are present in the blend. However, further efforts should be made on the study of the effect of increasing the quantity of graphite on the porosity of the samples.

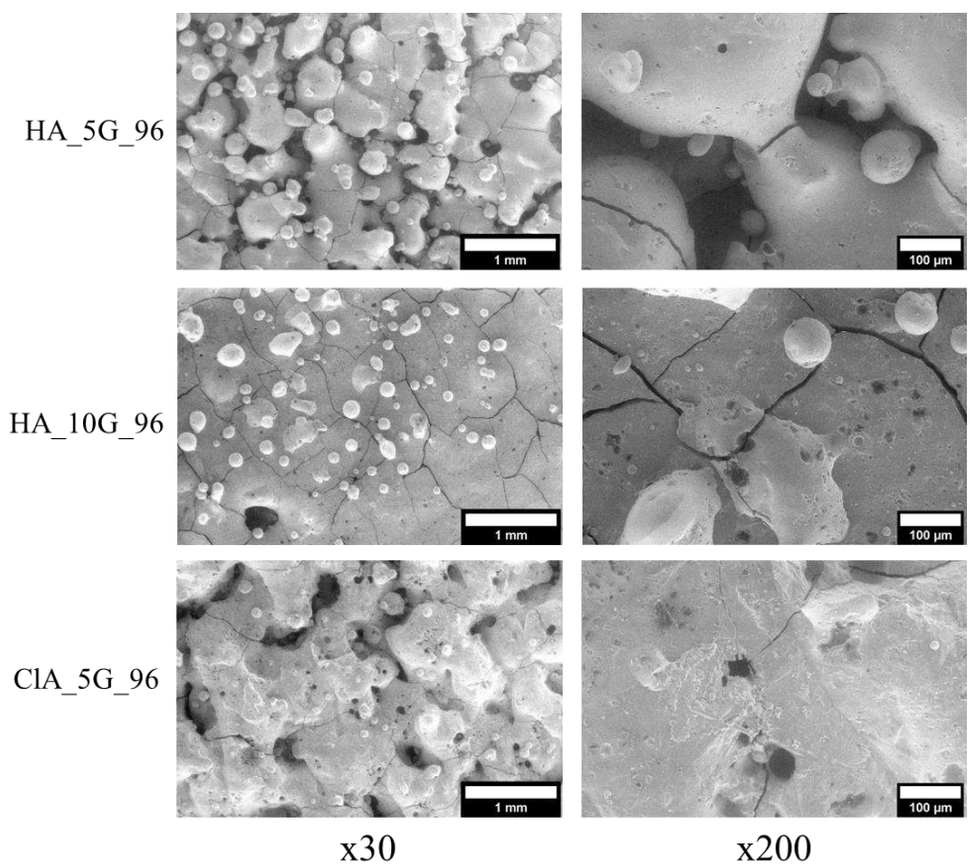

Figure 11. SEM analyses of laser-induced circular patterns produced at same Ed (96 J.cm^{-3}) with different powder feedstock blends: HA_5G_96, HA_10G_96, ClA_5G_96.

The comparison of the microstructures of the samples produced using HA_10G feedstock blend at different E_d is offered in Figure 12. The samples produced at higher E_d (288 J.cm^{-3} and 96 J.cm^{-3}) showed both the second type of balling phenomenon (apparition of molten micrometric balls). However, in the

sample printed at lower E_d (57.6 J.cm^{-3}), the surface showed a clear diminution of the number of balls produced, indicating a diminution of the splashing of molten balls. The surface finishing of this last one was found to be flatter due to the absence of balls. The grain boundary cracking (2D defects) in the surfaces of the three kinds of samples was detected. Grain boundaries are known to have a strong effect on the propagation of cracks and the generation of impurity-controlled porosity. At high temperatures, they are also the main starting point for the deformation in polycrystalline ceramics [31]. An increase in the dimensions of the grains and cracking incidence was observed when increasing the E_d used during the process.

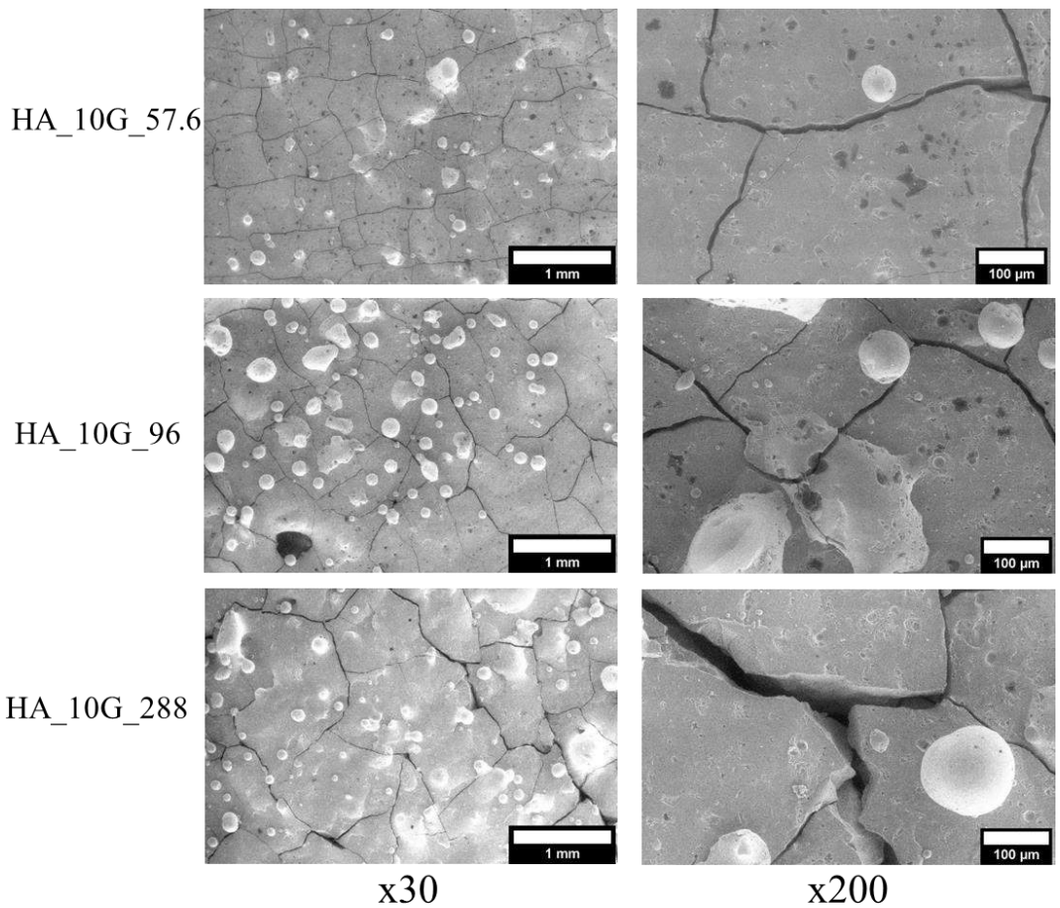

Figure 12. SEM analyses of laser-induced circular patterns produced with same powder feedstock blend (HA_10G) at different E_d: 288 J.cm^{-3}, 96 J.cm^{-3}, 57.6 J.cm^{-3}. Analyses of sample HA_10G_96 are repeated here for better comparison.

The ClA sample produced at higher E_d (ClA_5G_336) was analysed for comparison. Figure 13 shows the resulting microstructure. This increase in E_d diminished the presence of the first type of balling phenomenon giving the sample a flatter surface compared with the ClA sample at lower E_d (Figure 11). Holes with approximatively 100 µm of diameter are distributed randomly over the surface. Most of these holes are filled with stick-shaped ClA particles parallel to the surface plane. This ClA particle morphology has been previously observed after the treatment of ClA at high temperatures [32,33].

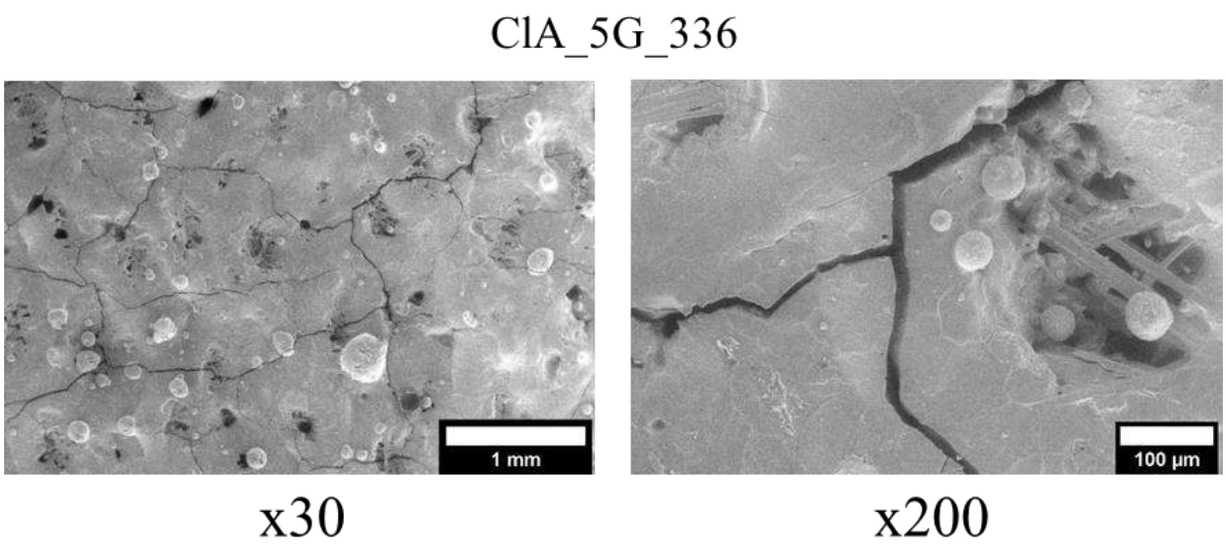

Figure 13. SEM analyses of laser-induced circular patterns produced with ClA_5G feedstock blend at E_d = 336 J.cm^{-3}.

The chemical and structural composition of the previous samples was analysed for comparison by Raman and XRD analyses. Figure 14a shows the comparison between the Raman spectra of the circular patterns obtained from different feedstock powders at the same printing parameters. For samples in which HA was used as main component feedstock (HA_5G and HA_10G), it was found that the most significant contributions come from the strongest spectral bands corresponding to the v_1PO_4 vibration of TTCP (961, 956, 946, 940 cm^{-1}), α-TCP (976, 964, 954 cm^{-1}), and HA (964 cm^{-1}) can be observed. This indicates that a phase transition occurred during the PBSLP process due to the high temperature reached. HA dehydroxylation into oxyapatite (OA) occurs at about 900ºC in air [14]:

$$Ca_{10}(PO_4)_6(OH)_2 \rightarrow Ca_{10}(PO_4)_6O + H_2O \quad (3)$$

(HA) (OA)

Then, two outcomes are stoichiometrically possible above 1050 ºC: (i) a mixture of TTCP and TCP (β-TCP at temperatures below 1200ºC or α-TCP at higher temperatures) or (ii) a mixture of TCP and CaO by the following reactions [14]:

$$Ca_{10}(PO_4)_6O \rightarrow 2Ca_3(PO_4)_2 + Ca_4P_2O_9 \quad (4)$$

(OA) (TCP) (TTCP)

and

$$Ca_{10}(PO_4)_6O \rightarrow 3Ca_3(PO_4)_2 + CaO \quad (5)$$

(OA) (TCP)

We could hypothesize that the temperature reached during the process is higher than 1200ºC. A slight difference can be observed between the relative intensities of the bands for the spectra of these two samples, thus indicating a different proportion between phases present in the samples. For the sample prepared from the feedstock ClA_5G, only the band corresponding to the v_1PO_4 vibration of ClA (960 cm^{-1}) was observed, indicating that there was no visible alteration of the phase.

Figure 14b shows the comparison between the Raman spectra obtained from samples produced with the same powder feedstock (HA_5G) but at different printing parameters. The Raman bands of the three studied spectra corresponded again with the v_1PO_4 vibration of TTCP (961, 956, 946, 940 cm^{-1}), α-TCP (976, 964, 954 cm^{-1}), and HA (964 cm^{-1}). In this case, no clear variation between the relative intensities of the bands was observed. Therefore, the calcium phosphate phases obtained in the three samples resulted in having very similar proportions for the range of parameters studied.

It should be pointed out that small variations on intensity and shift of bands can be due to several reasons such as:

- If the band is characteristic of more than one compound, then the intensity would be the contribution of these compounds.
- The crystal orientation can affect the relative intensity of the characteristic Raman band of a compound.
- HA and ClA reference spectra were obtained at different laser radiation (780 nm) to the rest of the samples (622 nm).

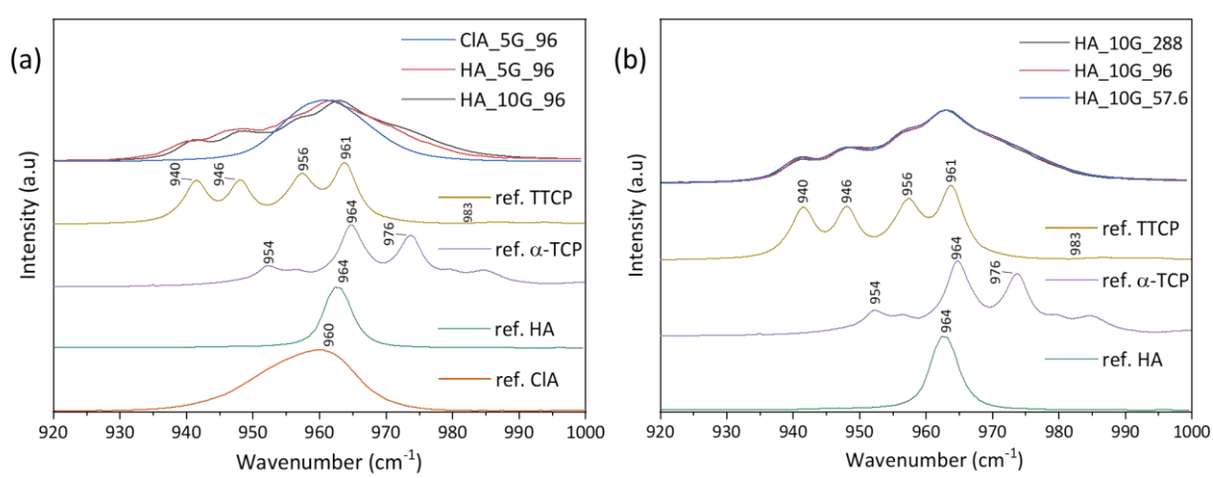

Figure 14. Raman spectra were obtained for the laser-induced circular samples printed with (a) different powder feedstock and (b) different printing parameters.

Figure 15a shows the X-ray diffractograms of the circular samples produced with powder blends of HA and different amounts of graphite (HA_5G_96 and HA_10G_96) at the same energy density (E_d = 96 $J.cm^{-3}$). The diffractogram of the initial HA powder was added for comparison. Both samples showed a phase transition. A combination of HA, TTCP, α-TCP, and graphite phases was observed in both

diffractograms. However, differences in the relative intensities of the peaks were detected. This indicates that the proportion between phases is different depending on the sample.

Figure 15b shows X-ray diffractograms of the initial HA powder and the samples printed with the powder blend of HA and 10 wt. % of graphite (HA_10G_57.6, HA_10G_96, and HA_10G_288) with different energy densities. The comparison between the peaks corresponding to graphite indicates that its diminution is higher with the increase in energy density. It could be caused by a more significant burnout of the graphite particles due to the higher temperatures generated. Regarding the calcium phosphate phases present in the samples, the three of them showed a HA transition into TTCP and α-TCP. Another difference between the diffractograms was the unlike HA crystals orientation depending on the energy density used. A lower energy density seemed to induce a higher preference on the HA crystals orientation to the 002 plane (peak at 25.70º). However, since it is found out of the scope of this study no further investigations were done on the laser-induced texture of HA crystals.

Figure 15c shows the XRD diffractograms of the sample printed with the powder blend of ClA and 5 wt. % (ClA_5G_96) at 96 $J.cm^{-3}$ and the initial ClA powder. The analysis did not show a phase transition from ClA into other calcium phosphate phases, however, a phase transition from monoclinic to hexagonal ClA was detected. A preferred crystals orientation or crystallographic texture to the 002 plane is also clearly visible for this sample. In addition, a small amount of graphite was observed in the sample apart from ClA.

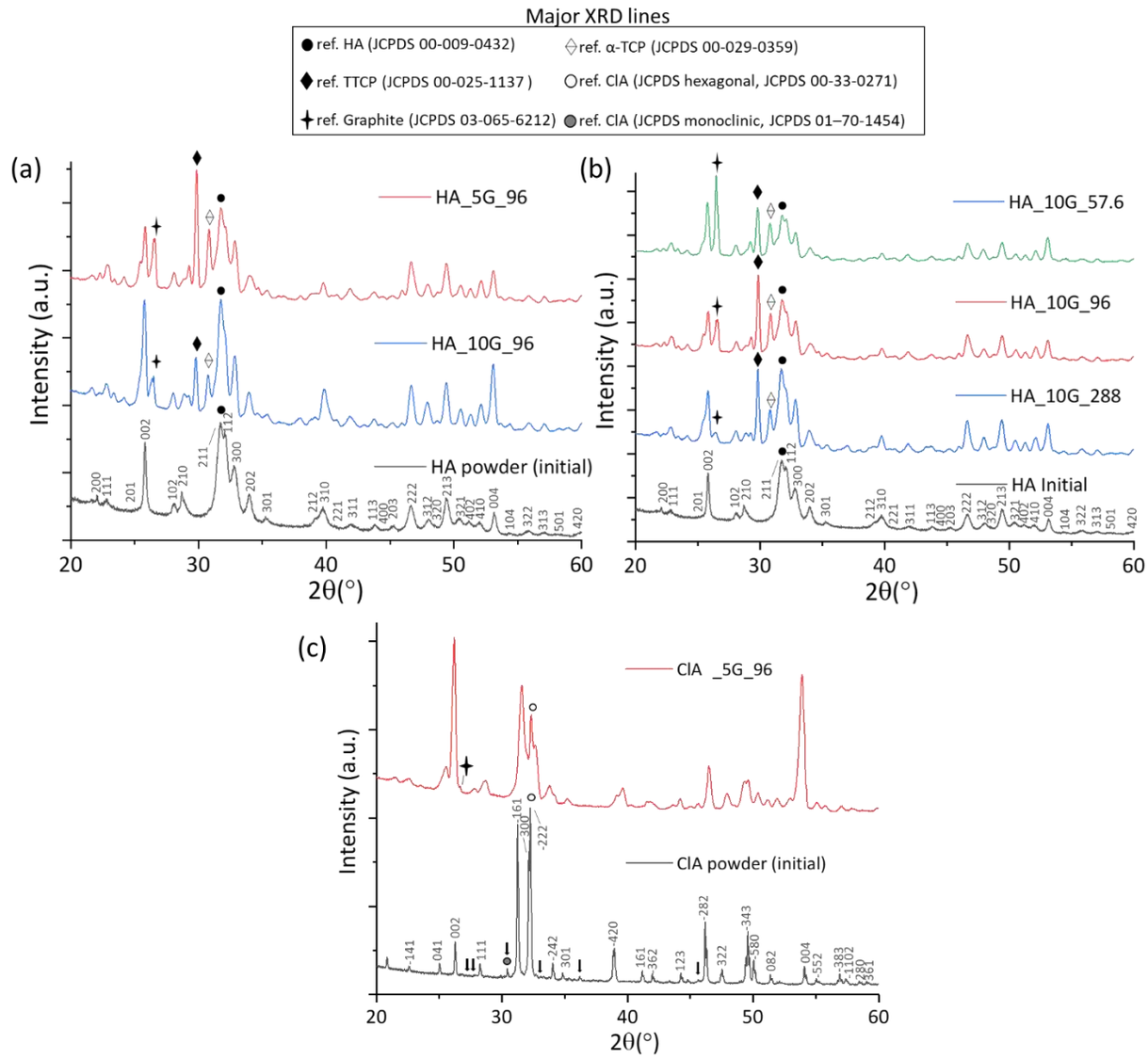

Figure 15. X-ray diffractograms were obtained for the laser-induced circular samples printed with (a) HA with different amounts of graphite (5 and 10 wt. %), (b) at different printing parameters, and (c) using chlorapatite with 5 wt. % graphite as feedstock. Superlattice lines on ClA pattern are shown by arrows.

The Rietveld refinement method was performed to quantify the different phases present in the HA samples after the phase transition. Plots of the Rietveld refinement of the samples analysed are offered in Figure S1. Table 5 shows the refined phase compositions and reliability factors obtained through Rietveld refinement for the calcium phosphate printed samples. Figure 16 shows the refined phase compositions plotted in stacked columns chart type to allow the part-to-whole comparison.

Table 5. The refined phase compositions and reliability factors for the calcium phosphate printed samples.

	Mean Rietveld composition (wt. %)			
Sample	HA_5G_96	HA_10G_57.6	HA_10G_96	HA_10G_288
HA (wt. %)	48.1±0.3	28.0±1.6	35.5±0.9	46.5±2.0
TTCP (wt. %)	13.2±0.1	13.7±0.6	25.5±0.6	19.90±0.9
α-TCP (wt. %)	33.2±0.5	50.1±2.1	31.1±0.8	29.0±1.3
Graphite (wt. %)	5.5±0.1	8.1±0.2	7.8±0.0	4.6±0.3
Sig (%)	2.19	8.03	3.63	3.74
R_b (%)	1.15	3.29	1.64	1.65
R_{wp} (%)	1.68	5.12	2.49	2.74
R_{exp} (%)	0.77	0.64	0.68	0.72

The sample containing less amount of graphite (HA_5G_96) was the one showing the highest HA amount (48.1%) to the other phases, thus indicating that the sample experimented with a weaker phase transition during the PBSLP process. For the samples containing the same level of graphite but printed at different scanning speeds *(HA_10G_57.6 / HA_10G_96 / HA_10G_288),* some differences were observed in the calcium phosphates proportions. The remaining amount of HA has a clear tendency to increase when the scanning speed is lower (higher energy density) indicating that a lower phase transition occurred at lower scanning speeds during the process (46.5 wt.% HA at 25 mm.s^{-1}, E_d = 288 J.cm^{-3}). This behaviour could be explained through the reversible character of the HA transformation. Liao et al. [34] studied the thermal decomposition and reconstitution of HA after heating at 1500ºC and cooling at a rate of 10ºC/min under air. They observed that the TTCP and α-TCP phases reconstructed gradually into HA, reaching a complete reconstitution under 1100ºC during the cooling phase. The different cooling rates and heat distributions produced by using different scanning speeds during the PBSLP process could affect differently to the decomposition and reconstitution behaviour of HA. However, to better understand this behaviour a deeper study on the effect of the cooling rate on the HA phase transition should be performed.

Additionally, it was observed that a higher E_d or lower scanning speed favoured the burnout and the corresponding removal of graphite (4.6 wt.% graphite at 288 J.cm^{-3}).

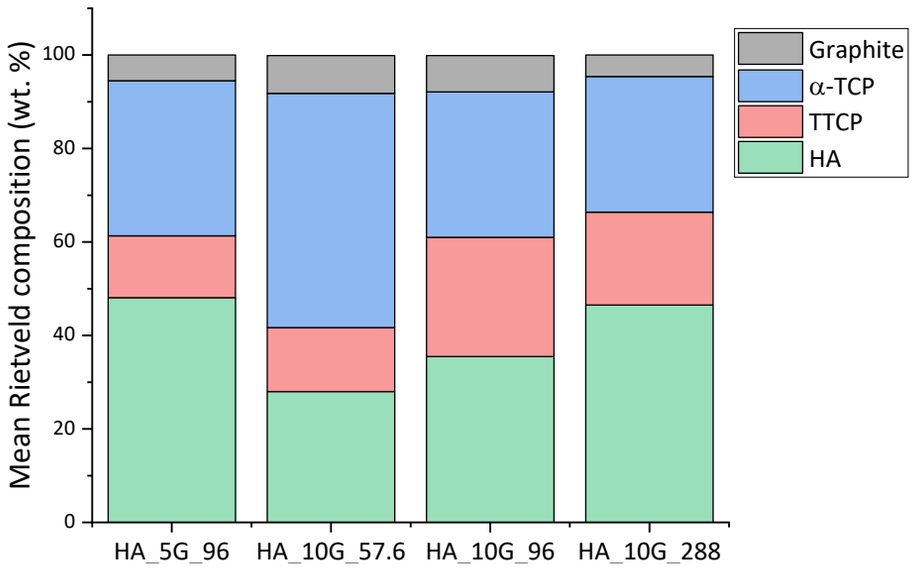

Figure 16. The refined phase compositions of the calcium phosphate printed samples

3.2.2 Second approach: HA complex parts

The printing of HA complex parts was performed in parallel to the previous approach. In this case, only the feedstock powder HA_5G composed of HA and a 5 wt. % of graphite was used. The 3D model used and the resulting parts are shown in Figure 17. Both samples were printed at 240 $J.cm^{-3}$ (30 W, 25 $mm.s^{-1}$) following the same hexagonal laser strategy. It is important to note that even if this combination of printing parameters did not show a good sintering/melting of the powder during the first approach, it was possible to print solid parts with a certain height. We could hypothesize that the changes in the thermal conductivity with the number of layers made possible the densification of the powder even if at the first layers the energy input was too low to sinter/melt the powder.

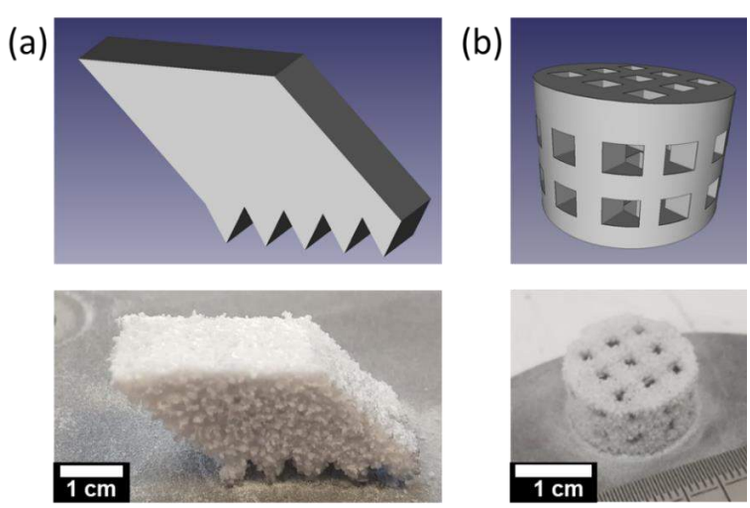

Figure 17. 3D model and printed HA complex parts: (a) HA_Trapezoid and (b) HA_Scaffold

Figure 18 shows the three-dimensional reconstructions of the printed samples using X-ray micro-computed tomography. Both parts presented a surface with high roughness. Two kinds of porosity were observed during the analysis of the internal microstructures. In Figure 18b it can be observed a homogeneous interconnected porosity presents on the whole volume of the samples together with a closed porosity of smaller size.

We found two possible hypotheses for the formation of the small closed porosity. A first option relates this kind of porosity (blowholes) to the pinholes previously observed in the surface of the samples of the first approach (Figure 11). The origin of these pores would be the formation of *CO* and CO_2 microbubbles during the graphite burnout in the liquid which remains enclosed in the microstructure. This kind of defect is common in the processing of metals containing carbon [35,36]. Our second hypothesis is that this porosity is originated from the decomposition of the carbonate present in the structure of the HA used as raw material. AB-type carbonated apatite starts to decompose at about 400ºC releasing mainly CO_2. Since AB-type carbonated HA retains its apatite structure and partly the carbonates groups at 1100ºC, it has been useful for the production of porous carbonated apatite ceramics intended for bone tissue engineering scaffolds [37].

An analysis of the cross-section and the volume of the parts shows a distortion of the parts and the presence of cracks due to the high stresses to which the material was submitted during the printing process. The total porosity of these parts was found to be around 24% of the total volume. The designed toothed bottom surface of the sample HA_Trapezoid facilitated the detachment of the part from the substrate surface. However, the HA_scaffold sample suffered some deterioration due to the detachment using the homemade endless diamond wire saw.

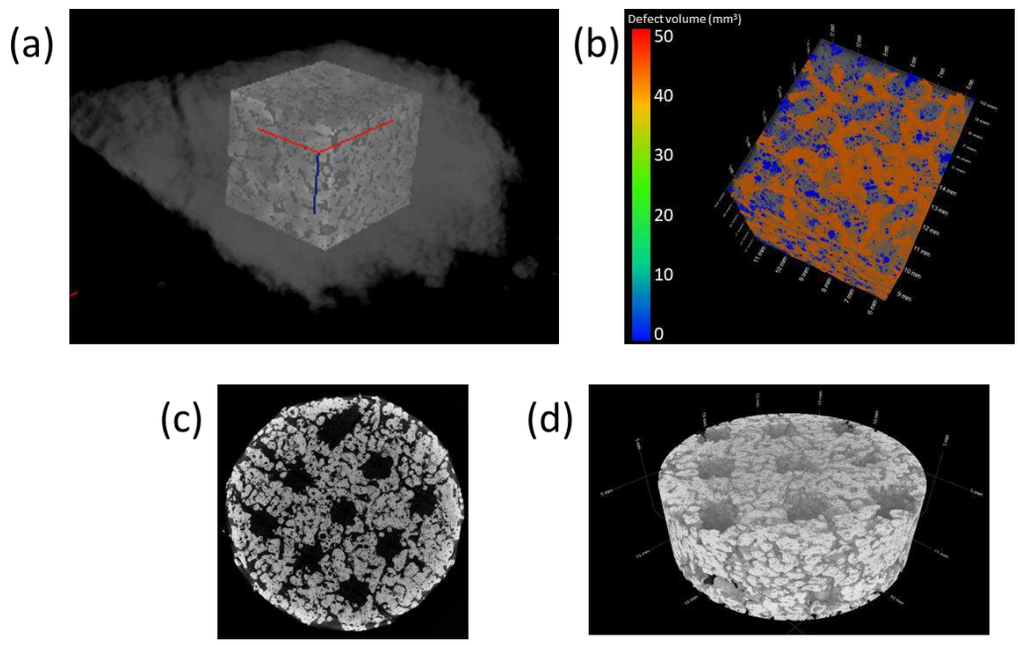

Figure 18. Visualization obtained using X-ray micro-computed tomography of the two kinds of printed parts: (a) Selection of the region of interest in HA_Trapezoid sample (b) Analysis of the porosity distribution in the region of interest (blue: closed porosity, orange: interconnected porosity) (c) Cross-section view of HA_Scaffold in the X-Y plane. (d) Volume analysis of the HA_Scaffold sample.

3.2.3 Third approach: HA cylinders

The previous approaches were carried out to evaluate the results of using different powder feedstock and printing parameters on the final composition and morphology of the printed parts. This approach instead, focused on the evaluation of the capacity of the HA_10G feedstock combined with an energy density of 96 J.cm^{-3} to produce solid parts with a certain shape intended for mechanical testing. A change of the laser strategy (from hexagonal to zig-zag) and parameters as needed to reduce the printing time of solid parts. The comparison between the time needed for the printing of the parts is done by calculating the build rate coefficient (*B*, cm^3.h^{-1}) (or productivity) of the process. This coefficient indicates the volume of material produced per hour and is proportional to the layer thickness, hatch distance, and laser scanning speed (equation 4). The higher the build rate the more productive will be the printing process [38].

$$B = v_{scan} \cdot h_{space} \cdot t_{layer} \quad (6)$$

Then, for the printing of the samples of the second approach, a $B = 0.45\ cm^3.h^{-1}$ was calculated while for this approach a $B = 1.35\ cm^3.h^{-1}$ was obtained. This productivity is three times higher than the previous one. Only the laser power and the scanning speed were modified (36W, 75 mm/s). Of course, this calculation should be taken as an approximation since factors like the overlapping rate of the layers are not taken into account. Moreover, this change of parameters does not aim to reach the maximum material processing speed of the PBSLP process but to speed up the process to facilitate the production of several cylinders intended

for the analysis of the mechanical properties. The produced cylinders with 10 mm of diameter and 15 mm of height are shown in Figure 19. The change in colour (from white powder to brown) could be due to the presence of the secondary phases in the sample. It was not detected any important variation of the colour after the thermal treatment, which could indicate a not complete HA reconstruction. They were analysed chemically, structurally, and mechanically.

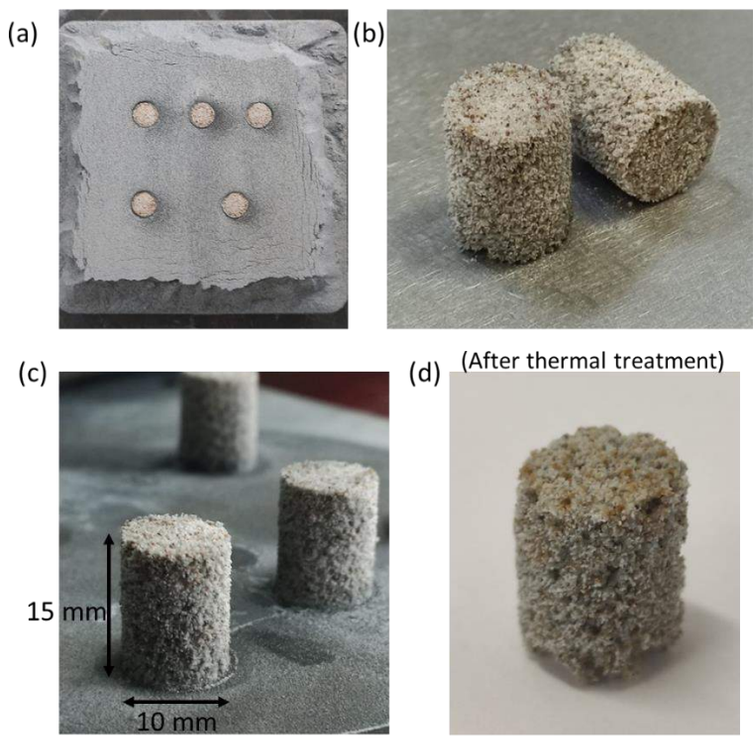

Figure 19. Photographs of HA cylinders samples produced by PBSLP at 96 J.cm^{-3} and a zig-zag laser scanning strategy (5 passes). (a) As printed, (b) after substrate removal, (c) general view, (d) sample after thermal-treatment.

The Figure 20a shows the Raman spectrum of the HA_Cyl sample in comparison with the TTCP, HA, and α-TCP spectra for comparison. The spectrum shows a contribution of the three calcium phosphate phases; however, the relative intensity of the bands is different from the one found for the samples produced during the first approach. The relative intensity related to the HA band is higher than the rest of the phases indicating a low phase transition. The X-ray diffractogram of the HA_Cyl sample before and after been post-treated is shown in Figure 20b. This result confirms the higher presence of the HA phase to the other phases in the HA_Cyl sample, these residual phases become invisible in the diffractogram after the thermal treatment. as was already observed in the Raman spectrum. Almost no presence of graphite was detected through XRD analysis. Once the sample is submitted to the thermal treatment, even a higher proportion of HA is detected, thus indicating a possible reverse phase transition from the others two phases (TTCP and α-TCP) into HA. Once again it can be observed that the crystal orientation of HA has been affected after PBSLP process (it is reflected in the change of the HA lines intensities).

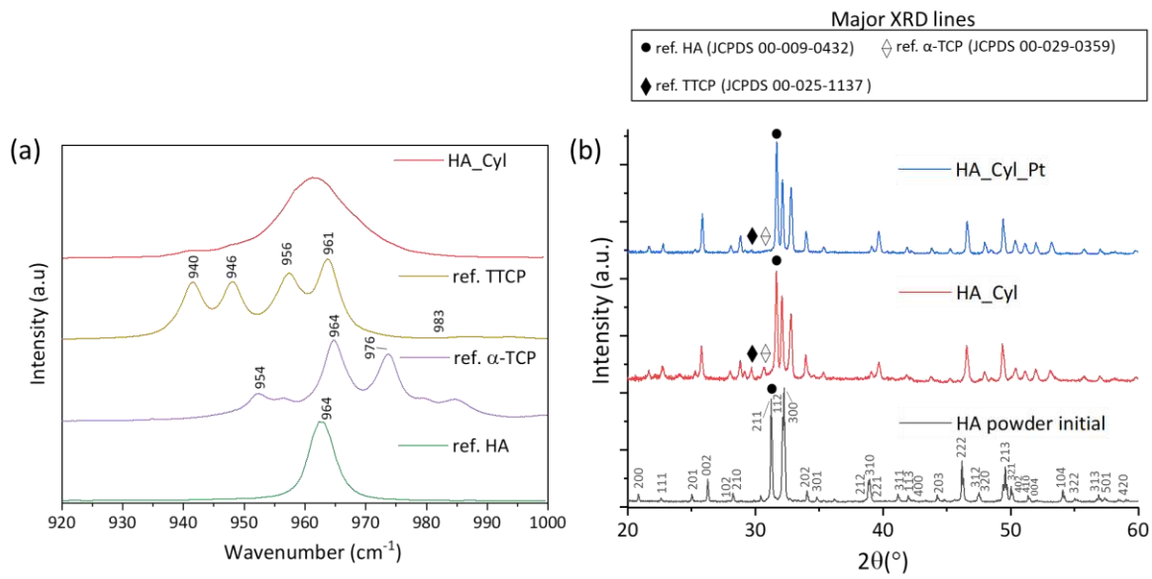

Figure 20. (a) Raman spectrum and (b) X-ray diffractograms were obtained for the cylinders printed at 96 J.cm^{-3}.

The FTIR spectra of the initial HA powder, the as-printed HA_Cyl, and after its post-treatment are shown in Figure 21. For reference, the characteristics FTIR line positions of the calcium phosphates HA, TTCP, and α-TCP are offered in Table S1. First, the presence of structural carbonate impurities located at the A and B sites (hydroxyl and phosphate sites, respectively) of apatite structure in the initial powder was detected. It is observed from the bands at 1454 cm^{-1} and 877 cm^{-1} in the three samples. However, a decrease in their intensities is detected after each process step being almost invisible after the post-treatment of the cylindric sample. All the characteristic frequencies of $PO4^{3-}$ modes [39] together with the bands corresponding to the structural OH^- of HA can also be found in the spectrum of the initial powder. Once the PBSLP process is performed to produce the HA_Cyl sample, the $PO4^{3-}$ bands corresponding to TTCP and α-TCP appeared in the spectrum (through the broadening of the bands) confirming a partial phase transition. Bands corresponding to the structural OH^- become invisible due to the loss of intensity. It is after the post-treatment of the cylinder at high temperature that the bands corresponding to the HA phase recover a certain intensity becoming sharper, indicating that a reverse phase transition occurred.

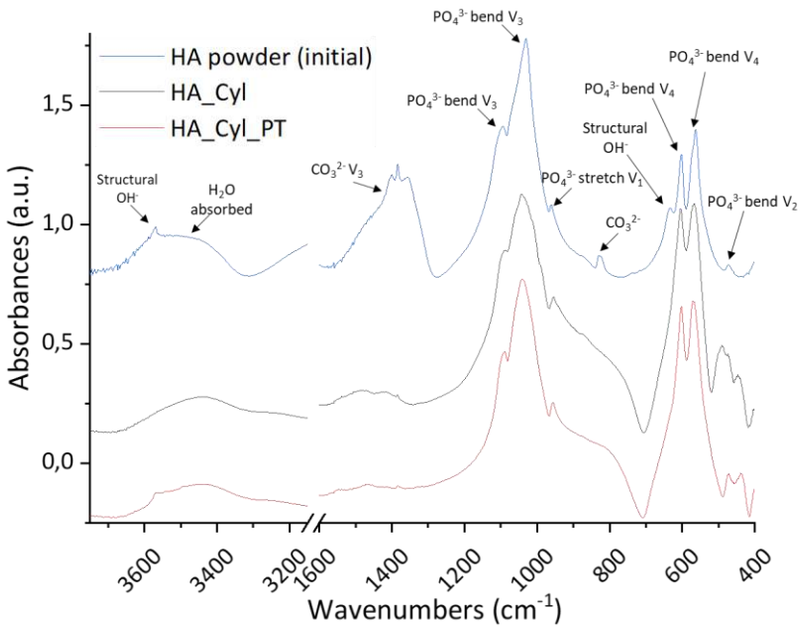

Figure 21. FTIR spectra of HA_Cyl and HA_Cyl_PT samples.

General information related to the microstructure and mechanical properties of HA_Cyl samples before and after the thermal treatment is offered in Table 6. Directional dimensions of the printed samples showed small variations to the dimensions of the original 3D model (10 x 15 mm). In laser processing of metals, the dimensional accuracy was found to be affected by two main factors, the solidification shrinkage and the mode of laser track filling and width [40]. Post-treatment of the sample did not show significant variations in the sample dimensions.

Table 6. Average directional dimensions, total porosity, relative densities (Archimedes and geometrical), and compression strength of HA cylinders before and after the post-treatment.

Sample	Directional dimensions		Total porosity (CT) (vol. %)	Relative density (Archimedes) ($g.cm^{-3}$)	Relative density (Geometrical) ($g.cm^{-3}$)	Compression strength (MPa)
	Height (mm)	Diameter (mm)				
HA_Cyl	14.6±0.4	11.2±0.1	50	2.77±0.02	2.47±0.10	0.010
HA_Cyl_PT	14.7±0.4	11.2±0.1	48	2.97±0.04	2.48±0.07	0.049±0.001

Figure 22 shows the three-dimensional reconstructions of the samples (before and after thermal treatment) using X-ray micro-computed tomography. The same kind of porosities (closed and interconnected) was observed for both samples, also it was similar to the observed in the samples obtained during the second approach (Figure 18). Regarding the comparison between the two types of density values measured by two different methods (Archimedes and geometrical) can give an idea of the porosity of the samples. Obtaining a higher value by Archimedes indicates that an open porosity exists. Its comparison with the initial HA powder density (3.16 $g.cm^{-3}$) also confirms the porosity observed by the CT technique (very close to the common cancellous bone porosity 50-90% [41]). Between the two different samples, the higher density obtained after post-treatment indicates that higher densification of the part occurred during the post-

treatment which could improve their mechanical properties. This hypothesis is supported by the higher compression strength obtained for the sample after post-treatment (0.049±0.001 MPa). However, it is still lower than the strength reported for cancellous bone (1-12 MPa) [41].

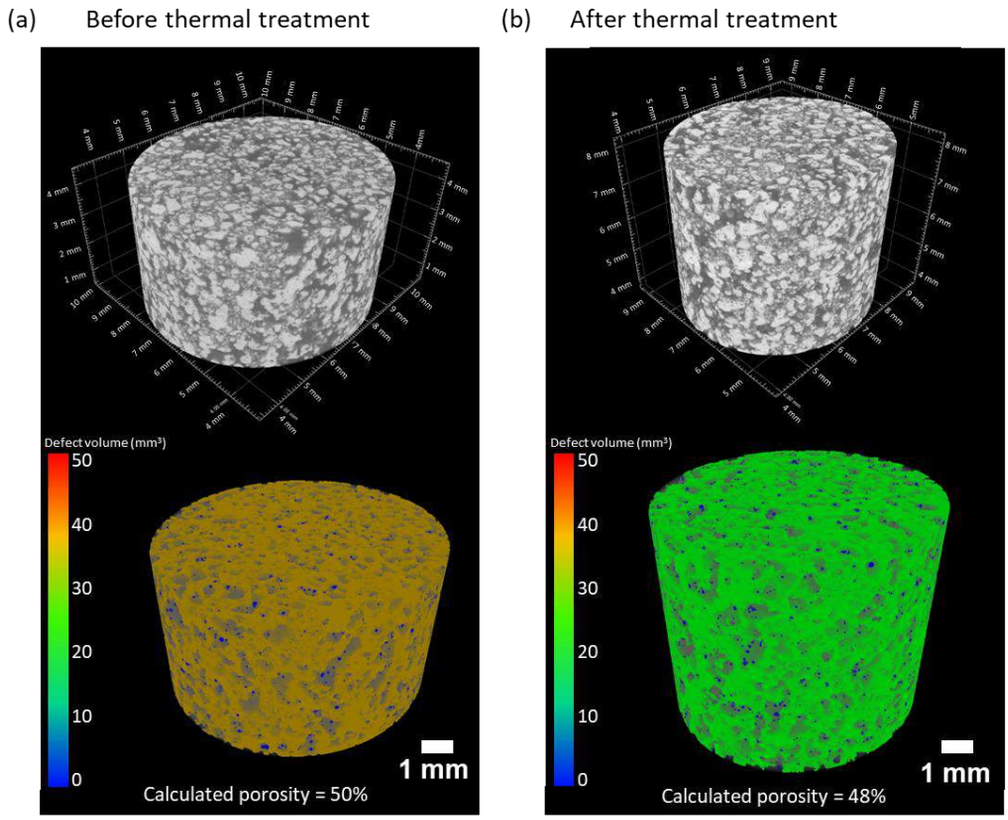

Figure 22. Visualization was obtained using X-ray micro-computed tomography of the sample HA_Cyl (a) before and (b) after the thermal treatment. Upper: Volume analysis of the samples. Down: Analysis of the porosity distribution in the region of interest (blue: closed porosity, orange and green: interconnected porosity

3.3 Heuristic procedure to determine the fixed PBSLP parameters

Heuristic research on the process parameters for the printing of CaP powders with graphite was carried out. A series of observations were obtained (underlined text) allowing us to reduce the range of parameters to evaluate during this work, thus fixing some of them. These first observations together with a review of the literature on laser processing of different materials explain the importance of these parameters and the reason for choosing determined values:

- During our study, the presence of oxygen in the chamber atmosphere was observed to have an important factor for the laser-induced ignition and combustion of graphite powder. This reaction can be described as exothermic (heat is evolved during the reaction), combustion (carbon burnt in presence of oxygen), and combination (carbon combines with oxygen to form carbon dioxide and carbon monoxide) reaction. Graphite starts reacting (burning) with O_2 above 700-800ºC producing CO_2 and CO gases that will escape into the atmosphere leaving a porosity in the printed parts that will depend on the graphite volume fraction used [42]. The quantities of CO_2, CO and effective heat of reaction depend on the amount of oxygen and carbon available during the reaction [43]. The reactions taking place can be described as:

$$C_{(s)} + O_{2(g)} \rightarrow CO_{2(g)} \quad (7)$$

$$2C_{(s)} + O_{2(g)} \rightarrow 2CO_{(g)} \quad (8)$$

- The compression of the powder bed was evaluated and an improvement on the surface finishing was observed when the powder was compacted before the laser scanning. It is known that the spreading and compression of the powder have an important effect on the properties of the printed parts. Beitz et al. [44] offered an interesting summary of the results obtained by different authors on the spreading and compression of powder beds with different devices. They concluded, through the study of the spreading of PA 12 powders, that an even compression of the powder bed is better achieved when using both, a scraper or blade and a counter-rotating roller. This combination, which is used in the present study, results in a more uniform and dense powder bed lowering the surface finish roughness of the parts. Sofia et al. [45] verified the effect of the compression of glass beads powder beds by bending tests indicating that the final sintered resistance increases by 198% in the case of compressed fine powder (x_{50} = 16 µm). However, it was pointed out that with the increase in the particle diameter, the compression process loses effectiveness. The effect of the roller-spreading parameters was studied by Zhang et al. [46] via discrete element simulation. They stated that lower roller translational velocity, higher roller diameter, and higher powder layer thickness increase the uniformity and density of the powder bed, although further research and experimental validation still have to be carried out to provide a more reliable basis for the optimization of the roller-spreading parameters.
- During our preliminary tests, it was observed that the laser scan strategy had also a high influence on the quality of the parts. Precisely, the “track overlapping” or the repetition of different laser

scans/passes over the same powder particles during the same layer step favoured the sintering/melting of the parts. This parameter has been rarely investigated, however, Changpeng et al. [47] offered a study on the prediction of the effect of the overlap rate and pattern on the residual stress (caused by the extremely uneven temperature distribution) induced by the island scanning strategy during a selective laser process. Some of their findings were that an overlap rate of 25% - 50% for a general island size (between 1 x 1 mm^2 and 10 x 10 mm^2) and a laser vertical re-scanning (90º rotation between layers) together with a short scanning length were recommended to reduce the residual stress.

- The influence of the laser defocusing by displacing the building platform in the z-axis was also evaluated. It was found that the defocusing strongly affects the laser-material interaction producing important variations in the final properties of the parts. It is known that the defocus distance alters the laser spot size and for hence the melt pool size. In addition, the direction in which the stage is moved in the z-axis is known to be a significant factor [11,48]. The production of solid parts was not possible when the laser was completely focused. A laser defocus of 3 cm downward the focus plane (positive sense) was tested and it allowed the densification of the parts. This laser defocus value distance was kept for the present study.
- The direct printing on the stainless-steel printing platform (absence of substrate), as well as the use of stainless steel and TA6V discs coated with HA, were evaluated in terms of printed part-building plane surface interaction. It was found that the distortion of the printed part was highly influenced by the kind of material used. The use of HA-coated discs seemed to improve this interaction enhancing the quality and density of the parts and their attachment to the substrate surface, better when using TA6V discs. In the field of laser processing (sintering/melting) of metallic powders, the influence of the material substrate has been widely studied. The substrates are commonly used to avoid the balling effect in powder melting and dislocation of the printed parts. Shen et al. [49] studied the effect of the substrate on the temperature distribution during the laser processing of metallic powders. They confirmed the importance of the substrate material's thermal conductivity (k). When the absence of substrate or when the thermal conductivity of the material used is poor the heat is confined in a small irradiated zone influencing negatively the quality of the parts. For the first printing layers, the heat absorbed by the powder bed is quickly transmitted to the substrate however when the process continues and the number of layers increases the distance between the irradiated powder layer and the substrate increases, reducing this heat transmission. Since the heat transference by the loose powder is much lower than by the full-density solid body of the substrate it leads to parts distortion (shrinkage and warping). For this reason, it is common the utilization of the same material substrate as the powder being printed reducing the differences between thermal conductivities [50]. The thermal conductivities of the material employed have been reported in the literature [23,51,52]: stainless-steel (15 $W.m^{-1}.K^{-1}$), TA6V (7.1 $W.m^{-1}.K^{-1}$), HA (<3% porosity) coating (0.72-3 $W.m^{-1}.K^{-1}$) and HA powder (0.10-0.15 $W.m^{-1}.K^{-1}$). Through our observation, we could

hypothesize that the lower differences between thermal conductivities of TA6V discs coated with HA and the HA powder bed, compared when using stainless steel, reduce the distortion and warping of the printed solid parts.

4. Conclusions

The present study shows our research on the PBSLP process of ceramic calcium phosphate powders. HA and ClA powders were mixed with graphite as an absorptance additive to be used as process feedstock. A preliminary analysis of the literature and heuristic research of the printing parameters was performed to close the wide range of parameters that the PBSLP technique involves fixing some of the parameters as the starting point. Three different approaches were employed for the analysis of materials feedstock performance.

First, the printing of laser-induced circular patterns at different printing parameters allowed us to obtain a process window for each one of the powders prepared and compare them. It was observed that from 5 to 10 wt. % the higher the amount of graphite the higher was the sintering/melting capacity of HA powder. These circular samples were analysed microscopically, chemically, and structurally showing a phase transition for the powder composed of HA into TTCP and α-TCP. Phase proportion was dependent on the E_d used during the process and the amount of graphite. The HA powder feedstock containing a 10 wt. % of graphite, printed at a energy density of 288 J.cm^{-3} (laser power: 36 W; scanning speed: 25 mm.s^{-1}) showed the lowest effect of the balling phenomena and low phase transition after the process (46.5 wt.% HA). In this first approach, the sample ClA_5G showed the most outstanding results due to its inherent higher thermal stability without phase transition. All samples showed balling phenomena, however, the use of ClA_5G with a high E_d and HA_10G with low E_d (in the range studied) produced smoother surface finishing.

The second approach was performed in parallel to the first one. The printing of complex samples was achieved using the HA_5G feedstock and the same hexagon-based laser scan strategy as in the first approach. However, the combination of printing parameters used (laser power: 30 W, scanning speed: 25 mm.s^{-1}, E_d: 240 J.cm^{-3}) yielded a too slow build rate needing long times to print samples in series. The total porosity of these samples was 24%.

Through the third approach, HA_10G powder feedstock was used to achieve the production of solid cylindrical samples in a faster way. An energy density of 96 J.cm^{-3} (laser power: 36 W, scanning speed: 75 mm.s^{-1}) together with a strategy based on the overlapping of 5 laser passes for each printing laser were the parameters used. Morphology, chemical composition, and mechanical properties analyses of the cylinders before and after their treatment at high temperature were carried out. It was found that a phase transition of the initial HA powder into other phases occurred after their printing. This transition was partially reverted by the thermal treatment. This treatment also enhanced the compression strength of the sample from 0.010 MPa to 0.049±0.001 MPa. Indeed, it slightly increased the density of the part from 2.77±0.02 to 2.97±0.04.

However, further research should be done on the improvement of the low mechanical properties observed through optimization of initial formulation, operating conditions, and/or additional post-treatments.

In conclusion, the processability of calcium phosphate powders in a PBSLP was examined by adding an absorption additive. Phase transition of HA into other phases was evaluated with different powder feedstock and printing parameters. Solid samples were successfully printed with a majority of HA phases in their composition. ClA showed promising results as starting powder feedstock to HA mainly due to its higher thermal stability, avoiding any phase change. This is the first step for the direct production of calcium phosphate bone substitutes through the PBSLP process. A deeper investigation should be made on the use of ClA powder as feedstock for the printing of solid parts. Further studies on the improvement of the mechanical properties of the parts could open a new possibility for the production of bioceramic scaffolds with interconnected porosity showing enhanced bioactive properties.

5. Acknowledgments

This project has received funding from the European Union's Horizon 2020 research and innovation programme under the Marie Skłodowska-Curie grant agreement No 764935.

6. Author contributions

P. Navarrete-Segado, C. Frances, M. Tourbin, and D. Grossin designed the followed methodology. P. Navarrete-Segado drafted the manuscript and conducted the majority of experiments. *C*. Tenailleau and B. Duployer performed the CT experiments. D. Grossin also supervised the project.

7. REFERENCES

[1] D. Grossin, A. Montón, P. Navarrete-Segado, E. Özmen, G. Urruth, F. Maury, D. Maury, C. Frances, M. Tourbin, P. Lenormand, G. Bertrand, A review of additive manufacturing of ceramics by powder bed selective laser processing (sintering / melting): Calcium phosphate, silicon carbide, zirconia, alumina, and their composites, Open Ceramics. 5 (2021) 100073. https://doi.org/10.1016/j.oceram.2021.100073.

[2] S. Eosoly, D. Brabazon, S. Lohfeld, L. Looney, Selective laser sintering of hydroxyapatite/poly-ε-caprolactone scaffolds, Acta Biomaterialia. 6 (2010) 2511–2517. https://doi.org/10.1016/j.actbio.2009.07.018.

[3] L. Hao, M.M. Savalani, Y. Zhang, K.E. Tanner, R.J. Heath, R.A. Harris, Characterization of selective laser-sintered hydroxyapatite-based biocomposite structures for bone replacement, Proceedings of the Royal Society A: Mathematical, Physical and Engineering Sciences. 463 (2007) 1857–1869. https://doi.org/10.1098/rspa.2007.1854.

[4] Y. Xia, P. Zhou, X. Cheng, Y. Xie, C. Liang, C. Li, S. Xu, Selective laser sintering fabrication of nano-hydroxyapatite/poly-ε-caprolactone scaffolds for bone tissue engineering applications, Int J Nanomedicine. 8 (2013) 4197–4213. https://doi.org/10.2147/IJN.S50685.

[5] F. Cruz, Fabrication of HA/PLLA Composite Scaffolds for Bone Tissue Engineering Using Additive Manufacturing Technologies, in: M. Elnashar (Ed.), Biopolymers, Sciyo, 2010. https://doi.org/10.5772/10264.

[6] H. Zeng, J.L. Pathak, Y. Shi, J. Ran, L. Liang, Q. Yan, T. Wu, Q. Fan, M. Li, Y. Bai, Indirect selective laser sintering-printed microporous biphasic calcium phosphate scaffold promotes endogenous bone regeneration via activation of ERK1/2 signaling, Biofabrication. 12 (2020) 025032. https://doi.org/10.1088/1758-5090/ab78ed.

[7] C. Shuai, P. Li, J. Liu, S. Peng, Optimization of TCP/HAP ratio for better properties of calcium phosphate scaffold via selective laser sintering, Materials Characterization. 77 (2013) 23–31. https://doi.org/10.1016/j.matchar.2012.12.009.

[8] L. Ferrage, G. Bertrand, P. Lenormand, Dense yttria-stabilized zirconia obtained by direct selective laser sintering, Additive Manufacturing. 21 (2018) 472–478. https://doi.org/10.1016/j.addma.2018.02.005.

[9] C. Colin, J.-D. Bartout, E. Shaker, Osseomatrix patent - WO2014154901A1, WO2014154901A1, 2014.

[10] K.G. Prashanth, S. Scudino, T. Maity, J. Das, J. Eckert, Is the energy density a reliable parameter for materials synthesis by selective laser melting?, Materials Research Letters. 5 (2017) 386–390. https://doi.org/10.1080/21663831.2017.1299808.

[11] P. Leo, M. Cabibbo, A. Del Prete, S. Giganto, S. Martínez-Pellitero, J. Barreiro, Laser Defocusing Effect on the Microstructure and Defects of 17-4PH Parts Additively Manufactured by SLM at a Low Energy Input, Metals. 11 (2021) 588. https://doi.org/10.3390/met11040588.

[12] M. Tourbin, F. Brouillet, B. Galey, N. Rouquet, P. Gras, N. Abi Chebel, D. Grossin, C. Frances, Agglomeration of stoichiometric hydroxyapatite: Impact on particle size distribution and purity in the precipitation and maturation steps, Powder Technology. 360 (2020) 977–988. https://doi.org/10.1016/j.powtec.2019.10.050.

[13] I. Demnati, D. Grossin, C. Combes, M. Parco, I. Braceras, C. Rey, A comparative physico-chemical study of chlorapatite and hydroxyapatite: from powders to plasma sprayed thin coatings, Biomed. Mater. 7 (2012) 054101. https://doi.org/10.1088/1748-6041/7/5/054101.

[14] L. Lutterotti, S. Matthies, H. Wenk, MAUD: a friendly Java program for material analysis using diffraction, UCr: Newsletter of the CPD. 21 (1999) 14–15.

[15] C.A. Schneider, W.S. Rasband, K.W. Eliceiri, NIH Image to ImageJ: 25 years of image analysis, Nat Methods. 9 (2012) 671–675. https://doi.org/10.1038/nmeth.2089.

[16] Implants for surgery ISO 13175-3 2012 — Calcium phosphates — Part 3: Hydroxyapatite and beta-tricalcium phosphate bone substitutes, (2008).

[17] K. Tõnsuaadu, K.A. Gross, L. Plūduma, M. Veiderma, A review on the thermal stability of calcium apatites, J Therm Anal Calorim. 110 (2012) 647–659. https://doi.org/10.1007/s10973-011-1877-y.

[18] N.K. Tolochko, Y.V. Khlopkov, S.E. Mozzharov, M.B. Ignatiev, T. Laoui, V.I. Titov, Absorptance of powder materials suitable for laser sintering, Rapid Prototyping Journal. 6 (2000) 155–161. https://doi.org/10.1108/13552540010337029.

[19] T. Laumer, T. Stichel, M. Sachs, P. Amend, M. Schmidt, Qualification and modification of new polymer powders for laser beam melting using Ulbricht spheres, in: P. da Silva Bártolo, A. de Lemos, A. Pereira, A. Mateus, C. Ramos, C. Santos, D. Oliveira, E. Pinto, F. Craveiro, H. da Rocha Terreiro Galha Bártolo, H. de Amorim Almeia, I. Sousa, J. Matias, L. Durão, M. Gaspar, N. Fernandes Alves, P. Carreira, T. Ferreira, T. Marques (Eds.), High Value Manufacturing: Advanced Research in Virtual and Rapid Prototyping, CRC Press, 2013: pp. 255–260. https://doi.org/10.1201/b15961-48.

[20] H.C.H. Ho, W.L. Cheung, I. Gibson, Effects of graphite powder on the laser sintering behaviour of polycarbonate, Rapid Prototyping Journal. 8 (2002) 233–242. https://doi.org/10.1108/13552540210441148.

[21] T.J. Levingstone, M. Ardhaoui, K. Benyounis, L. Looney, J.T. Stokes, Plasma sprayed hydroxyapatite coatings: Understanding process relationships using design of experiment analysis, Surface and Coatings Technology. 283 (2015) 29–36. https://doi.org/10.1016/j.surfcoat.2015.10.044.

[22] V.V. Sobolev, J.M. Guilemany, Flattening of Droplets and Formation of Splats in Thermal Spraying: A Review of Recent Work— Part, Journal of Thermal Spray Technology. 8 (1999) 301–314.

[23] M. Chambard, Revêtements nanostructurés d'hydroxyapatite multisubstituée élaborés par projection de suspension par plasma inductif : de la chimie du précurseur aux propriétés mécaniques et biologiques, (2019) 331.

[24] J. Liu, B. Zhang, C. Yan, Y. Shi, The effect of processing parameters on characteristics of selective laser sintering dental glass-ceramic powder, Rapid Prototyping Journal. 16 (2010) 138–145. https://doi.org/10.1108/13552541011025861.

[25] M. Prakasam, J. Locs, K. Salma-Ancane, D. Loca, A. Largeteau, L. Berzina-Cimdina, Fabrication, Properties and Applications of Dense Hydroxyapatite: A Review, J Funct Biomater. 6 (2015) 1099–1140. https://doi.org/10.3390/jfb6041099.

[26] I. Demnati, D. Grossin, O. Marsan, G. Bertrand, G. Collonges, C. Combes, M. Parco, I. Braceras, J. Alexis, Y. Balcaen, C. Rey, Comparison of Physical-chemical and Mechanical Properties of Chlorapatite and Hydroxyapatite Plasma Sprayed Coatings, The Open Biomedical Engineering Journal. 9 (2015). https://doi.org/10.2174/1874120701509010042.

[27] L. Moniz, Q. Chen, G. Guillemot, M. Bellet, C.-A. Gandin, C. Colin, J.-D. Bartout, M.-H. Berger, Additive manufacturing of an oxide ceramic by laser beam melting—Comparison between finite element simulation and experimental results, Journal of Materials Processing Technology. 270 (2019) 106–117. https://doi.org/10.1016/j.jmatprotec.2019.02.004.

[28] S. Liu, H. Guo, Balling Behavior of Selective Laser Melting (SLM) Magnesium Alloy, Materials (Basel). 13 (2020) 3632. https://doi.org/10.3390/ma13163632.

[29] D. Gu, Y. Shen, Balling phenomena in direct laser sintering of stainless steel powder: Metallurgical mechanisms and control methods, (2009). https://doi.org/10.1016/J.MATDES.2009.01.013.

[30] Z. Wang, X. Wang, X. Zhou, G. Ye, X. Cheng, P. Zhang, Investigation into Spatter Particles and Their Effect on the Formation Quality During Selective Laser Melting Processes, Computer Modeling in Engineering & Sciences. 124 (2020) 243–263. https://doi.org/10.32604/cmes.2020.09934.

[31] M.H. Leipold, T.H. Nielsen, E.C. de Wys, The Effect of Grain Boundaries on Mechanical Behavior in Polycrystalline Ceramics, Technical Report. (1967) 16.

[32] L. de A. Cavalcante, L.S. Ribeiro, M.L. Takeno, P.T.P. Aum, Y.K.P.G. Aum, J.C.S. Andrade, Chlorapatite Derived from Fish Scales, Materials. 13 (2020) 1129. https://doi.org/10.3390/ma13051129.

[33] E. García-Tuñón, R. Couceiro, J. Franco, E. Saiz, F. Guitián, Synthesis and characterisation of large chlorapatite single-crystals with controlled morphology and surface roughness, J Mater Sci Mater Med. 23 (2012) 2471–2482. https://doi.org/10.1007/s10856-012-4717-0.

[34] C.-J. Liao, F.-H. Lin, K.-S. Chen, J.-S. Sun, Thermal decomposition and reconstitution of hydroxyapatite in air atmosphere, Biomaterials. 20 (1999) 1807–1813. https://doi.org/10.1016/S0142-9612(99)00076-9.

[35] M. Hashiura, K. Mori, Formation of CO Macroblowholes during Solidification of Iron-Carbon Alloys Containing below 0.03% Carbon, (1988). https://doi.org/10.2355/TETSUTOHAGANE1955.74.6_1006.

[36] A. Goel, Material Science and Metallurgy: Fundamentals and Importance, Technical Publications, 2021.
[37] S.M. Barinov, J.V. Rau, S.N. Cesaro, J. Ďurišin, I.V. Fadeeva, D. Ferro, L. Medvecky, G. Trionfetti, Carbonate release from carbonated hydroxyapatite in the wide temperature rage, J Mater Sci: Mater Med. 17 (2006) 597–604. https://doi.org/10.1007/s10856-006-9221-y.
[38] N. Makoana, I. Yadroitsava, H. Möller, I. Yadroitsev, Characterization of 17-4PH Single Tracks Produced at Different Parametric Conditions towards Increased Productivity of LPBF Systems—The Effect of Laser Power and Spot Size Upscaling, Metals. 8 (2018) 475. https://doi.org/10.3390/met8070475.
[39] C. Rey, O. Marsan, C. Combes, C. Drouet, D. Grossin, S. Sarda, Characterization of Calcium Phosphates Using Vibrational Spectroscopies, in: B. Ben-Nissan (Ed.), Advances in Calcium Phosphate Biomaterials, Springer Berlin Heidelberg, Berlin, Heidelberg, 2014: pp. 229–266. https://doi.org/10.1007/978-3-642-53980-0_8.
[40] L. Zhang, S. Zhang, H. Zhu, Z. Hu, G. Wang, X. Zeng, Horizontal dimensional accuracy prediction of selective laser melting, Materials & Design. 160 (2018) 9–20. https://doi.org/10.1016/j.matdes.2018.08.059.
[41] T.-R. Kim, M.-S. Kim, T.S. Goh, J.S. Lee, Y.H. Kim, S.-Y. Yoon, C.-S. Lee, Evaluation of Structural and Mechanical Properties of Porous Artificial Bone Scaffolds Fabricated via Advanced TBA-Based Freeze-Gel Casting Technique, Applied Sciences. 9 (2019) 1965. https://doi.org/10.3390/app9091965.
[42] D.M. Crumpton, R.A. Laitinen, J. Smieja, D.A. Cleary, Thermal Analysis of Carbon Allotropes: An Experiment for Advanced Undergraduates, ACS Publications. (1996). https://doi.org/10.1021/ed073p590.
[43] Y. Wang, M. Zhang, S. Chang, S. Li, X. Huang, Laser-Induced Ignition and Combustion Behavior of Individual Graphite Microparticles in a Micro-Combustor, Processes. 8 (2020) 1493. https://doi.org/10.3390/pr8111493.
[44] S. Beitz, R. Uerlich, T. Bokelmann, A. Diener, T. Vietor, A. Kwade, Influence of Powder Deposition on Powder Bed and Specimen Properties, Materials. (2019). https://doi.org/10.3390/ma12020297.
[45] D. Sofia, M. Lupo, D. Barletta, M. Poletto, Validation of an Experimental Procedure to Quantify The Effects of Powder Spreadability on Selective Laser Sintering Process, Chemical Engineering Transactions. 74 (2019) 397. https://doi.org/10.3303/CET1974067.
[46] J. Zhang, Y. Tan, T. Bao, Y. Xu, X. Xiao, S. Jiang, Discrete Element Simulation of the Effect of Roller-Spreading Parameters on Powder-Bed Density in Additive Manufacturing, Materials. 13 (2020) 2285. https://doi.org/10.3390/ma13102285.
[47] C. Changpeng, J. Yin, H. Zhu, Z. Xiao, L. Zhang, X. Zeng, Effect of overlap rate and pattern on residual stress in selective laser melting, International Journal of Machine Tools and Manufacture. 145 (2019) 103433. https://doi.org/10.1016/j.ijmachtools.2019.103433.
[48] J. Metelkova, Y. Kinds, K. Kempen, C. de Formanoir, A. Witvrouw, B. Van Hooreweder, On the influence of laser defocusing in Selective Laser Melting of 316L, Additive Manufacturing. 23 (2018) 161–169. https://doi.org/10.1016/j.addma.2018.08.006.
[49] X. Shen, Y. Wang, J. Yang, Effect of substrate on temperature field in selective laser sintering of metal powders, in: International Congress on Applications of Lasers & Electro-Optics, Laser Institute of America, Orlando, Florida, USA, 2009: pp. 821–829. https://doi.org/10.2351/1.5061650.
[50] S. Liu, S. Chang, H. Zhu, J. Yin, T. Wang, X. Zeng, Effect of substrate material on the molten pool characteristics in selective laser melting of thin wall parts, Int J Adv Manuf Technol. 105 (2019) 3221–3231. https://doi.org/10.1007/s00170-019-04540-1.
[51] S.S. Sib, J.W. Barlow, Measurement and prediction of the thermal conductivity of powders at high htemperatrues, (1994) 9.
[52] Thermal Conductivity of Metals, Metallic Elements and Alloys, (2005). https://www.engineeringtoolbox.com/thermal-conductivity-metals-d_858.html.

8. Supplementary information

Table S1. FTIR line positions of TTCP, HA, and α-TCP. (cm^{-1}; m medium, s strong, sh shoulder, v very, w weak). Adapted from Rey et al [39].

	TTCP	HA	α-TCP
PO_4 V_3	1,105 w		
	1,093 w	1,092 s	
	1,073 w		
	1,062 s		1,055 s
	1,046 s	1,040 vs	1,039 s
	1,033 m		1,025 s
			1,013 s
	1,010 s		997 s
	989 s		984 s
PO_4 V_1	962 w	962 w	
	956 w		954 m
	946 w		
	941 w		
PO_4 V_4	620 w		613 m
	594 w	601 m	597 m
			585 m
	571 s	575 m,sh	563 m
		561 m	551 m
	501 w		
PO_4 V_2	471 m	472 vw	471 w
		462 sh	463 w
			454 w
	450 w		430 w
	429 w		415 w
	399 m		

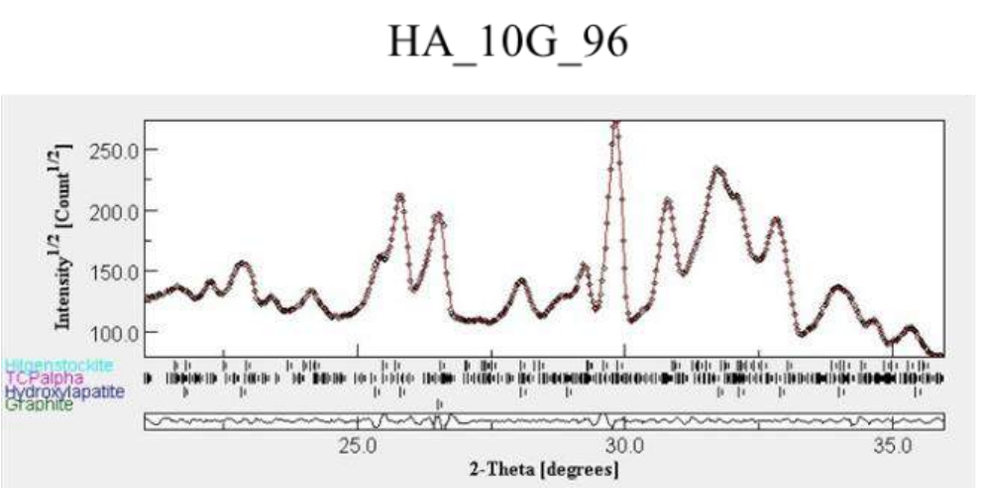

Figure S1. Example of one plot of the Rietveld refinement of the HA laser-induced sample (HA_10G_96), with the Bragg reflections of each phase, labelled on the left. Hilgenstockite = TTCP phase.

Chapter VI. Masked stereolithography of hydroxyapatite bioceramic scaffolds: From powder tailoring to evaluation of 3D printed parts properties

Masked stereolithography of hydroxyapatite bioceramic scaffolds through an integrative approach: From powder tailoring to evaluation of 3D printed parts properties

Pedro Navarrete-Segado,[a,b] Christine Frances,[b] Mallorie Tourbin,[b] David Grossin[a,*]

[a] CIRIMAT, Université de Toulouse, CNRS, 4 Allée Émile Monso, 31432 Toulouse Cedex 4, France

[b] Laboratoire de Génie Chimique (LGC), Université de Toulouse, CNRS, 4 Allée Émile Monso, 31432 Toulouse Cedex 4, France

Abstract. In this paper, the tailoring of hydroxyapatite powders properties for the preparation of highly hydroxyapatite-loaded photocurable organic slurries was discussed. A methodical study was conducted to investigate suspensions properties and processability to find the most outstanding formulation for the production of hydroxyapatite scaffolds by stereolithography-based additive manufacturing technique. A debinding-sintering process was designed to avoid the formation of cracks during the pyrolysis of the resin and sintering of the ceramic part. A total porosity of 35 vol. % was observed for the scaffolds with an interconnected macroporosity, which could facilitate the flow transport of nutrients necessary to maintain living cells. A compression strength of 4.9±0.3 MPa was obtained for the specimens printed diagonally (45º to the printing stage surface). A slow degradation rate was shown for the printed parts mainly due to the high degree of crystallinity and the intrinsic stability of the hydroxyapatite phase. Our findings indicate that the tailoring of hydroxyapatite powders is needed for better processability as filler in photocurable suspensions. Moreover, it was demonstrated the feasibility of printing hydroxyapatite parts showing promising results for their application in surgery in the case of minor or non-load bearing implants requiring slow resorption properties.

Keywords: hydroxyapatite, rheology, sedimentation, suspensions, mechanical properties, VAT photopolymerisation; additive manufacturing

***Corresponding author: david.grossin@ensiacet.fr

1. Introduction

People are living longer than ever before and will soon become one of the major problems worldwide, with the median age projected to increase by 4.5 years between 2019 and 2050 [1]. This ageing increase leads to a growth of incidence of bone injuries and deficiencies [2]. In the last decades, the rising interest for new efficient therapies has brought wide progress on the use of biomaterials such as calcium phosphate-based bioceramics [3]. Reparation of fractured or diseased bone needs to start from a scaffold or three-dimensional (3D) construct providing the necessary support for the attachment, growth, and proliferation of bone cells [4]. Hydroxyapatite (HA) is one of the most commonly used calcium phosphates bioceramic phases for bone tissue engineering in orthopaedic and dental communities for its excellent biocompatibility, slow degradation, and osteointegration [5]. HA can withstand resorption during healing providing a good scaffold for natural bone growth, their slow resorption properties could be an advantage in maintaining the volumetric stability of the augmented bone. The presence of hard tissue around a dental implant is crucial for the long-term success of implant placement in surgical techniques such as guided bone regeneration and autogenous bone blocks transfer for dental implant placement [6–8]. For block grafts used in regeneration, an ideal biomaterial, should meet at least the following characteristics: (i) biocompatibility and controlled biodegradability with sufficient durability to carry out the task for which it was developed [9], (ii) a porous and interconnected design enabling osteoblasts (15-50 μm) and stem cells (5-12 μm) migration, proliferation, and flow transport of nutrients and metabolic waste through the pores [10] (ideal size of the micropores should be at least 400 μm) [11], (iii) mechanical properties matching those of the target tissue at the site of implantation [12], (iv) suitable surface chemistry for cell anchorage, promotion and differentiation [12].

Additive manufacturing (AM) technologies have emerged as an excellent method to fabricate parts suitable for their use in bone tissue engineering applications [13]. They allow the production of allograft custom blocks with defined and reproducible internal structures [14]. Depending on the AM technique, the process basis, methodology, and primary feedstock properties can vary widely [15,16]. Techniques included in the VAT photopolymerization category uses a laser or UV-light source to cross-link a photocurable resin feedstock (composed of a photoinitiator, monomers, or oligomers, reactive diluents, and various additives such as bioceramic powders) [17].

Masked stereolithography (MSLA), also called LCD technique, is the last of these technologies arriving on the market and it has substantially grown in the last years [18]. It uses a direct and perpendicular UV light projection from an array of LEDs and an LCD device acting as a mask to selectively polymerize the photocurable feedstock. Some advantages of this LCD technique are the low cost compared with other technologies (laser SLA, DLP…) and the good resolution, although they have a shorter service life and need to be replaced regularly [19]. This and similar techniques have been recently employed for the production of calcium phosphates-based parts [17,20,21]. However, still, some research is needed on the intrinsic relationship between ceramic powder characteristics, solid loading, and dispersion behaviour on the

ceramic-loaded photocurable slurry properties [22]. Dispersed powder feedstock inducing a low increase of viscosity, keeping the stability of the suspensions, and showing a good sintering behaviour are pursued since these are crucial properties for a correct performance during the printing process as well as during post-treatments [23–25]. The maximum viscosity for a slurry intended for VAT photopolymerization is approximately 5 Pa.s at a low shear rate [26]. Then, certain stability of the suspensions should be reached avoiding the sedimentation of the particles, which could block the LCD screen and UV light during the printing process [23]. It is also important to use particles which size allows the subsequent debinding-sintering process preventing the formation of cracks. More often, this is achieved by calcium phosphate particles within the micron range (1-20µm) [27]. This can be reached by modifying the powder particle size distribution through different processes (e.g., milling, sieving…).

Thus, the objective of the present study is to evaluate the effect of the HA-tailored powders with different characteristics on the properties of the highly HA-loaded photocurable slurries. First, the powder showing the most outstanding performance in terms of slurry viscosity (< 5 Pa.s at a low shear rate (1 s^{-1})), and dispersion stability (Turbiscan stability index < 2) during the whole process will be found through comparison. Then, the processability of the suspension will be tested with the printing of HA parts with controlled macroporosity (pore size > 400 µm). Finally, the mechanical properties and the dissolution rate of the scaffolds will be determined to assess the HA bioceramic scaffolds efficacy as a bone substitute.

2. Material and methods

2.1 Materials

2.1.1 Stoichiometric hydroxyapatite powders

Stoichiometric hydroxyapatite powder (HA, $Ca_{10}(PO_4)_6(OH)_2$) was used as filler for the suspensions prepared in the present work. The initial powder was produced by Urodelia (SA Company, Saint-Lys, France) via a wet precipitation process (product reference 206.93.003). A deeper explanation of the production of this powder through wet-chemical precipitation was offered in a previous work [28].

HA-filled organic slurries for the MSLA process were produced with three kinds of HA powders (two of them produced by different milling processes) for suspension properties comparison (e.g., stability, rheology…):

- $HA_{Initial}$ powder: the starting HA powder was used as received.
- HA_{PBM} powder: A second powder was crushed through the planetary ball milling (PBM) process of $HA_{Initial}$. A Retsch® planetary-ball mill S 1000 was used to reduce the size of the largest agglomerates present in $HA_{Initial}$ powder. A previously weighted amount of powder (140 g) is poured inside of the 250 ml alumina grinding jar with lid together with the following alumina grinding balls (bulk density: 3600 kg/m^3, mass: 346 g): 3 balls of 30mm + 12 balls of 20mm + 9 balls of 10 mm. Then, a ball filling degree

of 0.38 (to total chamber volume) and powder filling degree of 0.44 (to ball-filled chamber volume) were used. After one hour of the milling process at 500 rpm, the HA_{PBM} powder was recovered.

- HA_{SBM} powder: Stirred bead milling process (SBM) was performed in a commercial equipment Labstar manufactured by NETZSCH (Germany) to reduce the size of the HA particles present in $HA_{Initial}$ powder. The detailed scheme of this SBM Labstar equipment and the experimental procedure were already detailed in previous works [29,30]. A water volume was added to the dispersing tank followed by the gradual addition of the weighted HA powder amount to have a final suspension batch of 2kg with a 10 wt.% of solid concentration. It was stirred during 10 minutes at 600 rpm at 25ºC before starting the pumping and comminution in the milling chamber. Yttrium Stabilized Zirconia 95% (YSZ, ZrO_2) micro grinding beads (Zirmil® Y from WAB-Group) were used for the milling in a 85% of chamber filling degree (total volume chamber 0.48l). The nominal size of the beads was 0.35-0.45 mm (laser diffraction particle analysed values x_{10} = 0.32 ± 0.00 mm, x_{50} = 0.39 ± 0.00 mm, and x_{90} = 0.45 ± 0.00, refractive and absorption indices of 2.148 and 1.000) with a density of 6020 $kg.m^{-3}$ (bulk density: 3700 $kg.m^{-3}$). The operational conditions were a stirrer speed of 7.7 $m.s^{-1}$ (2000 rpm), a constant product flow rate 8.8 x 10^{-6} $m^3.s^{-1}$, and specific energy of 720 $kJ.kg^{-1}$ (it was equivalent to 60 minutes of the process). From now on, we will refer to this ground powder as HA_{SBM}. After this wet grinding process, the HA_{SBM} powder had to be vacuum filtered, washed, and dried at 70ºC overnight before its utilization as filler.

2.1.2 Photocurable resin components

The commercial photoreactive resin Dentifix-3D, Modelling HR (high reactive) transparent (clear), from FunToDo® was used as a monomeric and photoinitiator base for the preparation of the organic suspensions. The exact composition of the resin is proprietary information; however, we could describe it as a mixture of approximately 50:50:1 in weight of acrylate monomers, glycol diacrylate monomers, and phosphine oxide base photoinitiator. To improve the rheological behaviour of the suspensions the addition of a reactive diluent was considered. Polyethylene glycol 200 (PEG200) was tested as a diluent and after a heuristic research process, it was found that the maximum amount that could be added without compromising the resin reactivity and performance was 25 vol. %. This volume proportion 3:1 of resin base:diluent was kept constant for all the slurries prepared during the study.

2.1.3 Preparation of HA-filled photocurable suspensions

A series of HA-filled photocurable suspensions were prepared to contain different types ($HA_{Initial}$, HA_{PBM}, HA_{SBM}) and concentrations of HA powders for comparison. The preparation consisted of the mixing/homogenization between the HA powder and the organic resin via the PBM process (same equipment used for the preparation of HA_{PBM}). It started with the addition of a previously weighted amount of HA powder (depending on the final concentration) into the grinding jar already containing the same proportion of grinding balls mentioned in the preparation of HA_{PBM}. Then, after pouring the organic resin (mass: 50g, already containing PEG200) the jar was closed with the lid and stirred by the PBM process at about 500 rpm for 30 min. Just after finishing the process, the resulting HA-filled suspensions were collected for rheology and dispersion stability evaluation and its utilization in an MSLA apparatus. A general view of the HA-filled photocurable slurry preparation is illustrated in Figure 1.

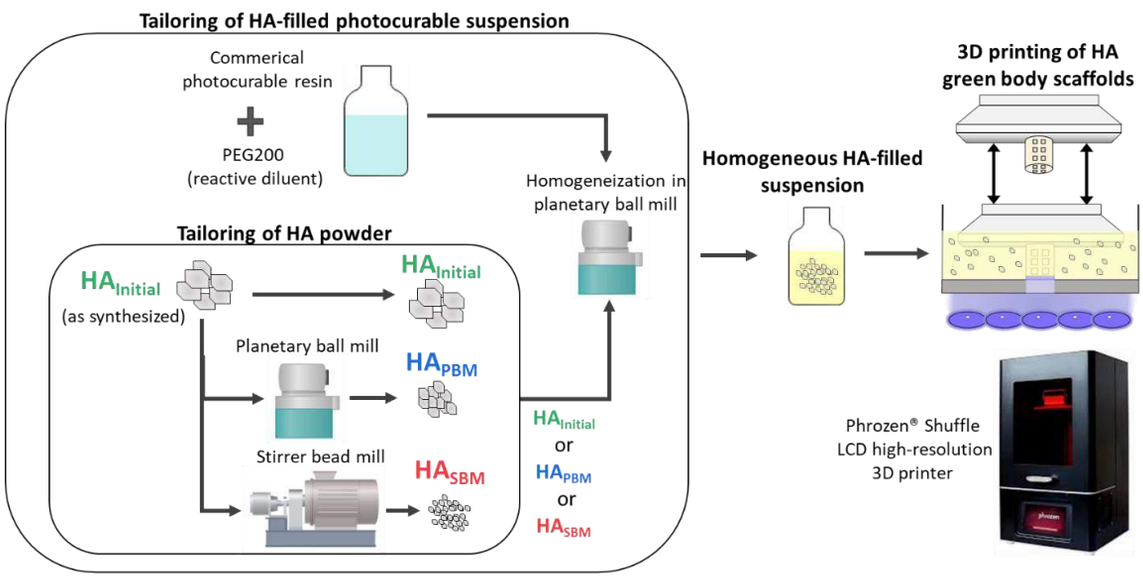

Figure 1. HA-filled photocurable slurry preparation process.

2.2 Production of HA scaffolds

2.2.1 3D printing of HA scaffolds via masked stereolithography

Three-dimensional bioceramic green bodies (HA/organic resin composite) were printed by intermittent and selective cross-linking of HA-filled suspension layers. A commercial MSLA equipment, Phrozen® Shuffle, LCD high-resolution 3D-printer was used [31]. It uses an LCD screen with a 5.5-inch 2K resolution reaching an XY resolution of 47 µm. A ParaLED matrix 1.0 optical engine is used as a UV light source with a 90% optical uniformity (better than conventional COB LED). The produced UV light has a wavelength of 405 nm and a power of 50W.

The process started by loading the previously designed 3D model (Figure 2) into the printer software. Since compression strength analyses were planned for the samples, the 3D model was designed according to the requirements described in the standard ISO 13175-3:2012 for the tests. The scaffolds model design consisted of a cylinder with 10 mm of diameter and 15 mm of height, with controlled internal and interconnected macro-porosity having circular overtures of 1000 µm in all three directions. Open-source FreeCAD and Chitubox basic software were employed for the design, creation of supports, placement of the models, and slicing. The resin profile was settled by fixing the printing parameters, which are described in Table 1. Basic information refers to the parameters followed during the whole process such as layer thickness, stage down speed, and lighting delay. Then, there is a distinction in the table between the printing parameters (cure time, stage lift height, and up speed) for the first 6 layers (burn layers) and the rest of the layers (normal layers). The same parameters profile was used for the printing of the scaffolds during the study.

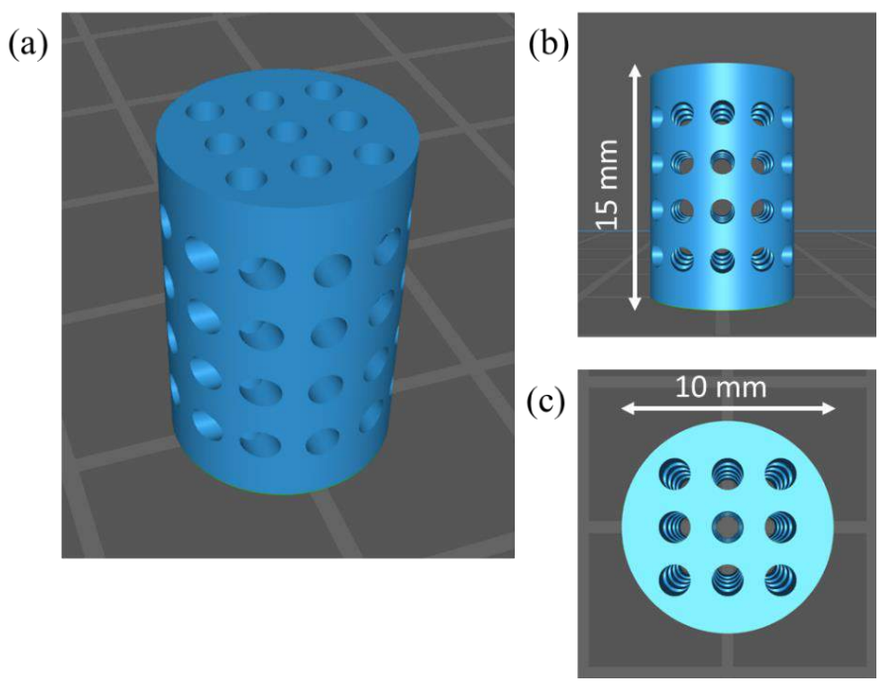

Figure 2. 3D model used to print the HA parts: (a) perspective, (b) front view, (c) top view.

Table 1. MSLA printing parameters profile used for the production of HA scaffolds.

	Basic information			**Burn layer (first 6 layers)**				**Normal layer**		
Parameter	Layer height (mm)	Down speed (mm/min)	Delay (ms)	Layers (number)	Cure time (ms)	Lift height (mm)	Up speed (mm/min)	Cure time (ms)	Lift height (mm)	Up speed (mm/min)
Value	0.1	150	1000	6	40000	8	100	10000	7	100

Once the printing platform has been calibrated in the z-axis, the slurry is poured inside of the tank container, and with the help of a plastic spatula, it is homogeneously spread to completely cover the FEP film, which separates the resin from the LCD screen. Then the printing process started constructing the model layer by layer combining the curing of the resin by UV light exposition and the movement of the platform in z-axis following the parameters defined. Figure 3 shows the MSLA process together with the resulting HA bioceramic scaffolds and the tank containing the HA-filled resin. Three different HA scaffold models were designed and printed varying the orientation. Three rotation degrees 0º, 45º, and 90º were applied to the models to study their influence on the quality of the printed parts. All models included supports and rafts to avoid the direct contact of the scaffolds with the printing platform surface.

One time the printing process finished, each raft supporting the scaffold was detached from the platform surface and the supports were carefully cut with tweezers freeing the HA green body scaffold. Then, the scaffolds were soaked in an ultrasonic bath with isopropyl alcohol (IPA) for 3 minutes. Finally, they were swirled around in the IPA to rinse off the extra uncured resin.

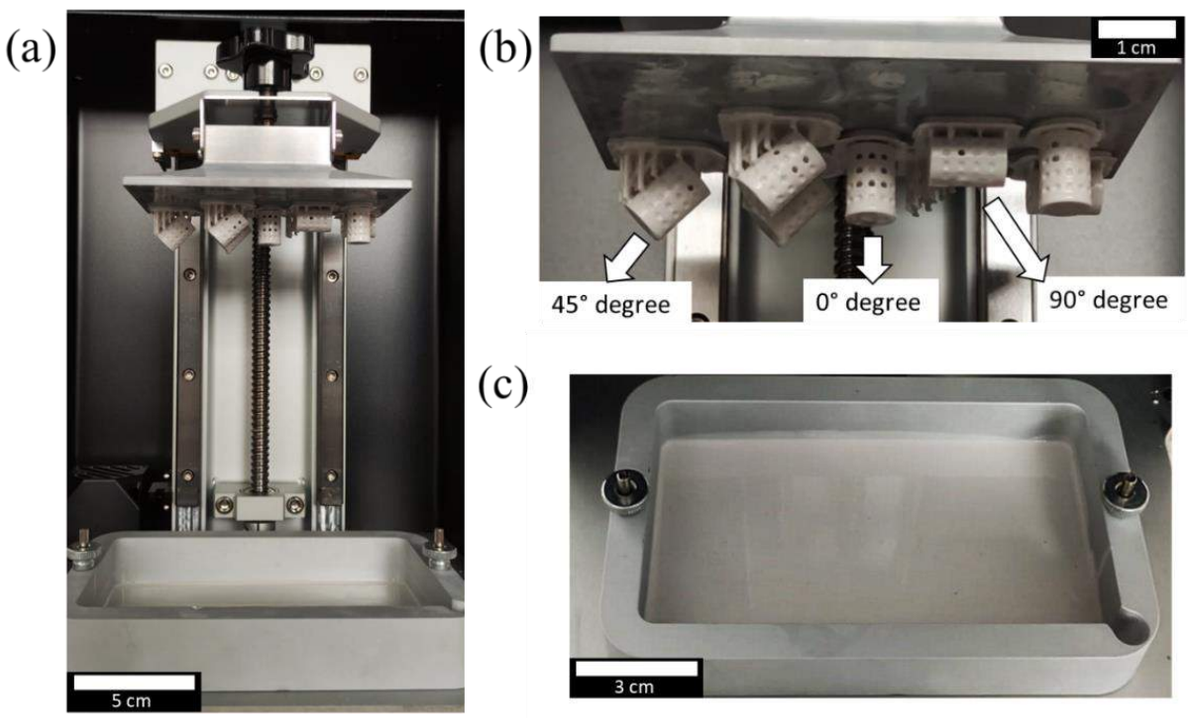

Figure 3. (a) General view of the MSLA process, (b) printing platform with HA scaffolds with three different printing orientations, and (c) HA-filled slurry container.

2.2.2 Debinding-sintering process

To obtain HA bioceramic scaffolds free of polymer it was necessary to design a one-step debinding-sintering process for the pyrolysis of the cured resin of the printed HA green bodies. Thus, producing in the same process the sintering of the HA particles keeping or improving the mechanical properties of the parts. To prepare the debinding-sintering process, the samples were placed in alumina crucibles and introduced in a muffle furnace Nabertherm® LT 9/13. They were located in a middle height and leaving the same space between the lateral walls inside of the muffle chamber to optimize the heat distribution. The process was carried out in the air and three different temperature phases (or heating ramps) could be distinguished. First, one heating ramp of 1ºC/min until 300ºC followed by another one of 0.2ºC/min until 650ºC performed the debinding phase. Then the heating was speeded up at 2ºC/min until 1250ºC and kept constant for two hours to achieve correct sintering of the HA particles. Finally, the furnace was inertially cooled down with an average speed of -1ºC/min to prevent the apparition of cracks due to thermal shocks. The complete temperature pattern followed is described in Figure 4.

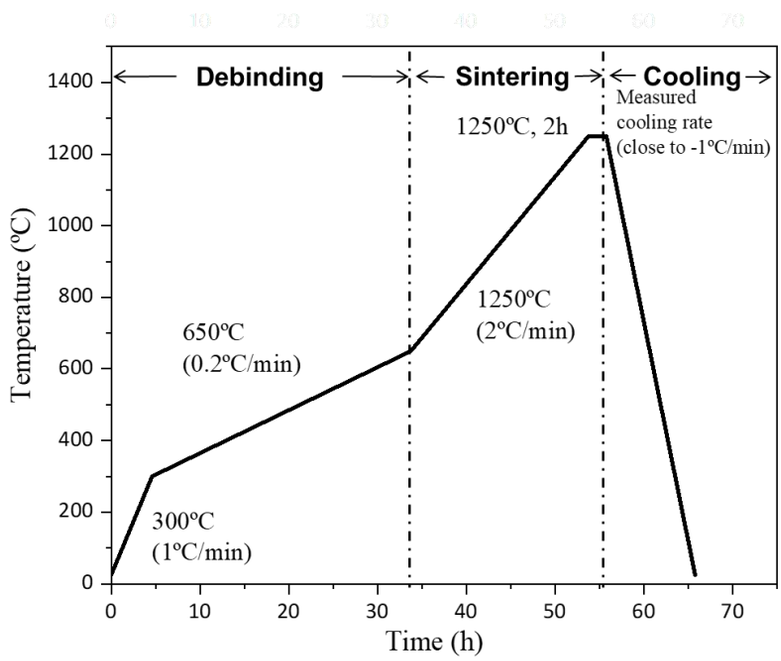

Figure 4. Programmed temperature pattern for the debinding-sintering process of HA scaffolds.

2.1 Characterization techniques

2.1.1 Particle size distribution

A Mastersizer MS 3000 (Malvern Panalytical®) laser particle size analyser (refractive indexes: 1.63 and 1.33 for particles and water, respectively) was used to analyse the PSD of the HA powders by laser diffraction in suspension. It was not possible to analyse the PSD of the HA powders suspended in the photocurable resin due to a risk of polymerization by the blue light (wavelength: 470 nm) used for the measurement. Instead, to simulate their dispersion state they were analysed in aqueous suspension.

Ultrapure water used as dispersion medium was produced by the equipment "Purelab Ultra" of VWS (UK) Ltd.

2.1.2 Turbidimetry analysis

Turbiscan stability index (TSI) (a Turbiscan specific parameter for stability comparison) and backscattered (BS) profiles of the different HA-filled slurries were obtained using a Turbiscan LAB™ (Formulaction®). The light source scanned the sample tube at 2 min intervals from top to bottom and measured the percentage of light BS or transmitted during a 3 h period at 25º C to cover the total time needed for the printing process of the green bodies (about two hours). Longer analyses (up to 66 hours) were performed to evaluate the time of destabilization. The analysis of the stability was performed as a variation of BS profiles as a function of time at the totality of the sample height. The curves obtained allow a better quantification of their dispersion stability and identify the phenomena taking place in the samples (sedimentation, flocculation…). The overall stability of slurries was examined using the TSI parameters calculated by the Turbiscan software using the formulae below [32]:

$$BS = \frac{1}{\sqrt{\lambda*}} \quad (1)$$

$$\lambda * (\varphi, x_{50}) = \frac{2x_{50}}{3\varphi(1-g)Qs} \quad (2)$$

$$TSI = \sqrt{\frac{\sum_{i=1}^{n}(\chi i - \chi BS)^2}{n-1}} \quad (3)$$

where $\lambda*$ is the photon transport mean free path in the sample, φ is the volume fraction of particles, x_{50} is the mean diameter of particles, g and Qs are optical parameters given by the Mie theory. χi is the average backscattering for each minute of measurement, χBS is the average χi, and n is the number of scans.

2.1.3 Rheological analysis of suspensions

The rheological behaviour of the organic resin and HA-filled suspensions at different concentrations was examined using a TA Instruments AR2000 rheometer. A 40mm crosshatched parallel plates system was used as geometry (gap = 1300 µm). Flow curves of each sample were produced at a constant plate temperature of 25ºC controlled by a Peltier plate. An increasing shear rate (steady-step flow step) in the range of 1-100 s^{-1} was used taking ten points by decade.

2.1.4 Chemical and structural analyses

The calcium phosphate crystalline phases in the sintered scaffolds were detected by X-ray diffraction (XRD) analysis at different temperatures by using a BRUKER's X-ray diffractometer D8 Advance system with Cu Kα radiation (wavelength λ = 0.15406 nm). Equipped with a high-temperature sample stage, a LYNXEYE XE-T detector (energy resolution of 0.38 keV) and a nickel filter at 40 kV and 40 mA. Samples were analysed in a 2θ range between 20º and 60º, a step of 0.03º 2θ and a time per step of 0.2 s. Measurements were performed at key temperature values of the temperature pattern used for the debinding-sintering process.

Sintered HA scaffold pieces obtained after the uniaxial compression test were hand-crushed using a mortar and pestle to produce a homogeneous powder. Powdered samples were examined by Fourier transform infrared spectroscopy (FTIR) analysis in a spectrometer FTIR iS50 using the KBr pellet preparation method to determine its chemical composition. Approximately 9 mg of sample powder are transferred to a clean mortar, then a weighed amount of dry KBr powder (300±5 mg) is added and mixed gently to produce a homogenous mixture, followed by compression at 6000 kg for the sample disk preparation. FTIR spectra were recorded in the 4000-400 cm^{-1} wavenumber range with a step width of 0,48 cm^{-1} for each sample disk.

2.1.5 Analysis of macro-structural properties of HA scaffolds

The morphology of HA powders, scaffolds surface, and the cross-section were examined with a scanning electron microscope (SEM) LEO 435 VP (Leica®) equipped with a Ge detector (Imix-PC, PGT) and a metallization of the ceramic surface was applied with a thin film of silver employing a Scancoat Six sputter coater. HA scaffolds surface was polished in the X, Y plane to analyse the cross-section of the parts. Firstly, the samples were coarse, medium, and fine ground using a Minitech 263 and silicon carbide papers of different grit sizes to reach the region of interest (about 3 mm depth in the X, Y plane). Then, a DiaPro alcohol-based 3µm high concentration diamond suspension from Struers® and a cloth paper were used in a Struers® Tegrapol 25 to obtain a better surface finishing. ImageJ was used for the processing of the images [33].

High-resolution X-ray micro-computed tomography (CT) analyses of the printed parts were performed in a Nanotom® 180 Phoenix - GE equipped with a 180 kV / 15 W high-power nanofocus X-ray tube (9 µm voxel size, resolution). This analysis allowed us to have a 3D perspective of the scaffold and evaluate their total porosity (microstructural porosity of sintered HA and lattice porosity of the scaffold architecture). The data sets were reconstructed and three-dimensionally visualized using VGStudio MAX 4.4 software.

The geometrical density of the scaffolds was calculated from the mass and dimensions of at least ten samples. The theoretical density of HA (3.16 $g.cm^{-3}$) was used as a reference to calculate the total volume

fraction of porosity. The open porosity of the scaffolds was measured by Archimedes' method using distilled water as liquid.

The shrinkage of the scaffolds after the debinding-sintering process was studied by comparison of the scaffold's dimensions before and after the thermal treatment. Three measurements of the height at different rotation angles (every 60º) were used to calculate the height average and the z-axis shrinkage of each printed part. For the diameter average and the x, y axes shrinkage, nine measurements were carried out (three measurements at three different heights of the part: bottom, middle, top) also at different rotation angles (every 60º).

Physisorption analysis of powders was quantified in a Micromeritics® TriStar II Plus 3.00 equipment. Samples were previously degassed at 40ºC overnight in a VacPrep™ 061. The data from BJH pore size distribution desorption was used to determine exactly the average pore volume and size. Nitrogen adsorption-desorption isotherm properties were used to calculate the specific surface area (BET) through the BET method. Only the measurement for the powder $HA_{Initial}$ was replicated three times (N = 3) to describe the measurement variation (mean ± standard deviation).

Mercury intrusion porosimetry was used to analyse the total connected porosity, volume of pores, and pore size distribution >50 nm (meso- and macropores) of the printed scaffolds. These analyses were performed in an AutoPore IV 9500. As for the physisorption analysis, only the measurement for the powder $HA_{Initial}$ was replicated three times (N = 3) to obtain the measurement variation (mean ± standard deviation).

2.1.6 Mechanical properties

The compressive strength of the sintered HA scaffolds with different orientations was measured in a universal mechanical testing press HOUNSFIELD H25KS (Tinius Olsen®, USA). A stainless-steel compression miniature load cell T22-252 U4000 with a range of 25kN was used to measure the shear force at a crosshead speed of 0.10 mm/min at room temperature. At least ten samples (N = 10) from the same batch were evaluated to calculate the mean values and the standard deviations (mean ± standard deviation). The procedure followed is described in the standard ISO-13175:2012. To measure the maximum compressive load taken by the specimens, the load given by the testing press in the direction shown in Figure 5, was increased till the complete failure of the specimens due to crack propagation.

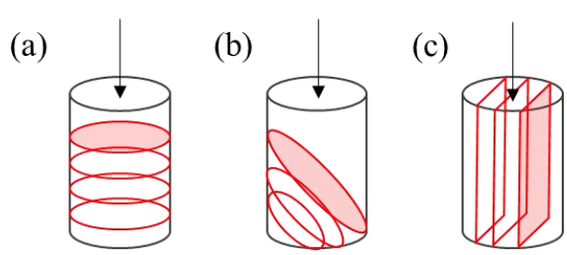

Figure 5. Direction of loading (black arrows) to printing orientation in compressive testing. (a) 0º, (b) 45º, and (c) 90º.

2.1.7 Dissolution rate and pH change

In vitro dissolution rate of the sintered scaffolds, Ca^{2+} ion release, and pH change of the dissolution medium were evaluated following the procedure also described in the standard ISO-13175:2012. Three samples of HA scaffold (printed at orientation 0º) were introduced in three flasks of 0.05M TRIS buffer solution after nitric acid addition for pH adjustment at 7.3±0.1 at 37±1 °C. The three solution flasks were placed on a plate agitator with a rotation speed of 200rpm for 24 h, 48 h, and 72 h respectively. The ratio of initial material mass to total dissolution media volume was kept constant at 4.0 $mg.ml^{-1}$. pH was measured after 0 h, 24 h, 48 h, and 72 h of immersion. Thus, ensuring that the initial pH value did not vary more than 0.3 during the testing. The Ca^{2+} ion content of the solutions was analysed by ICP/AES in an inductively coupled plasma atomic emission spectrometry (ICP/AES, Ultima2R HORIBA®). The concentrations versus time curves were determined. The test was repeated three times (N = 3) to calculate the mean values and the standard deviations (mean ± standard deviation).

2.1.8 Thermal analysis

Thermogravimetric (TGA) and differential scanning calorimetry (DSC) analyses were performed to study and confirm the mass loss evolution of the products and the energy transferred to or from the sample during the debinding-sintering process. It was performed by introducing a small portion (0.02 g) of the ceramic green body in a Setsys Evolution TG92 (Setaram®) and applying a heating ramp of 10ºC/min until 1250ºC in air.

3. Results and discussion

3.1 HA-filled suspension preparation

This section involves the analysis of the three different HA powders ($HA_{Initial}$, HA_{PBM}, HA_{SBM}) properties and the evaluation of their influence on the final HA-filled suspension stability and rheological behaviour. Only the HA-filled suspension showing the best attributes for its application in an MSLA printer will be finally used for the preparation of the HA scaffolds.

3.1.1 HA powders properties comparison

Particle size distribution (PSD) and scanning electron microscopy (SEM) micrographs of each of the three HA powders ($HA_{Initial}$, HA_{PBM}, HA_{SBM}) used for the preparation of the photocurable organic suspensions in the present study are shown in Figure 6. Clear differences in the particle median sizes and spans can be observed between the three powders. $HA_{Initial}$ is composed of mainly one population composed of agglomerates produced by the calcination of the powder with an x_{50} of 25 µm.

The use of specific milling conditions during the SBM process (wet grinding) of this powder causes the particle size reduction giving as result the HA_{SBM} powder, as was already described in chapter III. In suspension and absence of dispersant, it is formed by two particles populations, one with submicronic size (0.7 µm) and another one close to 2.5 µm.

The application of a lower energetic milling process as PBM produces a less intense particle size reduction of the $HA_{Initial}$ powder [34]. As result, the PSD of the HA_{PBM} powder becomes more disperse with two particles populations, one of 20 µm and another one of 2.5 µm. Regarding the particles form, all three powders show irregular shapes with no noticeable variations between them.

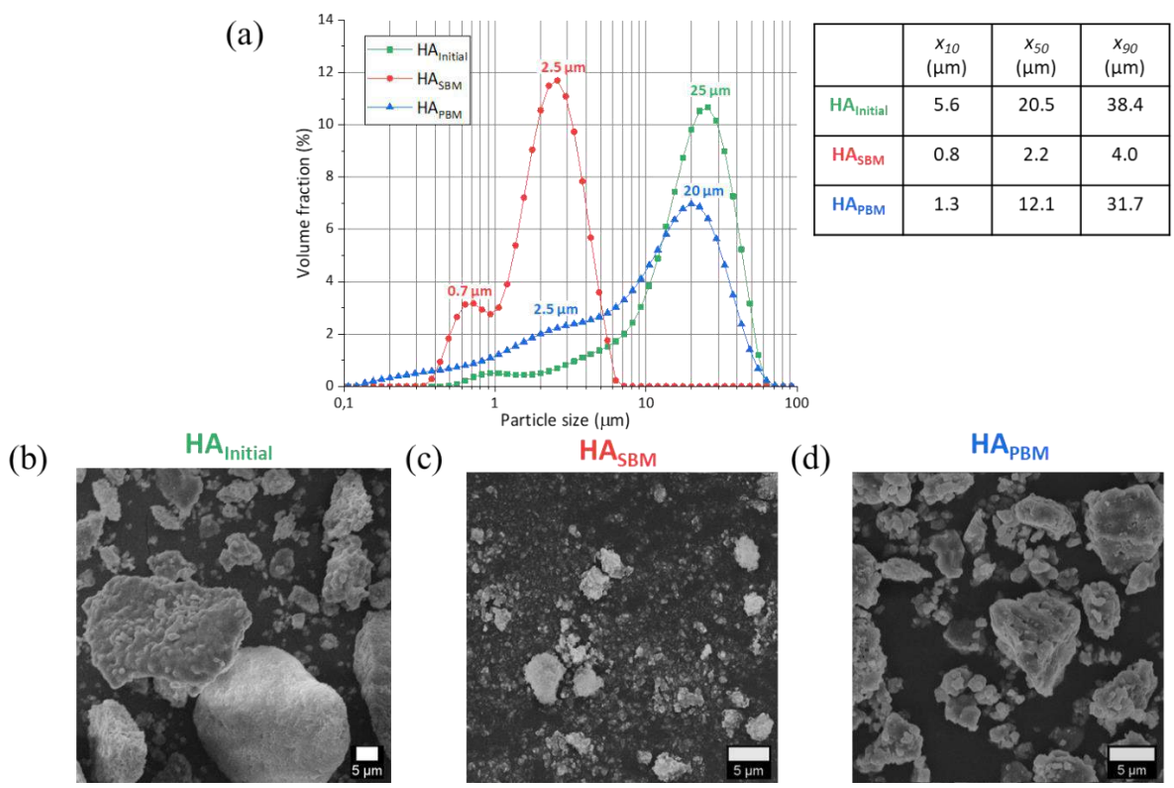

	x_{10} (µm)	x_{50} (µm)	x_{90} (µm)
$HA_{Initial}$	5.6	20.5	38.4
HA_{SBM}	0.8	2.2	4.0
HA_{PBM}	1.3	12.1	31.7

Figure 6. (a) PSD and SEM micrographs of HA powders used in the study: (b) $HA_{Initial}$, (b) HA_{SBM}, (d) HA_{PBM}.

It was observed that the surface area of the initial HA powder (6.9 $m^2.g^{-1}$) is increased after undergoing SBM process (23.8 $m^2.g^{-1}$) while after PBM process the surface area diminished (4.6 $m^2.g^{-1}$). Logically, an increase in the surface area of the powder would be expected after both milling processes because of a reduction of particle size [35]. However, the obtained values show the contrary in the case of the PBM process. This phenomenon was already observed by Granados-Correa et al. [34] in their study on the ball milling effect on tribasic calcium phosphate powders. The explanation offered by Granados-Correa et al. referred to the fact that apart from the calcium phosphate grains breakage and size diminution, the ball mill strikes induced compression of the resulting particles reducing their pore volume. It results then in a

decrease in the total surface area of the powder. This theory gains reliability after the analyses of the total pore volume of powders. The values obtained were 0.017, 0.015, and 0.112 $cm^3.g^{-1}$ for $HA_{Initial}$, HA_{PBM}, and HA_{SBM} respectively, confirming the unforeseen decrease of the specific surface area of the PBM treated powder.

3.1.2 Suspension's stability and rheology behaviour comparison

Before start preparing the HA-filled suspensions the effect of the addition of a 25% vol. of PEG200 (maximum concentration suitable without compromising the reactivity of the resin) on the rheological behaviour of the commercial organic resin base was evaluated. Figure 7a shows the comparison between the flow curves obtained for the Dentifix® resin base before and after the addition of a 25% vol. of PEG200 compound acting as a reactive diluent. Both samples showed a shear-thinning character with a decrease in ramp average viscosity from ~0.076 Pa.s to ~0.065 Pa.s after the addition of the active diluent PEG200. This proportion resin/diluent was used for the preparation of all HA-filled slurries.

The flow curves obtained for suspensions containing a 20% vol. of different HA powders ($HA_{Initial}$, HA_{PBM}, HA_{SBM}) with different median particle sizes is shown in Figure 7b. The comparison of the three viscosity-shear rate curves shows that the suspension with the highest viscosity was obtained when using the HA_{SBM} powder. The effect of the SBM process on the slurry's rheological behaviour was already studied in chapter III. It was already explained that for similar sample volume and solid concentration, smaller particle size means a higher number of particles present in the suspension, which can show Brownian motion acting against an applied shear [36,37]. Since this suspension containing HA_{SBM} showed viscosity values at a low shear rate over the maximum viscosity limit for its utilization in stereolithography (5 Pa.s), it was discarded as feedstock for the printing process. When comparing the viscosity-shear rate curves obtained by $HA_{Initial}$ and HA_{PBM} suspensions no big differences were observed, which could be due to the less significant variation between their PSDs.

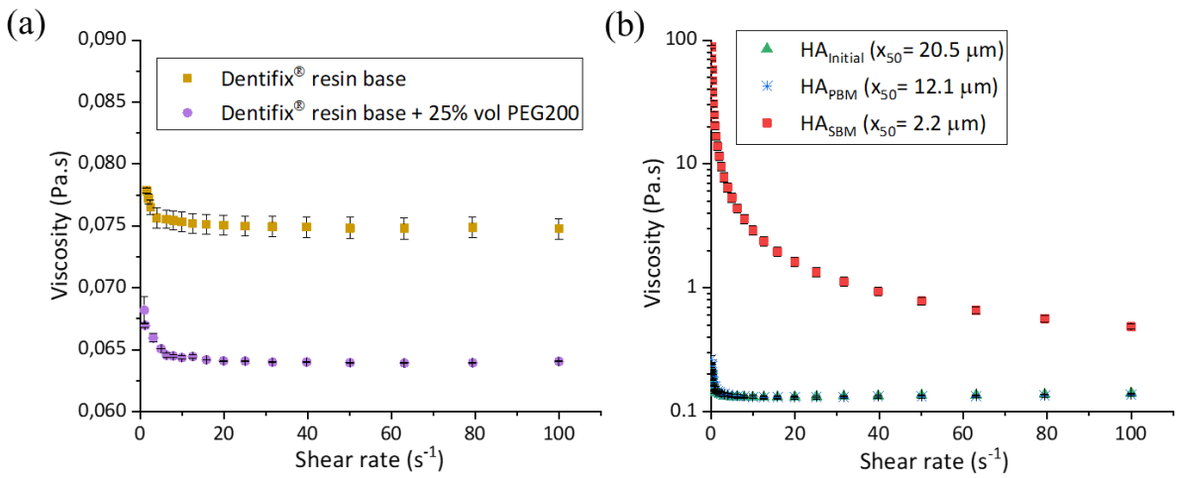

Figure 7. (a) The flow data for Dentifix® resin base with and without the addition of 25% vol. of PEG200 as diluent. (b) The flow data for photocurable suspensions filled a 20% vol. with different HA powders ($HA_{Initial}$, HA_{PBM}, HA_{SBM}) with different median particle sizes ($HA_{Initial}$ and HA_{PBM} show very close viscosities).

A comparison between the stabilities of the three types of HA-filled suspensions was carried out.

Figure 8 shows the BS profiles of the HA-filled suspensions for three hours. The suspensions prepared with HA_{SBM} showed the highest stability since it showed almost no alteration of the BS profile during the whole time of analysis. The slurries containing $HA_{Initial}$ and HA_{PBM} showed both particles sedimentation (BS increases at the bottom of the tube) and clarification (BS decreases at the top) phenomena, however, it was less pronounced in the second case. The differences between the stabilities can be due to different factors that can affect the rate of sedimentation of the prepared suspensions, such as the particle size and the viscosity of the suspensions. It is known that the smaller the particle size and higher the viscosity of a suspension, the slower will be the sedimentation rate of the particles [38]. Which, could explain the results obtained.

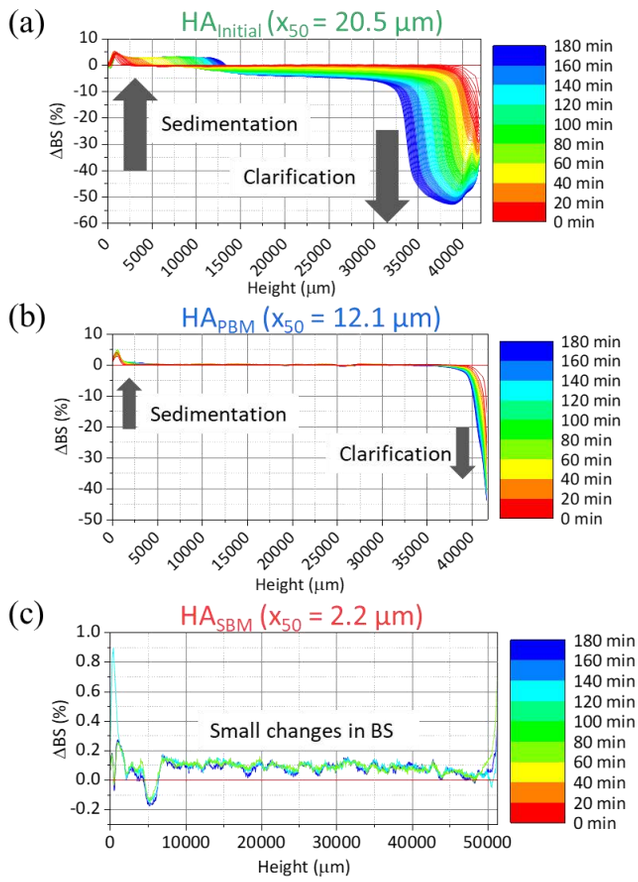

Figure 8. Backscattering profiles of HA-filled suspensions prepared with different HA powders. (a) $HA_{Initial}$, (b) HA_{PBM}, (c) HA_{SBM} (T = 25 °C).

As mentioned in the introduction, the overall stability of slurries described as a TSI value lower than 2 was pursued for the duration of the HA parts fabrication. Figure 9 shows the evolution of the TSI values obtained for the HA-filled slurries as a function of time.

The suspension containing the $HA_{Initial}$ powder showed the worst stability (TSI ≅ 2.75) after three hours of the three suspensions. The highest stability was obtained by the slurry with HA_{SBM} powder constituted by the smallest particles, whose TSI value remained almost unaltered for the whole duration of the analysis. HA_{PBM} suspension showed intermedium stability with a TSI value close to 1.48 after three hours.

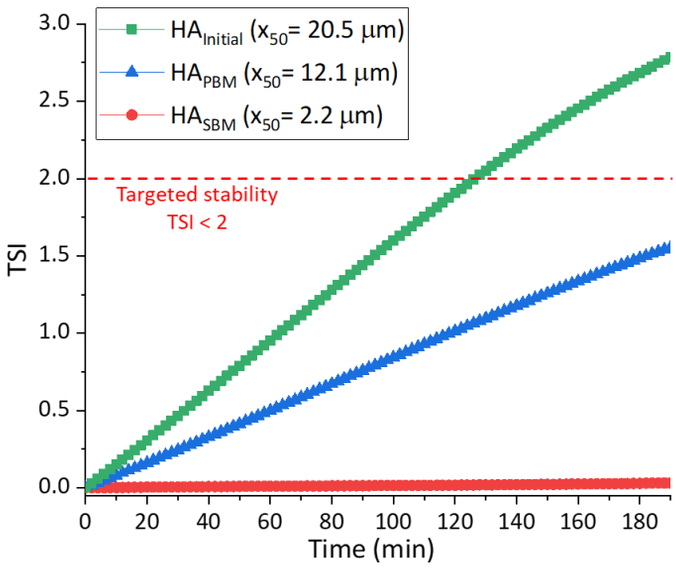

Figure 9. TSI values of HA-filled suspensions as a function of time (T = 25 °C).

The previous stability and rheological behaviour analyses allowed us to compare the properties of the suspensions prepared with different HA powders. The order for the stabilities observed for the three kinds of slurries was HA_{SBM} >> HA_{PBM} > $HA_{Initial}$ with a clear difference between the powder of finer particle size (HA_{SBM}) to the others two. However, the study of the rheology of the suspensions showed the following viscosity order for the slurries HA_{SBM} >> HA_{PBM} ≅ $HA_{Initial}$. The high viscosity showed by the suspension prepared with HA_{SBM} (low shear rate viscosity > 5 Pa.s) hindered the homogeneous spread of the suspension to be employed as feedstock in the MSLA printer. Indeed, the apparatus employs the vertical movement of the printing stage to refill with suspension the space between the stage and the LCD screen. The poor flow of this suspension makes impossible this indispensable refilling step. For this reason, the use of this powder as filler was discarded for the production of photocurable HA-filled suspension feedstock. The suspension showing the most favourable results on suspension rheology (low shear viscosity < 5 Pa.s) and stability (TSI < 1.5) was the prepared with the powder HA_{PBM}. For this reason, only this powder was considered for the preparation of the highly-loaded photocurable HA-filled resins that will be used as feedstock for the production of HA scaffolds via the MSLA process.

The powder concentration is known to be an important factor influencing the degree of shrinkage during the posterior debinding process. The higher the solid loading the lower the shrinkage, but a too high solid loading makes difficult the debinding process due to the impeding of the gases diffusion [24]. It is then of special interest to know the maximum concentration reachable without affecting negatively the handling and processability of the suspension as well as the debinding process. To be sure that the properties for the suspension are still valid for its utilisation at higher concentration, a study of the influence of the solid volume concentration of HA_{PBM} powder in the slurry properties was carried out.

Figure 10a shows the comparison between viscosity-shear rate curves for different HA-filled suspensions containing HA_{PBM} concentrations ranging 20-50 vol. %. A shorter flow ramp was produced for the sample at 50 vol. % due to geometry limitations measuring high concentrated suspensions at high shear rates. However, this ramp was enough for the comparison of the rheological behaviour between suspensions. Even if an increase in the suspension viscosity is visible when a higher solid volume concentration (50 vol. %) is used for the preparation of the slurries (~ 2 Pa.s at a shear rate of 1 s^{-1}), it did not exceed the settled maximum limit of 5 Pa.s.

Regarding the suspension behaviour at different solid volume concentrations, at a concentration of 40%, we observed a transition from shear-thinning to a shear-thickening character. The behaviour of suspension changes at different volume fractions [39]. At higher concentrations, an increase of the shear rate may lead to the formation of particles clusters and jamming showing a shear thickening behaviour. The transition from shear-thinning to shear-thickening is sample-specific and is known to be controlled by factors such as particle shape and particle size [40].

Collisions between particles present in a suspension are expected. Thus, they act as obstacles, and their friction demands further shear force. The higher is the solid volume fraction, the more significant the ongoing particle-particle interactions increasing the force needed to shear the suspension. This is defined as the 'crowding' effect which has been described by many semi-empirical models, however, the most popular equation was the one developed by Krieger and Dougherty (K-D) [41]:

$$\eta_r = \frac{\eta}{\eta_{medium}} = \left(1 - \frac{\varphi}{\varphi_m}\right)^{-[\eta]\varphi_m} \quad (4)$$

Where η_r is the relative viscosity between η the viscosity of the suspension and η_{medium} the viscosity of the medium. φ is the volume fraction of solids in the suspension, φ_m is the maximum volume fraction of solids in the suspension (0.64 for spheres of similar size), and $[\eta]$ is the intrinsic viscosity (2.5 for spheres). Different authors have used a modified version of the K-D equation which includes the effective packing factor of ceramic powder, β, which can be determined experimentally achieving a better fitting for ceramic suspensions [42,43]. This modified version is written as follows:

$$\eta_r = \left(1 - \frac{\beta\varphi}{\varphi_m}\right)^{-[\eta]\varphi_m} \quad (5)$$

Since this analysis for correlation was out of the scope of the chapter no further effort was employed on the determination of the effective packing factor of the specific suspensions under study. Instead, to perform a preliminary evaluation of the fits a value of β =1.58 was used. This value was previously determined by Chu and Halloran [43] for HA-filled non-aqueous ceramic suspensions. A maximum volume fraction of solids in the suspension, φ_m = 0.51 was considered for the calculation. The fitting for both equations (K-D and modified K-D) to the obtained experimental values is shown in Figure 10b. It can be observed that, still, a deeper study could be performed to obtain a better fitting between calculated and experimental values. However, between both K-D equations, the modified version showed a smaller residual sum of squares (313.78) indicating a better fit to our data.

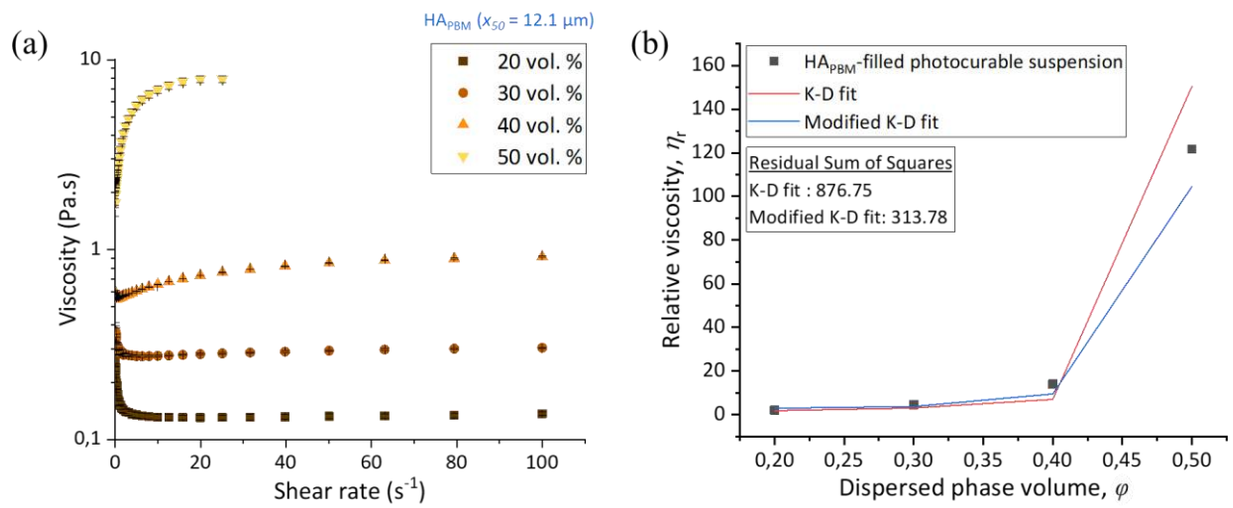

Figure 10. (a) The viscosity-shear rate curves obtained for several HA-filled suspensions containing different HA$_{PBM}$ concentrations. (b) Krieger-Dougherty (red line) and modified Krieger-Dougherty (blue line) fits for relative viscosities in HA$_{PBM}$-filled suspensions.

The study of the stability of the suspension containing HA$_{PBM}$ powder at 50 vol. % is shown in Figure 11. The phenomena occurring during the duration of the test in the suspension at 50 vol. % was examined by analysing its BS profile shown in Figure 11a. A sedimentation behaviour was observed for this suspension although less pronounced than the one observed for the suspension at a concentration of 20 vol. % already seen in Figure 8c. Figure 11a compares the TSI values of the HA$_{PBM}$ suspensions at 20 and 50 vol. % concentrations. A lower TSI value (0.85) was observed for the slurry with a higher concentration after 180 minutes. It indicates higher stability compared with the slurry at a lower concentration, which shows a higher TSI (1.48) for the same duration. It took about 5h for the suspension at 20 vol. % to exceed the fixed limit of destabilization (TSI = 2), while the suspension at 50 vol. % needed almost 10h to reach this value. This confirms the principle for high concentrated suspensions showing a slow sedimentation rate [38]. The influence of sediment particle concentration on the settling velocity has been amply investigated

[44,45]. It has been demonstrated that the settling velocity is lower at a higher concentration by a factor usually given by the widely used semiempirical equation offered by Richardson and Zaki [46]:

$$\frac{w_m}{w} = (1-\varphi)^n \qquad (6)$$

Where w ($m.s^{-1}$) is the terminal settling velocity of an individual particle in a fluid; φ is the sediment volumetric concentration (-)*;* and w_m ($m.s^{-1}$) is the settling velocity of sediment particles dispersed at the volumetric concentration φ. n is an empirically determined exponent dependent on the particle Reynolds number R. Researchers have made an effort determining n-values to increase the accuracy of the prediction associated with equation (5) [45].

The terminal velocity of an individual particle of HA was calculated by stokes' law ($w = 1.04 \cdot 10^{-2}$ $m.s^{-1}$). Then, following the equation (6), the terminal settling velocities for the HA_{PBM} particles dispersed in the photocurable resin (including diluent) at different concentrations (w_m) were obtained. The ratios between both velocities (w/w_m) at different volume concentrations are shown in Table 2. For the calculation, a laminar regime ($R < 0.2$) was considered with an n-value of 4.65. It can be observed how, for example, the settling velocity of the particles is delayed by $2{,}51 \cdot 10^1$ with a concentration of 50 vol. %. Then, the decrease in settling velocity with the increase in concentration was demonstrated.

Table 2. Settling velocities of particles dispersed at different volume concentrations. n=4.65, $w = 1.04 \cdot 10^{-2}$ $m.s^{-1}$ (obtained by stokes' law)

Volume concentration (%)	w/w_m
20	2.82
30	5,25
40	$1{,}08 \cdot 10^1$
50	$2{,}51 \cdot 10^1$

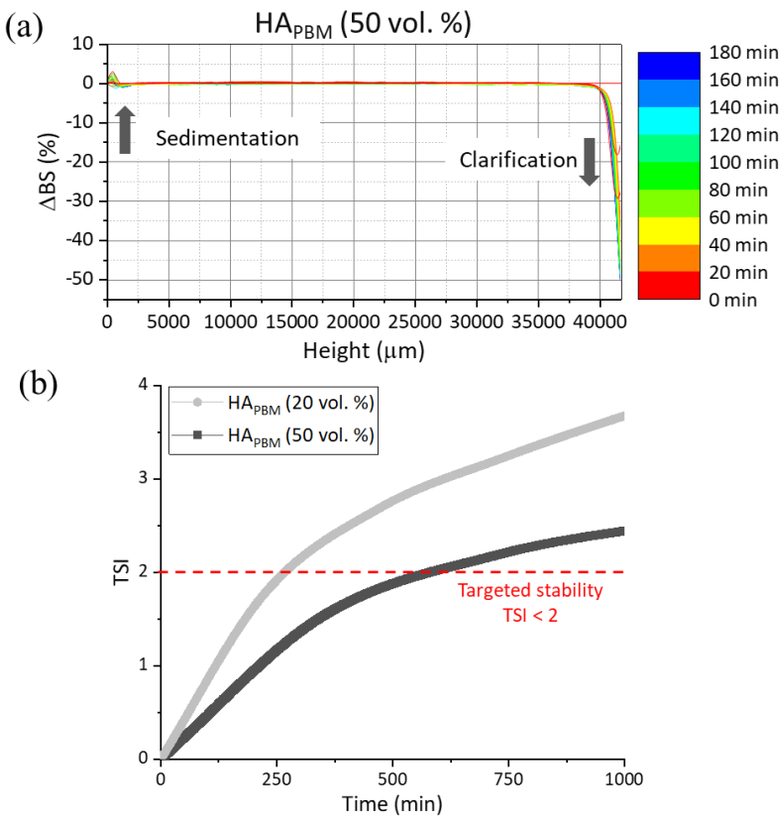

Figure 11. (a) Backscattering profile of HA_{PBM} suspension at 50% vol. (T = 25 °C). (b) TSI values of HA_{PBM} filled suspensions at different concentrations as a function of time (T = 25 °C).

We concluded this study on the tailoring of HA powders and their influence on the suspension's properties (target properties: viscosity < 5 Pa.s at a shear rate 1 s^{-1} and TSI < 2 for the duration of the process) by choosing the HA_{PBM}-loaded suspension at 50 vol. % for its use in the MSLA process.

3.2 Printing of HA scaffolds

The suspension containing a 50% vol. of HA_{PBM} was employed for the production of the HA scaffolds following the MSLA printing and debinding-sintering procedures already described. This section will be then focused on the characterization of the parts produced. The composition of the parts will be analysed to discard any alteration of the HA phases during the process. The morphology of the parts will be evaluated through the comparison with the 3D model to analyse the possible shrinkage due to the debinding-sintering process. The bioactivity will be examined through the standard analysis of the dissolution rate of the part. Then the mechanical properties of the parts will be assessed to evaluate the anisotropy behaviour caused due to change in build orientation.

3.2.1 Composition

To confirm the crystalline phases of the sintered scaffolds XRD analyses were carried out. The analyses were performed at different temperatures reproducing the debinding-sintering temperature pattern to study the evolution of the phase. Figure 12 shows the in-situ XRD diffractogram of the HA scaffold obtained at different temperatures under air atmosphere. The absence of secondary crystalized calcium phosphate phases was confirmed and only the stoichiometric hydroxyapatite phase (JCPDS 00-009-0432) was observed before, during, and after the debinding-sintering process [47]. This result confirms the thermal stability reported for HA in literature [48,49], indicating stability up to 1350 ºC when it starts to decompose into other calcium phosphate phases such as tricalcium phosphate, and tetracalcium phosphate that could affect negatively the properties of the printed parts (different dissolution rates in physiological conditions, uneven grain growth…) [50]. It is known that the densification of HA reaches a saturation limit between ~1100–1300 °C with closed porosity [50].

Since the hydroxyapatite used was initially well crystallized, non-alteration of its crystallinity was observed. However, a decrease in the spectra intensity or resolution can be noticed after reaching 1250ºC. It was attributed to the loss of signal due to the movement in the z-axis of the sample during the in-situ measurement caused for the shrinkage of the part due to the pyrolysis of the resin and sintering.

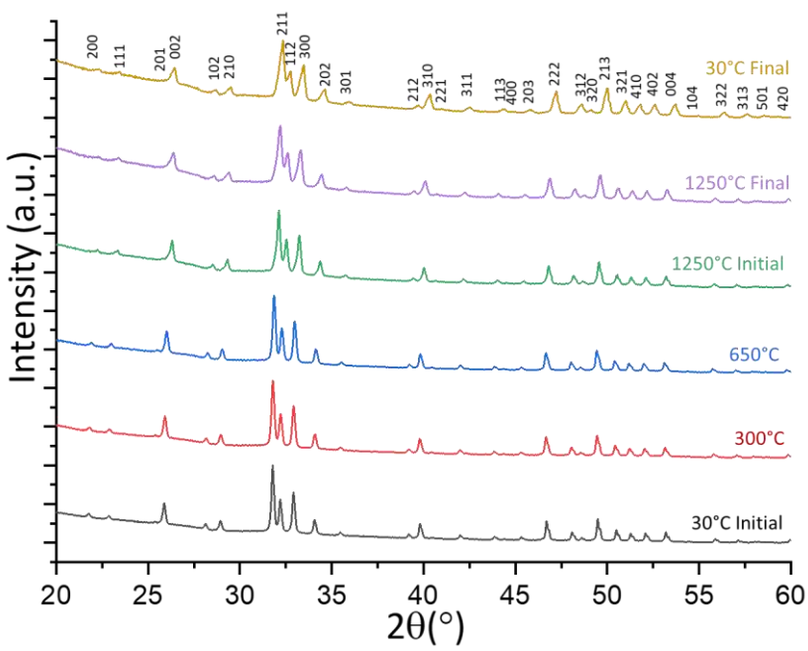

Figure 12. In-situ XRD diffractograms of the HA scaffolds during the debinding-sintering process at different temperatures. All the diffraction peaks correspond to stoichiometric hydroxyapatite (JCPDS 00-009-0432).

Characterization of the cured resin with HA powder was performed by differential scanning calorimetry (DSC) and thermogravimetric analysis (TGA) to better understand the thermal treatments, especially the critical process of debinding. This characterization gives information on weight loss and

involved energy during the debinding and sintering processes. The purpose of this study is to analyse the thermal degradation of the cured resin in the HA scaffold green body under air atmosphere. The TGA and DSC results for cured green body HA scaffold, optimized at 25 wt. % (base resin + PEG200 diluent) and 75 wt. % HA_{PBM} powder is shown in Figure 13. The curve represents the weight loss and the energy involved during the thermal treatment, at a constant heating rate of $10^{o}C.min^{-1}$ from room temperature until 1250ºC in air atmosphere.

Three main weight loss stages can be distinguished related to the formation of volatiles, which diffuse from the interior of the part to the outside. These events represent the most critical temperature ranges during the debinding process since they indicate the escape of the gases generated and the probability of cracking of the green body.

- The first stage finishes at 240ºC with a 3 wt. % of weight loss indicated by an exothermic peak, which was related to the loss of physically adsorbed water. At the same time, some organic matter such as acrylate resin or PEG200 experience soften, melt, and crack [25].
- The second stage is observed from 240ºC to 498ºC corresponding to the highest rate of weight loss, removing 22 wt. % of the material. This was related to the thermal decomposition of the photocurable resin, including carbon-containing compounds [51]. Some organic components were burned and carbonized step by step.
- The third stage was defined as the thermal oxidation of the carbonized residue which does not substantially consume heat and has a minor influence on the TGA analysis [25]. When the temperature reached 1200ºC, the mass curve tended to be stable.

Two exothermic events were detected, associated with the three weight-loss events. Thus, indicating that the thermal degradation of the resin used for the suspensions releases energy during the thermal process. Indeed, the most intense exothermic peak is related to the weight loss event corresponding to the degradation of the carbon-containing compounds during the polymer degradation. On the whole, total organic removal is observed with a weight loss of ~25 wt. %. It is important to point out that the heating rates used during the debinding-sintering process of the scaffolds are between 10 and 5 times lower than the used for the TGA and DSC analyses. It is expected to produce deeper pyrolysis of the polymeric phase and at the same time control the diffusion of gases avoiding the formation of cracks. The results obtained for the thermal analyses are in correlation with the observed in literature for similar resin photocurable thermal degradation studies [21,25,51].

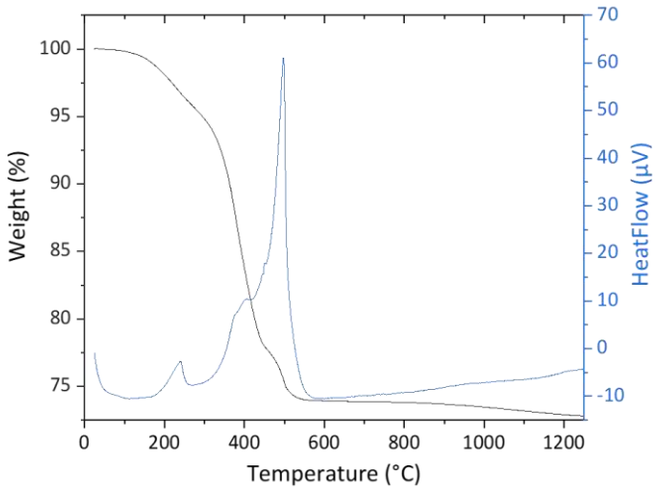

Figure 13. Differential scanning calorimetry (DSC) and thermogravimetric analysis (TGA) of HA green body scaffold.

A FTIR analysis was performed to confirm the compounds present in the parts after the whole production process. For comparison, the powder (HA_{PBM}) used as filler during the preparation of the slurry was also analysed. Figure 14 shows the FTIR spectra of the starting powder and the HA scaffold produced. Small variations can be noticed between them. In both spectra the PO_4^{3-} and structural OH^- vibration bands corresponding to HA are clearly visible at 1092 cm^{-1}, 1040 cm^{-1}, 962 cm^{-1}, 601 cm^{-1}, 575 cm^{-1}, 561 cm^{-1}, and at 650 cm^{-1}, 3600 cm^{-1} [47]. No secondary species were detected before or after the whole HA scaffold production process.

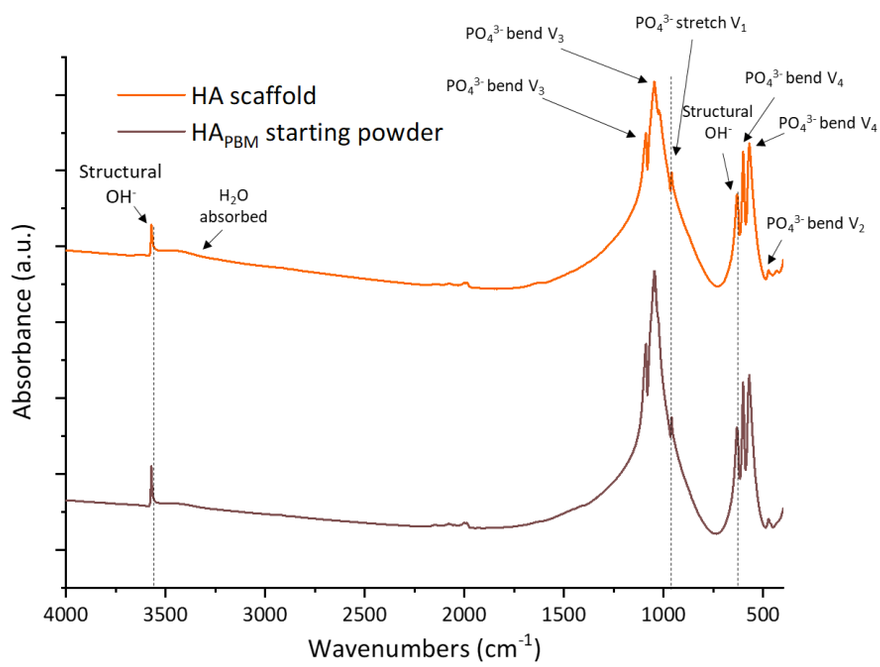

Figure 14. FTIR spectrum analysis of the HA before and after the SD process.

3.2.2 Macro-structural properties and physical changes of sintered HA scaffolds

HA bioceramic scaffolds were examined to evaluate their macro-structural properties (surface finishing, porosity, and density) and physical changes (shrinkage) after the debinding-sintering process. Figure 15 shows the photographs of the green body and sintered HA scaffolds produced by the MSLA process. Figure 15a shows the differences in dimension between the green body scaffold and its homologous after the debinding-sintering process due to the pyrolysis-induced shrinking. However, no fracture or crack was detected after the debinding-sintering process. Figure 15b shows differences between the dimensions of the scaffolds printed at different orientation angles (shrinkage values can be observed in Table 3). The differences in dimension were only observed once the parts were submitted to the debinding-sintering process. It indicates a physical anisotropic effect produced by the shrinkage which depends on the orientation in which the layers forming the part was printed. This kind of anisotropic physical change has been reported in previous studies on the 3D printing of ceramic parts [21,52].

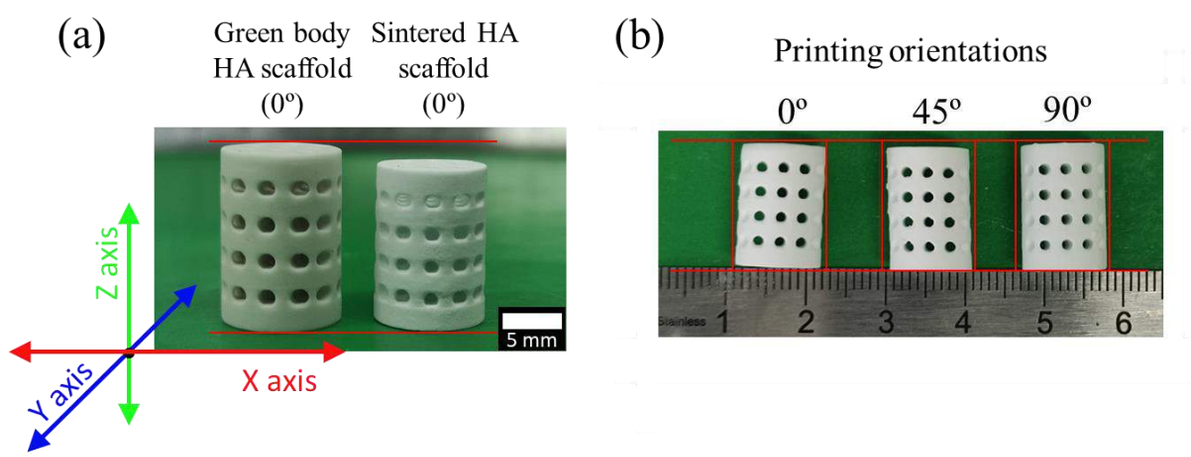

Figure 15. Visual examination of HA parts: (a) comparison between green body and sintered HA scaffolds (including axes arrows), (b) comparison between sintered HA scaffolds printed at three different orientations (0º, 45º, and 90º).

Table 3 shows the general information related to the macro-structural properties of the produced HA scaffolds. The calculated average pyrolysis-induced shrinkage shows that there is a different effect depending on the axis. For parts printed at the same orientation, a higher distortion effect was measured for the axes perpendicular to the printing direction (e.g., z-axis for parts printed at 0º or x-y plane).

No big differences in the total porosity were observed between the three orientations. A higher porosity was obtained when using the Hg intrusion porosimetry method, this could indicate that the resolution of the CT analysis (9 µm) was not enough to take into account the microporosity. The total porosity of the scaffolds is close to the common cancellous bone porosity of 50-90% [53].

Almost similar relative densities were obtained for the three kinds of scaffolds (2.84 $g.cm^{-3}$) demonstrating a good capability of the MSLA technique in the reproduction of HA scaffolds with an

accurate controlled and interconnected macroporosity. The obtained density is lower than the hydroxyapatite density (3.16 $g.cm^{-3}$), thus corresponding to the expected values for a porous scaffold.

Table 3. Average shrinkage in x-y and z-axis of parts after the debinding-sintering process for each of the three printing orientations. Average porosity and relative densities of sintered HA scaffolds determined by different methods. (N=10, mean ± standard deviation)

Printing orientation (º)	Average shrinkage x-y axes (%)	Average shrinkage z-axis (%)	Total porosity (CT) (% vol.)	Total porosity (Hg) (%vol.)	Relative density (Archimedes) ($g.cm^{-3}$)	Relative density (Geometrical) ($g.cm^{-3}$)
0	5.33±0.07	9.72±0.07	31.4	35.8	2.84±0.04	2.31±0.13
45	6.20±0.02	7.13±0.05	30.6	35.5	2.84±0.01	2.31±0.66
90	7.72±0.03	5.09±0.04	32.7	35.6	2.85±0.02	2.25±0.52

The SEM micrographs of the HA scaffolds surface printed at three different orientations are shown in Figure 16. SEM micrographs were taken at a similar X-Z plane (front view) of the parts for comparison. The macroporosity of the scaffolds is composed of an interconnected porosity with a pore size of about 1000 µm. This result fulfills the objective of producing scaffolds with controlled macroporosity (pore size > 400 µm) which could promote the attachment, growth, and proliferation of bone cells inside of the scaffold enhancing the new bone formation and the formation of capillaries. This macro-porosity should then provide transport pathways for oxygen, wastes, and nutrients necessary to maintain living cells [54,55]. Different surface finishings are observed in this plane depending on the printing orientation with a clear view of the layers for the scaffolds printed at 0º and 45º. However, no significant pores in the microstructures can be observed due to any delamination or imperfect bonding between layers. This indicates a good sinterability of the HA powder.

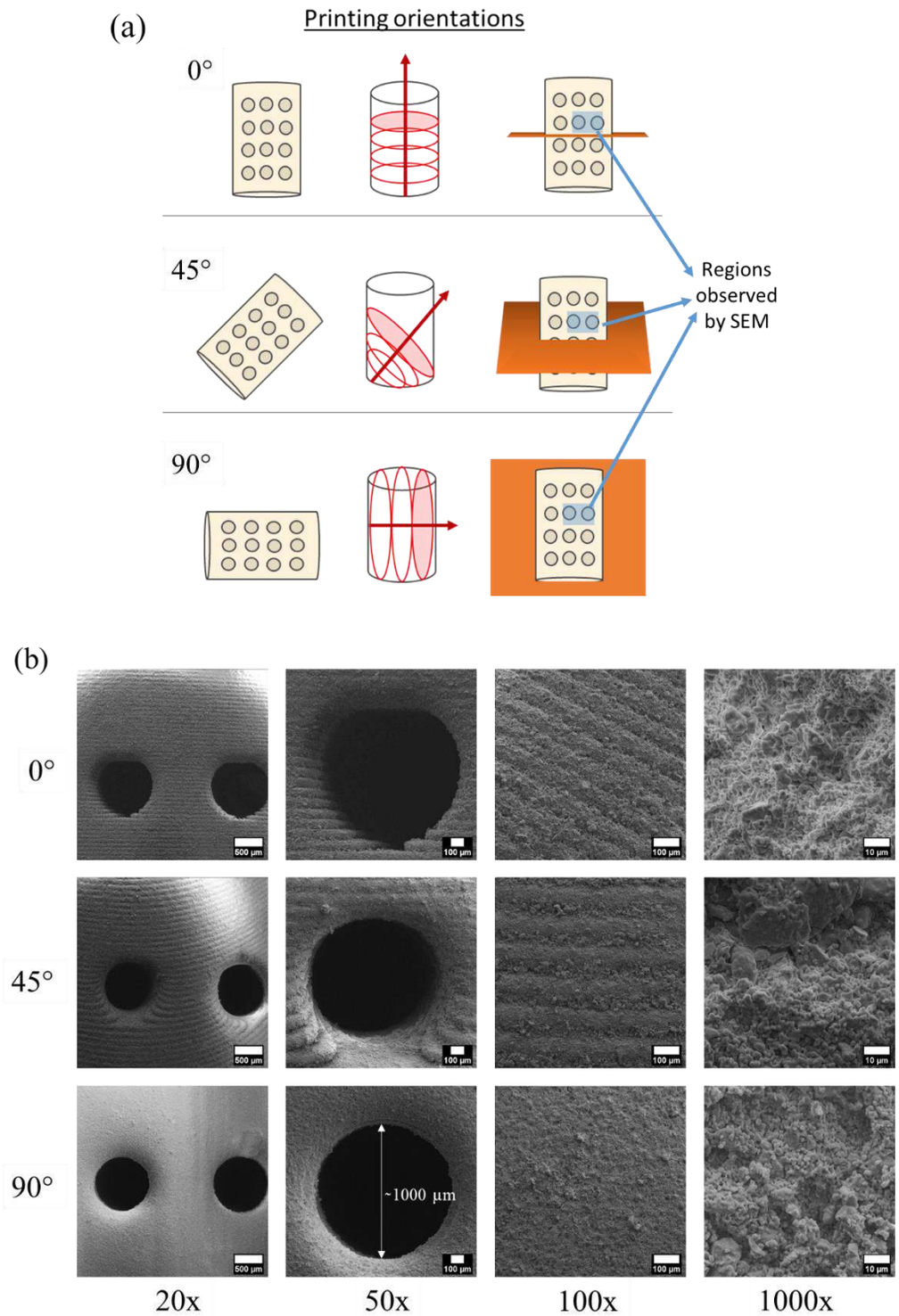

Figure 16. (a) Three different schematic representations of the three printing orientations employed. (b) SEM micrographs at different magnifications of the HA scaffolds (X, Z plane) printed at three different orientations.

Additionally, to analyse the internal microstructure of the HA scaffolds the cross-section at the X-Y plane (top view) was observed by SEM. These micrographs are shown in Figure 17. From a general view, no induced anisotropy was identified due to the printing process on the three types of scaffolds. The three samples presented micropores of about 10-15 µm of diameter corresponding to the microstructural porosity of the sintered HA. This porosity could allow the migration and proliferation of osteoblasts (15-50 µm), and especially stem cells (5-12 µm). The HA crystal sizes correspond with the particle size of the HA_{PBM} powder used for the preparation of the scaffolds. A dispersed distribution of HA grains was observed with sizes from 2.5 µm to 20 µm of diameter.

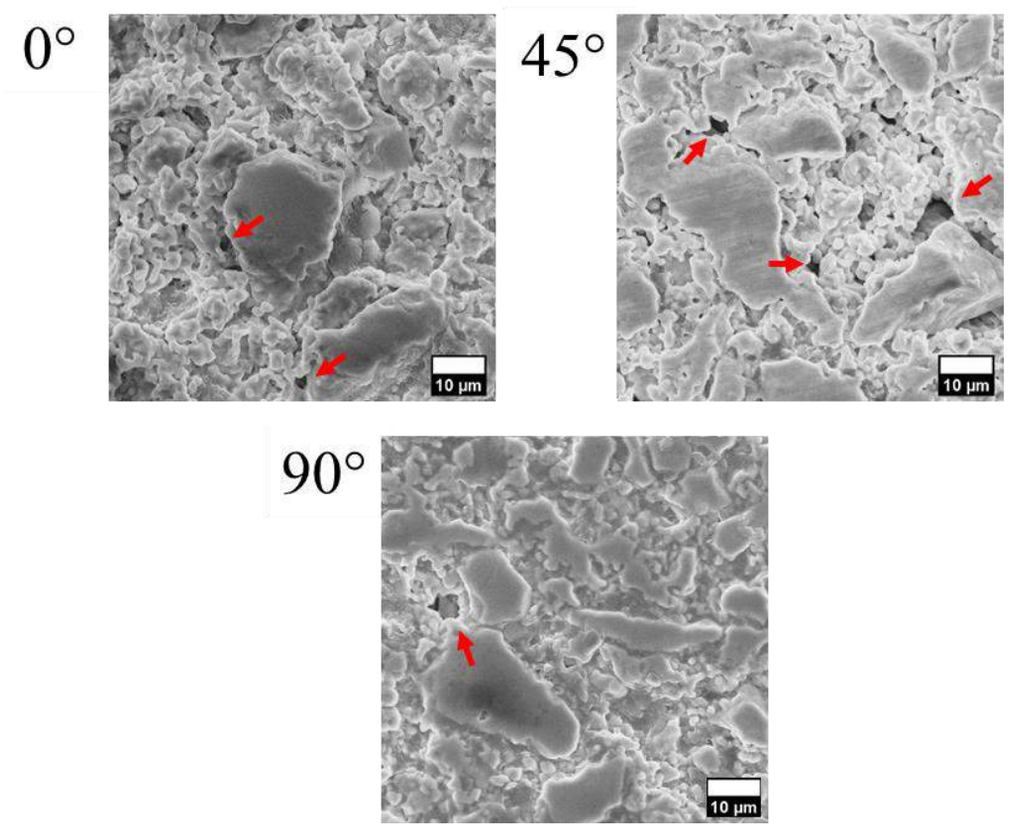

Figure 17. Cross-section of parts of the HA scaffolds (X, Y plane) printed at three different orientation degrees. Micropores are remarked by red arrows.

Three-dimensional reconstructions of the sintered scaffolds using X-ray micro-computed tomography are also illustrated in Figure 18. A defect volume scale was added for a better comparison of the pore volume. The three samples showed accurate controlled and interconnected macroporosity with a total volume in the range of 300-350 mm^3. The cross-section views of HA scaffolds in X-Y and Y-Z planes did not show any kind of anisotropy induced by the MSLA process. This homogeneity observed for the whole volume of the parts indicates suitability for the processing of suspensions by MSLA technique on the production of HA scaffolds with controlled macroporosity. Additional CT results showing the internally interconnected porosity of the scaffold printed at 0º can be found in Figure S1.

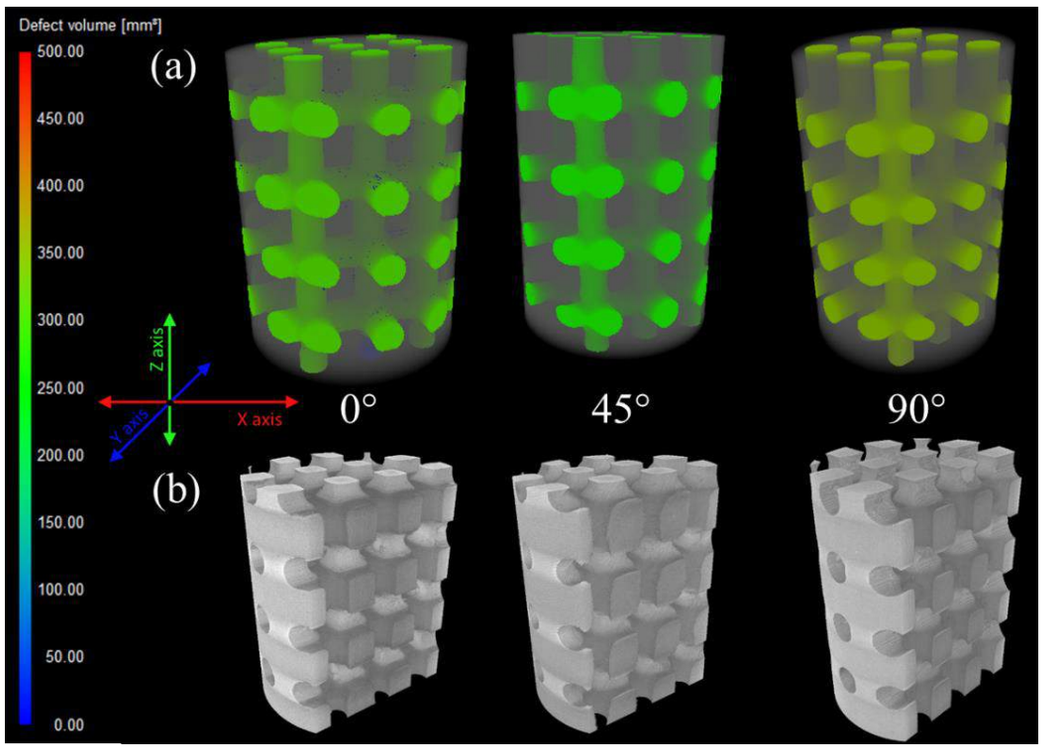

Figure 18. Visualization obtained using X-ray micro-computed tomography of the three kinds of HA scaffolds (0º, 45º, and 90º) produced by MSLA after the debinding-sintering treatment. (a) The pore distribution of HA scaffolds with previously modelled interconnected macroporosity and circular overtures of 1000 µm in the three directions. (b) Cross-section views of HA scaffolds in X-Y, and Y-Z planes.

3.2.3 Mechanical properties

The anisotropic effect of the printing orientation on the scaffolds mechanical properties was examined. Table 4 shows the compression strength of the sintered scaffolds as a function of the orientation in which they were printed. Mechanical strength is primarily controlled by pore volume and distribution, however, in this case, the total porosity of the scaffolds has been demonstrated to not be affected by the printing orientation. Thus, the total pore volume of the samples studied was almost similar (Table 3). Scaffolds with 0º orientation are weakest in compressive strength (4.3±0.4 MPa) since the plane in which they are printed is perpendicular to the direction of load. With the inclination of the plane, it becomes diagonal to the loading direction (45º) resisting more compressive load (4.9±0.3 MPa). Then, a decrease in the compressive load is observed for (90º) as the printing orientation is parallel to the direction of loading (4.8±0.2 MPa). These results are in line with Lee et al. [56] and Saini et al. [57] which said that the diagonally printed specimens (45º) have higher compressive strength as compared to axial and transverse 3D printed parts. Indeed, they are in accordance with the results obtained by Feng et al. [21] whose HA

printed scaffolds (at orientation 0º and using a 50 vol. % suspension) with higher porosity than the ones produced in the present study showed lower compressive strength. The values obtained for the three types of scaffolds are found to be within the range of values reported for cancellous bone compressive strength (1-12 MPa) for porosity between 50 and 90%. Then, to advance this study, the porosity of the scaffolds (~31%) could be increased to reproduce closer conditions [53].

Table 4. Compressive strength of HA scaffolds depending on the printing orientation. (N =10, mean ± standard error)

Printing orientation (º)	Compression strength (MPa)
0	4.2±0.4
45	4.9±0.3
90	4.8±0.2

The compressive stress-strain curves obtained for the bioceramic HA scaffolds printed at 45º are shown in Figure S2a. These curves are characterized by an initial non-linear toe region (first strain stage) followed by a main linear region till the failure point. The inexistence of a concave shape before the failure point and the sharp peaks are common in brittle materials as ceramics. It is known that brittle materials, when subjected to stress, break with little elastic deformation and without significant plastic deformation. For this reason, brittle materials absorb relatively little energy before the fracture, even those of high strength [58]. Cracks propagate rapidly along the compression loading direction as shown in Figure S2b. The fluctuations (or serration) in the compression stress-strain response are essentially attributed to the spalling of a small specimen volume, as the growing cracks either meet the free/unconstrained surface of the material or, coalesce between them [59]. This is in accordance with other works in the literature [21,52]. Brittle fracture with a transgranular cleavage is observed (cracks grow through the material grains) and no apparent plastic deformation takes place before fracture. No preferred direction was observed for the fracture as an effect of the orientation in which the specimens were printed.

3.2.4 Dissolution rate

The *in vitro* behaviour of the sintered HA scaffolds was preliminarily evaluated in terms of dissolution rate, Ca^{2+} ion release, and pH change of the dissolution medium (0.05M TRIS buffer solution) at 37±1ºC. The pH value evolution of the TRIS buffer solution is shown in Figure 19a. The initial pH of the TRIS buffer solution was 7.3. Then, this value was decreasing with the increase of the HA scaffold soaking time. After 72h the pH reached a value of 7.24. The pH variation surrounding an implant is an indicator of the *in vivo* degradation. A fast unintentional degradation in contact with the environment can deteriorate the mechanical properties of the implant [60]. In this case, a low variation of the pH was observed (lower than ±0.3) indicating a low degradation of the HA scaffold. The scaffold weight loss and Ca^{2+} ion concentrations in the solution at different soaking times are given in Figure 19b. A slight weight loss of the HA scaffolds was observed after 24h. It increased with the soaking time until a 0.12% of loss of the total scaffold mass at 72h. In addition, a low Ca^{2+} ion release (1.26 $mg.l^{-1}$) was observed during the time of the measurement. These results were attributed to the high crystallinity of the HA phase (due to the sintering process) which is known to decrease the dissolution rate [61].

It is known that depending on the calcium phosphate phase the dissolution rate varies, being HA one of the phases showing low rates [62]. Some phases like TCP may dissolve fast and replace the coating or cement with bone. This property depends on the calcium phosphate phase content of the scaffold, crystallinity, particle size, and porosity. A higher degree of porosity means a higher surface area in contact between the implant and the body fluids, inducing a faster dissolution rate. Then, a higher degree of crystallinity of the calcium phosphate structure can reduce the solubility of the scaffolds, thus explaining the large differences in solubility between scaffolds prepared with the same calcium phosphate phase [61,63]. The rate of bone substitution also depends on the age, sex, and general metabolic health of the recipient, even on the anatomic site, thus the desired resorption rate is the rate comparable to the formation of bone tissue (between a few months and a few years), in the case of calcium phosphate it may take 3 to 36 months to be replaced by bone [64].

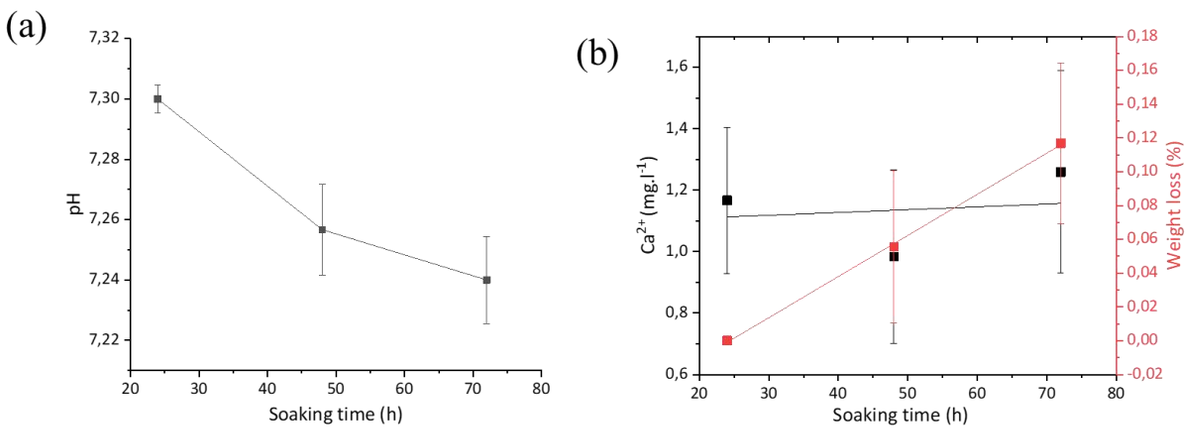

Figure 19. (a) TRIS solution pH evolution, (b) Ca^{2+} ion release, and scaffold weight loss evolution as a function of the sintered HA scaffold soaking time. (N = 3, mean ± standard error)

4. Conclusions

In the present work, HA scaffolds were obtained by MSLA innovative AM process. HA powders with different characteristics were produced and employed for the preparation of HA-filled photocurable suspensions. The influence of the different powders on the properties of suspensions was evaluated. After a comparison of the rheological behaviour and dispersion stability of the suspensions, it was found that the powder tailored through the planetary ball mill process having an intermedium particle size showed the most outstanding results (viscosity < 5 Pa.s at a shear rate 1 s^{-1} and TSI < 2 for the duration of the process) at 50 vol. %. The processability of suspensions was tested in a commercial MSLA apparatus through the production of scaffolds with controlled macroporosity. The process showed high accuracy in producing the macroporosity (pore size of 1000 µm) at three printing orientations (0º, 45º, and 90º). A debinding-sintering process at 1250ºC was employed for the complete pyrolysis of the resin and sintering of the scaffold. The chemical composition and macro-structural properties of the scaffolds were examined. It was observed that the debinding-sintering shrinkage of the parts was dependent on the printing orientation, with a higher shrinkage in the direction perpendicular to the printed plane. The analysis of the mechanical properties also showed an anisotropic effect induced by the printing orientation with the highest compressive strength (4.92±0.33 MPa) obtained for the scaffolds printed diagonally (45º). Then, the dissolution rate test of the scaffolds showed a low variation in the TRIS solution pH with the soaking time and a slow dissolution rate, which was attributed to the high crystallinity of the HA phase. In conclusion, the tailoring of HA powder suitable for its use as a filler in photocurable suspensions was confirmed. The HA specimens produced showed promising results for their use in surgery for guided bone regeneration in the case of minor or non-load bearing voids requiring slow resorption properties.

5. Acknowledgements

This project has received funding from the European Union's Horizon 2020 research and innovation programme under the Marie Skłodowska-Curie grant agreement No 764935.

6. REFERENCES

[1] Ageing Europe - statistics on population developments, (2020). https://ec.europa.eu/eurostat/statistics-explained/index.php?title=Ageing_Europe_-_statistics_on_population_developments.

[2] Office of the Surgeon General (US), Bone Health and Osteoporosis: A Report of the Surgeon General, Office of the Surgeon General (US), Rockville (MD), 2004. http://www.ncbi.nlm.nih.gov/books/NBK45513/.

[3] I. Benjumeda Wijnhoven, R. Vallejos, J.F. Santibanez, C. Millán, J.F. Vivanco, Analysis of cell-biomaterial interaction through cellular bridge formation in the interface between hGMSCs and CaP bioceramics, Sci Rep. 10 (2020) 16493. https://doi.org/10.1038/s41598-020-73428-y.

[4] D.W. Hutmacher, Scaffolds in tissue engineering bone and cartilage, Biomaterials. 21 (2000) 2529–2543. https://doi.org/10.1016/S0142-9612(00)00121-6.

[5] L. Zhang, Y. Morsi, Y. Wang, Y. Li, S. Ramakrishna, Review scaffold design and stem cells for tooth regeneration, Japanese Dental Science Review. 49 (2013) 14–26. https://doi.org/10.1016/j.jdsr.2012.09.001.

[6] H. Schliephake, F.W. Neukam, Bone replacement with porous hydroxyapatite blocks and titanium screw implants: An experimental study, Journal of Oral and Maxillofacial Surgery. 49 (1991) 151–156. https://doi.org/10.1016/0278-2391(91)90103-S.

[7] B.A. Gultekin, E. Bedeloglu, T.E. Kose, E. Mijiritsky, Comparison of Bone Resorption Rates after Intraoral Block Bone and Guided Bone Regeneration Augmentation for the Reconstruction of Horizontally Deficient Maxillary Alveolar Ridges, BioMed Research International. 2016 (2016) e4987437. https://doi.org/10.1155/2016/4987437.

[8] M. Tumedei, P. Savadori, M. Del Fabbro, Synthetic Blocks for Bone Regeneration: A Systematic Review and Meta-Analysis, Int J Mol Sci. 20 (2019) 4221. https://doi.org/10.3390/ijms20174221.

[9] A. Monje, H.-L. Wang, Biological and physical properties of bone block grafting biomaterials for alveolar ridge augmentation, (n.d.) 14.

[10] J.T. Mellonig, Bone allografts in periodontal therapy, Clin Orthop Relat Res. (1996) 116–125. https://doi.org/10.1097/00003086-199603000-00014.

[11] E. Pamula, E. Filová, L. Bačáková, V. Lisá, D. Adamczyk, Resorbable polymeric scaffolds for bone tissue engineering: The influence of their microstructure on the growth of human osteoblast-like MG 63 cells, J. Biomed. Mater. Res. 89A (2009) 432–443. https://doi.org/10.1002/jbm.a.31977.

[12] A. Kurella, N.B. Dahotre, Review paper: Surface Modification for Bioimplants: The Role of Laser Surface Engineering, J Biomater Appl. 20 (2005) 5–50. https://doi.org/10.1177/0885328205052974.

[13] H. Qu, Additive manufacturing for bone tissue engineering scaffolds, Materials Today Communications. 24 (2020) 101024. https://doi.org/10.1016/j.mtcomm.2020.101024.

[14] H.H. Yen, P.G. Stathopoulou, CAD/CAM and 3D-printing Applications for Alveolar Ridge Augmentation, Curr Oral Health Rep. 5 (2018) 127–132. https://doi.org/10.1007/s40496-018-0180-4.

[15] L.C. Hwa, S. Rajoo, A.M. Noor, N. Ahmad, M.B. Uday, Recent advances in 3D printing of porous ceramics: A review, Current Opinion in Solid State and Materials Science. 21 (2017) 323–347. https://doi.org/10.1016/j.cossms.2017.08.002.

[16] K. Lin, R. Sheikh, S. Romanazzo, I. Roohani, 3D Printing of Bioceramic Scaffolds—Barriers to the Clinical Translation: From Promise to Reality, and Future Perspectives, Materials. 12 (2019) 2660. https://doi.org/10.3390/ma12172660.

[17] S. Zakeri, M. Vippola, E. Levänen, A comprehensive review of the photopolymerization of ceramic resins used in stereolithography, Additive Manufacturing. 35 (2020) 101177. https://doi.org/10.1016/j.addma.2020.101177.

[18] J.R. Zyzalo, Masked Projection Stereolithography: Improvement of the Limaye Model for Curing Single Layer Medium Sized Parts, (2008) 274.

[19] H. Quan, T. Zhang, H. Xu, S. Luo, J. Nie, X. Zhu, Photo-curing 3D printing technique and its challenges, Bioactive Materials. 5 (2020) 110–115. https://doi.org/10.1016/j.bioactmat.2019.12.003.

[20] X. Li, Y. Yuan, L. Liu, Y.-S. Leung, Y. Chen, Y. Guo, Y. Chai, Y. Chen, 3D printing of hydroxyapatite/tricalcium phosphate scaffold with hierarchical porous structure for bone regeneration, Bio-Des. Manuf. 3 (2020) 15–29. https://doi.org/10.1007/s42242-019-00056-5.

[21] C. Feng, K. Zhang, R. He, G. Ding, M. Xia, X. Jin, C. Xie, Additive manufacturing of hydroxyapatite bioceramic scaffolds: Dispersion, digital light processing, sintering, mechanical properties, and biocompatibility, J Adv Ceram. 9 (2020) 360–373. https://doi.org/10.1007/s40145-020-0375-8.

[22] K. Zhang, C. Xie, G. Wang, R. He, G. Ding, M. Wang, D. Dai, D. Fang, High solid loading, low viscosity photosensitive Al2O3 slurry for stereolithography based additive manufacturing, Ceramics International. 45 (2019) 203–208. https://doi.org/10.1016/j.ceramint.2018.09.152.

[23] S.Y. Song, M.S. Park, D. Lee, J.W. Lee, J.S. Yun, Optimization and characterization of high-viscosity ZrO2 ceramic nanocomposite resins for supportless stereolithography, Materials & Design. 180 (2019) 107960. https://doi.org/10.1016/j.matdes.2019.107960.

[24] M. Pfaffinger, G. Mitteramskogler, R. Gmeiner, J. Stampfl, Thermal Debinding of Ceramic-Filled Photopolymers, MSF. 825–826 (2015) 75–81. https://doi.org/10.4028/www.scientific.net/MSF.825-826.75.

[25] Q. Chen, B. Zou, Q. Lai, Y. Wang, R. Xue, H. Xing, X. Fu, C. Huang, P. Yao, A study on biosafety of HAP ceramic prepared by SLA-3D printing technology directly, Journal of the Mechanical Behavior of Biomedical Materials. 98 (2019) 327–335. https://doi.org/10.1016/j.jmbbm.2019.06.031.

[26] F.P.W. Melchels, J. Feijen, D.W. Grijpma, A review on stereolithography and its applications in biomedical engineering, Biomaterials. 31 (2010) 6121–6130. https://doi.org/10.1016/j.biomaterials.2010.04.050.

[27] H. Li, Y. Liu, Y. Liu, K. Hu, Z. Lu, J. Liang, Effects of Solvent Debinding on the Microstructure and Properties of 3D-Printed Alumina Ceramics, ACS Omega. 5 (2020) 27455–27462. https://doi.org/10.1021/acsomega.0c03944.

[28] M. Tourbin, F. Brouillet, B. Galey, N. Rouquet, P. Gras, N. Abi Chebel, D. Grossin, C. Frances, Agglomeration of stoichiometric hydroxyapatite: Impact on particle size distribution and purity in the precipitation and maturation steps, Powder Technology. 360 (2020) 977–988. https://doi.org/10.1016/j.powtec.2019.10.050.

[29] M.A. Inam, S. Ouattara, C. Frances, Effects of concentration of dispersions on particle sizing during production of fine particles in wet grinding process, Powder Technology. 208 (2011) 329–336. https://doi.org/10.1016/j.powtec.2010.08.025.

[30] P. Navarrete-Segado, M. Tourbin, D. Grossin, C. Frances, Tailoring hydroxyapatite suspensions by stirred bead milling as pre-processing step for additive manufacturing technologies., Adv. Powder Technol. (Under Review). (2021).

[31] Phrozen Shuffle & Shuffle XL User Manuals, Dropbox Paper. (n.d.). https://phrozen3d.com/pages/manual.

[32] V. Raikos, Encapsulation of vitamin E in edible orange oil-in-water emulsion beverages: Influence of heating temperature on physicochemical stability during chilled storage, Food Hydrocolloids. 72 (2017) 155–162. https://doi.org/10.1016/j.foodhyd.2017.05.027.

[33] C.A. Schneider, W.S. Rasband, K.W. Eliceiri, NIH Image to ImageJ: 25 years of image analysis, Nat Methods. 9 (2012) 671–675. https://doi.org/10.1038/nmeth.2089.

[34] F. Granados-Correa, J. Bonifacio-Martínez, J. Serrano-Gómez, The ball milling effect on tribasic calcium phosphate and its chromium (VI) ion sorption properties, Journal of The Chilean Chemical Society - J CHIL CHEM SOC. 54 (2009). https://doi.org/10.4067/S0717-97072009000300010.

[35] P.L. Guzzo, J.B. Santos, R.C. David, Particle size distribution and structural changes in limestone ground in planetary ball mill, International Journal of Mineral Processing. 126 (2014) 41–48. https://doi.org/10.1016/j.minpro.2013.11.005.

[36] R. Newburgh, J. Peidle, W. Rueckner, Einstein, Perrin, and the reality of atoms: 1905 revisited, American Journal of Physics - AMER J PHYS. 74 (2006). https://doi.org/10.1119/1.2188962.

[37] D. Komissarenko, P. Sokolov, A. Evstigneeva, I. Shmeleva, A. Dosovitsky, Rheological and Curing Behavior of Acrylate-Based Suspensions for the DLP 3D Printing of Complex Zirconia Parts, Materials. 11 (2018) 2350. https://doi.org/10.3390/ma11122350.

[38] M. Nutan, I. Reddy, General Principles of Suspensions, in: Pharmaceutical Suspensions: From Formulation Development to Manufacturing, 2009: pp. 39–65. https://doi.org/10.1007/978-1-4419-1087-5_2.
[39] D. Quemada, Rheological modelling of complex fluids. I. The concept of effective volume fraction revisited, Eur. Phys. J. AP. 1 (1998) 119–127. https://doi.org/10.1051/epjap:1998125.
[40] J.J. Stickel, R.L. Powell, Fluid Mechanics and Rheology of Dense Suspensions, Annual Review of Fluid Mechanics. 37 (2005) 129–149. https://doi.org/10.1146/annurev.fluid.36.050802.122132.
[41] I.M. Krieger, T.J. Dougherty, A Mechanism for Non-Newtonian Flow in Suspensions of Rigid Spheres, Transactions of the Society of Rheology. 3 (1959) 137–152. https://doi.org/10.1122/1.548848.
[42] V. Tomeckova, J.W. Halloran, Flow behavior of polymerizable ceramic suspensions as function of ceramic volume fraction and temperature, Journal of the European Ceramic Society. 31 (2011) 2535–2542. https://doi.org/10.1016/j.jeurceramsoc.2011.01.019.
[43] T.-M.G. Chu, J.W. Halloran, High-Temperature Flow Behavior of Ceramic Suspensions, Journal of the American Ceramic Society. 83 (2004) 2189–2195. https://doi.org/10.1111/j.1151-2916.2000.tb01534.x.
[44] T.E. Baldock, M.R. Tomkins, P. Nielsen, M.G. Hughes, Settling velocity of sediments at high concentrations, Coastal Engineering. 51 (2004) 91–100. https://doi.org/10.1016/j.coastaleng.2003.12.004.
[45] N.-S. Cheng, Effect of Concentration on Settling Velocity of Sediment Particles, Journal of Hydraulic Engineering-ASCE. 123 (1997) 728–731. https://doi.org/10.1061/(ASCE)0733-9429(1997)123:8(728).
[46] J.F. Richardson, W.N. Zaki, Sedimentation and fluidisation. Part 1., Trans. Inst. Chem. Eng. 32 (1954) 35–53.
[47] C. Rey, O. Marsan, C. Combes, C. Drouet, D. Grossin, S. Sarda, Characterization of Calcium Phosphates Using Vibrational Spectroscopies, in: B. Ben-Nissan (Ed.), Advances in Calcium Phosphate Biomaterials, Springer Berlin Heidelberg, Berlin, Heidelberg, 2014: pp. 229–266. https://doi.org/10.1007/978-3-642-53980-0_8.
[48] K. Tõnsuaadu, K.A. Gross, L. Plūduma, M. Veiderma, A review on the thermal stability of calcium apatites, J Therm Anal Calorim. 110 (2012) 647–659. https://doi.org/10.1007/s10973-011-1877-y.
[49] S. Ramesh, K.L. Aw, R. Tolouei, M. Amiriyan, C.Y. Tan, M. Hamdi, J. Purbolaksono, M.A. Hassan, W.D. Teng, Sintering properties of hydroxyapatite powders prepared using different methods, Ceramics International. 39 (2013) 111–119. https://doi.org/10.1016/j.ceramint.2012.05.103.
[50] M. Prakasam, J. Locs, K. Salma-Ancane, D. Loca, A. Largeteau, L. Berzina-Cimdina, Fabrication, Properties and Applications of Dense Hydroxyapatite: A Review, J Funct Biomater. 6 (2015) 1099–1140. https://doi.org/10.3390/jfb6041099.
[51] J.G. Fernandes, Development and optimization of a Low Temperature Co-fired Ceramic suspension for Mask-Image-Projection-based Stereolithography, Ph.D. Thesis, Universitat de Barcelona, 2019. http://www.tdx.cat/handle/10803/667478.
[52] A. Farzadi, M. Solati-Hashjin, M. Asadi-Eydivand, N.A.A. Osman, Effect of Layer Thickness and Printing Orientation on Mechanical Properties and Dimensional Accuracy of 3D Printed Porous Samples for Bone Tissue Engineering, PLOS ONE. 9 (2014) e108252. https://doi.org/10.1371/journal.pone.0108252.
[53] T.-R. Kim, M.-S. Kim, T.S. Goh, J.S. Lee, Y.H. Kim, S.-Y. Yoon, C.-S. Lee, Evaluation of Structural and Mechanical Properties of Porous Artificial Bone Scaffolds Fabricated via Advanced TBA-Based Freeze-Gel Casting Technique, Applied Sciences. 9 (2019) 1965. https://doi.org/10.3390/app9091965.
[54] V. Karageorgiou, D. Kaplan, Porosity of 3D biomaterial scaffolds and osteogenesis, Biomaterials. 26 (2005) 5474–5491. https://doi.org/10.1016/j.biomaterials.2005.02.002.
[55] M. Houmard, Q. Fu, M. Genet, E. Saiz, A.P. Tomsia, On the structural, mechanical, and biodegradation properties of HA/β-TCP robocast scaffolds, Journal of Biomedical Materials Research. 101 (2013) 9. https://doi.org/10.1002/jbm.b.32935.
[56] C.S. Lee, S.G. Kim, H.J. Kim, S.H. Ahn, Measurement of anisotropic compressive strength of rapid prototyping parts, Journal of Materials Processing Technology. 187–188 (2007) 627–630. https://doi.org/10.1016/j.jmatprotec.2006.11.095.

[57] J. Saini, L. Dowling, J. Kennedy, D. Trimble, Investigations of the mechanical properties on different print orientations in SLA 3D printed resin, Proceedings of the Institution of Mechanical Engineers, Part C: Journal of Mechanical Engineering Science. 234 (2020) 2279–2293. https://doi.org/10.1177/0954406220904106.

[58] I. Sabree, J.E. Gough, B. Derby, Mechanical properties of porous ceramic scaffolds: Influence of internal dimensions, Ceramics International. 41 (2015) 8425–8432. https://doi.org/10.1016/j.ceramint.2015.03.044.

[59] B. Basu, Mechanical Properties of Biomaterials, in: Biomaterials for Musculoskeletal Regeneration, Springer Singapore, Singapore, 2017: pp. 175–222. https://doi.org/10.1007/978-981-10-3059-8_6.

[60] P.N. Sudha, S. Kirubanandam, J. Av, V. N, R. Kannan, Corrosion of ceramic materials, in: Fundamental Biomaterials: Ceramics, 2018: pp. 223–250. https://doi.org/10.1016/B978-0-08-102203-0.00009-3.

[61] M. Fulmer, I. Ison, C. Hankermayer, B. Constantz, J. Ross, Measurements of the Solubilities and Dissolution Rates of Several Hydroxyapatites, Biomaterials. 23 (2002) 751–5. https://doi.org/10.1016/S0142-9612(01)00180-6.

[62] N. Eliaz, N. Metoki, Calcium Phosphate Bioceramics: A Review of Their History, Structure, Properties, Coating Technologies and Biomedical Applications, Materials. 10 (2017) 334. https://doi.org/10.3390/ma10040334.

[63] S. Vahabzadeh, M. Roy, A. Bandyopadhyay, S. Bose, Phase stability and biological property evaluation of plasma sprayed hydroxyapatite coatings for orthopedic and dental applications, Acta Biomater. 17 (2015) 47–55. https://doi.org/10.1016/j.actbio.2015.01.022.

[64] S.V. Dorozhkin, M. Epple, Biological and medical significance of calcium phosphates, Angew Chem Int Ed Engl. 41 (2002) 3130–3146. https://doi.org/10.1002/1521-3773(20020902)41:17<3130::AID-ANIE3130>3.0.CO;2-1.

7. Supplementary material

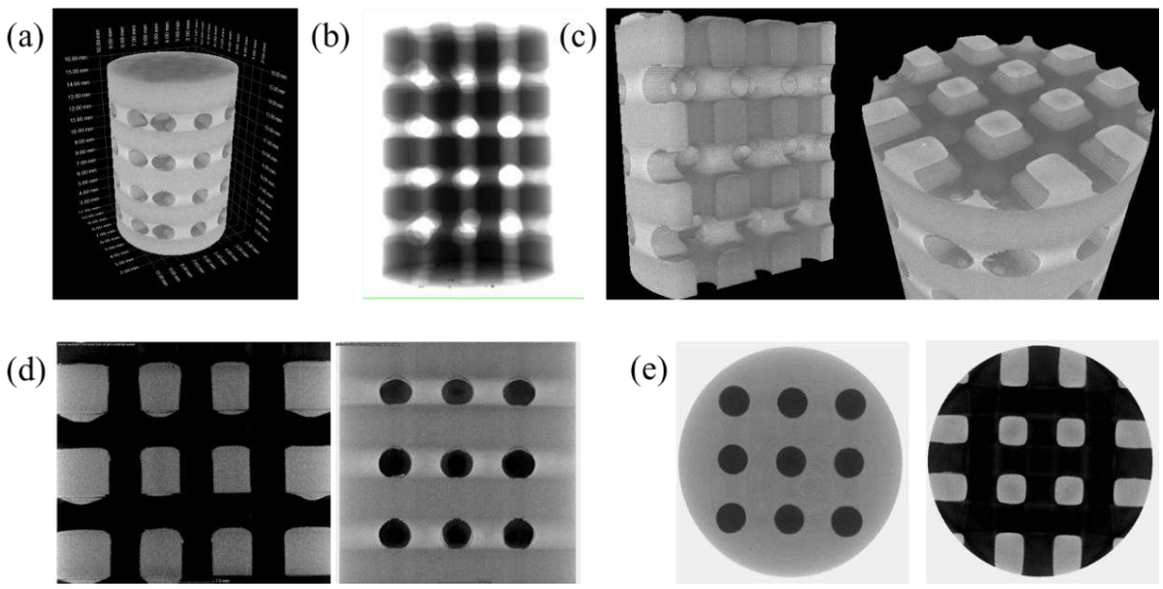

Figure S1. CT results for sintered HA scaffold printed at 0º: (a) Volume reconstruction, (b) lateral view of the scaffold, (c) volume cross-sectional views, (d) middle cross-sectional views (X, Z plane) of pores and struts, (e)middle cross-sectional views (X-Y plane) of pores and struts.

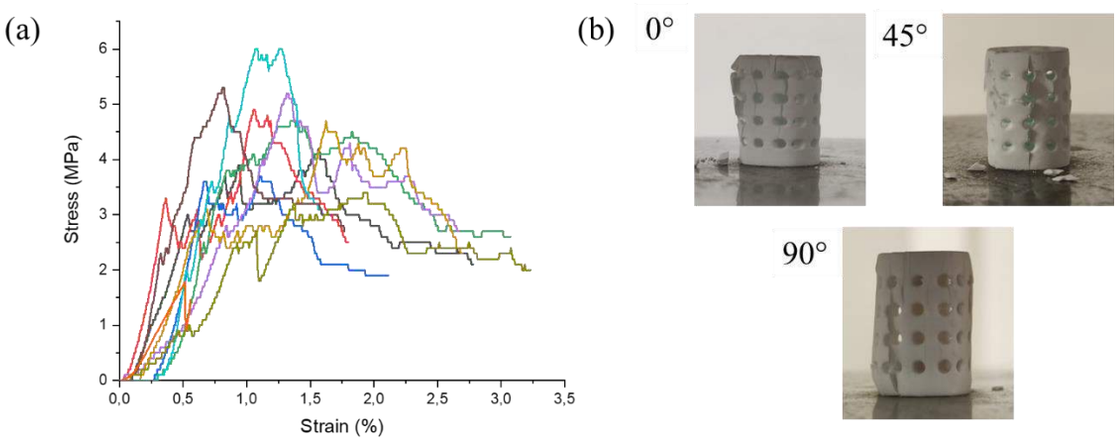

Figure S2. (a) Compilation of ten compressive stress-strain curves obtained for the sintered HA scaffolds at 45º and (b) photographs of the specimens printed at different orientations (0º, 45º, and 90º) after failure

General conclusions and future perspectives

The general objective of this thesis consisted of the development of a multi-step process for the tailoring of calcium phosphate powder properties intended for additive manufacturing technologies. These emergent technologies allow the three-dimensional shaping of parts which in combination with the bioceramic calcium phosphate materials could bring together a promising contribution for the bone tissue engineering field. However, there is not a clear definition for the steps needed to attain a powder suitable to be used as additive manufacturing feedstock. It was in our scope to develop a well-defined multi-step process for their production. Since two different additive manufacturing techniques with different feedstock requirements were designated for testing, two different groups of targeted powder properties were aimed. The synthesis of HA calcium phosphate powder was settled as the starting point of the work. Once the feasibility of a wet precipitation method for the production of stoichiometric HA powder was confirmed the following steps would be dependent on the technique envisaged.

In the first place, the power bed selective laser process (sintering/melting) (powder bed fusion category) by Nd:YAG laser (λ = 1070 nm) was established as the final application of the HA powder. This technique involves the use of a powder layer creation device that will create powder beds with controlled thickness before being selectively laser processed for densification. The quality of the powder bed is a factor influencing the performance of the printed parts. To create homogeneous powder beds the use of highly flowable powder is preferred (Hausner ratio of less than 1.25). A higher flowability is better achieved by polydisperse (span > 1) spherical microspheres (x_{50} = 30-70 µm). Another important factor influencing the properties of the printed parts is the laser absorption (should be > 60%) of the powder which affects the laser-material interaction influencing the sintering/melting phenomena, thus enlarging the processing window.

Since the as-synthetised HA particles do not meet the required properties for their use as feedstock, a series of processes were employed for the tailoring of the powder. The preparation of highly loaded HA-filled suspensions constituted of particles with reduced size was carried out by comminution via wet stirred bead milling. The control of the dispersion stability and rheological behaviour was significant to evaluate their processability. Indeed, the suspension formulation (e.g., the addition of polyelectrolyte dispersant) and operating parameters (e.g., stirrer speed, beads size, solid concentration…) were evaluated for the optimization of the process. HA-filled suspensions with characteristics such as a high concentration ($w_{HA} \geq$ 0.50) of fine particles (x_{50} = 0.2-1.5 µm) dispersed by addition of a polyelectrolyte (2.1 $mg.m^{-2}$ of dispersant Darvan C) and showing a low viscosity (< 0.1 Pa.s) were prepared for their use as feedstock in a posterior spray drying step.

A spray drying step would dry the particles while shaping them into microspherical agglomerates. In the same way as for the wet milling step, the suspension formulation (binder content) and the dryer parameters (e.g., feed rate, air pressure, inlet temperature…) were examined to control the recovery rate and the properties (morphology, distribution, hardness…) of the resulting HA microspheres to better tailor them for laser processing. After the process, the resulting HA microspheres fulfilled the different targeted

properties such as particle size (x_{50} = 59.6 µm), dispersion (span = 1.78), and flowability (Hausner ratio = 1.12) for its utilisation in 3D laser processing.

To increase the laser absorption of the microspheres, mixing with a near-infrared absorption additive as carbon graphite was assessed to produce powder blends. A laser absorption of 66.8±0.1% at λ = 1070 nm was measured by adding a 5 wt. % of graphite, thus making the powder processable by the laser. The processability of the powder produced was confirmed in a commercial powder bed laser process equipment. After a methodical study of the printing parameters (e.g., laser power, scanning speed, laser defocus…), different processing windows were obtained depending on the amount of graphite or by substitution of HA by ClA microspheres. The surface finishing and calcium phosphate transitions from HA into other phases, such as α-TCP and TTCP, were studied and discussed to provide an overview of the effect of the experimental conditions. The HA powder feedstock showing a balance between low balling phenomena and a high amount of HA after the process (46.5 wt.% HA) was the one containing a 10 wt. % of graphite, printed at E_d = 288 J.cm^{-3} (laser power: 36 W; scanning speed: 25 mm.s^{-1}). Then, it was possible to produce solid parts mainly composed of HA with properties that could be valuable for their utilisation in bone tissue engineering like an interconnected porosity (50 vol. %) through the whole piece. However, even after a posterior thermal treatment, they presented low compressive strength (0.049±0.001 MPa) which could limit its use, needing further optimization. The low mechanical properties were in part attributed to the phase transition from HA into other calcium phosphate phases causing an uneven grain growth. For comparison, the synthesis of a small batch of ClA powder, a more thermally stable calcium phosphate phase, was carried out. This powder did not show phase transition during the treatment by laser confirming improved suitability for the process. Indeed, the circular pattern samples printed at higher energy density, E_d = 336 J.cm^{-3} (laser power: 42 W, scanning speed: 25 mm.s^{-1}) showed a smoother surface finishing with fewer signs of balling phenomena. However, the amount of powder prepared during this work was not enough for the printing of solid parts for mechanical testing.

Our second goal for the tailoring of HA powders was their use in a masked stereolithography apparatus, also called LCD manufacturing process, which is one of the VAT photopolymerization techniques. In this case, the feedstock should be composed of a highly concentrated HA-filled photocurable slurry showing suitable dispersion stability, rheological behaviour, and, after printing, a good response to debinding-sintering (avoiding the formation of cracks). More specifically, it is expected that the suspension shows slow sedimentation of the particles (overall stability defined by a Turbiscan stability index < 2) to avoid the block of the LCD screen and low viscosity (< 5 Pa.s at a shear rate of 0.1 s^{-1}) for a proper spreading in the resin tank. The suspension should contain HA particles with particle size, x_{50} = 1-20 µm since it would allow a correct debinding-sintering of the parts. A commercially available organic photocurable resin base, PEG200 (as diluent), and three HA powders having different particle size distributions were employed for the preparation of the slurries and comparison of their properties. These powders were obtained from the direct synthesis and calcination of HA, from the wet milling process, and an alternative planetary ball milling process. The slurry prepared with the powder obtained from the planetary ball milling process and with an intermedium particle size, x_{50} = 12.1 µm, exhibited the most suitable properties for masked

stereolithography. At a concentration of 50 vol. %, it presented a low viscosity (< 5 Pa.s at a shear rate 1 s^{-1}) and high stability (TSI < 2) for a duration of three hours, corresponding to the time needed for the process. The suitability of the suspension was confirmed by direct testing in a commercial MSLA printer.

After printing of the green body scaffold, (ceramic-polymer composite) a debinding-sintering process (1250ºC as maximum temperature) was performed to completely pyrolyze the organic resin and obtain the sintered ceramic part free of polymer. This step was designed after the thermal analysis of the resin degradation to define a temperature pattern allowing a controlled diffusion of gas formed during the pyrolysis avoiding the formation of cracks. The macrostructural and mechanical properties of the parts were examined as well as its dissolution rate. The parts printed at 45º from the printing surface showed the highest mechanical properties (compressive strength of 4.92±0.33 MPa) and a slow degradation rate (a Ca^{2+} ion release of 1.26 $mg.l^{-1}$ for 72h). These results indicate that this process could be an interesting method for the production of bioceramic parts intended for bone tissue engineering. Especially, in surgery for guided bone regeneration in case of minor or non-load bearing voids requiring slow resorption properties.

This thesis work gathers a series of arguments in favour of the different particle tailoring processes chosen for the production of calcium phosphate powders intended for the two additive manufacturing techniques. Additional ideas and future perspectives were raised during the course of the present work; however, they could not be developed due to the time limitation of the project. A brief description of these concepts is offered below:

The shortening of the processing time compared with other beads milling methods and the energy effectiveness of the process confirmed the stirrer bead milling as an interesting addition to the production line of HA powder intended for additive manufacturing technologies. An interesting modification for the production of controlled-size powders for VAT photopolymerization on a higher scale, such as in industry, could be the direct milling of the powder suspended in a photocurable resin (instead of water). This modification could shorten the production process and increases the energy efficiency skipping the filtering, drying, and resuspension steps. However, special attention should be paid to the viscosity of the slurry which could bring handling difficulties. In this case, the use of diluents could be crucial for the decrease in viscosity during the process.

The spray drying process was demonstrated to be an excellent method for the control of the microspherical particle morphology during the drying of the powder. Still, a deeper experimental design could allow us to better understand the effect of the different operating parameters and the synergy between them (e.g., the feed rate and inlet temperature) into the process outcomes such as the process recovery rate. It would be interesting to perform a deeper study on the hardness and resistance to deformation of the HA microspheres containing an organic binder and their effect on the performance in a 3D laser process. Moreover, a more exhaustive flowability comparison of powders with different particle size distributions could help us to improve the flowability of the powder. Indeed, the mixing of two microspherical powders with different particle sizes to produce bimodal powders could improve the flowability of the individual powder. In this case, one of the powders could act as a lubricant.

The processability of the HA microspheres was then evaluated through direct testing in a powder bed selective laser process equipment and it was demonstrated that the use of graphite as a near-infrared absorption additive enlarged successfully the processing window. Indeed, ClA powder appeared to be an excellent solution to solve the phase transition observed in HA. However, further effort should be made on the analysis of the processing window produced by ClA at different graphite amounts. The use of this powder could improve the mechanical properties of the solid parts if their printing is achieved. Moreover, once the solid parts are printed the conversion from ClA to HA could be possible at high-temperature hydrothermal conditions, thus recovering the HA properties if preferred. Another possibility for the enhancement of the properties of the 3D printed ceramic parts could be their toughening and functionalization by biopolymer coatings and infiltration [1]. This could result in a combination of bioactivity, improved mechanical properties, and drug or growth factor delivery capability, being a candidate for bone regeneration strategies. The use of water-soluble powders (e.g., NaCl and NaNO3) instead of graphite as absorption additives could facilitate their removal after laser printing through dissolution in a water immersion step [2]. During this work, a second 3D laser printer with a different design was tested, however the absence of powder bed compaction, the more limited range of laser parameters, and the impossibility to print under air instead of N_2 made impossible the printing of any sample (also influenced by the very narrow processing window of this kind of materials). The study of the effect of these parameters (e.g. degree of powder bed compaction, the flowability of powders, O_2 level in the chamber atmosphere…) on the properties of the printed parts could be an interesting contribution to the understanding of the HA laser printing process. Works focused on the simulation of the laser-material interaction would shorten the time needed by foreseen the results obtained by experimental analysis. They could also serve as a support for the interpretation of the process.

The preparation of HA-filled photocurable suspensions intended for masked stereolithography (or LCD manufacturing process) was achieved by comparison of powders. In this case, a short planetary ball milling step was enough to improve the behaviour of the powder in suspension. Even if the printed scaffolds showed promising results for their use as non-weight-bearing implants, still further investigations should be done on the evaluation of their bioactivity (e.g., cell proliferation). The increase in temperature (up to 120ºC) during the printing to reduce the viscosity of the resin and printing times is named hot lithography. This technology would allow the printing of highly loaded HA-filled suspensions (> 50 vol. %) whose handling is not possible at room temperature due to the high viscosity. This would lead to a faster production of more dense ceramic parts and better control of the porosity. One of the disadvantages of this technique is the debinding-sintering temperatures which reduce the biocompatibility of the process. The use of biocompatible photocurable compounds which could be used as-printed, such as hydrogels, would avoid this drawback, opening the possibility of combining, in addition to bioceramics, cells, and growth factors in the suspension feedstock.

[1]A. Philippart, A.R. Boccaccini, C. Fleck, D.W. Schubert, J.A. Roether, Toughening and functionalization of bioactive ceramic and glass bone scaffolds by biopolymer coatings and infiltration: a review of the last 5 years, Expert Review of Medical Devices. 12 (2015) 93–111. https://doi.org/10.1586/17434440.2015.958075.
[2]N.K. Tolochko, Y.V. Khlopkov, S.E. Mozzharov, M.B. Ignatiev, T. Laoui, V.I. Titov, Absorptance of powder

materials suitable for laser sintering, Rapid Prototyping Journal. 6 (2000) 155–161. https://doi.org/10.1108/13552540010337029.
[3]C. Shuai, P. Feng, C. Gao, Y. Zhou, S. Peng, Simulation of dynamic temperature field during selective laser sintering of ceramic powder, Mathematical and Computer Modelling of Dynamical Systems - MATH COMPUT MODEL DYNAM SYST. 19 (2012) 1–11. https://doi.org/10.1080/13873954.2012.689769.